# Towards reliable modeling of excited states of uranium compounds

Paweł Tecmer

VRIJE UNIVERSITEIT

# Towards reliable modeling of excited states of uranium compounds

ACADEMISCH PROEFSCHRIFT

te verkrijging van de graad Doctor aan
de Vrije Universiteit Amsterdam,
op gezag van de rector magnificus
prof. dr. L. M. Bouter
in het openbaar te verdedigen
ten overstaan van de promotiecommissie
van de faculteit der Exacte Wetenschappen
op 2 oktober 2012 om 11:45 uur
in de aula van de universiteit
De Boelaan 1105

door
Paweł Tecmer
geboren te Kwidzyn, Polen

promotor: prof. dr. Lucas Visscher

# Contents

# Part I

# INTRODUCTION

# 1 Introduction

> One never notices what has been done; one can only see what remains to be done.
>
> Maria Skłodowska-Curie

## 1.1 Preface

Actinides are $f$-block elements and possess properties that are different from the rest of elements in the periodic table, *e.g.*, all of them have very large atomic radii and their isotopes are radioactive. Moreover, most actinides have a large number of oxidation states, with the most stricking example of plutonium which in aqueous solution may contain four oxidation states at the same time [1, 2]. The unique coordination possibilities [3, 4] and broad application in nuclear chemistry of actinides attracted attention of many experimentalists and theoreticians during the last decades. However, actinide chemistry remains a developing field which requires further explanations and calls for quantum chemical calculations.

## 1.2 Quantum Chemistry of Actinides — Features and Difficulties

Actinides cover the elements with atomic numbers in the range of 90–103 (Ac: [Rn]$6d^1 7s^2 5f^0$ – Lr: [Rn]$5f^{14} 6d^1 7s^2$) and, apart from actinium and thorium, contain a fully filled $4f$-shell and a partially filled $5f$-shell. The high degeneracy of the $f$-shell gives rise to a large number of possible (nearly) degenerate electronic

states. In addition to that, the $f$-shell might be accompanied by an open $6d$- and $7s$-shell, respectively, which further increases the complexity of the valence electronic structure because electrons can be distributed in three spatially different, yet energetically closely-lying orbitals [5, 6]. More difficulties for standard quantum chemical methods arise when a large number of fully occupied orbitals must be considered in order to account for a significant amount of the correlation energy. Even more challenging from a computational point of view is the proper description of electron correlation where the electron density is high as it often occurs in actinides.

Since the actinide series concerns heavy elements, relativistic effects have also to be taken into account. Within the relativistic picture, the actinide $s$- and $p$-orbitals become contracted which causes a change of the electronic shielding of the nuclear attraction and an indirect destabilization of the orbital energy [7]. Besides, significant expansion of the valence $5f$-orbitals makes the electrons chemically more active [1, 2].

Also, the interaction of the electron spin with the magnetic field induced by a charge in relative motion, referred to as *spin–orbit effects* [8], increases and inclusion of spin–orbit coupling (SOC) is mandatory. The relativistic splitting of open-shell $p$-, $d$- and $f$-orbitals into the $p_{1/2}$ and $p_{3/2}$, $d_{3/2}$ and $d_{5/2}$, and $f_{5/2}$ and $f_{7/2}$ counterparts further increases the number of nearly degenerate states.

Complex electronic structures are observed for molecular actinide compounds [6], in particular, those containing early actinides, *e.g.*, U, Np and Pu, where donation from the nearest ligands to the actinide center shifts and reorders the close-lying energy levels. While this poses difficulties for (relativistic) quantum chemistry, it gives rise to a number of novel actinide compounds coordinated in a way that has not been observed anywhere else in the periodic table and still requires a proper understanding on a sound theoretical basis [9–14]. Therefore, the challenge for quantum chemists is not simply to predict structures and molecular properties of actinide-containing molecules, but also to explain their unusual chemical behavior.

## 1.3 Chemistry of Uranium

Uranium oxides were the first uranium-containing compounds discovered by Klaproth already in 1789. Yet, the chemistry of uranium was not explored much until the XX-th century required the development of the nuclear fuel and isotopic enrichment technology [15].

Nowadays, a number of uranium-containing complexes, in which the oxidation

state of the uranium atom varies from +III to +VI, while the coordination number lies in the range of 3 to 8 is known [1, 4]. The most important groups of uranium compounds are halides, *e.g.*, $UF_{3-6}$, $UCl_{3-6}$, $UBr_{4-5}$ and $UI_3$, hydrides, *e.g.*, $UH_{1-3}$, and oxides, *e.g.*, $UO_2$, $U_4O_9$, $U_3O_8$ and $UO_3$ [1, 2].

Half of the 2000 X-ray structures of uranium complexes available at the Cambridge Structural Database [16] contain the uranyl dication [17]. A dominant feature of uranium chemistry is therefore the uranyl ion $[UO_2]^{2+}$ which represents a particularly stable molecule and forms a variety of composites containing 3 to 6 ligands in the equatorial plane. Such compounds are very attractive for chemistry and gives rise to a continued development of this field of research. Of special importance are those uranyl complexes that are essential for reprocessing of nuclear waste as well as catalysis [18–21]. Besides, a new group of uranium-containing complexes that are isoelectronic equivalences of $[UO_2]^{2+}$, *i.e.*, $NUO^+$, and CUO gained a lot of interest in experimental and theoretical studies in the past few years [22–28]. Accurate spectroscopic experiments have been supported by reliable quantum chemical calculations and provided further insights into the properties of these class of compounds [29–36].

# 2

# Electronic Spectroscopy

> The methods of theoretical physics should be applicable to all those branches of thought in which the essential features are expressible with numbers.
>
> Paul A. M. Dirac

In general, spectroscopy deals with the energetical structure and properties of atoms and molecules as well as elementary particles by observation and analysis of the energy distribution of radiation (X-rays, light, *etc.*) emitted, absorbed or scattered by the physical object. In 1900, the German physicist Max Planck [37] showed that matter interacts only with a certain portion ("quanta") of energy,

$$E = h\nu, \tag{2.1}$$

where $E$ is the energy in J, $h = 6.626 \times 10^{-34}$ Js is Planck's constant and $\nu$ denotes the frequency [1/s]. This interaction results in unique spectral lines of each individual system under study, called a *spectrum*. While Planck considered the quantum as a portion of energy, Einstein [38] extended its meaning to a particle with an energy quantum of $h\nu$ and named it photon [39–41]. Dependent on the photon wavelength involved in the transition from one discrete energy level to another different kinds of spectroscopy can be distinguished which is illustrated in Figure (2.1). When the electron in the molecule is promoted from the electronic ground state to one of the excited states, *i.e.*, the potential energy surface of the molecule is changed, we refer such phenomena to as *electronic excitations*. This can occur when an electron absorbs a photon or the energy of another electron. In this type of spectroscopy, called *electronic spectroscopy*, transition energies between the

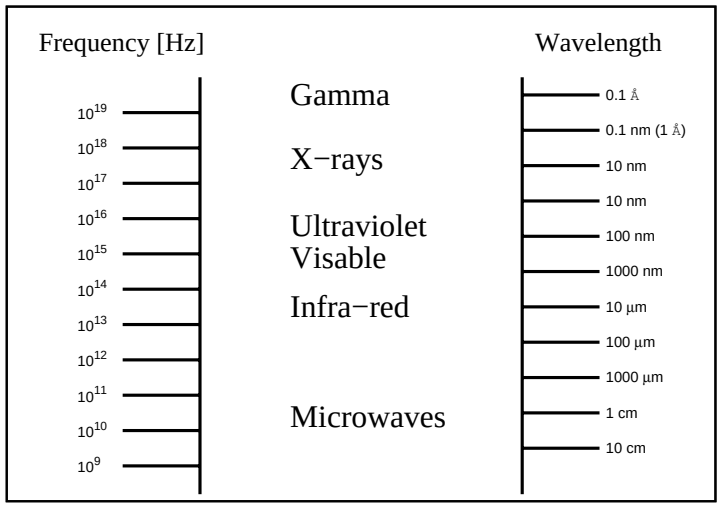


**Figure 2.1**: *Part of the electromagnetic spectrum which is important for molecular spectroscopy.*

ground state and the $n$-th excited electronic state, $h\nu = E_0 - E_n$, as well as their intensities, are measured.

The energy necessary for such an electron rearrangement in the valence region is usually detected in the visible and ultraviolet region of the electromagnetic spectrum (see Figure (2.1)), *i.e.*, in the range of some few eV (usually 2–20 eV) [40, 42].

A detailed analysis of the electronic spectrum becomes more complex for molecules than for atoms due to the considerable amount of available states. In the molecular case, the spectrum contains additionally many (sub)levels which result from the discrete vibrational and rotational energy levels, their contribution being often in the range of 0.1 and 0.005 eV, respectively. Since the influence of the latter is usually beyond the desired accuracy, it can be omitted for most purposes [42].

When the electron is transferred from the ground state to one of the higher-lying unoccupied orbitals (excited-state), it might end in the higher-lying vibrational state ($\nu_0 \rightarrow \nu_n$ transition), while the structure of the molecule remains the same, or it might go to the same ground vibrational state ($\nu_0 \rightarrow \nu_0$), but its geometry changes. The former case is referred to as *vertical excitations*, and the latter one to *adiabatic excitations*. The process of vertical excitation is illustrated in Figure (2.2), where the horizontal lines indicate different vibrational levels. The vertical excitation energies can overlap with a number of vibrational states at the same

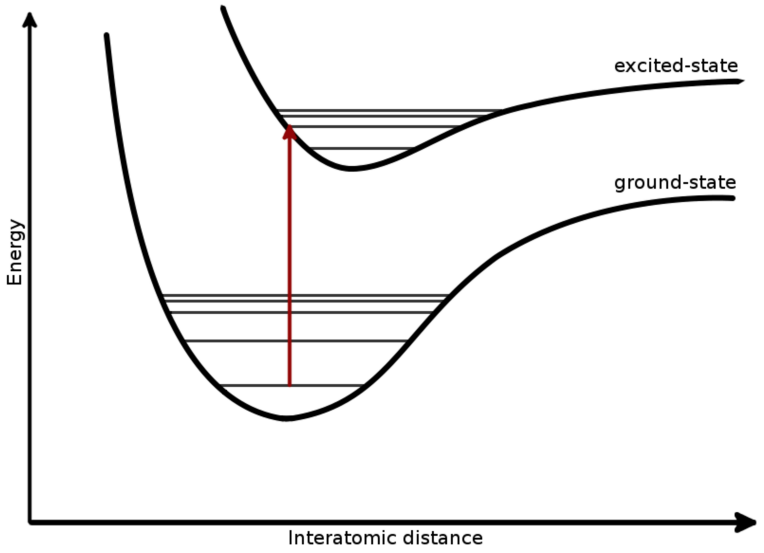


**Figure 2.2**: *Vertical excitation.*

time, as illustrated by the red vertical arrow in Figure (2.2). According to the Franck–Condon principle, this results in high intensities for the transitions [42].

## 2.1 Electronic Transitions in Actinides

The excitation energies in uranium-containing complexes possess a rather mixed character, for which several characteristic types of transitions can be distinguished:

(i) *vibronic.* In centrosymmetric molecules, dipole transitions that conserve parity, symmetry or asymmetry with respect to an inversion center — *gerade (g)* and *ungerade (u)* — are forbidden. This is known as Laporte selection rule. Hence, only transitions where the symmetry changes — g $\rightarrow$ u and u $\rightarrow$ g — are allowed. However, forbidden transitions can have nonzero intensities if the center of symmetry is distorted, which can be caused, for instance, by asymmetric vibrations of the molecule. Such a transition energy is therefore called vibronic [43, 44].

(ii) *local.* In the lower part of the electronic spectrum of uranium complexes, electronic transitions occur more or less in the same region of the molecule and have a local (L) character. Most of the excitation energies of that type

are associated with short electronic movements and cover the (internal) uranium $f$–$f$ transitions [5].

(iii) *charge-transfer.* Electrons in a molecule can be transferred over a distance and carry charge from one part of the molecule to another. Such transitions are called charge-transfer (CT). In particular, if an electron is transferred from one of the ligands to the metal center, a ligand-to-metal charge-transfer (LMCT) is observed. In uranium compounds, charge is usually transferred from one of the ligand $\pi$-orbitals to the non-bonding $\phi$- or $\delta$-orbitals of the uranium atom ($\pi \rightarrow \phi$ and $\pi \rightarrow \delta$ electronic transitions). However, a charge-transfer in the opposite direction can also be possible, which is denoted as metal-to-ligand charge-transfer (MLCT) [42, 44]. A CT from one ligand of the uranium complex to another ligand presents a third class of observable charge redistributions.

(iv) *Rybdberg.* Rydberg (R) transitions comprise the promotion of electrons to the outer region of the molecule, *i.e.*, over a long distance, yet, without charge-transfer, and usually into a state with a very high principal quantum number [40].

# 3 Outline

> One can measure the importance of a scientific work by the number of earlier publications rendered superfluous by it.
>
> David Hilbert

Actinides are $f$-block elements and exhibit interesting chemical properties. Their unique coordination possibilities [3, 4] and broad application in nuclear chemistry attracted the attention of many experimentalists and theorists. An accurate description of electronic transitions in uranium-containing complexes remains a challenge for quantum chemistry since an accurate treatment of both electron correlation and relativistic effects is required. The aim of this thesis is therefore to study the performance of different quantum chemical methods in balancing accuracy and computational expenses in the calculation of electronic spectra of uranium-containing complexes, in particular, compounds with large ligands, which was not investigated so far.

In part II, that covers chapters 4 – 8, a short overview of the theoretical methods employed in this thesis is given, with a special focus on density functional theory and its time-dependent generalization as well as on coupled cluster methods.

In part III, the electronic spectra of actinide compounds investigated in this thesis are discussed. In chapter 9, a benchmark study of available approximate exchange–correlation functionals in calculating electronic spectra of the $[UO_2]^{2+}$, $[NUO]^+$ and NUN molecules is presented. The complete active space second order perturbation theory and the multi-reference coupled cluster methods are used to obtain highly accurate reference data. Moreover, the influence of the adiabatic local density approximation in the exchange–correlation kernel on the excitation energies is analyzed.

In chapter 10, charge-transfer excitation energies of the uranyl molecule as well as the uranyl tetrachloride complex are investigated. Four-component relativistic time-dependent density functional theory is devoted to study the vertical excitation energies of the $[UO_2]^{2+}$ and $[UO_2Cl_4]^{2-}$ molecules and the adiabatic excitation energies as well as vibrational frequencies of the excited-states of the $[UO_2Cl_4]^{2-}$ molecule.

In chapter 11, electronic transitions of the CUO and $CUONg_4$ (Ng=Ne, Ar, Kr, Xe) molecules are investigated with different theoretical methods. For the $CUONg_4$ complexes, time-dependent density functional theory (TD-DFT) is utilized to study vertical excitation energies, upon which the frozen density embedding (FDE) scheme is employed to investigate the accuracy of currently available kinetic energy functionals. Besides, the wave function theory in density functional theory (WFT-in-DFT) approach is also applied, where the intermediate Hamiltonian Fock-space coupled cluster with singles and doubles method is utilized for the active system (CUO), while the embedding potential for the $Ng_4$ environment is obtained from DFT calculations.

The experience gained in chapters 9 – 11 in studying small uranium model compounds is then applied to large uranium-containing complexes presented in chapter 12. In particular, we focus on the electronic spectrum of the $U^{VI}O_2$(saldien) and $[U^{V}O_2(\text{saldien})]^{-}$ complexes. For the first system, TD-DFT and the active space variant of completely renormalized equation of motion coupled cluster with singles, doubles and non-iterative triples (CR-EOMCCSD(T)) calculations were performed. The second complex was investigated within the TD-DFT framework and compared to available experimental data, including the intensities of spectral lines.

Finally summaries in English and Dutch, the list of acronyms, the bibliography and the list of publications are given.

# Part II

# THE ELECTRONIC STRUCTURE PROBLEM

# 4 Introduction

> To those who do not know mathematics it is difficult to get across a real feeling as to the beauty, the deepest beauty, of nature. If you want to learn about nature, to appreciate nature, it is necessary to understand the language that she speaks in.
>
> Richard Feynmann

Within the Born–Oppenheimer approximation [45], the time-dependent Schrödinger equation [46] represents the fundamental quantum mechanical equation of physics and chemistry. It describes the evolution of the electronic wave function $\tilde{\Psi}(\mathbf{r}, t)$ with time,

$$i\hbar \frac{\partial \tilde{\Psi}(\mathbf{r}, t)}{\partial t} = \hat{H}\tilde{\Psi}(\mathbf{r}, t), \tag{4.1}$$

where $\tilde{\Psi}(\mathbf{r}, t)$ depends on all electronic coordinates $\mathbf{r} = \{\mathbf{r}_1, \mathbf{r}_2, \ldots, \mathbf{r}_N\}$ and an universal time $t$.

In general, $\hat{H}$ is some time-dependent Hamiltonian which describes the interaction of the electrons of the system under study. A special case arises when the Hamiltonian does not depend explicitly on time, so that the time-dependence of the electronic wave function can be separated exactly. The electronic wave function is then a simple product of the solutions of a pure spatial problem and of a pure time-dependent problem, $\tilde{\Psi}(\mathbf{r}, t) = \Psi(\mathbf{r})\tau(t)$. The former is commonly known as the time-independent Schrödinger equation which reads

$$\hat{H}\Psi(\mathbf{r}) = E\Psi(\mathbf{r}), \tag{4.2}$$

where $E$ represents the energy eigenvalue of the Hamiltonian, and $\Psi(\mathbf{r})$ depends only on the spatial coordinates $\mathbf{r}$ of the electrons. Note that the total electronic wave function $\tilde{\Psi}(\mathbf{r}, t) = \Psi(\mathbf{r})\tau(t)$ depends exponentially on time. In general, the time-independent Hamiltonian can be written as follows

$$\hat{H} = \hat{T} + \hat{W} + \hat{V}, \tag{4.3}$$

where $\hat{T}$ is the kinetic energy operator,

$$\hat{T} = \sum_{i=1}^{N} \left( -\frac{1}{2}\nabla_i^2 \right), \tag{4.4}$$

$\hat{W}$ the two-electron operator,

$$\hat{W} = \sum_{i}^{N} \sum_{j<i}^{N} \left( \frac{1}{|\mathbf{r}_i - \mathbf{r}_j|} \right), \tag{4.5}$$

describing the Coulomb interaction between electrons $i$ and $j$, and $\hat{V}$ some external potential (field),

$$\hat{V} = \sum_{i=1}^{N} v(\mathbf{r}_i). \tag{4.6}$$

In Eqs. (4.4)–(4.6), the summation goes over the number of electrons in the system $N$ and the double sum in Eq. (4.5) is restricted ($j < i$) in order to avoid double counting of the inter-electronic repulsion. We should note that in the above equations Hartree atomic units ($\hbar = m_e = e = 4\pi\epsilon_0 = 1$) have been employed, which will be continued throughout this thesis.

Since the electronic wave function $\Psi(\mathbf{r})$ is a function of 3N coordinates, it requires high computational cost to solve Eq. (4.2) for large systems, in particular, molecules containing heavy elements. Instead of describing the electronic structure of the atom or molecule by its wave function, its electron density $\rho(\mathbf{r})$ can be used. The electron density [41, 47] is given by [1],

$$\rho(\mathbf{r}_1) = N \int d\mathbf{r}_2 \ldots d\mathbf{r}_N d\sigma_{\mathbf{1}} \ldots d\sigma_N |\Psi(\mathbf{r}_1\sigma_1, \mathbf{r}_2\sigma_2, \ldots, \mathbf{r}_N\sigma_N)|^2, \tag{4.7}$$

where the integration is carried out over all spin and spatial coordinates apart from one set of spatial coordinates, which was taken to be that of electron 1. As a result we obtain a three-dimensional function which contains the position of

[1] Since the electrons in the system are indistinguishable, the $\mathbf{r}_i$-notation is employed which denotes one arbitrary electron $i$.

only one electron. Note that, in addition to the 3N spatial coordinates, N spin coordinates are considered. Electrons as fermions with a half spin should obey the Fermi-Dirac statistics and follow the Pauli exclusion principle [40]. Since the Schrödinger equation do not depend on any spin variable, the spin is introduced *ad hoc* in the electronic wave function, which now should read $\Psi(\mathbf{x}) = \Psi(\mathbf{r}, \sigma) = \Psi(\mathbf{r}_1, \ldots, \mathbf{r}_N, \sigma_1, \ldots, \sigma_N)$. Integration of the electron density over the whole space — per definition — results in the number of electrons,

$$\int d\mathbf{r}\rho(\mathbf{r}) = N. \tag{4.8}$$

An alternative expression for the electron density can be derived using the Dirac delta function $\delta(\mathbf{r}_i - \mathbf{r}_1)$,

$$\rho(\mathbf{r}_1) = \sum_{i=1}^{N} \langle \Psi(\mathbf{r}) | \delta(\mathbf{r}_i - \mathbf{r}_1) | \Psi(\mathbf{r}) \rangle. \tag{4.9}$$

# 5

# Density Functional Methods

> On the ordinary view of each species having been independently created, we gain no scientific explanation.
>
> Charles Darwin

## 5.1 Hohenberg–Kohn Theorems

In 1964, Hohenberg and Kohn [48] proved — by *reductio ad absurdum* — that there is a one-to-one correspondence between the external potential $v(\mathbf{r}_1)$ and the electron density $\rho(\mathbf{r}_1)$ up to an arbitrary constant. Therefore, $\rho(\mathbf{r}_1)$ uniquely determines the non-degenerate ground-state wave function $\Psi(\mathbf{r})$ and *vice versa*. This statement is known as the first Hohenberg–Kohn theorem.

The second Hohenberg–Kohn [48] theorem states that there exists a functional of the electron density [1] $E_v[\rho(\mathbf{r})]$ and its corresponding external potential $v(\mathbf{r})$, which minimizes the ground-state energy of the N-electron system described by Eq. (4.8),

$$E_v[\rho(\mathbf{r})] \geq E_v[\rho_0(\mathbf{r})] = E_0, \tag{5.1}$$

where $\rho(\mathbf{r})$ represents an approximate electron density, and $\rho_0(\mathbf{r})$ the ground-state density with ground-state energy $E_0$. In Eq. (5.1), the subscript $v$ was introduced to denote the $v$-representability of the system, *i.e.*, to assure that a given density after minimization still correspond to the ground state of the potential $v(\mathbf{r})$. Another important aspect is that only densities associated with an anti-symmetric $N$-electron wave function $\Psi(\mathbf{r})$ should be considered which are termed

[1] Note that, the $\mathbf{r}_i$-notation has been dropped out here and will be used only when necessary.

$N$-representable densities [41]. The necessary conditions are that the density has to be positive everywhere in space, integrate to the total number of electrons (Eq. (4.8)), and satisfy the square-integrability condition

$$\int d\mathbf{r} |\nabla \rho^{\frac{1}{2}}|^2 < \infty. \tag{5.2}$$

Unfortunately, the exact expression for $E_v[\rho(\mathbf{r})]$ is unknown and has to be approximated.

## 5.2 The Kohn–Sham Equation

A very convenient way to find an accurate expression for the energy functional $E_v[\rho(\mathbf{r})]$ was proposed by Kohn and Sham [49]. They introduced the idea of a reference system of non-interacting electrons with an external — also called effective — potential chosen in such a way that its electron density equals the electron density of the fully interacting system. In other words, the external potential $v_s$ is described in such a way that its electron density $\rho(\mathbf{r})$ does not change in comparison with the electron density of the fully-interacting system [41].

The Kohn–Sham (KS) theorem facilitated to overcome the problems encountered at the early stage of density functional theory (in the 1920s) by Thomas, Fermi and Dirac [50, 51] with a qualitative description of the kinetic energy functional. While there were known explicit density functionals for the classical electron-electron and nuclei-electron interaction terms, the kinetic energy functional posed a challenge and could only be determined very inaccurately, leading to results that were qualitatively incorrect. The situation changed altogether with the introduction of the fictitious KS system, since the kinetic energy of the non-interacting system is a very good approximation to the fully interacting one.

The Hamiltonian of the non-interacting reference system possesses a very simple form

$$\hat{H} = -\sum_{i=1}^{N} \frac{1}{2}\nabla_i^2 + \sum_{i=1}^{N} v_s(\mathbf{r}_i), \tag{5.3}$$

where the sum runs over the total number of electrons in the molecule under study.

The Kohn–Sham ground-state solution is given by a single Slater determinant constructed from the so called KS orbitals $\{\phi_i\}$, which are solutions of the following eigenvalue problem

$$\left(-\frac{1}{2}\nabla^2 + v_s(\mathbf{r})\right)\phi_i(\mathbf{r}) = \epsilon_i \phi_i(\mathbf{r}), \tag{5.4}$$

where $\phi_i$ is a single-particle function of the non-interacting reference system. The potential $v_s(\mathbf{r})$ — usually called the Kohn–Sham potential — is written as

$$v_s(\mathbf{r}) = v_{\text{ext}}(\mathbf{r}) + v_{\text{H}}(\mathbf{r}) + v_{\text{xc}}(\mathbf{r}), \tag{5.5}$$

where the $v_{\text{ext}}(\mathbf{r})$ is the external potential that typically results from the electron–nuclei interaction, but might also contain contributions from other external potentials [41], $v_{\text{H}}(\mathbf{r})$ is the Hartree potential,

$$v_{\text{H}}(\mathbf{r}) = \frac{\delta J[\rho]}{\delta \rho(\mathbf{r})} \tag{5.6}$$

and $v_{\text{xc}}(\mathbf{r})$ is the unknown exchange–correlation potential,

$$v_{\text{xc}}(\mathbf{r}) = \frac{\delta E_{\text{xc}}}{\delta \rho(\mathbf{r})}. \tag{5.7}$$

For convenience of analysis, the total energy functional $E_v[\rho(\mathbf{r})]$ is decomposed into

$$E_v[\rho] = v^{\text{nuc}}(\mathbf{R}) + \int d\mathbf{r}\rho(\mathbf{r})v(\mathbf{r}) + T_s[\rho] + J[\rho] + E_{\text{xc}}[\rho], \tag{5.8}$$

where $v^{\text{nuc}}(\mathbf{R})$ is nuclear repulsion energy with the electron-nuclei distance of $\mathbf{R}$ and $T_s[\rho]$ denotes the kinetic energy of a system of non-interacting electrons with density $\rho$, [2]

$$T_s[\rho] = \sum_{i=1}^{N} \langle \phi_i | -\frac{1}{2}\nabla^2 | \phi_i \rangle. \tag{5.9}$$

$J[\rho]$ is the classical Coulomb repulsion (Hartree) energy,

$$J[\rho] = \frac{1}{2}\int\int d\mathbf{r}_1 d\mathbf{r}_2 \frac{\rho(\mathbf{r}_1)\rho(\mathbf{r}_2)}{|\mathbf{r}_1 - \mathbf{r}_2|}, \tag{5.10}$$

while the last term $E_{\text{xc}}[\rho]$ represents the exchange–correlation energy from the unknown exchange–correlation energy functional. The latter one covers all contributions from many-body exchange–correlation effects that are not included in the first three terms of Eq. (5.8), *i.e.*,

$$E_{\text{xc}}[\rho] = T[\rho] - T_s[\rho] + V_{\text{ee}}[\rho] - J[\rho], \tag{5.11}$$

[2] For simplicity, the dependence of $\rho$ on $\mathbf{r}$ has been dropped out and used explicitly only when it is necessary to emphasize it.

where $V_{\mathrm{ee}}[\rho]$ is the electron-electron repulsion energy given by

$$V_{\mathrm{ee}}[\rho] = \sum_{i}^{N} \sum_{j<i}^{N} \langle \Psi(\mathbf{r}) | \frac{1}{\mathbf{r}_i - \mathbf{r}_j} | \Psi(\mathbf{r}) \rangle, \tag{5.12}$$

with $\Psi$ being the true wave function. The differences $T[\rho] - T_s[\rho]$ and $V_{\mathrm{ee}}[\rho] - J[\rho]$ in Eq. (5.11) are corrections to the kinetic energy of the non-interacting model system and to the classical electron–electron repulsion interaction, respectively. The generalization of approximations to the energy functional $E_{\mathrm{xc}}[\rho]$ (Eq. (5.11)) is a key problem in DFT. While there is no general strategy for developing approximations to the exchange–correlation functional, a number of different approaches appeared in the past decades which are — more or less — appropriate for different, particular quantum chemical systems or certain group of properties [47]. Based on direct comparison to results obtained by more accurate wave function based methods or to accurate experimental data, more knowledge has been gained considering the functional form of the exchange–correlation potential. However, its unique mathematical structure remains unknown. Hence, some functionals can perform well for a certain group of molecules or particular properties for which they have been designed, but fail for others [52, 53]. Some approximations for the exchange–correlation functional are discussed in more details in section (5.4).

The advantage of the Kohn–Sham approach described above (Eq. (5.4)) is that the density of a non-interacting system equals the density of the fully-interacting system given by Eq. (4.8). Moreover, the kinetic energy of a single-particle can be evaluated using the set of orbitals $\{\phi_i\}$ and contains the largest part of the kinetic energy of the fully-interacting system. Besides, the computational cost of solving the non-linear Kohn–Sham equations (Eq. (5.4)) is low and scales as $O(N^3)$, where $N$ denotes the number of electrons in the system. As a result the time-independent Schrödinger equation can be solved in affordable time even for larger molecules or heavy elements.

## 5.3 Time-Dependent Density Functional Theory

Standard DFT represents a ground-state theory which yields the ground-state density and energy, and hence is limited to ground-state properties. This poses a considerable restriction since many important properties in chemistry and physics involve electronic excitations. In order to study them within KS-DFT, the ground-state DFT formulation has been extended to its time-dependent variant — time-dependent density functional theory (TD-DFT).

In the time-dependent Schrödinger equation (Eq. (4.1)), the external potential in the Hamiltonian introduced in Eq. (4.3) is substituted by the time-dependent one resulting in the following time-dependent form

$$\hat{H}(t) = \hat{T} + \hat{W} + \hat{V}(t), \tag{5.13}$$

where the first two operators are still described by Eqs. (4.4) and (4.5), while the third one is replaced by

$$\hat{V}(t) = \sum_{i=1}^{N} v(\mathbf{r}_i, t). \tag{5.14}$$

In 1984 Runge and Gross [54] formulated the foundation for the time-dependent analog to the first Hohenberg–Kohn theorem and proved that the time-dependent external potential $v(\mathbf{r}, t)$ can be determined by the charge density $\rho(\mathbf{r}, t)$ [55]. As a consequence, the total time-dependent wave function is unique up to a time-dependent phase factor,

$$\tilde{\Psi}(\mathbf{r}, t) = e^{-i\beta(t)}\Psi[\rho, \Psi_0](t) \approx e^{-i\beta(t)}\Psi[\rho](t). \tag{5.15}$$

It is assumed here that the initial state $\Psi_0$ is a stationary ground-state, completely determined by the ground-state density and can therefore be eliminated from Eq. (5.15). Furthermore, in TD-DFT only scalar potentials are considered. Inclusion of vector potentials leads to an extension of DFT to time-dependent current-density functional theory [56].

Since in TD-DFT no energy minimum exists and the total energy is no longer a conserved quantity, the second Hohenberg–Kohn theorem [48] cannot be directly applied, and the energy functional has been replaced by the so-called action functional [57]. The latter can be regarded as a density functional of the form

$$A[\rho(\mathbf{r}, t)] = \int_{t_0}^{t_1} dt \langle \Psi[\rho](t) | i\frac{\partial}{\partial t} - \hat{H}(t) | \Psi[\rho](t) \rangle, \tag{5.16}$$

with a stationary point at the exact time-dependent density [55]. In Eq (5.16), $t_0$ and $t_1$ determine the beginning and the end of the time step and $\Psi[\rho](t)$ is as given in Eq. (5.15). For convenience, the action functional is rewritten in an alternative way

$$A[\rho(\mathbf{r}, t)] = B[\rho(\mathbf{r}, t)] - \int_{t_0}^{t_1} dt \int d\mathbf{r} v(\mathbf{r}, t)\rho(\mathbf{r}, t), \tag{5.17}$$

where the $B[\rho(\mathbf{r}, t)]$ functional is independent of the external potential $v(\mathbf{r}, t)$, and

reads

$$B[\rho(\mathbf{r},t)] = \int_{t_0}^{t_1} dt \langle \Psi[\rho](t)| i\frac{\partial}{\partial t} - \hat{T} - \hat{W}|\Psi[\rho](t)\rangle. \tag{5.18}$$

In analogy to time-independent density functional theory, the time-dependent Schrödinger equation (Eq. (4.1)) can be solved for an effective time-dependent external potential ($v_s(\mathbf{r},t)$) for an independent-particle system, which gives the same charge density,

$$\rho(\mathbf{r},t) = \sum_i f_i |\phi_i(\mathbf{r},t)|^2, \tag{5.19}$$

with $f_i$ being orbital occupation numbers (or diagonal elements of the density matrix in some KS orbital basis). Hence, minimization of the action functional (Eq. (5.17)) yields the time-dependent Kohn–Sham (TD-KS) equation,

$$\left[-\frac{1}{2}\nabla^2 + v_s(\mathbf{r},t)\right]\phi_i(\mathbf{r},t) = i\frac{\partial}{\partial t}\phi_i(\mathbf{r},t), \tag{5.20}$$

where the first term on the left hand side is the kinetic energy operator and the second one, is the time-dependent effective potential of non-interacting particles

$$v_s(\mathbf{r},t) = v_{\text{ext}}(\mathbf{r},t) + v_{\text{SCF}}(\mathbf{r},t). \tag{5.21}$$

The first operator on the right hand side of Eq. (5.21) is the external potential that has a stationary and time-dependent part and the latter one is usually treated in a perturbative manner. The second term of Eq. (5.21) is the self-consistent field potential that reads

$$v_{\text{SCF}}(\mathbf{r},t) = \int d\mathbf{r}' \frac{\rho(\mathbf{r}',t)}{|\mathbf{r}-\mathbf{r}'|} + v_{\text{xc}}(\mathbf{r},t). \tag{5.22}$$

The first term in the above equation is the Coulomb potential and the latter one, is the time-dependent xc kernel evaluated for the ground-state density [58],

$$v_{\text{xc}}(\mathbf{r},t) = \frac{\delta \tilde{A}_{\text{xc}}}{\delta\rho(\mathbf{r}',t)}\Big|_{\rho(\mathbf{r},t)}. \tag{5.23}$$

The mathematical expression of the functional $A_{\text{xc}}$, which depends non-locally on the density both in spatial and in time variables, the so called memory dependence, is unknown and has to be approximated by some $\tilde{A}_{\text{xc}}$ [59–63]. In practical applications, the adiabatic approximation is used, where the time-dependent exchange–correlation kernel of Eq. (5.23) is substituted by the time-independent

one, which is local in time, *i.e.*,

$$v_{\mathrm{xc}}^{\mathrm{adiab}}(\mathbf{r},t) = \tilde{v}_{\mathrm{xc}}[\rho_t](\mathbf{r}). \tag{5.24}$$

It is important to note that the adiabatic approximation is valid only when the time-dependent potential varies very slowly with time, which is not always the case [58]. The potential described by Eq. (5.24) resembles the exchange–correlation potential introduced in Eq. (5.7), but it is evaluated for a density at a fixed time. As a consequence, the quality of $v_{\mathrm{xc}}^{\mathrm{adiab}}(\mathbf{r},t)$ is strongly affected by the failures of the ground-state approximations to $v_{\mathrm{xc}}(\mathbf{r})$ [64–67].

In this thesis, the description of the TD-DFT formalism is focused on vertical excitation energies, which can be obtained as solutions to the generalized eigenvalue problem [55, 58]

$$\begin{pmatrix} \mathbf{A} & \mathbf{B} \\ \mathbf{B}^* & \mathbf{A}^* \end{pmatrix} \begin{pmatrix} \mathbf{X} \\ \mathbf{Y} \end{pmatrix} = \omega \begin{pmatrix} \mathbf{1} & \mathbf{0} \\ \mathbf{0} & -\mathbf{1} \end{pmatrix} \begin{pmatrix} \mathbf{X} \\ \mathbf{Y} \end{pmatrix}, \tag{5.25}$$

with

$$A_{ia,jb} = \delta_{ij}\delta_{ab}(\epsilon_a - \epsilon_i) + \langle ij|ab\rangle - \eta\langle ia|jb\rangle + (1-\eta)\langle ij|f_{\mathrm{xc}}|ab\rangle \tag{5.26}$$

and

$$B_{ia,jb} = \langle ij|ab\rangle - \eta\langle ia|jb\rangle + (1-\eta)\langle ij|f_{\mathrm{xc}}|ab\rangle, \tag{5.27}$$

where $a, b$ and $i, j$ denote occupied and virtual orbitals, respectively, and $\langle ij|f_{\mathrm{xc}}|ab\rangle$ is the exchange–correlation kernel

$$\langle ij|f_{\mathrm{xc}}|ab\rangle = \int d\mathbf{r}d\mathbf{r}'\phi_i(\mathbf{r})\phi_j(\mathbf{r}')\frac{\delta^2 E_{\mathrm{xc}}}{\delta\rho(\mathbf{r})\rho(\mathbf{r}')}\phi_a(\mathbf{r}')\phi_b(\mathbf{r}) \tag{5.28}$$

and indicates the admixture of exact exchange which is introduced via an $\eta$ parameter in Eqs. (5.26)–(5.27). The vectors $\mathbf{X}$ and $\mathbf{Y}$ in Eq. (5.25) are the virtual-occupied (hole-particle) and occupied-virtual (particle-hole) density changes, *i.e.*, the orbital rotations associated with the excitation of the response density $\delta\rho(\mathbf{r},t)$ to a time-dependent external perturbation $\delta v_{\mathrm{pert}}(\mathbf{r}',t')$, namely

$$\delta\rho(\mathbf{r},t) = \int d\mathbf{r}' \int dt' \chi(\mathbf{r},t,\mathbf{r}',t')\delta v_{\mathrm{pert}}(\mathbf{r}',t'), \tag{5.29}$$

where the linear response function (point-wise susceptibility) describes the varia-

tion of a given observable in the weak external perturbation [58],

$$\chi(\mathbf{r}, t, \mathbf{r}', t') = \frac{\delta\rho(\mathbf{r}, t)}{\delta v_{\text{pert}}(\mathbf{r}', t')}. \tag{5.30}$$

Importantly, the response density of the non-interacting Kohn–Sham system has to be the same as the fully-interacting one,

$$\delta\rho(\mathbf{r}, t) = \int d\mathbf{r}' \int dt' \chi_{\text{KS}}(\mathbf{r}, t, \mathbf{r}', t') \cdot \{\delta v_{\text{ext}}(\mathbf{r}', t') + \delta v_{\text{SCF}}(\mathbf{r}', t')\}. \tag{5.31}$$

By comparing Eqs. (5.29) to (5.31) and employing the definition of the exchange–correlation kernel of Eq. (5.23), a fundamental expression for the excitation energies in the time-dependent linear response theory can be obtained. After Fourier transformation to the frequency domain $\omega$, the linear response function reads

$$\begin{aligned}\chi(\mathbf{r}, \mathbf{r}', \omega) &= \chi_{\text{KS}}(\mathbf{r}, \mathbf{r}', \omega) \\ &+ \int d\mathbf{r}_1 \int d\mathbf{r}_2 \chi_{\text{KS}}(\mathbf{r}, \mathbf{r}_1, \omega) \left\{ \frac{1}{|\mathbf{r}_1 - \mathbf{r}_2|} + f_{\text{xc}}(\mathbf{r}_1, \mathbf{r}_2, \omega) \right\} \chi_{\text{KS}}(\mathbf{r}_2, \mathbf{r}', \omega),\end{aligned} \tag{5.32}$$

where

$$\chi_{\text{KS}}(\mathbf{r}, \mathbf{r}', \omega) = 2 \lim_{\eta \to 0^+} \sum_q \left\{ \frac{\zeta_q(\mathbf{r})\zeta_q(\mathbf{r}')}{\omega - \epsilon_a + \epsilon_i + i\eta} - \frac{\zeta_q(\mathbf{r})\zeta_q(\mathbf{r}')}{\omega + \epsilon_a - \epsilon_i - i\eta} \right\}, \tag{5.33}$$

$\eta$ is a positive infinitesimal quantity, $q$ denotes a double index, combining $i$ for occupied and $a$ for virtual Kohn–Sham orbitals,

$$\zeta_q = \phi_i(\mathbf{r})\phi_a(\mathbf{r}). \tag{5.34}$$

The energies $\epsilon_a$ and $\epsilon_i$ refer to the eigen-energies of the ground-state orbitals $\phi_a$ and $\phi_i$, respectively. The poles of Eq. (5.32) correspond to the single-particle excitation energies, while the residues indicate the oscillator strengths of the Kohn-Sham system [58]. In Eq. (5.32), the kernel $f_{xc}(\mathbf{r}_1, \mathbf{r}_2, \omega)$ corrects the fictitious Kohn–Sham susceptibility $\chi_{\text{KS}}$ and improves the excitation energies by shifting the eigenvalues towards the ideal values.

The TD-DFT oscillator strength of the $I$-th excited state is given by

$$f_I = \frac{2}{3} \sum_{v=x,y,z} \left[ \sum_{i,a} d^v_{ia} (\epsilon_a - \epsilon_i)^{\frac{1}{2}} \chi^I_{ia} \right]^2, \tag{5.35}$$

where $d^v_{ia}$ is the transition dipole moment between the occupied $i$ and virtual $a$

orbitals,

$$d_{ia}^{v} = \int d\mathbf{r}\phi_i^*(\mathbf{r})r_v\phi_a(\mathbf{r}), \tag{5.36}$$

and $\chi_{ia}^{I}$ is a response function. In practical applications and in most of quantum chemical program packages, the exchange–correlation kernel is assumed to be frequency-independent, while the excitation energies $\omega_q$ are obtained from Casida's equation [55],

$$\sum_{q'} R_{q,q'}\chi_{q'} = \omega_q^2\chi_q. \tag{5.37}$$

In the above expression, $\chi_q$ is again the response function and $R_{q,q'}$ represents the four-index matrix and $q$ denotes a double index as resolved previously in Eq. (5.34). In particular, we have the following identities

$$R_{q,q'} = \omega_q^4\delta_{q,q'} + 4\sqrt{\omega_q\omega_{q'}}\int d\mathbf{r}\int d\mathbf{r}'\zeta_q(\mathbf{r})f_{\mathrm{Hxc}}(\mathbf{r},\mathbf{r}')\zeta_{q'}(\mathbf{r}') \tag{5.38}$$

and

$$f_{\mathrm{Hxc}}(\mathbf{r},\mathbf{r}') = \frac{1}{|\mathbf{r}-\mathbf{r}'|} + f_{\mathrm{xc}}(\mathbf{r},\mathbf{r}'), \tag{5.39}$$

where $f_{\mathrm{Hxc}}(\mathbf{r},\mathbf{r}')$ is called the Hartree exchange–correlation kernel and $\delta_{q,q'}$ is the Kronecker delta,

$$\delta_{q,q'} = \begin{cases} 1 & : q = q' \\ 0 & : q \neq q' \end{cases}$$

Solving Casida's equation of Eq. (5.37) is both memory and CPU demanding, mainly due to the storage and calculation of the $R_{q,q'}$ matrix, and hence more efficient iterative techniques have been developed [68] and applied to obtain only the lowest transitions, instead of the full electronic spectrum within a given basis set.

## 5.4 Approximate Exchange–Correlation Functionals

In this section a short overview of selected exchange–correlation functionals which are employed in this dissertation are given.

### 5.4.1 Local Density Approximations (LDA)

The simplest approach that can be made for the exchange–correlation energy functional is known as the local density approximation (LDA). In the early work of Thomas and Fermi [50] on the homogenous electron gas the approximation was made that the electrons are distributed uniformly in each small volume element (locally), however, the electron density could still vary from one small volume element to another. The total energy functional can therefore be written as

$$E_{\mathrm{xc}}^{\mathrm{LDA}}[\rho] = \int d\mathbf{r}\rho\epsilon_{\mathrm{xc}}^{\mathrm{LDA}}(\rho), \tag{5.40}$$

where $\epsilon_{\mathrm{xc}}^{\mathrm{LDA}}(\rho)$ is the exchange–correlation energy of the uniform electron gas (UEG) evaluated at the local density $\rho$. The $\epsilon_{\mathrm{xc}}^{\mathrm{LDA}}(\rho)$ term can be separated into exchange and correlation contributions,

$$\epsilon_{\mathrm{xc}}^{\mathrm{LDA}}(\rho) = \epsilon_{\mathrm{x}}^{\mathrm{LDA}}(\rho) + \epsilon_{\mathrm{c}}^{\mathrm{LDA}}(\rho). \tag{5.41}$$

The exchange part of the energy is usually approximated by the Dirac functional [51]

$$\epsilon_{\mathrm{x}}^{\mathrm{LDA}}(\rho) = -\frac{3}{4}\left(\frac{3}{\pi}\rho\right)^{\frac{4}{3}}. \tag{5.42}$$

The analytical expression for the correlation energy $\epsilon_{\mathrm{c}}^{\mathrm{LDA}}(\rho)$ is unknown. Accurate values can be, however, obtained from Monte–Carlo simulations [69] and fitted with analytical functions. The parametrization of Vosko, Wilk and Nusair [70] was recognized as the most accurate $\epsilon_{\mathrm{c}}(\rho)$ and implemented under the LDA acronym in most quantum chemical packages.

In order to stress that the electron density in open-shell molecules can be partitioned into its $\alpha$ (spin-up) and $\beta$ (spin-down) components,

$$\rho = \rho^{\alpha} + \rho^{\beta}, \tag{5.43}$$

the local spin-density approximation (LSDA) is used [71]. Electron densities resolved for a particular spin $\sigma$ will be abbreviated as $\rho^{\sigma}$, where $\sigma \in \{\alpha, \beta\}$.

The LDA approximation performs remarkably well even for molecular structures that are far away from a uniform distribution of the electron gas, and represent inhomogeneous systems instead. Furthermore, LDA provides a balanced treatment of exchange and (static/non-dynamic) correlation effects. Nevertheless, it also comprises limitations, like its local character as well as the significant tendency to overbind molecules [47, 72, 73]. In addition, the LDA model fails to

describe the proper asymptotic behavior of the exchange–correlation potential in the limit of large inter-electronic distances, which should fall off as $-\frac{1}{r}$, *i.e.*,

$$\lim_{r\to\infty} v_{\mathrm{xc}}(\mathbf{r}) = -\frac{1}{\mathbf{r}}. \tag{5.44}$$

As a consequence, this leads to large errors in Rydberg and charge-transfer electronic excitation energies.

### 5.4.2 Generalized Gradient Approximations (GGA)

An improvement over the non-locality of the LDA exchange–correlation functional can be achieved when gradient expansion approximations (GEA) to the exchange–correlation energy functional are employed. Within this framework, the LDA model is the zeroth order approximation to the GEA functional,

$$E_{\mathrm{xc}}^{\mathrm{GEA}}[\rho] = E_{\mathrm{xc}}^{\mathrm{LDA}}[\rho] + E_{\mathrm{xc}}^{\mathrm{GGA}}[\rho], \tag{5.45}$$

where $E_{\mathrm{xc}}^{\mathrm{GGA}}[\rho]$ is a general gradient approximation (GGA) that reads

$$E_{\mathrm{xc}}^{\mathrm{GGA}}[\rho] = \int d\mathbf{r} F_{\mathrm{xc}}(\rho, \nabla\rho), \tag{5.46}$$

where $F_{\mathrm{xc}}$ is a parametrized analytic function of the electron density and its gradient.

Well-known representatives of this class are the Becke–Lee–Yang–Parr (BLYP) [74, 75] and the Perdew–Burke–Ernzerhof (PBE) [76] approximations to the exchange–correlation energy. The first one comprises Becke's expression for the exchange energy,

$$E_{\mathrm{x}}^{B88}[\rho^\sigma] = E_{\mathrm{x}}^{\mathrm{LSDA}}[\rho^\sigma] - K \sum_{\sigma=\alpha,\beta} \int d\mathbf{r} (\rho^\sigma)^{\frac{3}{4}} \frac{x_\sigma^2}{1 + K x_\sigma \sinh^{-1} x_\sigma}, \tag{5.47}$$

with $K$ being an empirical parameter determined by a least-square fit to exact Hartree-Fock data. $x_\sigma$ in Eq. (5.47) is the reduced spin-density of the form

$$x_\sigma = \frac{|\nabla\rho^\sigma|}{(\rho^\sigma)^{\frac{4}{3}}}. \tag{5.48}$$

The correlation part of this functional consists of the Lee–Yang–Parr energy ex-

pression,

$$E_{\mathrm{c}}^{\mathrm{LYP}}[\rho^{\sigma}] = -\,\mathrm{A}\int d\mathbf{r}\frac{\zeta}{1+\mathrm{D}\rho^{-\frac{1}{3}}} \left\{\rho + 2\mathrm{B}\rho^{-\frac{5}{3}}\left[2^{\frac{2}{3}}C_F(\rho^{\sigma})^{\frac{8}{3}} - \rho\tau_W + \frac{1}{9}\left(\rho^{\sigma}\tau_W\right) + \frac{1}{18}\left(\rho^{\sigma}\nabla^2\rho^{\sigma}\right)\right]e^{\mathrm{C}\rho^{-\frac{1}{3}}}\right\}, \tag{5.49}$$

where $C_F = \frac{3}{10}(3\pi^2)^{\frac{2}{3}}$ is the Thomas–Fermi constant, $\zeta$ denotes the spin polarization,

$$\zeta = \frac{\rho^{\alpha} - \rho^{\beta}}{\rho}, \tag{5.50}$$

$\tau_W$ is the von Weizsäcker kinetic energy and $\mathrm{A} = 0.049, \mathrm{B} = 0.132, \mathrm{C} = 0.2533, \mathrm{D} = 0.349$ are constants.

The PBE correlation functional reads

$$E_{\mathrm{c}}^{\mathrm{PBE}}[\rho^{\sigma}] = \int d\mathbf{r}\rho[\epsilon_{\mathrm{c}}^{\mathrm{LDA}}(r_s,\zeta) + H(r_s,\zeta,t)], \tag{5.51}$$

where $r_s$ is local Seitz radius[3] and $t$ is a dimensionless density gradient that describes non-local effects,

$$t = \frac{1}{2}k_s|\nabla\rho|\rho\left[(1+\zeta)^{\frac{2}{3}} + (1-\zeta)^{\frac{2}{3}}\right], \tag{5.52}$$

with $k_s$ being the Thomas–Fermi screening wave number,

$$k_s = \sqrt{\frac{4C_F}{\pi a_0}}. \tag{5.53}$$

In the above equation, $a_0$ is the Bohr radius and

$$C_F = \frac{3}{5}(6\pi^2)^{\frac{2}{3}}. \tag{5.54}$$

The PBE exchange counterpart is describes as

$$E_x^{\mathrm{PBE}}[\rho^{\sigma}] = \int d\mathbf{r}\rho\epsilon_x^{\mathrm{LDA}}(\rho)F_x(s), \tag{5.55}$$

[3]This parameter is used to describe the density of the system from the Wigner–Seitz formula: $\frac{1}{\rho} = \frac{4}{3}\pi r_s^3$.

with the enhancement factor

$$F_x(s) = 1 + \kappa - \frac{\kappa}{1 + \frac{\mu s^2}{\kappa}}. \tag{5.56}$$

$\kappa$ and $\mu$ are constants equal to 0.804 and 0.2195, respectively.

Inclusion of the first order gradient corrections to the LDA energy functional via Eq. (5.40) results in the expansion and softening of atomic bonding, and hence gives more accurate atomization and binding energies as well as molecular geometries [53]. The advantage of the PBE exchange–correlation functional over the other GGA-type exchange–correlation approximations is that it has a simpler form and contains only a small number of non-empirical parameters. The semi-local behavior of the BLYP and PBE exchange–correlation functionals does not improve the quality of excitation energies compared to the LDA model, because the long-distance behavior is still incorrect (see Eq. (5.44)).

### 5.4.3 Meta-GGAs

Inclusion of second order corrections, *i.e.*, the Laplacian of the electron density in the LSDA, can yield further improvement in the exchange–correlation energy functional,

$$E_{\mathrm{xc}}^{\text{meta-GGA}}[\rho^\sigma] = \int d\mathbf{r}\rho^\sigma \epsilon_{\mathrm{xc}}^{\mathrm{LDA}}(\rho^\sigma, \nabla\rho^\sigma, (\nabla^2\rho^\sigma, \tau^\sigma)), \tag{5.57}$$

where $\tau^\sigma$ is the kinetic energy density,

$$\tau^\sigma = \frac{1}{2}\sum_i |\nabla\phi_{i,\sigma}|^2. \tag{5.58}$$

The group of such functionals belongs to the family of meta-GGA functionals. As an example, the M06-L [77] exchange–correlation functional will be discussed, which is essentially a combination of the functional forms of VSXC [78] and M05 [79]. The M06-L functional depends on various variables: the local spin-density $\rho^\sigma$, the reduced density gradient defined in Eq. (5.48), the kinetic energy density $\tau^\sigma$ of Eq. (5.58), a working variable $z_\sigma$,

$$z_\sigma = \frac{\tau^\sigma}{(\rho^\sigma)^{\frac{5}{3}}} - C_F, \tag{5.59}$$

with $C_F$ being defined in Eq. (5.54), and additionally two working functions, $\gamma(x_\sigma, z_\sigma)$ and $h(x_\sigma, z_\sigma)$, with following explicit forms

$$\gamma(x_\sigma, z_\sigma) = 1 + \alpha(x_\sigma^2 + z_\sigma), \tag{5.60}$$

and

$$h(x_\sigma, z_\sigma) = \left( \frac{d_0}{\gamma(x_\sigma, z_\sigma)} + \frac{d_1 x_\sigma^2 + d_2 z_\sigma}{\gamma^2(x_\sigma, z_\sigma)} + \frac{d_3 x_\sigma^4 + d_2 x_\sigma^2 z_\sigma}{\gamma^3(x_\sigma, z_\sigma)} \right). \tag{5.61}$$

The parameters $d_0, d_1, d_2$ and $d_3$ in the above expression are determined by fitting to properties of large molecular training sets [77, 80]. Within this notation, the exchange part of the M06-L energy functional is given by

$$E_{\mathrm{x}}^{\text{M06-L}}[\rho^\sigma] = \sum_{\sigma=\alpha,\beta} \int d\mathbf{r} [E_{\mathrm{x}\sigma}^{\mathrm{PBE}}(\rho^\sigma, \nabla\rho^\sigma) f(\omega_\sigma) + \epsilon_{\mathrm{x}\sigma}^{\mathrm{LSDA}}(\rho^\sigma) h_x(x_\sigma, z_\sigma)], \tag{5.62}$$

where $E_{\mathrm{x}\sigma}^{\mathrm{PBE}}$ is the exchange energy density of the PBE exchange–correlation functional (Eq. (5.55)), $\epsilon_{\mathrm{x}\sigma}^{\mathrm{LSDA}}$ is the local spin-density approximation for exchange, and $f(\omega_\sigma)$ is the spin kinetic energy enhancement factor. The correlation energy term of M06-L reads

$$E_{\mathrm{c}} = E_{\mathrm{c}}^{\sigma\sigma'} + E_{\mathrm{c}}^{\sigma\sigma}, \tag{5.63}$$

where

$$E_{\mathrm{c}}^{\sigma\sigma'} = \int d\mathbf{r} \epsilon_{\sigma\sigma'}^{\mathrm{UEG}} \left[ g_{\sigma\sigma'}(x_\sigma, z_{\sigma'}) + h_{\sigma\sigma'}(x_\sigma, z_{\sigma'}) \right] \tag{5.64}$$

is the antiparallel spin contribution and

$$E_{\mathrm{c}}^{\sigma\sigma} = \int d\mathbf{r} \epsilon_{\sigma\sigma}^{\mathrm{UEG}} \left[ g_{\sigma\sigma}(x_\sigma, z_\sigma) + h_{\sigma\sigma}(x_\sigma, z_\sigma) \right] D_\sigma \tag{5.65}$$

is the parallel spin contribution. In Eqs. (5.64) to (5.65), $g_{\sigma,\sigma'}$ ($g_{\sigma,\sigma}$) denotes the reduced spin density gradient and $\epsilon_{\sigma\sigma'}^{\mathrm{UEG}}$ ($\epsilon_{\sigma\sigma}^{\mathrm{UEG}}$) spin correlation energy of the uniform electron gas, with $\sigma, \sigma = (\alpha, \alpha)$ or $(\beta, \beta)$ and $\sigma, \sigma' = (\alpha, \beta)$ or $(\beta, \alpha)$. $D_\sigma$ is the self-interaction error (SIE) correction[4].

The M06-L functional is nowadays widely used in studies of transition metal complexes, where it performs statistically better for the determination of bond

[4]The self-interaction error (SIE) is an unphysical interaction of an electron with itself (one-electron self interaction error — 1-SIE) or with other electrons (many-electron self interaction error — N-SIE) [53].

lengths, thermochemistry, kinetics and local excitation energies than any other GGA representative [80, 81]. However, Rydberg and charge-transfer excitation energies are still largely underestimated.

### 5.4.4 Hybrids

Another approach for the exchange–correlation energy functional is to combine some GGA-type functional with a fraction (admixture) of exact exchange from Hartree-Fock,

$$E_{\mathrm{x}}^{\mathrm{HF}}[\rho] = -\frac{1}{4}\int\int d\mathbf{r}_1 d\mathbf{r}_2 \frac{\rho(\mathbf{r}_1,\mathbf{r}_2)^2}{|\mathbf{r}_1-\mathbf{r}_2|}. \tag{5.66}$$

The basic idea of this strategy is based on the adiabatic connection requirements,

$$E_{\mathrm{xc}}[\rho] = \int_0^1 d\lambda U_\lambda, \tag{5.67}$$

where $0 \leq \lambda \leq 1$ is the switching parameter of the Coulomb interaction, and $U_\lambda$ is the exchange–correlation potential energy for the non-interacting Kohn–Sham reference system $\lambda = 0$, for partially interacting electrons $0 < \lambda < 1$, and in the fully interacting system $\lambda = 1$ [72, 82]. This allows us to write the general form of the hybrid functional as follows

$$E_{\mathrm{xc}}[\rho^\sigma] = \int d\mathbf{r}\left(F(\rho^\sigma, \nabla\rho^\sigma) + \xi E_{\mathrm{x}}^{\mathrm{HF}}(\rho^\sigma)\right), \tag{5.68}$$

where $\xi$ is the fraction of exact exchange defined in Eq. (5.66). The most widely used hybrid exchange–correlation functional is B3LYP [83, 84],

$$\begin{aligned} E_{\mathrm{xc}}^{\mathrm{B3LYP}}[\rho^\sigma] = {} & 0.2\left(E_{\mathrm{x}}^{\mathrm{HF}}[\rho^\sigma]\right) + 0.8\left(E_{\mathrm{x}}^{\mathrm{LSDA}}[\rho^\sigma]\right) \\ & + 0.72\left(E_{\mathrm{x}}^{\mathrm{B88}}[\rho^\sigma]\right) + 0.81\left(E_{\mathrm{c}}^{\mathrm{LYP}}[\rho^\sigma]\right) + 0.19\left(E_{\mathrm{c}}^{\mathrm{LSDA}}[\rho^\sigma]\right), \end{aligned} \tag{5.69}$$

which contains 20% of Hartree–Fock exchange (Eq. (5.66)).

Another representative of this group is named PBE0 [85, 86] and combines 25% of exact exchange with the PBE [76] xc functional,

$$E_{\mathrm{xc}}^{\mathrm{PBE0}}[\rho^\sigma] = E_x^{\mathrm{PBE}}[\rho^\sigma] + 0.25\left(E_{\mathrm{x}}^{\mathrm{HF}}[\rho^\sigma] - E_{\mathrm{x}}^{\mathrm{PBE}}[\rho^\sigma]\right) + E_{\mathrm{c}}^{\mathrm{PBE}}[\rho^\sigma]. \tag{5.70}$$

The hybrid approach improved atomistic energies, bond lengths, reaction barriers and gradually became the most widely used exchange–correlation approximation in DFT, before meta-GGAs were invented [47, 53]. B3LYP and PBE0 correct the exchange potential of Eq. (5.44) by $-0.2\frac{1}{r}$ and $-0.25\frac{1}{r}$, respectively, in comparison

to the local and semi-local xc functionals, where the $-\frac{1}{r}$ dependence is simply missing, which is often referred to as zero asymptotic. As a result, all Rydberg and some of the charge-transfer transitions are described more accurately employing hybrid density functionals.

Combining meta-GGA types of exchange–correlation functionals with an admixture of exact exchange results in meta-hybrid exchange–correlation functionals. Well-known examples for this class are M06 [77, 80] and M06-2X [87] with 27% and 54% of Hartree–Fock exchange, respectively.

### 5.4.5 Long-Range Separated Hybrids

An interesting extension to the hybrid class of functionals was proposed by Tsuneda and co-workers [88] in which the exact-exchange is present not only globally at the short- and long inter-electronic distances, but also at the long-range orbital-orbital interaction. The electron repulsion operator is partitioned into a short- and long-range contributions as follows

$$\frac{1}{r_{12}} = \frac{1-\mathrm{erf}(\mu r_{12})}{r_{12}} + \frac{\mathrm{erf}(\mu r_{12})}{r_{12}}, \tag{5.71}$$

where $\mu$ determines the ratio of the two parts. The short-range exchange interaction is defined as

$$E_{\mathrm{x}}^{\mathrm{sr}} = -\frac{1}{2}\sum_{\sigma}\int d\mathbf{r}\rho^{\sigma}K_{\sigma}\left\{1-\frac{8}{3}\left[\sqrt{\pi}\,\mathrm{erf}\left(\frac{1}{2a_{\sigma}}\right)+2a_{\sigma}(b_{\sigma}-c_{\sigma})\right]\right\}, \tag{5.72}$$

where

$$a_{\sigma} = \frac{\mu K_{\sigma}^{\frac{1}{2}}}{6\sqrt{\pi}\rho_{\sigma}^{\frac{1}{3}}}, \tag{5.73}$$

$$b_{\sigma} = exp(-\frac{1}{4a_{\sigma}^{2}}-1), \tag{5.74}$$

and

$$c_{\sigma} = 2a_{\sigma}^{2}b_{\sigma}+\frac{1}{2}. \tag{5.75}$$

In Eq. (5.72), $K_{\sigma}$ is a dimensionless parameter that is used to determine the spin-density and depends on the applied exchange–correlation functional (for instance, Eq. (5.52)) [89]. The long-range exchange counterpart reads

$$E_{\mathrm{x}}^{\mathrm{lr}} = \frac{1}{2}\sum_{\sigma}\sum_{i}\sum_{j}\int\int d\mathbf{r}_1 d\mathbf{r}_2\phi_{i\sigma}(\mathbf{r}_1)\phi_{j\sigma}(\mathbf{r}_1)\times\frac{\mathrm{erf}(\mu r_{12})}{r_{12}}\phi_{i\sigma}(\mathbf{r}_2)\phi_{j\sigma}(\mathbf{r}_2). \tag{5.76}$$

Later on, Yanai and co-workers [90] combined the Coulomb attenuation procedure with the B3LYP exchange–correlation functional and generalized the form of Eq. (5.71) using two additional parameters,

$$\frac{1}{r_{12}} = \frac{1 - [\alpha + \beta \operatorname{erf}(\mu r_{12})]}{r_{12}} + \frac{\alpha + \beta \operatorname{erf}(\mu r_{12})}{r_{12}}, \tag{5.77}$$

where the separation parameter $\mu = 0.33$, and $\alpha = 0.19$ and $\beta = 0.46$ correspond to a fraction of Hartree–Fock exchange at short- and long inter-electronic distances, respectively. The resulting exchange–correlation approximation, which comprises a proper asymptotic behavior with B3LYP accuracy, was named Coulomb attenuating method-B3LYP (CAM-B3LYP) [90].

The CAM-B3LYP functional did overcome the problem with underestimating Rydberg transitions and significantly improved the charge-transfer excitations as well as oscillator strengths, and quickly became an alternative to the B3LYP exchange–correlation functional in calculation of response properties within the TD-DFT framework.

### 5.4.6 The Model SAOP Potential

An alternative way to represent the correct asymptotic behavior of Eq. (5.44) is to use model functionals such as LB94 [91] or SAOP [92, 93], *i.e.*, properties which do not correspond to the functional derivative of the energy with respect to the density. The latter is especially designed to predict excitation energies, polarizability and hyper-polarizability correctly, which depend critically on the quality of the potential in the outer region of the system. The statistical average orbital potential (SAOP) is build up from the GLLB [94, 95] and LB$\alpha$ [93] (parametrized LB94) model functionals in such a way that the first one is applied for the inner and the second one for the outer orbitals. The exponential interpolation between these two different potentials reads

$$v_{\mathrm{xc},i\sigma}^{\mathrm{mod}}(\mathbf{r}) = e^{-2(\epsilon_{N\sigma}-\epsilon_{i\sigma})^2} v_{\mathrm{xc},\sigma}^{\mathrm{LB}\alpha}(\mathbf{r}) + \left\{1 - e^{-2(\epsilon_{N\sigma}-\epsilon_{i\sigma})^2}\right\} v_{\mathrm{xc},\sigma}^{\mathrm{GLLB}\alpha}(\mathbf{r}), \tag{5.78}$$

where $\epsilon_{i\sigma}$ and $\epsilon_{N\sigma}$ are one of the occupied and the highest occupied orbital energies, respectively. With a small energy difference $(\epsilon_{i\sigma} - \epsilon_{N\sigma})$ the potential remains close to $v_{\mathrm{xc},\sigma}^{\mathrm{GLLB}}(\mathbf{r})$, otherwise it approaches $v_{\mathrm{xc},\sigma}^{\mathrm{LB}\alpha}(\mathbf{r})$ [92]. The resulting SAOP model potential has the form,

$$v_{\mathrm{xc},\sigma}^{\mathrm{SAOP}}(\mathbf{r}) = \sum_{i=1}^{N} v_{\mathrm{xc},\sigma}^{\mathrm{mod}}(\mathbf{r}) \frac{|\phi_{i\sigma}(\mathbf{r})|}{\rho(\mathbf{r})}, \tag{5.79}$$

with $\phi_{i\sigma}(\mathbf{r})$ being the $i$-th occupied molecular orbital. The model SAOP potential reproduces very accurately atomic shell structures (slopes) and is very close to the exact $v_{\mathrm{xc}}$ in both the inner and outer range of the system under study [93]. This results in rather accurate Rydberg excitations, but it does not significantly improve charge-transfer transitions [36, 96, 97].

# 6 Wave Function Methods

God used beautiful mathematics in creating the world.

Paul A. M. Dirac

An alternative way to determine the structure and properties of atoms and molecules is to solve the Schrödinger equation (Eq. (4.2)) directly [98, 99]. Such methods are commonly known as wave function approaches. In opposite to DFT, wave function methods do not rely on the density but depend directly on the quality of the obtained wave function. In general in wave function approaches, the accuracy can be systematically increased, yet at the same time, leading to a significant rise in computational expenses, *e.g.*, computer time, memory, and disk space with respect to DFT. Hence, the application of wave function methods is limited to rather small system sizes.

The simplest approach for the determination of the ground-state wave function and ground-state energy is the Hartree–Fock (HF) method [39, 98], which relies on a single-reference Slater determinant. One can derive the HF equations by applying the variational principle to the Schrödinger equation and minimizing the energy with respect to the (spin-)orbitals,

$$\hat{F}(i)\psi_i(\mathbf{r}) = \epsilon_i\psi_i(\mathbf{r}), \tag{6.1}$$

where $\hat{F}(i)$ is the one-electron Fock operator which in the restricted formulation for closed-shell molecules reduces to

$$\hat{F}(i) = -\frac{1}{2}\nabla_i^2 - \sum_A \frac{Z_A}{r_{iA}} + \sum_{j=1}^{N/2}\left[2\hat{J}_j(i) - \hat{K}_j(i)\right]. \tag{6.2}$$

The first two terms in the above equation are the kinetic energy and the nuclei-electron repulsion operators, respectively, while the last term represents the average potential of the interaction of the $i$-th electron with the other electrons (distributed in $\frac{N}{2}$ spin-orbitals) and comprises the Coulomb $\hat{J}_j(i)$ and the exchange $\hat{K}_j(i)$ operators, respectively.

The HF approach accounts properly for the exchange energy and obeys the Pauli principle. In general, the HF method is a very good approach to the total energy for which very small errors, less than one percent, are often found [100]. However, since the electrons move in the mean field generated by the other electrons, this approach does not account for electron correlation effects. As a result this can lead to large deviations from the exact ground-state energy in cases where the electron-electron interaction is strong, which is usually the case for heavy elements like actinides. Therefore, a set of approaches that improve upon this mean-field approximation for the electron-electron interaction have been developed [101] and these are called post-Hartree–Fock (post-HF) methods in which the HF method is the central starting point and the correlation energy is added on top of it.

The full configuration interaction (FCI) wave function represents the exact solution of the Schrödinger equation within a given basis set [98] and hence fully accounts for both *dynamic* and *static/non-dynamic* correlation effects. The dynamic correlation energy usually involves a large number of configurations with small weights and is essential for the qualitative description of atomic and molecular energies. The static/non-dynamic correlation energy, on the other hand, involves a small number of nearly degenerate orbitals and is important for molecules where the ground state is correctly described only with more than one Slater determinant. This type of energy is essential for an accurate determination of ground-state energies of open-shell molecules and for an accurate description of dissociation processes. The FCI wave function has the following form

$$\Psi_{\mathrm{FCI}} = (1 + \hat{C}_0)\Psi_0, \tag{6.3}$$

where $\Psi_0$ is an independent-particle model reference configuration, in our case the HF determinant, and $\hat{C}_0$ is the linear excitation operator that can be written in second quantized form as

$$\hat{C}_0 = \sum_{i,a} c_i^a a_a^\dagger a_b + \sum_{i>j,a>b} c_{ij}^{ab} a_a^\dagger a_b^\dagger a_j a_i + \ldots, \tag{6.4}$$

$c_i^a$ and $c_{ij}^{ab}$ are the excitation amplitudes and $a^\dagger$ and $a$ are the creation and annihi-

lation operators, respectively [1]. The symbols $i, j, \ldots$ refer to the occupied orbitals in $\Psi_0$, and $a, b, \ldots$ refer to the unoccupied ones. The above series continues until $N$-electron excitations are reached.

Due to the binomial scaling of the CI expansion of Eq. (6.3) with the size of the system, the FCI method is only applicable to atoms and molecules that contain up to 10 electrons. In order to treat a larger number of electrons in the system, a truncation of the CI expansion of Eq. (6.3) is employed. When this is done at the single, double or triple excitation level,, than the CI with singles (CIS), CI with singles and doubles (CISD) and CI with singles, doubles and triples (CISDT) methods are obtained, respectively [98]. However, the truncated CI approaches are neither *size-consistent* nor *size-extensive*, which limits their applicability in chemistry. Size-consistency of the system should guaranty that the computed energy of the entire system equals the sum of the energies of the subsystems calculated separately, *e.g.*, as it takes place during the dissociation process. Size-extensivity, on the other hand, ensures proper (linear) scaling of the calculated (extensive) quantities with respect to the number of electrons in the system [102]. Therefore, for larger systems present in chemistry an alternative treatment of the correlation energy is favored. Such approximate methods that are also applicable to excited-state calculations will be briefly describe in the next part of this chapter.

## 6.1 The Complete Active Space Second Order Perturbation Theory

One way to reduce the computational expense of FCI method is to apply the FCI expansion of Eq. (6.3) only to the subspace of active orbitals, *i.e.*, orbitals important from a chemical point of view in the system under study. This is a basic concept of the complete active space (CAS) [100] method, where the molecular orbital space is divided into three subspaces: inactive, active and external orbitals. Inactive orbitals are doubly occupied in all configurations. The occupancy of active orbitals varies in different configurations. The external orbitals, sometimes also called virtuals, are unoccupied in all configurations.

The proper CAS space should include the most important configuration state functions (CSFs) that is, symmetry adapted linear combinations of Slater determinants, from the FCI wave function (Eq. (6.3)). This requires *a priori* knowledge about the system under study and is not always easy to determine.

[1] Note that for notation simplicity the creation and annihilation operators $\hat{a}^\dagger$ and $\hat{a}$ are simply written as $a^\dagger$ and $a$, respectively.

If the CAS orbitals are optimized, then the CASSCF wave function is obtained. The CASSCF wave function accounts mostly for the static/non-dynamic correlation energy. The dynamic correlation energy can be, however, added in the second step using the multi-configurational second order perturbation theory. This results in the CAS second order perturbation theory (CASPT2) method [103, 104]. Such approach is nearly size-consistent and approximately size-extensive.

One of the main problems encountered in the CASPT2 method is the proper description of the zeroth order Hamiltonian $\hat{H}_0$ for the CASSCF wave function as an eigenfunction. While in case of the single-configurational perturbation theory, the choice of $\hat{H}_0$ is simple and comprises the sum of the HF orbital energies, it becomes a much more complex expression in the multi-configurational (CASSCF) case, since the Fock operator of Eq. (6.2) cannot be uniquely defined [105]. In the CASPT2 method only one-electron terms are used to define $\hat{H}_0$ and as a result systematic errors appear in the ground- and excited-state energies. More precisely, the problem is that the relative energies for the open-shell molecules and as a consequence excitation energies are too low. However, the recently developed modified zeroth order Hamiltonian [106] that is based on average atomic electron affinities (EA) and ionization potentials (IP) significantly reduces the above mentioned errors. It has been shown that such a choice of $\hat{H}_0$ leads to an accurate excited-state calculations and quickly became the most widely used approximation [100].

## 6.2 The Coupled Cluster (CC) Method

One of the most accurate methods to account for the (dynamic) correlation energy, usually used as reference in quantum chemical calculations, is the coupled cluster (CC) approach [107, 108]. The CC wave function, in opposite to the FCI expansion of Eq. (6.3), is based on the cluster operator $\hat{T}$ with the following *ansatz*

$$\Psi_{\mathrm{CC}} = e^{\hat{T}}\Psi_0 = \left(1 + \hat{T} + \frac{\hat{T}^2}{2!} + \frac{\hat{T}^3}{3!} + \ldots\right)\Psi_0 = \hat{\Omega}\Psi_0, \tag{6.5}$$

where $\hat{\Omega}$ is a wave operator. The cluster operator $\hat{T}$ is composed of a series of an increasing rank order excitation operators

$$\hat{T} = \hat{T}_1 + \hat{T}_2 + \hat{T}_3 + \ldots + \hat{T}_n, \tag{6.6}$$

where

$$\hat{T}_1 = \sum_{i,a} t_i^a a_a^\dagger a_i, \tag{6.7}$$

$$\hat{T}_2 = \frac{1}{4} \sum_{i,j,a,b} t_{ij}^{ab} a_a^\dagger a_b^\dagger a_j a_i, \tag{6.8}$$

...

and in general,

$$\hat{T}_n = \left(\frac{1}{n!}\right)^2 \sum_{i,j\ldots,a,b\ldots} t_{ij\ldots}^{ab\cdots} a_a^\dagger a_b^\dagger \ldots a_j a_i \tag{6.9}$$

are single, double and higher level excitations in second quantized form, respectively [101, 109]. The $t_i^a, t_{ij}^{ab}$ and $t_{ij\ldots}^{ab\cdots}$ in the above equations are the coupled cluster amplitudes defining the given operator. The cluster operators of Eq. (6.9) introduce single $\Psi_i^a$, double $\Psi_{ij}^{ab}$ and higher rank excitations, respectively,

$$\hat{T}_1 \Psi_0 = \sum_{i,a} t_i^a \Psi_i^a, \tag{6.10}$$

$$\hat{T}_2 \Psi_0 = \sum_{i>j,a>b} t_{ij}^{ab} \Psi_{ij}^{ab}, \tag{6.11}$$

...

The CC energy, for computational convenience, is usually defined as follows

$$\langle \Psi_0 | e^{-\hat{T}} \hat{H} e^{\hat{T}} | \Psi_0 \rangle = E, \tag{6.12}$$

where the $e^{-\hat{T}} \hat{H} e^{\hat{T}}$ term is called the effective Hamiltonian and $\Psi_0$ is again the HF reference determinant. Because the above equation represents a nonlinear optimization problem with respect to the cluster amplitudes, Eq. (6.12) is solved non-variationally [102]. The unknown cluster amplitudes $t_{ij\ldots}^{ab\cdots}$, (Eq. (6.9)) in Eq. (6.12) can be obtained by left-projecting the Schrödinger equation by the excited determinants $\Psi_{ij\ldots}^{ab\cdots}$, as a result of action of the cluster operator $\hat{T}$, on the reference state $\Psi_0$ (*e.g.*, Eq. (6.11)),

$$\langle \Psi_{ij\ldots}^{ab\cdots} | e^{-\hat{T}} \hat{H} e^{\hat{T}} | \Psi_0 \rangle = 0. \tag{6.13}$$

The above amplitude equations are formally exact if the cluster operator $\hat{T}$, is not truncated. Having obtained the amplitudes, the CC energy can be calculated according to Eq. (6.12).

The advantage of using an effective Hamiltonian together with an intermediate

normalization of the CC wave function

$$\langle \Psi_{\mathrm{CC}} | \Psi_0 \rangle = 1 \tag{6.14}$$

is that the mathematical formulas that need to be evaluated in Eqs. (6.12) and (6.13) are simplified. The effective Hamiltonian can be expressed in terms of commutators. Employing the Campbell–Baker–Hausdorff formula [101], the effective Hamiltonian simplifies to

$$e^{-\hat{T}} \hat{H} e^{\hat{T}} = \hat{H} + [\hat{H}, \hat{T}] + \frac{1}{2!}[[\hat{H}, \hat{T}], \hat{T}] + \frac{1}{3!}[[[\hat{H}, \hat{T}], \hat{T}], \hat{T}] + \dots \tag{6.15}$$

The normal ordered cluster operators commute with each other, but not with the Hamiltonian [109]. The right-hand-side of the above expression (Eq. (6.15)) truncates naturally after the first five terms. The contribution from higher than four-fold commutators is simply zero.

The $\hat{T}_n$ operators of Eq. (6.9) cannot be reduced any further, therefore they are called *connected* terms. However, due to the nonlinear terms in the CC expansion of Eq. (6.5), the so called *disconnected* terms show up as in Eq. (6.15), that are combination of the connected operators, *e.g.*,

$$\frac{1}{2}\hat{T}_1^2 \Psi_0 = \sum_{i,a,j,b} t_i^a t_j^b \Psi_{ij}^{ab}, \tag{6.16}$$

$$\hat{T}_1 \hat{T}_2 \Psi_0 = \sum_{i,a,j>k,b>c} t_i^a t_{jk}^{bc} \Psi_{ijk}^{abc}, \tag{6.17}$$

$$\frac{1}{2}\hat{T}_2^2 \Psi_0 = \sum_{i>j,a>b,k>l,c>d} t_{ij}^{ab} t_{kl}^{cd} \Psi_{ijkl}^{abcd}. \tag{6.18}$$

Such terms lead to higher rank excitations that are constructed from the lower rank coefficients (amplitudes) [101].

Let us now compare more closely the CC expansion of Eq. (6.5) with the FCI expansion of Eq. (6.3). If we truncate both equations at the single and double excitation level, *i.e.*, compare the coupled cluster with singles and doubles (CCSD) to the CISD wave function,

$$\Psi_{\mathrm{CCSD}} = \left(1 + \hat{T}_1 + \hat{T}_2 + \frac{1}{2}\hat{T}_1^2 + \hat{T}_2\hat{T}_1 + \frac{1}{6}\hat{T}_1^3 + \frac{1}{2}\hat{T}_2^2 + \frac{1}{2}\hat{T}_2\hat{T}_1^2 + \frac{1}{24}\hat{T}_1^4\right)\Psi_0 \tag{6.19}$$

and

$$\Psi_{\mathrm{CISD}} = \left(1 + \sum_{i,a} c_i^a a_a^\dagger a_i + \sum_{i>j,a>b} c_{ij}^{ab} a_a^\dagger a_b^\dagger a_j a_i\right)\Psi_0, \tag{6.20}$$

we can identify the same number of amplitudes ($t_i^a, t_{ij}^{ab}$ like in Eqs. (6.16)–(6.18) and $c_i^j, c_{ij}^{ab}$, respectively). The only difference between both of them is that the CCSD amplitudes intrinsically include higher excitation levels, that is, triples and quadruples in the disconnected terms (Eqs. (6.16)–(6.18)). This has a significant consequences for the quality of the obtained wave function and associated energy in both CISD and CCSD methods when the system approaches the dissociation limit or the number of electrons is increased. The general advantage of the truncated CC theory over truncated CI is that it guaranties both size-consistency and size-extensivity [109].

In practical quantum chemical calculations the $\hat{T}_n$ operator is truncated, usually at the level of $\hat{T}_2$ – $\hat{T}_4$. Nevertheless, the truncated CC method still can give very accurate results in cases when the dynamic correlation energy is important due to the presence of disconnected terms.

### 6.2.1 Equation Of Motion Coupled Cluster

The equation of motion coupled cluster (EOMCCSD) formalism [110–112] provides an excited state extension of the single-reference CC theory. The basic idea of this method relies on simultaneously considering two Schrödinger equations, one for the ground state and one for the $k$-th excited state,

$$\hat{H}\Psi_{\mathrm{CC}}^0 = E^0\Psi_{\mathrm{CC}}^0 \tag{6.21}$$

and

$$\hat{H}\Psi_{\mathrm{CC}}^k = E^k\Psi_{\mathrm{CC}}^k, \tag{6.22}$$

where $E^0$ and $E^k$ are the CC energies for the ground- and excited-states, respectively [101, 111]. The CC wave function for the $k$-th excited state is created by action of the cluster excitation operator $\hat{\Omega}_k$ on the ground state CC wave function $\Psi_{\mathrm{CC}}^0$,

$$\Psi_{\mathrm{CC}}^k = \hat{\Omega}_k\Psi_{\mathrm{CC}}^0 \tag{6.23}$$

The linear excitation operator $\hat{\Omega}_k$, changes the coefficients of the $\Psi_{\mathrm{CC}}^0$ wave function to the corresponding $\Psi_{\mathrm{CC}}^k$ state. The form of $\hat{\Omega}_k$ depends on the level of excitations in $\hat{T}$,

$$\hat{\Omega}_k = \hat{\Omega}_{k,0} + \hat{\Omega}_{k,1} + \hat{\Omega}_{k,2} + \ldots + \hat{\Omega}_{k,n}, \tag{6.24}$$

where

$$\hat{\Omega}_{k,0} = r_0(k), \tag{6.25}$$

$$\hat{\Omega}_{k,1} = \sum_{i,a} r_i^a(k) a_a^\dagger a_i, \tag{6.26}$$

$$\hat{\Omega}_{k,2} = \sum_{a>b,i>j} r_{ij}^{ab}(k) a_a^\dagger a_b^\dagger a_j a_i, \tag{6.27}$$

$$\dots$$

$$\hat{\Omega}_{k,n} = \sum_{a>b\dots,i>j\dots} r_{ij\dots}^{ab\cdots}(k) a_a^\dagger a_b^\dagger \dots a_j a_i \dots. \tag{6.28}$$

The role of the $\hat{\Omega}_{k,0}$ operator corresponds to the multiplication of function by a scalar $r_0(k)$, which represents the contribution to the excited state of interest stemming from the reference function $\Psi_0$. The amplitudes $r(k)$ need to be determined in order to obtain $\Psi_{\mathrm{CC}}^k$ and the corresponding energy $E^k$.

The EOMCC equations are obtained by substituting wavefunction expansion Eq. (6.21) into the Schrödinger equation and subsequent multiplying both sides of resulting equation from the left by $e^{-\hat{T}}$. This leads to the following form of the equations:

$$[\hat{H}, \hat{\Omega}_k]\Psi_0 = \omega_k \hat{\Omega}_k \Psi_0. \tag{6.29}$$

In the above equation $\omega_k = E^k - E^0$ denotes the excitation energy [111, 112].

Eq. (6.29) can be solved iteratively in the same manner as the regular CC method, however, is computationally more demanding since in addition to the ground state CC amplitudes the $r(k)$ amplitudes have to be determined.

The most frequently used EOMCC methods are the EOMCC with singles and doubles (EOMCCSD) and EOMCC with singles, doubles and triples (EOMCCSDT). In many cases, incorporation of triples is mandatory to obtain a qualitatively good description of excited states, however, the steep scaling of the EOMCCSDT with the size of the system limits its applicability. Therefore a group of methods that account for the triples contribution in an approximate manner have been developed. One of these approaches is the completely renormalized equation of motion coupled cluster with singles doubles and non-iterative triples (CR-EOMCCSD(T)) developed by Kowalski and Piecuch [113, 114].

In the CR-EOMCCSD(T) approach, a correction to the EOMCCSD excitation energies $\delta_k^{\text{CR-EOMCCSD(T)}}$ is added to the EOMCCSD vertical excitation energies

$\omega_k^{\text{EOMCCSD}}$,

$$\omega_k^{\text{CR-EOMCCSD(T)}} = \omega_k^{\text{EOMCCSD}} + \delta_k^{\text{CR-EOMCCSD(T)}}, \tag{6.30}$$

where the second term on the right-hand-side is defined through the trial wave function $\tilde{\Psi}_{\text{CC}}^k$ and the triply excited EOMCCSD moment operator $M_{k,3}^{\text{EOMCCSD}}$ [115],

$$\delta_k^{\text{CR-EOMCCSD(T)}} = \frac{\langle \tilde{\Psi}_{\text{CC}}^k | M_{k,3}^{\text{EOMCCSD}} | \Psi_0 \rangle}{\langle \tilde{\Psi}_{\text{CC}}^k | (\hat{\Omega}_{k,0} + \hat{\Omega}_{k,1} + \hat{\Omega}_{k,2}) e^{\hat{T}_1 + \hat{T}_2} | \Psi_0 \rangle}. \tag{6.31}$$

More numerically efficient approach than the CR-EOMCCSD(T) method is the CR-EOMCCSd(t) method that employ a truncated orbital space for the triples contribution, which is often referred to as the active space variant of CR-EOMCCSD(T) [116].

The EOMCCSD(T) family of methods is suitable for the calculation of vertical excited-state energies for small and large molecules, since the absolute energies are size-extensive and the excitation energies are size-intensive [2]. The advantage of the EOMCC approach is that many excited states can be calculated in one single run.

## 6.3 Multi-Reference Coupled Cluster Approaches

In order to account for the static/non-dynamic correlation energy within the CC method, its extension to the multi-reference case is necessary. In contrast to the single-reference CC approach, the multi-reference formulation defines a number of determinants $\Psi_m$ (including the ground-state determinant $\Psi_0$) that form a certain subspace $\mathbf{M_0}$. The whole configurational space $\mathbf{M}$, is therefore divided into a model space $\mathbf{M}_0$ and its orthogonal counterpart $\mathbf{M}_\perp$. The model space $\mathbf{M}_0$ is defined through the projection operator $\hat{P}$,

$$\hat{P} = \sum_m^{m_0} |\Psi_m\rangle\langle\Psi_m| \tag{6.32}$$

and the orthogonal space ($\hat{Q} = 1 - \hat{P}$) through the operator $\hat{Q}$,

$$\hat{Q} = \sum_x^{m_x} |\Psi_x\rangle\langle\Psi_x|. \tag{6.33}$$

[2] Size-intensive properties are those that do not depend on the system size.

In the above equations, $\Psi_m$ is a model determinant, $m_0$ denotes the size of the active space, $\Psi_x$ is a determinant created by excitations outside the model space and $m_x$ indicates the size of the orthogonal space [101, 102].

The model function $\Psi_k^0$ is defined through the action of the operator $\hat{P}$ on the exact wave function $\Psi_k$, *i.e.*, a linear combination (with coefficients $c_{mk}$) of the model determinants,

$$\Psi_k^0 = \hat{P}\Psi_k = \sum_m^{m_0} c_{mk}\Psi_m. \tag{6.34}$$

Similar to the single-reference CC, the intermediate normalization is also used in the multi-reference case,

$$\langle\Psi_k^0|\Psi_k\rangle = \langle\Psi_k^0|\hat{\Omega}_{\mathrm{MR}}|\Psi_k^0\rangle = 1, \tag{6.35}$$

where $\hat{\Omega}_{\mathrm{MR}}$ is a multi-reference excitation operator that fulfills the following relations

$$\hat{P}\hat{\Omega}_{\mathrm{MR}} = \hat{P}, \tag{6.36}$$

$$\hat{\Omega}_{\mathrm{MR}}\hat{P} = \hat{\Omega}_{\mathrm{MR}}, \tag{6.37}$$

$$\hat{\Omega}_{\mathrm{MR}}^2 = \hat{\Omega}_{\mathrm{MR}}. \tag{6.38}$$

The $\hat{\Omega}_{\mathrm{MR}}$ acts on the model space, while excitations occur only outside the $\hat{P}$ space. In the multi-reference CC theory, the exact energy of the system is obtained via diagonalization of the so-called effective Hamiltonian $\hat{H}^{\mathrm{eff}}$ that transform the eigenvalue from the entire Hilbert-space to the model space [102]

$$\hat{H}^{\mathrm{eff}}\Psi_k^0 = E_k\Psi_k^0, \tag{6.39}$$

where $\hat{H}^{\mathrm{eff}} = \hat{P}\hat{H}\hat{\Omega}_{\mathrm{MR}}\hat{P}$. The Bloch equation [117, 118] is used to determine the multi-reference wave function operator

$$\hat{H}\hat{\Omega}_{\mathrm{MR}}\hat{P} = \hat{\Omega}_{\mathrm{MR}}\hat{H}^{\mathrm{eff}}\hat{P}. \tag{6.40}$$

The above mentioned diagonalization of $\hat{H}^{\mathrm{eff}}$ describes the static/non-dynamic part of the correlation energy, while the remaining dynamic correlation energy is covered by virtual excitations to the $\hat{Q}$ space determinants via the wave or cluster operators [102].

In general, there are two possible choices of the operator $\hat{\Omega}_{\mathrm{MR}}$:

(i) it is defined as a sum of independent operators for each model function $\Psi_0$,

$$\hat{\Omega}_{\mathrm{HS}} = \sum_{\mu} e^{\hat{S}^{\mu}} \hat{P}_{\mu}, \tag{6.41}$$

where the summation over $\mu$ runs over all model determinants and $\hat{S}$ is a cluster operator [119]. Such a formulation is often referred to as the *Hilbert-space* or *state-specific* multi-reference CC approach.

(ii) it is assumed to have the same form for all reference determinants,

$$\hat{\Omega}_{\mathrm{FS}} = \left\{ e^{\hat{S}+\hat{T}} \right\} = e^{\hat{T}} \left\{ e^{\hat{S}} \right\}, \tag{6.42}$$

where $\{\}$ denotes the normal ordered product form that avoids contractions between cluster operators [109]. This is the *Fock-space* or *valence-universal* formulation of the multi-reference CC approach [120].

In the following subsection, we will focus on the Fock-space variant of the multi-reference CC approach, as it is employed in the study of excited states in actinide-containing complexes in Chapters (9) and (11).

### 6.3.1 Fock-Space Coupled Cluster

The Fock-space is defined as a direct sum, for $N$ from 0 to $\infty$, of the $N$-particle Hilbert-space,

$$\mathcal{F}_{\infty} = \bigoplus_{N=0}^{\infty} \mathcal{H}_N, \tag{6.43}$$

where $\mathcal{F}_{\infty}$ indicates the Fock-space and $\mathcal{H}_N$ the $N$-particle Hilbert-space, respectively, and allows therefore for description of systems with an unknown numbers of particles. $\mathcal{F}_{\infty}$ contains the spaces $\mathcal{F}_N$,

$$\mathcal{F}_N = \bigoplus_{n=0}^{N} \mathcal{H}_n \tag{6.44}$$

as subspaces of states with at most $N$ particles which are used in the Fock-space CC (FSCC) [101, 102, 120–122] method.

In the FSCC approach, operators are defined for different numbers of particles via so called *hole-particle formalism* that leads to different sectors of the Fock-space [102]. Every sector consists of a model space created by removal or attachment of electrons from the Fermi vacuum, *i.e.*, apart from the reference ground state $\Psi_0$ that was chosen in the single-reference CC, the ionized, electron attached and

mixed-states are also considered. In general, each sector is defined by $k$ number of holes and $l$ number of electrons attached with respect to the Fermi vacuum, which is usually denoted as $(k,l)$. Therefore, the cluster operator $\hat{S}$ in Eq. (6.42) which can be represented as

$$\hat{S} = \hat{S}_1 + \hat{S}_2 + \hat{S}_3 + \ldots + \hat{S}_n, \tag{6.45}$$

where

$$\hat{S}_n = \frac{1}{(n!)^2} \sum_{\bar{\bar{a}}\bar{\bar{b}}\ldots\bar{\bar{i}}\bar{\bar{j}}\ldots}{}' s_{\bar{\bar{i}}\bar{\bar{j}}\ldots}^{\bar{\bar{a}}\bar{\bar{b}}\ldots} \bar{\bar{a}}^{\dagger}\bar{\bar{b}}^{\dagger}\ldots\bar{\bar{j}}\bar{\bar{i}} \tag{6.46}$$

with indices $\bar{\bar{a}}\bar{\bar{b}}\ldots$ and $\bar{\bar{i}}\bar{\bar{j}}$ running over inactive particle, inactive holes, and all valence levels, respectively (the $'$ in the summation indicates here that excitations within the model space are excluded), defines every operator that differ in amount of quasi-degeneracy

$$\hat{S}_n = \hat{S}_n^{(0,0)} + \hat{S}_n^{(0,1)} + \hat{S}_n^{(1,0)} + \hat{S}_n^{(1,1)} + \ldots + \hat{S}_n^{(k,l)}. \tag{6.47}$$

In the above equation, the sector $(0,0)$ corresponds to the ground-state, $(0,1)$ represent EA's, $(1,0)$ IP's and $(1,1)$ excitation energies with respect to the sector $(0,0)$, *etc.* Such a separation of operators does not involve any approximation and simultaneously reduces the computational effort [123]. Similar decomposition is invoked for the projection operators $\hat{P}$ and $\hat{Q}$ [102].

The amplitudes for each sector can be determined in hierarchical order, that is, in order to solve the equations for the $(k,l)$ sector, first all the lower sectors must be determined [101], which can be written as

$$\hat{S}^{(k,l)}\hat{P}^{(i,j)} = 0 \quad \text{if } k > i \text{ or } l > j. \tag{6.48}$$

Since the above relation is also applicable to an arbitrary amount of products of operators $\hat{S}^{(k,l)}$, *e.g.*, $\hat{S}^{(a,b)}\hat{S}^{(k-a,l-b)}$, many terms in the expansion $\{e^{\hat{S}}\}\hat{P}^{(i,j)}$ reduce to 0 [102]. This is often referred to as the *subsystem embedding condition* [124].

Within this formulation, the amplitudes for each separate sector of the Fock-space are determined from the following expression,

$$\langle \Psi_{ij\ldots}^{ab\ldots(k,l)} | \hat{H}\hat{\Omega}_{\mathrm{FS}} - \hat{\Omega}_{\mathrm{FS}}\hat{H}^{\mathrm{eff}(k,l)} | \Psi_0^{(k,l)} \rangle = 0, \tag{6.49}$$

where the effective Hamiltonian

$$\hat{H}^{\mathrm{eff}(k,l)} = \hat{P}^{(k,l)}\hat{H}\{e^{\hat{S}}\}\hat{P}^{(k,l)} \tag{6.50}$$

yields electronic energies that correspond to a certain sector $(k,l)$. The above equation reduces to Eq. (6.13) when the sector $(0,0)$ is considered.

In the FSCC method, the total energies are size-extensive, while the excitation energies are size-intensive. Therefore it represents an adequate approach to study electronic spectra of systems with a large number of electrons, such as actinides. In practical FSCC calculations one usually starts by choosing the closed-shell (nondegenerate) reference determinant or the high-spin open-shell reference determinant. However, for qualitatively good results, it is important that the reference determinant possesses a dominant contribution. After having chosen the sector $(0,0)$, excitation energies can be usually obtained from the sector $(1,1)$ [125, 126]. Yet, transition energies from other sectors, *e.g.*, $(0,1)$, $(0,2)$ and $(1,2)$ were also investigated [127]. Most often the FSCC with singles and doubles (FSCC-SD) is employed in combination of the above mentioned sectors [123].

While an advantage of the FSCC method is that it enables to calculate a large number of excitation energies in a single run, accounting at the same time for both dynamic and static/non-dynamic correlation effects, it suffers from the intruder state problem. This can occur when the definition of the $\hat{P}$ and $\hat{Q}$ spaces is not straightforward or the gap between them is simply too small, more precisely, when some low-lying states in the $\hat{Q}^{(k,l)}$ subspace have energies that are close to the higher-lying states in the $\hat{P}^{(k,l)}$ subspace. As a consequence small energy denominators appear in Eq. (6.49) which lead to serious convergence problems when larger $\hat{P}$ spaces are considered, *e.g.*, similar to the size required in actinides [126].

#### 6.3.1.1 Intermediate Hamiltonian Fock-Space Coupled Cluster

A remedy for the intruder state problem in the FSCC approach is to apply the intermediate Hamiltonian technique introduced by Malrieu in the multi-reference perturbation theory [128] and adopted to FSCC by Mukherjee [129], Koch [130], Meissner [131–134] and Landau [135–139].

In the intermediate Hamiltonian FSCC (IHFSCC) method of Landau and Kaldor [135–137], the $\hat{P}$ space is divided into a model space $\hat{P}_m$ of dimension $N_m$ and the intermediate space $\hat{P}_i$ of dimension $N_i$ as follows

$$\hat{P} = \hat{P}_i + \hat{P}_m. \tag{6.51}$$

The $\hat{P}_i$ space serves as a buffer between the $\hat{P}_m$ and $\hat{Q}$ spaces that separates the space of interest ($\hat{P}$ space) from contaminating states in $\hat{Q}$. This allows one to alleviate convergence problems encountered in the regular FSCC approach.

The main goal of this method is to obtain an intermediate Hamiltonian $\hat{H}_I$ within the $\hat{P}$ space,

$$\hat{H}_I \hat{P}|\Psi_m\rangle = E_m \hat{P}|\Psi_m\rangle, \tag{6.52}$$

that will give the exact solutions of the real Hamiltonian,

$$\hat{H}|\Psi_m\rangle = E_m|\Psi_m\rangle. \tag{6.53}$$

It is important to note that only the eigenvalues corresponding to $\Psi_m$ are required to satisfy the above equation, while the eigenvalues corresponding to states $\Psi_i$ with the largest components in the $\hat{P}$ space may include larger errors.

The intermediate Hamiltonian has the form

$$\hat{H}_I = \hat{P}\hat{H}\{e^{\hat{T}}\}\hat{P}. \tag{6.54}$$

The diagonalization of $\hat{H}_I$ in the entire $\hat{P}$ space accounts for the static/non-dynamic correlation energy that arises from both $\hat{P}_m$ and $\hat{P}_i$ states.

Having all the advantages of the FSCC and being intruder-state-free, the IHF-SCC approach has become a standard method for treating small model molecules, also those containing heavy elements [101, 125, 126, 136, 138–141].

# 7 Embedding Methods

> A new scientific truth does not triumph by convincing its opponents and making them see the light, but rather because its opponents eventually die, and a new generation grows up that is familiar with it.
>
> Max Planck

Electronic spectra of large and highly complex systems can be understood on the basis of transition energies of small building blocks. In some cases it is particularly useful to partition the whole system under study into an *active* part that is treated very accurately and the *environment* that is described less accurately, usually at lower computational cost.

A number of theoretical methods have been developed and employed in the past decade to study electronic spectra in such a hybrid approach, among which the most important are continuum models [142, 143], mixed molecular mechanic/quantum mechanics (QM/MM) [144], effective fragment potential (EFP) [145] and frozen density embedding (FDE) [146–148] schemes. The latter one is the most rigorous approach since it treats both the active and environment subsystems at the quantum chemical level as well as being parameter free [122, 149]. While it appears to be the most suitable approximation to study local transition energies in large actinide molecules, it has not yet been fully explored in this field.

## 7.1 Frozen Density Embedding

The FDE method, also called DFT-in-DFT (density functional theory in density functional theory) is an alternative approach to KS DFT that relies on the partitioning of the total density into two contributions: the density $\rho_I(\mathbf{r})$ of the active

system and one or more densities $\rho_{II}(\mathbf{r})(1)$, $\rho_{II}(\mathbf{r})(2)$ $\ldots$ $\rho_{II}(\mathbf{r})(S)$ of the environment, where $S$ denotes the number of subsystems in the environment. In the simplest case, the partitioning is performed into $\rho_I(\mathbf{r})$ and $\rho_{II}(\mathbf{r})$ where the latter represents the whole environment,

$$\rho_{\text{tot}}(\mathbf{r}) = \rho_I(\mathbf{r}) + \rho_{II}(\mathbf{r}). \tag{7.1}$$

After having defined the partitioning accordingly to the above equation, the total DFT energy is expressed as a functional of the two subsystem densities

$$E_{\text{tot}}[\rho_I(\mathbf{r}), \rho_{II}(\mathbf{r})] = E_I[\rho_I(\mathbf{r})] + E_{II}[\rho_{II}(\mathbf{r})] + E_{\text{int}}[\rho_I(\mathbf{r}), \rho_{II}(\mathbf{r})], \tag{7.2}$$

where $E_I[\rho_I(\mathbf{r})]$ and $E_{II}[\rho_{II}(\mathbf{r})]$ are the energies of two individual subsystems, and $E_{\text{int}}[\rho_I(\mathbf{r}), \rho_{II}(\mathbf{r})]$ is the interaction energy between them. The first two terms in Eq. (7.2) are defined accordingly to Eq. (5.8) and the third one reads

$$E_{\text{int}}[\rho_I(\mathbf{r}), \rho_{II}(\mathbf{r})] = \int d\mathbf{r}\rho_{II}(\mathbf{r})v^I(\mathbf{r}) + \int d\mathbf{r}\rho_I(\mathbf{r})v^{II}(\mathbf{r}) + \frac{1}{2}\int d\mathbf{r}d\mathbf{r}'\frac{\rho_I(\mathbf{r})\rho_{II}(\mathbf{r}')}{|\mathbf{r}-\mathbf{r}'|} + T_s^{\text{nadd}}[\rho_I(\mathbf{r}), \rho_{II}(\mathbf{r})] + E_{\text{xc}}^{\text{nadd}}[\rho_I(\mathbf{r}), \rho_{II}(\mathbf{r})], \tag{7.3}$$

where the non-additive exchange–correlation and kinetic energy functionals are defined as follow

$$E_{\text{xc}}^{\text{nadd}}[\rho_I(\mathbf{r}), \rho_{II}(\mathbf{r})] = E_{\text{xc}}[\rho_I(\mathbf{r}) + \rho_{II}(\mathbf{r})] - E_{\text{xc}}[\rho_I(\mathbf{r})] - E_{\text{xc}}[\rho_{II}(\mathbf{r})] \tag{7.4}$$

and

$$T_s^{\text{nadd}}[\rho_I(\mathbf{r}), \rho_{II}(\mathbf{r})] = T_s[\rho_I(\mathbf{r}) + \rho_{II}(\mathbf{r})] - T_s[\rho_I(\mathbf{r})] - T_s[\rho_{II}(\mathbf{r})]. \tag{7.5}$$

Both Eqs. (7.4) and (7.5) account for the non-classical contributions to the interaction energy.

The density of the individual subsystems is evaluated employing the KS orbitals

$$\rho_I(\mathbf{r}) = \sum_{i=1, i\in I}^{N^I} \phi_i^*(\mathbf{r})\phi_i(\mathbf{r}), \quad \rho_{II}(\mathbf{r}) = \sum_{i=1, i\in II}^{N^{II}} \phi_i^*(\mathbf{r})\phi_i(\mathbf{r}), \tag{7.6}$$

therefore the kinetic energy of the non-interacting reference systems can be simply obtained from Eq. (5.9). However, the total kinetic energy $T_s[\rho_I(\mathbf{r})+\rho_{II}(\mathbf{r})]$ cannot be evaluated in the same way and remains unknown [147]. As a consequence the non-additive kinetic energy functional of Eq. (7.5) has to be approximated. The

same holds for $E_{\mathrm{xc}}^{\mathrm{nadd}}[\rho_I(\mathbf{r}), \rho_{II}(\mathbf{r})]$, yet its contribution to the interaction energy being much smaller.

In practical calculations $T_s^{\mathrm{nadd}}[\rho_I(\mathbf{r}), \rho_{II}(\mathbf{r})]$ is expressed in some density-depended formulas [150–153], while $E_{\mathrm{xc}}^{\mathrm{nadd}}[\rho_I(\mathbf{r}), \rho_{II}(\mathbf{r})]$ is most often modeled on the basis of the exchange–correlation functional used for the separate subsystems. Furthermore, it became a common procedure to employ the same functional for both $E_{\mathrm{xc}}[\rho_I(\mathbf{r})]$ and $E_{\mathrm{xc}}[\rho_{II}(\mathbf{r})]$ [154], yet using different functionals for the two subsystems has also been investigated [155, 156].

Minimization of the total energy functional of Eq (7.2) with respect to $\rho_I(\mathbf{r})$ carried out under constraining the number of electrons in the active system to $N_I$, leads to a set of coupled KS-like equations

$$\left(-\frac{1}{2}\nabla^2 + v_i^{\mathrm{eff}}[\rho_I(\mathbf{r}), \rho_{II}(\mathbf{r})]\right)\phi_i = \epsilon_i\phi_i, \quad i = 1, 2, \ldots, \frac{N_I}{2}, \tag{7.7}$$

where

$$v_i^{\mathrm{eff}}[\rho_I(\mathbf{r}), \rho_{II}(\mathbf{r})] = v_i^{\mathrm{KS}}[\rho_I(\mathbf{r})] + v_i^{\mathrm{emb}}[\rho_I(\mathbf{r}), \rho_{II}(\mathbf{r})]. \tag{7.8}$$

In the above equation, $v^{\mathrm{emb}}[\rho_I(\mathbf{r}), \rho_{II}(\mathbf{r})]$ is the embedding potential that describes the effect of subsystem $II$ on subsystem $I$, *i.e.*, the interaction of the subsystem $I$ with the nuclei and the environment density of subsystem $II$,

$$\begin{aligned} v^{\mathrm{emb}}[\rho_I(\mathbf{r}), \rho_{II}(\mathbf{r})] =& v_{II}^{\mathrm{nuc}}(\mathbf{r}) \\ &+ \int d\mathbf{r}' \frac{\rho_{II}(\mathbf{r}')}{|\mathbf{r} - \mathbf{r}'|} + \frac{\delta E_{\mathrm{xc}}^{\mathrm{nadd}}[\rho_I, \rho_{II}]}{\delta\rho_I} + \frac{\delta T_s^{\mathrm{nadd}}[\rho_I, \rho_{II}]}{\delta\rho_I}. \end{aligned} \tag{7.9}$$

Furthermore, it is possible to update the electron density of an active subsystem and then freeze it again while the electron density of the embedded subsystem is updated. This is done in a self-consistent fashion until convergence is reached. Such a procedure is referred to as the *freeze-and-thaw* cycles [148].

The FDE scheme has been extended to electronic excited-state calculations, in which the response to an external electromagnetic field is localized on the active subsystem. Such an approach, in which the response of the environment subsystem is completely neglected, leads to an effective embedding potential which reads

$$f_{\mathrm{xc}}^{\mathrm{emb}}(\mathbf{r}, \mathbf{r}') = \frac{\delta^2 E_{\mathrm{xc}}[\rho_I + \rho_{II}]}{\delta\rho(\mathbf{r})\delta\rho(\mathbf{r}')} - \frac{\delta^2 E_{\mathrm{xc}}[\rho_I]}{\delta\rho(\mathbf{r})\delta\rho(\mathbf{r}')} + \frac{\delta^2 T_s^{\mathrm{nadd}}[\rho_I, \rho_{II}]}{\delta\rho(\mathbf{r})\delta\rho_I(\mathbf{r}')}. \tag{7.10}$$

This framework reduces the computational effort for obtaining local (uncoupled) excitation energies in large molecular systems and simplifies the analysis of complex electronic spectra. An extension to coupled excitations energies within the FDE

framework is also available [157].

### 7.1.1 Wave Function Theory in Density Functional Theory

The excitation energies obtained in a FDE scheme can also be described by combining wave function theory with DFT. In the approach developed by Carter and coworkers [158–160], called wave function theory in density functional theory (WFT-in-DFT), the electron density of the active subsystem $\rho_I(\mathbf{r})$ and the environment $\rho_{II}(\mathbf{r})$ are obtained from the wave function and DFT calculations, respectively. The effect of the environment in the WFT calculations of subsystem $I$ is included via an embedding potential as defined in Eq. (7.9).

The total energy as given in Eq. (7.2) can be therefore defined in a similar way and now reads

$$E[\Psi_I(\mathbf{r})^{\mathrm{WFT}}, \rho_{II}(\mathbf{r})^{\mathrm{DFT}}] = E_I[\Psi_I(\mathbf{r})^{\mathrm{WFT}}] + E_{II}[\rho_{II}(\mathbf{r})^{\mathrm{DFT}}] + E_{\mathrm{int}}[\rho_I(\mathbf{r})^{\mathrm{WFT}}, \rho_{II}(\mathbf{r})^{\mathrm{DFT}}]. \tag{7.11}$$

Furthermore, these embedding approaches employed in the static formulation, *i.e.*, without any freeze-and-thaw cycles, but with a frozen density in the environment, have been extended to relativistic calculations and successfully applied in actinide chemistry [161].

# 8 Relativistic Effects

> A great deal of my work is just playing with equations and seeing what they give.
>
> Paul A. M. Dirac

In general, relativistic effects are defined as anything arising from the finite speed of light[1] $c$ as compared to $c = \infty$ [162]. In chemistry, relativistic effects are usually considered as perturbations, or small corrections, to the nonrelativistic Schrödinger equation (4.2). However, in a more accurate treatment of relativistic effects, one has to start from the purely relativistic theory developed by Dirac [163].

The relativistic mass of the electron increases with its velocity by

$$m_{\mathrm{rel}} = \frac{m_e}{\sqrt{1 - \left(\frac{v_e}{c}\right)^2}}, \tag{8.1}$$

where $m_{\mathrm{rel}}$ and $m_e$ are the relativistic and rest (nonrelativistic) mass of the electron, respectively, while $v_e$ is the velocity of electron,

$$v_e = \frac{Z}{n}, \tag{8.2}$$

with $Z$ being the nuclear charge and $n$ the main quantum number. This results in a change of the nonrelativistic Bohr radius $a_0$ from

$$a_0 = \frac{1}{m_e c \alpha} \tag{8.3}$$

[1] Speed of light equals $299792458 \frac{m}{s}$ which is $\approx 137$ au.

to

$$a_{\mathrm{rel}} = \frac{\sqrt{1-\left(\frac{v_e}{c}\right)^2}}{m_e c\alpha} = a_0\sqrt{1-\left(\frac{v_e}{c}\right)^2}, \tag{8.4}$$

where $a_{\mathrm{rel}}$ is the relativistic Bohr radius and $\alpha$ is the fine-structure constant [164]. By substituting Eq. (8.2) into Eq. (8.4), it becomes evident that the electrons of various atomic orbitals with quantum number $n$ and the same nuclear charge $Z$ are effected differently due to the relative velocity of these electrons with respect to the speed of light. If we consider, for instance, a $1s$ electron of the uranium atom which has a speed of $\approx 0.67c$, its mass increases, accordingly to Eq. (8.1), up to $1.35m_e$ and as a result the $1s$-orbital shrinks by 35% [1]. As a consequence, the uranium valence $f$-orbitals are less attracted by the nuclei, which has a significant impact on the bonding properties of uranium compounds. This underlines the importance of going beyond the Schrödinger equation (Eq. (4.2)) which is based on a purely nonrelativistic theory.

At the very beginning, the more complex relativistic quantum theory introduced by Dirac suffered from primary difficulties due to its nontrivial interpretation and lacking acceptability within the chemical community. However in the course of time, relativistic quantum chemistry has developed to a standard approach, especially in the study of heavy elements like actinides [6]. Some basic concepts of relativistic quantum chemistry, starting from the one-electron problem, will be briefly described in the following.

## 8.1 The One-Electron Dirac Equation

The relativistic energy of a free particle with rest mass $m_e$ and momentum $p$ which reads

$$E = c\sqrt{p^2 + m_e^2 c^2}, \tag{8.5}$$

can be recognized as the classical relativistic Hamiltonian. After replacing the observables by the quantum mechanical operators in Eq. (8.5), one obtains the relativistic Hamiltonian which contains the square root of operators. In order to avoid the evolution of the square root into an infinite sum, Dirac assumed that the relativistic Hamiltonian should have a form that is similar to the one employed in the Schrödinger's equation,

$$\hat{h}_D \Psi = E\Psi, \tag{8.6}$$

in which the Dirac Hamiltonian $\hat{h}_D$ is a linear operator with respect to momentum

$$\hat{h}_D = c(\boldsymbol{\alpha}\cdot\boldsymbol{p}) + \beta m_e c^2, \tag{8.7}$$

where $\boldsymbol{\alpha} = \{\alpha_x, \alpha_y, \alpha_z\}$ and $\beta$ are the quantities that have to be determined, and $\boldsymbol{p} = \{-i\nabla_x, -i\nabla_y, -i\nabla_z\}$ is a three dimensional momentum operator. The product of $\boldsymbol{\alpha} \cdot \boldsymbol{p}$ is defined as follows

$$\boldsymbol{\alpha} \cdot \boldsymbol{p} = \alpha_x p_x + \alpha_y p_y + \alpha_z p_z. \tag{8.8}$$

Requiring that the square root of $\hat{h}_D$ yields the energies corresponding to Eq. (8.5), the following relations need to be fulfilled

$$\beta^2 = I, \tag{8.9}$$

$$\alpha_k \beta + \beta \alpha_k = 0, \tag{8.10}$$

$$\alpha_k \alpha_l + \alpha_l \alpha_k = 2\delta_{kl}, \tag{8.11}$$

where $\delta_{kl}$ is the Kronecker delta defined according to Eq. (5.3). These conditions can only be fulfilled if both $\boldsymbol{\alpha}$ and $\beta$ are matrices of at least dimension four[2],

$$\alpha_x = \begin{pmatrix} 0 & 0 & 0 & 1 \\ 0 & 0 & 1 & 0 \\ 0 & 1 & 0 & 0 \\ 1 & 0 & 0 & 0 \end{pmatrix}, \qquad \alpha_y = \begin{pmatrix} 0 & 0 & 0 & -i \\ 0 & 0 & i & 0 \\ 0 & -i & 0 & 0 \\ i & 0 & 0 & 0 \end{pmatrix},$$

$$\alpha_z = \begin{pmatrix} 0 & 0 & 1 & 0 \\ 0 & 0 & 0 & -1 \\ 1 & 0 & 0 & 0 \\ 0 & -1 & 0 & 0 \end{pmatrix}, \qquad \beta = \begin{pmatrix} 1 & 0 & 0 & 0 \\ 0 & 1 & 0 & 0 \\ 0 & 0 & -1 & 0 \\ 0 & 0 & 0 & -1 \end{pmatrix}.$$

The four dimensional form of $\boldsymbol{\alpha}$ and $\boldsymbol{\beta}$ requires the wave function to be a four-component vector, which in the time-independent case is written as

$$\Psi_D(\mathbf{r}) = \begin{pmatrix} \Psi_1(\mathbf{r}) \\ \Psi_2(\mathbf{r}) \\ \Psi_3(\mathbf{r}) \\ \Psi_4(\mathbf{r}) \end{pmatrix}. \tag{8.12}$$

[2]matrices of higher (even) dimensions also obey the above conditions and are hence possible representations.

Importantly, the $\boldsymbol{\alpha}$ matrices automatically include the spin information encoded in the Pauli spin-matrices,

$$\sigma_x = \begin{pmatrix} 0 & 1 \\ 1 & 0 \end{pmatrix}, \qquad \sigma_y = \begin{pmatrix} 0 & -i \\ i & 0 \end{pmatrix}, \qquad \sigma_z = \begin{pmatrix} 1 & 0 \\ 0 & -1 \end{pmatrix},$$

which account for the spin in a proper, *i.e.*, non-*ad-hoc* way. This leads to the superiority of the relativistic Dirac theory over the nonrelativistic Schrödinger's theory, where the existence of spin was postulated *a posteriori*.

The two possible spectra of energies separated by $2m_ec^2$ are associated with the solutions of the Hamiltonian as defined in Eq. (8.7),

$$E = -\sqrt{p^2c^2 + m_ec^4} \tag{8.13}$$

and

$$E = +\sqrt{p^2c^2 + m_ec^4}. \tag{8.14}$$

After adding the Coulomb term to the Dirac Hamiltonian $\hat{h}_D$, which is responsible for the electrostatic interaction between the nucleus and the electron $\hat{V}$, the equation for hydrogen-like atoms is obtained which reads

$$\hat{h}_D = c(\boldsymbol{\alpha} \cdot \boldsymbol{p}) + \beta m_ec^2 + \hat{V}\mathbf{I} \tag{8.15}$$

where $\mathbf{I}$ is a $4 \times 4$ identity matrix. The above equation represents a very good model for the analysis of the relativistic theory.

The energy spectrum of the Hamiltonian of Eq. (8.15) consists of three characteristic parts:

(i) a continuous spectrum with energies in the range of $-\infty$ to $-m_ec^2$

(ii) a continuous spectrum with energies in the range of $+m_ec^2$ to $+\infty$

(iii) a discrete energy spectrum that is located slightly below $+m_ec^2$.

Especially, the discrete energy spectrum is of interest for chemical processes and can be described employing the following expression [8, 165]

$$E_{n,\kappa} = m_ec^2 \left[ 1 + \left( \frac{\frac{Z}{c}}{n - |\kappa| + \sqrt{\kappa^2 - \frac{Z^2}{c^2}}} \right)^2 \right]^{-\frac{1}{2}}, \tag{8.16}$$

where $n = 1, 2, 3, \ldots$ is the main quantum number, and $\kappa = \pm(j + \frac{1}{2}) =$

$\pm 1, \pm 2, \pm 3, \pm \ldots$ with $j$ being the combined magnetic and spin quantum number, *i.e.*, $j = l \pm s$.

Taylor expansion of Eq. (8.16) with respect to $\frac{Z}{c}$ results in the following energy expression

$$E = m_e c^2 + \frac{Z^2}{2n^2} + \frac{Z^4}{2n^4 c^2} \left\{ \frac{3}{4} - \frac{n}{j + \frac{1}{2}} \right\} + O\left( \frac{Z^6}{c^4} \right), \tag{8.17}$$

in which the terms on the right hand side are the rest mass energy, the nonrelativistic binding energy, and the relativistic corrections (mass-velocity, Darwin, spin–orbit, *etc*), respectively. Setting $c = \infty$, the above equation reduces to the nonrelativistic Schrödinger energy expression [166].

## 8.2 The Many-Electron Dirac Hamiltonian

A many-electron Dirac equation can be formed by a sum of one-electron operators as defined in Eq. (8.15) and the two-electron Coulomb interaction,

$$\left( \sum_k \hat{h}_D^k + \sum_{k<l} \hat{g}_{DC}^{kl} \right) \Psi_D^i(\mathbf{r}) = E^i \Psi_D^i(\mathbf{r}), \tag{8.18}$$

where the Dirac–Coulomb term $\hat{g}_{DC}^{kl} = \frac{1}{r_{kl}}$ represents the charge-charge interaction. However, treating the many-body interactions as described in the above equation results in a Hamiltonian which is not Lorentz-invariant. In oder to fulfill the requirements of the theory of special relativity, only retarded potentials should be considered [166]. The most important correction that mimics the retarded potential is obtained by taking the Breit [167] interaction into account

$$\hat{g}_{\text{Breit}}^{kl} = -\frac{1}{2c^2 r_{kl}} \left( c\alpha_k \cdot c\alpha_l + \frac{(c\alpha_k \cdot \mathbf{r}_{kl})(c\alpha_l \cdot \mathbf{r}_{kl})}{r_{kl}^2} \right). \tag{8.19}$$

The Breit term can be rearranged to a more convenient form

$$\hat{g}_{\text{Breit}}^{kl} = -\frac{c\alpha_k \cdot c\alpha_l}{c^2 r_{kl}} - \frac{(c\alpha_k \cdot \nabla_k)(c\alpha_l \cdot \nabla_l) r_{kl}}{2c^2}, \tag{8.20}$$

in which the first and the second term are called Gaunt [168] and gauge, respectively. The former represents the current-current (magnetic) interaction and is the leading term in the above expression [8].

It is important to stress that the relativistic Hamiltonian as defined in Eq. (8.18) has no bound solutions since the discrete energy levels would be embedded

in a sea of continuous (negative) energy levels. Hence, minimization of the energy without any additional constraints most often results in the positronic-like solutions, which is usually referred to as the Brown–Ravehall disease [169]. In order to avoid the collapse into the negative energy spectrum, the *no-pair approximation* is applied in practical calculations, where the $N$-particle space is build of determinants containing only the positive-energy spinors [166]. Furthermore, this approximation is also employed in relativistic correlated calculations [170].

## 8.3 Two-Component Methods

It is desirable to employ as much as possible from the nonrelativistic theory in solving the Dirac equation. This can be achieved, for instance, by reduction of the four-component theory of Dirac to a much simpler two-component (two-spinor) framework, in which only the electronic solutions will be considered. Therefore, the basic idea of the two-component formalism is to completely separate the electronic and positronic solutions of the Dirac equation [171]. While this is a rather straightforward procedure for the one-electron Dirac equation [172], it becomes more complicated for realistic systems, in particular, the inclusion of the two-electron terms requires a correction for picture change errors [173].

In the past decade, a number of these two-component approaches have been developed, which not only simplify the four-component formalism, but also reduce the computational expenses [8, 174, 175]. Two methods that are of considerable importance in electronic spectroscopy of heavy elements are briefly described below.

### 8.3.1 The Zeroth Order Regular Approximation (ZORA)

The one-electron Dirac equation in its two-component form can be written as

$$\begin{pmatrix} V & c(\boldsymbol{\sigma}\cdot\boldsymbol{p}) \\ c(\boldsymbol{\sigma}\cdot\boldsymbol{p}) & -2m_ec^2+V \end{pmatrix} \begin{pmatrix} \Psi^L(\mathbf{r}) \\ \Psi^S(\mathbf{r}) \end{pmatrix} = E \begin{pmatrix} \Psi^L(\mathbf{r}) \\ \Psi^S(\mathbf{r}) \end{pmatrix}, \tag{8.21}$$

where $\boldsymbol{\sigma}$ denotes the Pauli matrices, and $\Psi^L(\mathbf{r})$ and $\Psi^S(\mathbf{r})$ are called the *large* and *small* component functions, respectively. The relation between $\Psi^L(\mathbf{r})$ and $\Psi^S(\mathbf{r})$,

$$\Psi^S(\mathbf{r}) = K(E,\mathbf{r})\frac{\boldsymbol{\sigma}\cdot\boldsymbol{p}}{2m_ec}\Psi^L(\mathbf{r}) \tag{8.22}$$

with a multiplicative operator defined as

$$K(E,\mathbf{r}) = \left(1 + \frac{E-V}{2m_e c^2}\right)^{-1} = \left(1 - \frac{V}{2m_e c^2}\right)^{-1} \left(1 + \frac{E}{2m_e c^2 - V}\right)^{-1} \tag{8.23}$$

leads to the ZORA (zeroth order regular approximation)[176, 177] Hamiltonian when only the first term on the right hand side is considered,

$$\left(\frac{1}{2m_e}(\boldsymbol{\sigma}\cdot\boldsymbol{p})\left(1 - \frac{V}{2m_e c^2}\right)^{-1}(\boldsymbol{\sigma}\cdot\boldsymbol{p})\right)\psi^{\mathrm{ZORA}}(\mathbf{r}) = E\psi^{\mathrm{ZORA}}(\mathbf{r}). \tag{8.24}$$

Despite having no singularities, the ZORA Hamiltonian as defined above is not gauge invariant. The latter can be overcome by either employing higher order approximations to Eq. (8.23) or by simple scaling [165, 171, 178].

### 8.3.2 The Douglas–Kroll–Hess (DKH) Method

Another, conceptual different two-component method was developed by Douglas, Kroll and Hess [179, 180] and takes the acronym DKH. The basic idea of their approach is based on the Foldy–Wouthuysen [172] transformation and an iterative decoupling of the large and small components of the Dirac equation,

$$\hat{H}^{\mathrm{DKH}} = U^{\dagger}\hat{H}_D U = \begin{pmatrix} h_+ & 0 \\ 0 & h_- \end{pmatrix}, \tag{8.25}$$

in such a way that $h_+$ will correspond to the purely electronic solutions. Douglas and Hess suggested to use the following transformation

$$U^{(i)} = \sqrt{1 + \hat{W}_i^2} + \hat{W}_i, \tag{8.26}$$

in the iterative procedure, with $\hat{W}_i$ being an anti-Hermitian operator (*cf.* Ref. [7] for more details).

The most widely used decoupling scheme is the second order Douglas–Kroll-Hess Hamiltonian (DKH2). Yet, extensions to higher order corrections, which allow for a more complete decoupling of the (one-electron) Dirac Hamiltonian, are also available [181–183].

# Part III

# ELECTRONIC SPECTRA OF ACTINIDES

# 9

# Electronic Spectroscopy of $UO_2^{2+}$, $NUO^+$ and NUN: An Evaluation of Time-dependent Density Functional Theory for Actinides

> The process of scientific discovery is, in effect, a continual flight from wonder.
>
> Albert Einstein

Adopted from:
Tecmer, P., Gomes, A. S. P., Ekström, U., Visscher, L.,
*Phys. Chem. Chem. Phys.*, **13** (2011) 6249.

## 9.1 Abstract

The performance of the time-dependent density functional theory (TD-DFT) approach has been evaluated for the electronic spectrum of the $UO_2^{2+}$, $NUO^+$ and NUN molecules. Different exchange–correlation functionals (LDA, PBE, BLYP, B3LYP, PBE0, M06, M06-L, M06-2X, CAM-B3LYP) and the SAOP model potential have been investigated, as has the relative importance of the adiabatic local density approximation (ALDA) to the exchange–correlation kernel. The vertical excitation energies have been compared with reference data obtained using accurate wave function theory (WFT) methods.

## 9.2 Introduction

The importance of theoretical modeling in furthering the understanding of the chemistry of actinide-containing systems, compared to other branches of chemistry, is by now well established. This prominent role has to do with the experimental difficulties involved in actinide research: besides the acute radiotoxicity of most species, which place severe restrictions on laboratory manipulations, the wide range of oxidation states possible for early actinides (U–Am), together with a relative ease of changing their oxidation states often makes it difficult to isolate and characterize species.

One of the most active areas of chemical research on actinides is related to the reprocessing of nuclear waste, whose objective is to separate uranium and plutonium from the other (minor) actinides. Such separation has implications both to the recycling of irradiated nuclear fuels (by allowing the retrieval of important quantities of U and Pu from spent fuel and their subsequent reconversion back to usable fuel) and to the disposal of nuclear waste (as it decreases the volume of material to be stored). While separation methods based upon liquid–liquid extraction ion-exchange, such as the plutonium uranium extraction (PUREX) [18, 19] or transuranic extraction (TRUEX) [184] processes are rather well established, the details of the interaction of the extraction ligand with the actinide species (such as the simple atomic ions $Ac^{n+}$ or the frequently found actinyl ($AcO_2^{n+}$) species) are still far from fully understood.

Bridging this gap in understanding would be particularly helpful in designing more efficient and selective complexing agents. Modeling this process is challenging, because it requires an accurate description of the actinide and the complexing species, as well as their interactions with the solvent environment. This is currently only possible within the DFT approach, as its modest computational cost facilitates the study of structures and energetics of large model complexes, even in the condensed phase [25, 185–190].

Notwithstanding this progress, the success of DFT still depends on careful parametrization and benchmarking studies that establish the reliability of exchange–correlation functionals for a particular application. This is especially serious for molecules containing heavy elements since such systems were usually not accounted for in the parametrization and validation stages of the currently available density functionals. One particular reason for concern is the strong (static and dynamic) electron correlation effects in actinides. The $5f$-, $7s$-, $6p$- and $6d$-orbitals should all be considered as valence orbitals that can contribute to chemical bonding. While energetically close, these orbitals have a rather different spatial character hampering the description of the exchange–correlation interac-

tion by a density functional compared to lighter elements. These difficulties have been investigated for uranium oxides [191], showing that DFT, using proper density functionals, is typically suitable for geometry optimization and thermochemistry of the electronic ground-state for these systems. Based on a series of studies of solvated uranium fluorides and oxofluorides, Schreckenbach and Shamov [192] conclude that GGA functionals yield accurate geometries and frequencies, while hybrid density functionals are found to be superior for thermochemistry.

The question of suitability of DFT for studying actinide-containing molecules carries over to its time-dependent generalization, TD-DFT (see Section (5.3)), which is employed to calculate properties depending upon the response of the density to an external perturbation. These calculations facilitate the prediction and analysis of electronic spectra, polarizabilities or magnetizabilities, and vibrational Raman spectra, all of which are useful tools in studying the interactions of the actinide system with the complexing agents, or of that complex with the environment. While TD-DFT has been shown to work rather well for some transition metal excited-states [193–195], its reliability for actinide-containing molecules is less assessed (see Refs. [36, 196, 197] for some examples).

The aim of this chapter is to explore different flavors of TD-DFT for the calculation of electronic spectra for different actinide-containing compounds, i.e., the evaluation of (meta-)GGAs and (meta-)hybrid functionals within the adiabatic approximation. We will also study the influence of replacing the functional derivatives in the exchange–correlation kernel by the simpler LDA approach (ALDA) that is often used to simplify the implementation of TD-DFT.

First, we will focus on three small molecules, $UO_2^{2+}$, $NUO^+$ and NUN, since (i) they represent closed-shell systems in their ground-states, thus problems with the validity of the reference state for TD-DFT are avoided; (ii) they are all isoelectronic species, hence the influence of the change in, for instance, the electronegativity on the spectra can be analyzed; (iii) since the -N=U=N- and O=U=N- groups appear in larger organometallic systems, they can serve as stepping stones for the description of their oxo(MO), imido (MNR) and phoshorane iminato ($MNPR_3$) [4, 24, 198, 199] analogs, which are very important in nuclear waste separation, and (iv) in contrast to $UO_2^{2+}$, which has received extensive attention from theoreticians [35, 36, 126, 197, 200–203], the electronic spectra of the isoelectronic species ($NUO^+$ and NUN [22, 204, 205]) have not yet been investigated in detail.

The lack of experimental data requires that our assessment need to be done by comparison to accurate wave function-based calculations, namely the CASPT2 [103, 104] and the IHFSCC-SD [136, 138, 139] methods. Employing both methods in tandem provides a cross-validation of WFT results, and accesses the rich set

of analysis tools available for CASPT2 (in our case population analysis of the excited-states).

CASPT2 and IHFSCC-SD are examples of multi-reference approaches to the electron correlation problem, and are known to perform well for actinide- and other heavy element-containing molecules since such systems often present (nearly-)degenerate electronic states [125, 196, 206] (*e.g.* half-filled $f$-shells etc.). Unsurprisingly, they also show a very good performance in cases where the reference wave function is still dominated by a single determinant [126, 207].

The IHFSCC-SD method is particularly interesting here because of its ability to yield a number of electronic states of the molecule in a single calculation due to electron attachment or detachment. Furthermore, as all states have a common Fermi vacuum, the elimination of a potential bias towards a given reference state represents a severe advantage. The Intermediate Hamiltonian ansatz thereby circumvents a well-known drawback of the Fock-space (and other multireference coupled cluster) approaches by largely eliminating the intruder states that could otherwise obstruct the convergence of the FSCC algorithm. The FSCCSD as well as IHFSCC-SD methods are briefly discussed in Section (6.2). More detailed information can be found in the following reviews [101, 102, 121, 141].

We note that SOC effects are small in the ground-states of these molecules, with scalar relativistic and four-component relativistic methods agreeing to within 1 pm on the bond distance of $UO_2^{2+}$ [126]. The effects on the electronic spectra are more important but do not affect the comparison between different correlation methods that is the subject of the current chapter. Therefore the focus will be exclusively on spin–free calculations to simplify the discussions. A detailed discussion and of the SOC-CASP2 and SOC-IHFSCC-SD results for $UO_2^{2+}$ can be found in Ref. [126]. Spin–orbit effects on the spectra of NUN and $NUO^+$ will be addressed in a subsequent publication.

## 9.3 Computational Details

All calculations were performed with spin–free relativistic methods using ADF2008 (and ADF2009 [208–210] for the (meta-)hybrid functionals), as well as with a development version of the DIRAC08 [211] program. To facilitate comparisons with the TD-DFT calculations of van Besien and Pierloot [36], the same structure for the $UO_2^{2+}$ ion was taken, i.e., a U–O bond distance of 1.708 Å. The geometries of NUN and $NUO^+$ were optimized with the PBE exchange–correlation functional employing the ADF TZ2P basis set and the all-electron scalar relativistic ZORA (Zero Order Regular Approximation) Hamiltonian [177]. The U–N distance was

determined to be 1.739 Åin the NUN molecule and 1.698 Åfor $NUO^+$, respectively, while the U–O distance in $NUO^+$ is calculated to be 1.761 Å.

### 9.3.1 TD-DFT

In the TD-DFT calculations, the adiabatic approximation is applied, where the frequency-dependent exchange–correlation kernel has been replaced by the local (in time) functional derivatives of the frequency-independent functional. In ADF, the ALDA approximation is used for all exchange–correlation functionals, while the full derivatives of the functionals, obtained via the XCFun DFT library [212], in the exchange–correlation kernel are used in our DIRAC calculations [197] in addition to the ALDA approach. We should note that, in the case of hybrid functionals, the fractional Hartree–Fock exchange is always included in the TD-DFT kernel in both ADF and DIRAC.

Six different exchange–correlation functionals have been evaluated in the ADF and DIRAC program packages: LDA [70], PBE [76], BLYP [74, 75, 213], B3LYP [83, 84], PBE0 [85] as well as the SAOP model potential [91, 93]. Additionally, the M06, M06-L, and M06-2X functionals [77, 87] were evaluated in the ALDA approximation using ADF, while CAM-B3LYP [90] was evaluated in DIRAC for both the ALDA and full (non-ALDA) TD-DFT kernels.

In all calculations with ADF TZ2P basis sets (U:15$s$13$p$9$d$5$f$; O:5$s$3$p$1$d$1$f$) [214] were used, while in DIRAC the triple zeta basis set of Dyall [215] for the uranium atom (33$s$29$p$20$d$13$f$5$g$2$h$), and the uncontracted aug-cc-pVTZ basis set for the oxygen and nitrogen atoms (11$s$6$p$3$d$2$f$) [216, 217] were employed. The scalar ZORA [177] Hamiltonian was used in ADF, and the spin–free Dirac–Coulomb [218] (DC) Hamiltonian in DIRAC. Furthermore, in the case of DC, the $(SS|SS)$ integrals have been approximated by a point charge model [219].

Our work focused on five low-lying vertical excitations determined by DFT calculations. For $UO_2^{2+}$ we studied transitions mainly consisting of excitations $3\sigma_u \rightarrow 1\phi_u$, $3\sigma_u \rightarrow 1\delta_u$, $2\pi_u \rightarrow 1\phi_u$, $3\sigma_g \rightarrow 1\phi_u$ and $3\sigma_g \rightarrow 1\delta_u$. For the $NUO^+$ molecule the following dominant excitations were studied: $6\sigma \rightarrow 1\phi$, $6\sigma \rightarrow 1\delta$, $3\pi \rightarrow 1\phi$, $3\pi \rightarrow 1\delta$ and $5\sigma \rightarrow 1\phi$, while for NUN the dominant excitations were $3\sigma_u \rightarrow 1\phi_u$, $3\sigma_u \rightarrow 1\delta_u$, $3\sigma_g \rightarrow 1\phi_u$, $2\pi_u \rightarrow 1\phi_u$ and $3\sigma_u \rightarrow 4\sigma_g$.

### 9.3.2 CASPT2

CASPT2 calculations were carried out with the MOLCAS 7.4 [220] program. For all CASPT2/MS-CASPT2 [103, 104, 221] calculations we utilized the scalar second-order Douglas–Kroll–Hess (DKH2) Hamiltonian [222, 223], together with

the (contracted) ANO-RCC basis sets, optimized specifically for this Hamiltonian: $(26s23p17d13f5g3h) \rightarrow [10s9p7d5f3g2h]$ for uranium, $(14s9p4d3f2g) \rightarrow [5s4p3d2f]$ for oxygen and $(14s9p4d3f2g) \rightarrow [4s3p2d1f]$ for nitrogen [224].

The most important point in the CASSCF calculation is the proper choice of the active space. In the investigated molecules, the U–O and U–N bonds are formed out of the $6p$-, $7s$-, $5f$-, $6d$-orbitals of the uranium atom and the $2s$- and $2p$-orbitals of the oxygen and nitrogen atoms. While it would be ideal to take all molecular orbitals that are formed out of these atomic orbitals of uranium, oxygen and nitrogen into account and correlate them in the CASPT2/MS-CASPT2 level, such an active space becomes computationally unfeasible, and hence the active space needs to be truncated. However, compared to the previous work by Réal [126], it was possible to enlarge the active space for the $UO_2^{2+}$ compound up to an active space comprising 12 electrons and 16 orbitals, CAS(12,16): $3\sigma_g$, $1\pi_g$, $2\pi_u$, $3\sigma_u$, $1\delta_u$, $1\phi_u$, $3\pi_u$, $4\sigma_g$, $4\sigma_u$ and $2\pi_g$. Similarly, for the $NUO^+$ and NUN molecules, 12 electrons are correlated in 16 orbitals resulting in CAS(12,16) calculations containing $5\sigma$, $2\pi$, $3\pi$, $6\sigma$, $1\delta$, $1\phi$, $7\sigma$, $2\delta$, $4\pi$ and $8\sigma$ in the case of $NUO^+$ and $3\sigma_g$, $1\pi_g$, $2\pi_u$, $3\sigma_u$, $1\delta_u$, $1\phi_u$, $4\sigma_g$, $3\pi_u$, $1\delta_g$ and $4\sigma_u$ in the case of NUN. Due to technical problems encountered with MOLCAS 7.4, it was not possible to obtain the CAS(12,16) results for some of the higher-lying states of $NUO^+$, in order to obtain these energies we also employed a CAS(12,15) active space in which the $7\sigma$ orbital was not included.

In order to eliminate weakly intruding states in the second-order perturbation theory, the imaginary shift method [225] with a shift parameter of 0.25 Hartree was applied when exploratory calculations indicated problems with intruder states.

### 9.3.3 IHFSCC-SD

The IHFSCC-SD calculations [136, 138, 139] were performed with a development version of the DIRAC08 program package [211] employing the spin–free DC Hamiltonian [218] with the same uncontracted basis sets as described above for the TD-DFT Dirac calculations.

In order to be consistent with our previous calculations on $UO_2^{2+}$, and due to the fact that in their ground-state the molecules are well described by a single determinant, we have essentially followed the procedure outlined in [126], yet with a different U–O bond length of 1.708 Å , i.e., the "one particle, one hole" sector $(1h, 1p)$ of Fock-space was utilized to obtain the excitation energies. Furthermore, orbitals with energies of $\varepsilon \in [-3.00; 20.00]$ (in a.u.) are included in the correlated calculations which correspond to 12 occupied and 253 (252) virtual orbitals for NUN ($NUO^+$).

In Fock-space calculations it is necessary to subdivide the space spanned by the active orbitals in two subspaces: the model or $P$ space, containing the active valence orbitals which are directly involved in the electronic excitations, and the complementary $Q$ space that includes the remaining "correlation-active" orbitals. Since we are employing a formulation based on an intermediate Hamiltonian [226], the $P$ space is further divided into a main model ($P_m$) space and an intermediate model ($P_i$) space that is not dressed and serves as a buffer between the $P_m$ and $Q$ spaces, in order to alleviate problems with the so-called intruder states (further details can be found in [126] and references therein). One must keep in mind, however, that accurate solutions are only obtained for states dominated by $P_m$ components.

Thus, in the definition of the Fock-space used here, $P$ contains all the occupied plus the 63 lowest-lying virtuals (for NUN, 29 virtuals are contained in gerade irreducible representations, and 34 in ungerade ones), while the remaining virtuals have been assigned to the $Q$ space. As for the partition into $P_m$ and $P_i$ orbital spaces we have, for the occupied orbitals, the five innermost orbitals in $P_i$, which correspond to $\{1\sigma_g, 1\sigma_u, 1\pi_u, 2\sigma_g\}$ for NUN and $\{1\sigma, 2\sigma, 1\pi, 3\sigma\}$ for $NUO^+$, and the remaining seven orbitals in $P_m$, namely $\{3\sigma_g, 2\sigma_u, 3\sigma_u, 1\pi_g, 2\pi_u\}$ for NUN and $\{4\sigma, 5\sigma, 6\sigma, 2\pi, 3\pi\}$ for $NUO^+$.

For the virtuals the $P_m$ active spaces contains 31 (22) orbitals for NUN ($NUO^+$), assuring that the resulting lowest-lying excited-states are dominated by $P_m$ components. These orbitals roughly correspond to approximately two to three lowest-lying $\phi(=\phi_u)$ and $\delta(=\delta_u, \delta_g)$ orbitals of uranium, apart from the same number of $\pi$ and twice as many $\sigma$ orbitals. The difference between these sets is due to the difference in charge for both systems and the nature of the Hartree–Fock virtuals; contrary of what is obtained with DFT, the $\phi, \delta$ orbitals of uranium are not the lowest-lying ones. A number of $\pi, \sigma$ orbitals lie below and in between these orbitals and had to be included in the model space as well.

## 9.4 Wave Function Benchmark Calculations

Since the main goal of this work is assessing the performance of TD-DFT by comparison to benchmark WFT values, we will begin with a brief discussion of the two WFT methods employed here, before having a closer look at the actual DFT and TD-DFT results.

### 9.4.1 Electronic Structure from IHFSCC-SD

We refer the reader to the paper of Réal and coworkers [126] for a detailed discussion of the $UO_2^{2+}$ IHFSCC-SD calculations. These calculations were performed at a different bond length, leading to slightly different numbers in Table (9.1) compared to those previously reported (see Table 2 of the aforementioned paper). Yet, analysis of the wave functions at both geometries yields essentially the same picture. For $UO_2^{2+}$ the lowest $\Phi_g$ and $\Delta_g$ states are dominated by excitations of the $\sigma_u \rightarrow \phi_u$ and $\sigma_u \rightarrow \delta_u$ kind, respectively, while the $\Gamma_g$ states arises from predominantly $\pi_u \rightarrow \phi_u$ excitations. The $\Phi_u$ and $\Delta_u$ states correspond to excitations from $\sigma_g \rightarrow \phi_u$ and $\sigma_g \rightarrow \delta_u$, respectively.

For NUN, the $\Phi_g$ and $\Phi_u$ states in Table (9.2) differ essentially in the occupied $\sigma$ orbital ($\sigma_u$ for the first and $\sigma_g$ for the second). These two $\sigma$ orbitals, in turn, differ only in the degree of contributions from the orbitals centered on N and U, with $\sigma_u$ having more U character and the $\sigma_g$ having more N character. In addition, since the $\phi_u$ orbital is essentially a pure $f$-orbital from U, we can argue that the two transitions have different degrees of charge-transfer character. The other higher-lying excitations are dominated by $\pi_u \rightarrow \phi_u$ (for $\Gamma_g$, where $\pi_u$ has dominant contributions from N, but still some U character), and $\sigma_u \rightarrow \sigma_g$ (for $\Sigma_u$, where both $\sigma$s have N and U character).

For $NUO^+$, shown in Table (9.3), the picture is similar, but having as significant differences that the lowest $\Phi$ and $\Delta$ states correspond to excitations to the uranium $\phi, \delta$ from $\sigma$ orbitals with either N–U character or U–O character, whereas the $\Gamma$ and $\Phi$ arise from excitations to the same uranium $\phi, \delta$ from a $\pi$ orbital with N–U character.

The Hartree–Fock virtual orbitals correspond to a system with one electron added relative to the reference determinant. While this is optimal for calculating electron affinities, it is not so for excitation energies calculated within the $(1h, 1p)$ sector of Fock-space. In order to compare to the TD-DFT results, the model spaces ($P$ and $P_m$) should include the $\delta_u, \phi_u$ orbitals. These are the lowest virtuals for $UO_2^{2+}$, both for Hartree–Fock and DFT, but the decreasing charge on the metal in $NUO^+$ and particularly in NUN places other orbitals at lower energy. For instance, for $NUO^+$, three $\sigma$ and two $\pi$ virtual orbitals have lower energies than the relevant $\delta, \phi$ orbitals, while for NUN several (*e.g.* two $\sigma_u$, three $\pi_u$, three $\sigma_g$ and one $\pi_g$) orbitals are in between the HOMO and the $\delta_u, \phi_u$. These differences illustrate the need for increased model spaces in this work, compared to $UO_2^{2+}$, for which the $\delta_u$ and $\phi_u$ are the lowest-lying virtuals.

A related difference to the $UO_2^{2+}$ case is the extent to which the participation of a second set of $\delta, \phi$ virtuals is important for $NUO^+$ and NUN. This is due to

**Table 9.1**: *Comparison of different exchange–correlation functionals for the $UO_2^{2+}$ molecule (in eV). S-T indicates singlet-triplet splitting, MUE the mean absolute error and Max the maximum absolute error, respectively.*

| xc/Hamiltonian | $1^3\Phi_g$ | $1^1\Phi_g$ | S-T | $1^3\Delta_g$ | $1^1\Delta_g$ | S-T | $1^3\Gamma_g$ | $1^1\Gamma_g$ | S-T | $1^3\Phi_u$ | $1^1\Phi_u$ | S-T | $1^3\Delta_u$ | $1^1\Delta_u$ | S-T | MUE | Max |
|---|---|---|---|---|---|---|---|---|---|---|---|---|---|---|---|---|---|
| ZORA/LDA | 2.02 | 2.46 | 0.44 | 2.36 | 3.07 | 0.71 | 3.37 | 3.57 | 0.20 | 2.99 | 3.07 | 0.08 | 3.47 | 3.48 | 0.01 | 1.04 | 1.70 |
| DC/LDA | 2.04 | 2.54 | 0.50 | 2.37 | 3.22 | 0.85 | 3.38 | 3.66 | 0.28 | 3.00 | 3.08 | 0.08 | 3.47 | 3.50 | 0.03 | 1.00 | 1.69 |
| ZORA/PBE(ALDA) | 2.01 | 2.45 | 0.44 | 2.40 | 3.10 | 0.70 | 3.38 | 3.58 | 0.20 | 3.04 | 3.12 | 0.08 | 3.57 | 3.59 | 0.02 | 1.00 | 1.65 |
| DC/PBE(ALDA) | 2.03 | 2.53 | 0.50 | 2.41 | 3.25 | 0.84 | 3.38 | 3.65 | 0.27 | 3.04 | 3.12 | 0.08 | 3.55 | 3.58 | 0.03 | 0.97 | 1.65 |
| DC/PBE | 1.73 | 2.46 | 0.73 | 2.05 | 3.16 | 1.11 | 3.20 | 3.59 | 0.39 | 2.99 | 3.11 | 0.12 | 3.51 | 3.57 | 0.06 | 1.09 | 1.70 |
| ZORA/BLYP(ALDA) | 2.01 | 2.46 | 0.45 | 2.43 | 3.11 | 0.66 | 3.31 | 3.52 | 0.21 | 3.00 | 3.08 | 0.08 | 3.55 | 3.56 | 0.01 | 1.02 | 1.69 |
| DC/BLYP(ALDA) | 2.05 | 2.55 | 0.50 | 2.45 | 3.26 | 0.81 | 3.31 | 3.58 | 0.27 | 3.00 | 3.09 | 0.09 | 3.53 | 3.56 | 0.03 | 0.99 | 1.69 |
| DC/BLYP | 1.84 | 2.45 | 0.61 | 2.22 | 3.13 | 0.91 | 3.19 | 3.50 | 0.31 | 2.98 | 3.08 | 0.10 | 3.50 | 3.55 | 0.05 | 1.08 | 1.71 |
| ZORA/M06-L(ALDA) | 2.38 | 2.84 | 0.46 | 2.71 | 3.46 | 0.75 | 3.77 | 3.97 | 0.20 | 3.60 | 3.68 | 0.08 | 4.08 | 4.08 | 0.00 | 0.61 | 1.09 |
| ZORA/B3LYP(XALDA) | 2.30 | 2.80 | 0.51 | 2.51 | 3.39 | 0.88 | 4.01 | 4.23 | 0.22 | 4.22 | 4.31 | 0.09 | 4.57 | 4.58 | 0.01 | 0.34 | 0.56 |
| DC/B3LYP(XALDA) | 2.37 | 2.92 | 0.55 | 2.58 | 3.59 | 1.01 | 4.04 | 4.31 | 0.27 | 4.23 | 4.33 | 0.10 | 4.56 | 4.61 | 0.05 | 0.29 | 0.53 |
| DC/B3LYP | 2.21 | 2.84 | 0.63 | 2.40 | 3.49 | 1.08 | 3.95 | 4.26 | 0.31 | 4.20 | 4.32 | 0.12 | 4.53 | 4.59 | 0.06 | 0.35 | 0.62 |
| ZORA/PBE0(XALDA) | 2.35 | 2.88 | 0.53 | 2.50 | 3.43 | 0.94 | 4.25 | 4.48 | 0.23 | 4.56 | 4.66 | 0.10 | 4.84 | 4.85 | 0.01 | 0.19 | 0.36 |
| DC/PBE0(XALDA) | 2.42 | 2.99 | 0.57 | 2.58 | 3.63 | 1.05 | 4.29 | 4.57 | 0.28 | 4.57 | 4.68 | 0.11 | 4.84 | 4.89 | 0.05 | 0.16 | 0.28 |
| DC/PBE0 | 2.15 | 2.94 | 0.79 | 2.24 | 3.57 | 1.33 | 4.15 | 4.54 | 0.39 | 4.53 | 4.67 | 0.14 | 4.79 | 4.88 | 0.09 | 0.22 | 0.55 |
| ZORA/M06(XALDA) | 2.42 | 2.97 | 0.54 | 2.52 | 3.50 | 0.98 | 4.26 | 4.49 | 0.23 | 4.60 | 4.70 | 0.10 | 4.84 | 4.85 | 0.01 | 0.16 | 0.31 |
| ZORA/M06-2X(XALDA) | 2.34 | 2.94 | 0.60 | 2.23 | 3.35 | 1.12 | 4.94 | 5.21 | 0.27 | 5.63 | 5.74 | 0.11 | 5.57 | 5.62 | 0.05 | 0.56 | 1.00 |
| ZORA/SAOP(ALDA) | 3.07 | 3.51 | 0.44 | 3.27 | 4.00 | 0.73 | 4.29 | 4.48 | 0.19 | 4.21 | 4.29 | 0.08 | 4.55 | 4.56 | 0.01 | 0.37 | 0.79 |
| DC/SAOP(ALDA) | 3.01 | 3.50 | 0.49 | 3.24 | 4.10 | 0.86 | 4.33 | 4.57 | 0.24 | 4.22 | 4.31 | 0.09 | 4.59 | 4.63 | 0.04 | 0.35 | 0.76 |
| DC/CAM-B3LYP(XALDA) | 2.56 | 3.13 | 0.57 | 2.71 | 3.77 | 1.06 | 4.41 | 4.69 | 0.26 | 4.70 | 4.81 | 0.11 | 4.93 | 5.00 | 0.07 | 0.15 | 0.29 |
| DC/CAM-B3LYP | 2.43 | 3.07 | 0.64 | 2.56 | 3.69 | 1.13 | 4.36 | 4.65 | 0.29 | 4.69 | 4.81 | 0.12 | 4.91 | 4.99 | 0.08 | 0.15 | 0.28 |
| ZORA/TDHF | 3.01 | 3.78 | 0.77 | 2.40 | 4.00 | 1.60 | 7.12 | 7.17 | 0.05 | 8.82 | 9.00 | 0.18 | 8.15 | 8.54 | 0.39 | 2.19 | 4.26 |
| CASPT2 | 2.91 | 3.40 | 0.49 | 2.77 | 3.88 | 1.11 | 4.61 | 4.83 | 0.22 | 4.82 | 4.85 | 0.03 | 4.72 | 4.64 | -0.08 | 0.16 | 0.31 |
| CASPT2[1] | 2.94 | 3.47 | 0.57 | 2.79 | 3.90 | 1.11 | 4.66 | 4.86 | 0.20 | 4.71 | 4.74 | 0.03 | 4.63 | 4.55 | -0.08 | 0.16 | 0.33 |
| IHFSCC-SD | 2.70 | 3.24 | 0.54 | 2.48 | 3.57 | 1.09 | 4.57 | 4.78 | 0.21 | 4.69 | 4.74 | 0.05 | 4.76 | 4.71 | -0.05 | | |

Ref. 35 [1]

**Table 9.2**: *Comparison of different exchange–correlation functionals for the NUN molecule (in eV). S-T indicates singlet-triplet splitting, MUE the mean absolute error and Max the maximum absolute error, respectively.*

| xc/Hamiltonian | $1^3\Phi_g$ | $1^1\Phi_g$ | S-T | $1^3\Delta_g$ | $1^1\Delta_g$ | S-T | $1^3\Phi_u$ | $1\ ^1\Phi_u$ | S-T | $1^3\Gamma_g$ | $1^1\Gamma_g$ | S-T | $1^3\Sigma_u$ | $1^1\Sigma_u$ | S-T | MUE | Max |
|---|---|---|---|---|---|---|---|---|---|---|---|---|---|---|---|---|---|
| ZORA/LDA | 1.07 | 1.51 | 0.44 | 1.64 | 2.24 | 0.58 | 1.88 | 1.97 | 0.09 | 2.26 | 2.47 | 0.21 | 2.34 | 2.60 | 0.26 | 0.78 | 1.55 |
| DC/LDA | 1.13 | 1.63 | 0.50 | 1.67 | 2.41 | 0.74 | 1.95 | 2.06 | 0.11 | 2.32 | 2.60 | 0.28 | 2.21 | 2.48 | 0.27 | 0.74 | 1.46 |
| ZORA/PBE(ALDA) | 1.05 | 1.49 | 0.44 | 1.68 | 2.26 | 0.58 | 1.90 | 2.00 | 0.10 | 2.28 | 2.49 | 0.21 | 2.35 | 2.60 | 0.25 | 0.77 | 1.52 |
| DC/PBE(ALDA) | 1.12 | 1.62 | 0.50 | 1.70 | 2.43 | 0.73 | 1.96 | 2.07 | 0.11 | 2.32 | 2.60 | 0.28 | 2.23 | 2.49 | 0.26 | 0.74 | 1.45 |
| DC/PBE | 0.72 | 1.54 | 0.82 | 1.31 | 2.34 | 1.03 | 1.89 | 2.05 | 0.16 | 2.13 | 2.54 | 0.41 | 2.14 | 2.47 | 0.33 | 0.83 | 1.49 |
| ZORA/BLYP(ALDA) | 1.07 | 1.51 | 0.44 | 1.73 | 2.28 | 0.65 | 1.92 | 2.01 | 0.09 | 2.22 | 2.43 | 0.21 | 2.24 | 2.51 | 0.27 | 0.80 | 1.51 |
| DC/BLYP(ALDA) | 1.16 | 1.66 | 0.50 | 1.76 | 2.44 | 0.68 | 1.98 | 2.09 | 0.11 | 2.27 | 2.54 | 0.27 | 2.14 | 2.41 | 0.27 | 0.76 | 1.43 |
| DC/BLYP | 0.90 | 1.55 | 0.65 | 1.53 | 2.32 | 0.79 | 1.94 | 2.08 | 0.14 | 2.13 | 2.46 | 0.33 | 2.10 | 2.40 | 0.30 | 0.82 | 1.44 |
| ZORA/M06-L(ALDA) | 1.32 | 1.77 | 0.45 | 1.91 | 2.55 | 0.64 | 2.20 | 2.30 | 0.10 | 2.63 | 2.83 | 0.20 | 3.13 | 3.31 | 0.18 | 0.52 | 1.22 |
| ZORA/B3LYP(XALDA) | 1.29 | 1.79 | 0.50 | 1.74 | 2.53 | 0.79 | 2.92 | 3.04 | 0.12 | 2.77 | 3.00 | 0.23 | 2.62 | 2.93 | 0.31 | 0.34 | 0.60 |
| DC/B3LYP(XALDA) | 1.40 | 1.95 | 0.55 | 1.81 | 2.74 | 0.93 | 2.98 | 3.11 | 0.13 | 2.84 | 3.13 | 0.29 | 2.56 | 2.87 | 0.31 | 0.31 | 0.53 |
| DC/B3LYP | 1.21 | 1.87 | 0.66 | 1.62 | 2.64 | 1.02 | 2.95 | 3.10 | 0.15 | 2.74 | 3.07 | 0.33 | 2.53 | 2.86 | 0.33 | 0.33 | 0.63 |
| ZORA/PBE0(XALDA) | 1.32 | 1.84 | 0.52 | 1.69 | 2.55 | 0.86 | 3.18 | 3.30 | 0.12 | 2.97 | 3.21 | 0.24 | 2.87 | 3.17 | 0.30 | 0.19 | 0.40 |
| DC/PBE0(XALDA) | 1.42 | 1.99 | 0.57 | 1.77 | 2.76 | 0.99 | 3.23 | 3.37 | 0.14 | 3.05 | 3.35 | 0.30 | 2.79 | 3.08 | 0.29 | 0.16 | 0.32 |
| DC/PBE0 | 1.09 | 1.94 | 0.85 | 1.38 | 2.70 | 1.32 | 3.16 | 3.36 | 0.20 | 2.92 | 3.31 | 0.39 | 2.69 | 3.06 | 0.37 | 0.21 | 0.45 |
| ZORA/M06(XALDA) | 1.34 | 1.88 | 0.54 | 1.70 | 2.59 | 0.89 | 3.16 | 3.29 | 0.13 | 2.98 | 3.21 | 0.23 | 2.97 | 3.26 | 0.29 | 0.20 | 0.39 |
| ZORA/M06-2X(XALDA) | 1.26 | 1.86 | 0.60 | 1.30 | 2.40 | 1.10 | 3.97 | 4.12 | 0.15 | 3.49 | 3.76 | 0.27 | 2.87 | 3.32 | 0.45 | 0.26 | 0.60 |
| ZORA/SAOP(ALDA) | 2.03 | 2.47 | 0.44 | 2.50 | 3.06 | 0.56 | 2.89 | 2.99 | 0.10 | 3.04 | 3.23 | 0.19 | 2.61 | 2.86 | 0.25 | 0.47 | 1.02 |
| DC/SAOP(ALDA) | 1.98 | 2.47 | 0.49 | 2.46 | 3.18 | 0.72 | 2.93 | 3.04 | 0.11 | 3.09 | 3.35 | 0.26 | 2.45 | 2.71 | 0.26 | 0.48 | 0.98 |
| DC/CAM-B3LYP(XALDA) | 1.75 | 2.14 | 0.39 | 1.91 | 2.91 | 1.00 | 3.43 | 3.57 | 0.14 | 3.21 | 3.48 | 0.27 | 2.82 | 3.16 | 0.34 | 0.19 | 0.43 |
| DC/CAM-B3LYP | 1.65 | 2.08 | 0.43 | 1.75 | 2.83 | 1.08 | 3.41 | 3.57 | 0.16 | 3.09 | 3.42 | 0.33 | 2.83 | 3.18 | 0.35 | 0.13 | 0.28 |
| ZORA/TDHF | 1.88 | 2.66 | 0.78 | 1.37 | 2.98 | 1.61 | 6.79 | 6.98 | 0.19 | 5.53 | 5.84 | 0.31 | 3.87 | 4.54 | 0.67 | 1.52 | 3.46 |
| CASPT2 | 1.80 | 2.30 | 0.50 | 1.77 | 2.66 | 0.89 | 3.23 | 3.29 | 0.06 | 3.04 | 3.51 | 0.47 | 2.62 | 2.85 | 0.23 | 0.22 | 0.33 |
| IHFSCC-SD | 1.51 | 2.06 | 0.55 | 1.48 | 2.56 | 0.88 | 3.38 | 3.52 | 0.14 | 3.37 | 3.58 | 0.21 | 2.87 | 3.14 | 0.27 | | |

**Table 9.3**: *Comparison of different exchange–correlation functionals for the $NUO^+$ molecule (in eV). S-T indicates singlet-triplet splitting, MUE the mean absolute error and Max the maximum absolute error, respectively.*

| xc/Hamiltonian | $1^3\Phi$ | $1^1\Phi$ | S-T | $1^3\Delta$ | $1^1\Delta$ | S-T | $1^3\Gamma$ | $1^1\Gamma$ | S-T | $1^3\Pi$ | $1^1\Pi$ | S-T | $2^3\Phi$ | $2^1\Phi$ | S-T | MUE | Max |
|---|---|---|---|---|---|---|---|---|---|---|---|---|---|---|---|---|---|
| ZORA/LDA | 0.77 | 1.09 | 0.32 | 1.34 | 1.73 | 0.39 | 2.00 | 2.14 | 0.14 | 2.61 | 2.98 | 0.37 | 2.61 | 2.65 | 0.04 | 0.80 | 1.31 |
| DC/LDA | 0.86 | 1.20 | 0.34 | 1.40 | 1.88 | 0.48 | 2.08 | 2.29 | 0.21 | 2.67 | 3.13 | 0.46 | 2.64 | 2.84 | 0.20 | 0.69 | 1.23 |
| ZORA/PBE(ALDA) | 0.85 | 1.17 | 0.32 | 1.45 | 1.86 | 0.41 | 2.13 | 2.27 | 0.14 | 2.79 | 3.16 | 0.37 | 2.79 | 2.82 | 0.03 | 0.66 | 1.18 |
| DC/PBE(ALDA) | 0.84 | 1.20 | 0.36 | 1.41 | 1.92 | 0.51 | 2.07 | 2.29 | 0.22 | 2.71 | 3.10 | 0.39 | 2.71 | 2.88 | 0.17 | 0.68 | 1.24 |
| DC/PBE | 0.52 | 1.15 | 0.63 | 1.11 | 1.87 | 0.76 | 1.91 | 2.24 | 0.33 | 2.59 | 3.07 | 0.48 | 2.54 | 2.82 | 0.28 | 0.81 | 1.40 |
| ZORA/BLYP(ALDA) | 0.87 | 1.19 | 0.32 | 1.50 | 1.90 | 0.40 | 2.06 | 2.21 | 0.15 | 2.75 | 3.12 | 0.37 | 2.75 | 2.78 | 0.03 | 0.68 | 1.25 |
| DC/BLYP(ALDA) | 0.87 | 1.23 | 0.36 | 1.47 | 1.96 | 0.49 | 2.01 | 2.23 | 0.22 | 2.66 | 3.05 | 0.39 | 2.66 | 2.84 | 0.18 | 0.69 | 1.30 |
| DC/BLYP | 0.67 | 1.17 | 0.50 | 1.28 | 1.88 | 0.60 | 1.89 | 2.15 | 0.26 | 2.59 | 3.01 | 0.42 | 2.54 | 2.74 | 0.20 | 0.80 | 1.42 |
| ZORA/M06-L(ALDA) | 1.13 | 1.48 | 0.35 | 1.68 | 2.15 | 0.47 | 2.55 | 2.70 | 0.15 | 3.18 | 3.54 | 0.36 | 3.18 | 3.21 | 0.03 | 0.34 | 0.76 |
| ZORA/B3LYP(XALDA) | 1.25 | 1.68 | 0.43 | 1.67 | 2.29 | 0.62 | 2.66 | 2.82 | 0.16 | 3.17 | 3.54 | 0.37 | 3.17 | 3.22 | 0.05 | 0.28 | 0.65 |
| DC/B3LYP(XALDA) | 1.29 | 1.75 | 0.46 | 1.68 | 2.40 | 0.72 | 2.62 | 2.85 | 0.23 | 3.11 | 3.51 | 0.40 | 3.12 | 3.29 | 0.17 | 0.26 | 0.69 |
| DC/B3LYP | 1.13 | 1.68 | 0.55 | 1.52 | 2.33 | 0.81 | 2.56 | 2.80 | 0.24 | 3.07 | 3.48 | 0.41 | 3.03 | 3.23 | 0.20 | 0.31 | 0.75 |
| ZORA/PBE0(XALDA) | 1.31 | 1.76 | 0.45 | 1.65 | 2.34 | 0.69 | 2.87 | 3.05 | 0.18 | 3.32 | 3.70 | 0.38 | 3.32 | 3.37 | 0.05 | 0.18 | 0.44 |
| DC/PBE0(XALDA) | 1.34 | 1.83 | 0.49 | 1.67 | 2.46 | 0.79 | 2.84 | 3.08 | 0.24 | 3.28 | 3.68 | 0.40 | 3.28 | 3.46 | 0.18 | 0.19 | 0.47 |
| DC/PBE0 | 1.06 | 1.78 | 0.68 | 1.35 | 2.41 | 1.06 | 2.70 | 3.05 | 0.35 | 3.18 | 3.66 | 0.48 | 3.14 | 3.42 | 0.28 | 0.27 | 0.61 |
| ZORA/M06(XALDA) | 1.33 | 1.79 | 0.46 | 1.64 | 2.36 | 0.72 | 2.92 | 3.09 | 0.17 | 3.35 | 3.72 | 0.37 | 3.35 | 3.40 | 0.05 | 0.16 | 0.39 |
| ZORA/M06-2X(XALDA) | 1.32 | 1.86 | 0.54 | 1.34 | 2.28 | 0.94 | 3.39 | 3.60 | 0.21 | 3.54 | 3.91 | 0.37 | 3.57 | 3.63 | 0.06 | 0.21 | 0.41 |
| ZORA/SAOP(ALDA) | 1.93 | 2.26 | 0.33 | 2.34 | 2.78 | 0.44 | 3.02 | 3.16 | 0.14 | 3.50 | 3.84 | 0.34 | 3.50 | 3.54 | 0.04 | 0.31 | 0.78 |
| DC/SAOP(ALDA) | 1.84 | 2.21 | 0.37 | 2.28 | 2.82 | 0.54 | 2.96 | 3.16 | 0.20 | 3.47 | 3.83 | 0.36 | 3.47 | 3.63 | 0.16 | 0.30 | 0.72 |
| DC/CAM-B3LYP(XALDA) | 1.50 | 1.99 | 0.49 | 1.83 | 2.63 | 0.80 | 2.91 | 3.16 | 0.25 | 3.35 | 3.76 | 0.41 | 3.35 | 3.53 | 0.18 | 0.18 | 0.40 |
| DC/CAM-B3LYP | 1.37 | 1.94 | 0.57 | 1.69 | 2.56 | 0.87 | 2.85 | 3.12 | 0.27 | 3.31 | 3.73 | 0.42 | 3.28 | 3.48 | 0.20 | 0.19 | 0.46 |
| ZORA/TDHF | 2.05 | 2.79 | 0.74 | 4.73 | 5.15 | 0.42 | 5.51 | 5.76 | 0.25 | 6.09 | 6.33 | 0.24 | 5.93 | 6.15 | 0.22 | 2.26 | 3.17 |
| CASPT2 | 1.88 | 2.23 | 0.35 | 1.84 | 2.42 | 0.58 | | 3.19 | | | 3.35 | | | | | 0.06 | 0.29 |
| CASPT2(12,15) | 1.89 | 2.32 | 0.43 | 1.90 | 2.55 | 0.65 | 3.18 | 3.26 | 0.08 | 3.20 | 3.39 | 0.19 | | | | 0.06 | 0.34 |
| IHFSCC-SD | 1.59 | 2.06 | 0.47 | 1.56 | 2.37 | 0.81 | 3.31 | 3.45 | 0.14 | 3.34 | 3.50 | 0.16 | 3.36 | 3.38 | 0.02 | | |

**Table 9.4**: *CASPT2 Mulliken charges for the ground- and excited-states of $UO_2^{2+}$, NUO+ and NUN.*

| | $UO_2^{2+}$ | | NUO+ | | | | NUN | | |
|---|---|---|---|---|---|---|---|---|---|
| State | U | O | State | U | N | O | State | U | N |
| $X^1\Sigma_g^+$ | 2.41 | -0.21 | $X^1\Sigma$ | 1.72 | -0.39 | -0.33 | $X^1\Sigma_g^+$ | 0.77 | -0.39 |
| $^1\Phi_g$ | 2.36 | -0.18 | $^1\Phi$ | 1.70 | -0.57 | -0.12 | $^1\Phi_g$ | 0.78 | -0.39 |
| $^3\Phi_g$ | 2.36 | -0.18 | $^3\Phi$ | 1.71 | -0.57 | -0.14 | $^3\Phi_g$ | 0.76 | -0.38 |
| $^1\Delta_g$ | 2.35 | -0.17 | $^1\Delta$ | 1.73 | -0.55 | -0.19 | $^1\Delta_g$ | 0.76 | -0.38 |
| $^3\Delta_g$ | 2.37 | -0.18 | $^3\Delta$ | 1.70 | -0.57 | -0.13 | $^3\Delta_g$ | 0.79 | -0.39 |
| $^1\Gamma_g$ | 2.25 | -0.13 | $^1\Gamma$ | 1.70 | -0.57 | -0.12 | $^1\Phi_u$ | 0.74 | -0.37 |
| $^3\Gamma_g$ | 2.26 | -0.13 | $^3\Gamma$ | – | – | – | $^3\Phi_u$ | 0.72 | -0.36 |
| $^1\Phi_u$ | 2.25 | -0.13 | $^1\Pi$ | 1.74 | -0.57 | -0.17 | $^1\Gamma_g$ | 0.78 | -0.39 |
| $^3\Phi_u$ | 2.26 | -0.13 | $^3\Pi$ | – | – | – | $^3\Gamma_g$ | 0.79 | -0.40 |
| $^1\Delta_u$ | 2.26 | -0.13 | $2^1\Phi$ | – | – | – | $^1\Sigma_u$ | 0.64 | -0.33 |
| $^3\Delta_u$ | 2.26 | -0.13 | $2^3\Phi$ | – | – | – | $^3\Sigma_u$ | 0.64 | -0.32 |

the energy separation of the first and second $\delta$ and $\phi$ virtuals, which for $UO_2^{2+}$ is of about 8 eV, but decreases to within 1.5 — 2 eV for $NUO^+$ and NUN, making these virtuals more important for orbital relaxation[1] in the latter case.

Last but not least, we note that in all three cases the $T_1$ diagnostic [227] for the $(0h, 0p)$ sector (which here is equivalent to a conventional CCSD calculation), namely 0.045 for $UO_2^{2+}$, 0.048 for $NUO^+$ and 0.049 for NUN, is rather similar and a bit higher than what is usually considered an indicator ($< 0.02$) of single-reference character in light systems. This is typical for heavy elements, and should not be taken as an indication of multi-reference character.

### 9.4.2 The CASPT2 Electronic Structure

The CASSCF wave function analysis points to ground-states of essentially single reference character, with weights for the HF determinant of about 0.86, 0.92 and 0.91 for $UO_2^{2+}$, $NUO^+$ and NUN, respectively. In particular, the determinants which contribute to the remaining 0.10 contain double excitations from the HF reference, and therefore do not indicate important orbital relaxation effects [228]. CASPT2 provides in a fairly straightforward manner information about the bond orders in the ground state which reduce to 2.935 (U–O) for $UO_2^{2+}$, 2.952 (U–N) for NUN, and 1.957 (U–O) and 2.977 (U–N) for $NUO^+$. Changes in the electron density upon excitation can be investigated by means of an analysis of the Mulliken charges for each excited state which are summarized in Table (9.4). A general trend

[1] Orbital relaxation refers to the changes in the Fock operator as well as Hartree–Fock orbitals when changing the number of electrons in the system.

of displacing a small amount of density towards the uranium atom in comparison to the ground state can be observed. This effect is of more systematic nature, i.e., all states show a charge transfer from the ligands to the uranium center, in the case of $UO_2^{2+}$ than compared to NUN for which only the $\Sigma_u$ states have a rather pronounced ligand to uranium charge-transfer relative to the ground-state. Furthermore for $NUO^+$, the most important effect is the migration of charge from one end of the molecule (the O atom) to the other (the N atom) rather than a net movement of charge towards the central atom.

### 9.4.3 Assessment of WFT Excitation Energies

In a previous study on the performance of IHFSCC-SD and CASPT2 in calculating the electronic spectrum of $UO_2^{2+}$ [126] it was observed that CASPT2 typically shows discrepancies with respect to IHFSCC-SD for individual excitation energies within a range of 0.1 to 0.4 eV. Furthermore, for the lowest $\Phi_g$ and $\Delta_g$ in both the singlet and triplet configuration, CASPT2 overestimated the excitation energies, while for higher-lying states an opposite behavior was found. However, similar singlet-triplet splittings were obtained for both methods. The results and trends obtained for $NUO^+$ and NUN presented in Tables (9.3) and (9.2), respectively, are related to the above observations. The differences between individual excitation energies for both methods are typically in the range of 0.1 to 0.3 eV. We may conclude that the two WFT methods yield the same semi-quantitative result. Yet, considering the fact that IHFSCC-SD allows a more systematic treatment of the excited-states and includes dynamic correlation effects beyond second order perturbation theory, the IHFSCC-SD method is taken as reference.

## 9.5 The Performance of DFT and TD-DFT

The TD-DFT tests were focused on a subset of exchange–correlation functionals, covering the following basic classes: LDA, GGAs (PBE, BLYP) and meta-GGAs (M06-L), hybrids (B3LYP and PBE0, with 20 and 25% of HF exchange, respectively) and meta-hybrids (M06 and M06-2X, with 27 and 54% of HF exchange, respectively), model potentials (SAOP) and range-separated hybrids (CAM-B3LYP).

All systems are represented by restricted (closed-shell) Kohn–Sham calculations, given the evidence both from our wave function calculations and from previous studies, *e.g.*, Kaltsoyannis [25], Pierloot and coworkers [35, 36], Réal and coworkers [200] and Fromager [228] and coworkers, that this yields a proper description for the corresponding ground-states. The suitability of this approach for

the uranyl molecule was further demonstrated in the recent Kramers-restricted TD-DFT calculations by Bast *et al.* [197].

### 9.5.1 Ground-State Electronic Structure

Before discussing the performance of (TD-)DFT for the different electronically excited-states, it is instructive to discuss the molecular orbitals (MOs) and the chemical bonding. The essentials of bonding in actinyls are nicely summarized in a review by Denning [5]; in particular, for $UO_2^{2+}$, the currently accepted picture, in terms of the highest-lying occupied MOs, is that of a system of $\sigma, \pi$ orbitals arising from the combination of oxygen $2p$-orbitals and the $5f$-, $6p$-orbitals of uranium, ordered as $\pi_g > \pi_u > \sigma_g > \sigma_u$. In $UO_2^{2+}$, the contribution from the uranium $6p$ shows up in the relatively large gap between the $\sigma$ orbitals, due to the repulsion between $\sigma_u$ and $6p$ [229], a so-called "pushing from below" interaction.

To our knowledge only the aforementioned work of Kaltsoyannis has paid attention to the valence MO picture of NUN and $NUO^+$. Using a GGA functional (PB86), he found: (i) the same orbital ordering for NUN and $UO_2^{2+}$, but with a smaller (larger) energy gap between the $\sigma$ ($\pi$) orbitals; and (ii) an ordering of type $\pi > \sigma > \pi > \sigma$ for $NUO^+$, with the (energetically) lower $\pi, \sigma$ pair mostly centered over the U–O bond, whereas the HOMO and HOMO-1 are mostly centered over the U–N bond. This picture is qualitatively consistent already with the Hartree–Fock results, but in order to obtain reliable information about the orbital ordering, electron correlation should also be included. To remain within an orbital picture, we shall do so by comparing the vertical ionization potentials (IPs) obtained from the $(1h, 0p)$ sector in the IHFSCC-SD calculations to those obtained from DFT.

The DFT IPs are here taken as approximations to the negative of the respective orbital energies, and while this is strictly valid only for the HOMO [230] our results, shown in Table (9.5), indicate that this is a good approximation, in line with the findings of Chong and coworkers [231].

#### 9.5.1.1 Describing the Occupied Space

From the numbers in Table (9.5), we can confirm that the orbital scheme outlined above is maintained for all three molecules, with one exception for M06-2X which for NUN places the $\sigma_u$ orbital below the $\sigma_g$. On the other hand, significant quantitative differences can be observed as far as the differences in energy between orbitals (for a given molecule) are concerned which are very much dependent on the type of functional in use (LDA/GGA, hybrids, metaGGAs/hybrids, etc); for instance, the energy difference between the HOMO and HOMO-1 for NUN or

**Table 9.5**: *Comparison of DFT and IHFSCC-SD for the first three ionization potentials (IPs) for $UO_2^{2+}$, NUO+ and NUN (in eV). Since these ionized states in the IHFSCC-SD are dominated by contributions from a single orbital and the DFT values are approximated by the negative of the orbital energies, we identify the IPs with the respective orbitals (which range from HOMO-2 to HOMO for DFT). ZORA and DC are Zero Order Regular Approximated and Dirac–Coulomb Hamiltonians, respectively.*

| | | NUN | | | $NUO^+$ | | | $UO_2^{2+}$ | | |
|---|---|---|---|---|---|---|---|---|---|---|
| | | $\pi_u$ | $\sigma_g$ | $\sigma_u$ | $\sigma$(U–O) | $\pi$ | $\sigma$(U–N) | $\pi_u$ | $\sigma_g$ | $\sigma_u$ |
| LDA | ZORA | 6.58 | 6.08 | 5.50 | 14.57 | 13.78 | 12.59 | 23.45 | 22.95 | 22.22 |
| | DC | 6.53 | 6.05 | 5.46 | 14.51 | 13.63 | 12.47 | 23.39 | 22.87 | 22.16 |
| PBE | ZORA | 6.32 | 5.84 | 5.22 | 14.33 | 13.52 | 12.32 | 23.19 | 22.74 | 21.94 |
| | DC | 6.29 | 5.82 | 5.21 | 14.28 | 13.38 | 12.23 | 23.12 | 22.66 | 21.90 |
| BLYP | ZORA | 6.18 | 5.76 | 5.15 | 14.22 | 13.36 | 12.24 | 23.02 | 22.59 | 21.84 |
| | DC | 6.16 | 5.77 | 5.17 | 14.18 | 13.22 | 12.16 | 22.95 | 22.52 | 21.81 |
| M06-L | ZORA | 6.25 | 5.72 | 5.07 | 14.40 | 13.53 | 12.12 | 23.19 | 22.91 | 21.93 |
| B3LYP | ZORA | 7.26 | 6.85 | 6.50 | 15.63 | 14.45 | 13.59 | 24.36 | 24.03 | 23.39 |
| | DC | 7.24 | 6.83 | 6.50 | 15.61 | 14.40 | 13.50 | 24.32 | 23.98 | 23.38 |
| PBE0 | ZORA | 7.57 | 6.85 | 6.50 | 16.01 | 14.90 | 13.92 | 24.76 | 24.45 | 23.78 |
| | DC | 7.54 | 7.08 | 6.79 | 15.98 | 14.76 | 13.82 | 24.72 | 24.39 | 23.76 |
| M06 | ZORA | 7.56 | 7.10 | 6.97 | 16.07 | 14.92 | 13.99 | 24.73 | 24.46 | 23.97 |
| M06-2X | ZORA | 8.86 | 8.30 | 8.58 | 17.66 | 16.24 | 15.45 | 26.27 | 25.90 | 25.64 |
| SAOP | ZORA | 10.16 | 9.92 | 9.28 | 18.73 | 17.69 | 16.69 | 27.82 | 27.64 | 26.72 |
| | DC | 10.08 | 9.83 | 9.10 | 18.62 | 17.52 | 16.49 | 27.76 | 27.55 | 26.57 |
| CAM-B3LYP | DC | 9.02 | 8.48 | 8.44 | 17.49 | 16.22 | 15.37 | 26.23 | 25.78 | 25.40 |
| IHFSCC-SD | DC | 10.15 | 9.45 | 9.43 | 18.66 | 17.76 | 16.74 | 27.76 | 27.15 | 27.08 |

$UO_2^{2+}$ can be halved just by going from GGAs to hybrids. Similarly striking are the small differences in energy between $\sigma_g$ and $\sigma_u$ obtained for IHFSCC-SD in the case of $UO_2^{2+}$ (of the order of 0.1 eV), while the DFT calculations yield differences between 0.3 and 1 eV.

These results are rather insensitive to the Hamiltonian; in general, discrepancies no larger than 0.1 eV (but generally lower than 0.05 eV) can be observed between the ZORA and DC Hamiltonians (keeping in mind possible effects due to the different basis sets used in ADF and DIRAC). This is in line with the experience that approximate (but computationally efficient) two-component relativistic schemes such as ZORA yield accurate valence energies.

Looking at the performance of the various DFT approaches, the best agreement is found with IHFSCC-SD for the SAOP potential. Comparing to the DC values, errors in the range of $-0.3$ to 0.5 eV are obtained, followed by CAM-B3LYP and

M06-2X, which systematically underestimate the IPs by about 1 eV and 1 to 1.5 eV, respectively. Next come two blocks consisting of the remaining (meta)hybrid functionals on the one hand, and encompassing LDA and the (meta)GGA functionals on the other, which underestimate the IPs by about 3 and 4 eV, respectively.

While other factors, like the correlation part of the functionals, also play a role, the observed trends may be rationalized by considering the degree to which self-interaction errors (SIE) are eliminated from each functional. The reader is referred to refs. [232–235] for detailed discussion of the self-interaction problem. Important to note in the present context is the inability of approximate functionals to, in a one-electron picture (1-SIE), correctly cancel out the Coulomb interaction of the electron with itself through the exchange interaction (which in Hartree–Fock theory is exactly cancelled out) or, in a many-electron case (N-SIE), to properly describe the discontinuity of the derivative of the total energy with respect to (fractional) changes in particle number (the so-called integer discontinuity). The inability of GGAs to properly represent such discontinuities in the energy and exchange–correlation potential (the latter denoted here by $\Delta_{xc}$) have been shown to be behind the failures of TD-DFT in describing charge-transfer excitations [65], or to reproduce the correct asymptotic behavior of the exchange–correlation potential [236, 237]. The latter defect is remedied by model potentials with the correct asymptotic (long-range) behavior, like LB94 [91] and SAOP [93].

Based on the analysis of Teale and coworkers [238], valid for the case of pure functionals, we can estimate the value of $\Delta_{xc}$ from the relation

$$\Delta_{xc} = 2(I^0 + \epsilon_{\mathrm{HOMO}}), \tag{9.1}$$

where $I^0$ is a reference ionization potential (taken to be the IHFSCC-SD value here) and $\epsilon_{\mathrm{HOMO}}$ is the Kohn–Sham orbital energy for the HOMO of the molecules (with the factor two arising from the assumption that, instead of a discontinuity, (meta)GGAs will exhibit an averaged potential over such discontinuities). The differences between the LDA or GGAs and IHFSCC-SD summarized in Table (9.5) denote that $\Delta_{xc}$ may have values of up to 8 eV, an indication that the effect of the integer discontinuity on the spectra of these systems is potentially large. We furthermore note that the asymptotically correct SAOP potential indeed provides a good agreement with the IHFSCC-SD values.

An alternative to imposing the proper asymptotic behavior with a model potential is to introduce non-locality and reduce SIE is via the inclusion of Hartree–Fock exchange (as in hybrid functionals), via an explicit dependence of the functional on the kinetic energy (metaGGAs) or a combination of both (meta-hybrids). This is also done in range-separated hybrids such as CAM-B3LYP or others [239, 240],

that offer a more detailed control over the incorporation of exact exchange than it is possible in conventional hybrids [233, 241, 242]. While the analysis of Teale is not applicable to (meta)hybrids, their better performance does indeed suggest improvements relative to the non-hybrid functionals, in particular when compared to the analogous GGA, as one can then suppose similar errors due to electron correlation or other factors.

#### 9.5.1.2 Remarks on the Virtual Space

A detailed discussion concerning the representation of the virtual orbital space will not be made here. The main reason for that lies at the very different meaning of the virtual orbital energies [243] when pure (*e.g.* LDA or (meta)GGAs) or hybrid functionals are employed. It is well-known that for pure functionals the virtual orbital energies are good approximations to the ionization potentials of excited-states, while in Hartree–Fock they represent approximations to electron affinities. For hybrids they are thus somewhere in between these two values making it difficult to compare these values with the IHFSCC-SD values that strictly represent electron affinities.

A consequence of the difference between Hartree–Fock and pure DFT is that one finds, for the GGA functionals employed here, the low-lying virtuals to be uranium-centered $f_\phi$ and $f_\delta$ orbitals (to which we will observe the transitions from the occupied $\sigma, \pi$ orbitals discussed above), while for the hybrid functionals these are often found higher in energy than other orbitals such as the $\sigma$ and $\pi$ antibonding orbitals.

### 9.5.2 Choosing the Appropriate Functinal for Excited States

All investigated exchange–correlation functionals were subsequently compared to the wave function methods in Tables (9.1) ($UO_2^{2+}$), (9.3) ($NUO^+$) and (9.2) (NUN), which are known to perform very well for molecules containing heavy elements [125, 126, 196, 206, 207]. Since previous studies indicate that IHFSCC-SD energies are generally in better agreement with experiment than those from CASPT2, the former have been chosen as reference.

Apart from the individual excitation energies and singlet-triplet splittings, the mean unsigned (MUE) and largest absolute (Max) errors with respect to IHFSCC-SD for each molecule are summarized in the Tables. We also provide a global picture in Figure (9.1), where the (signed) errors are depicted for each individual excitation.

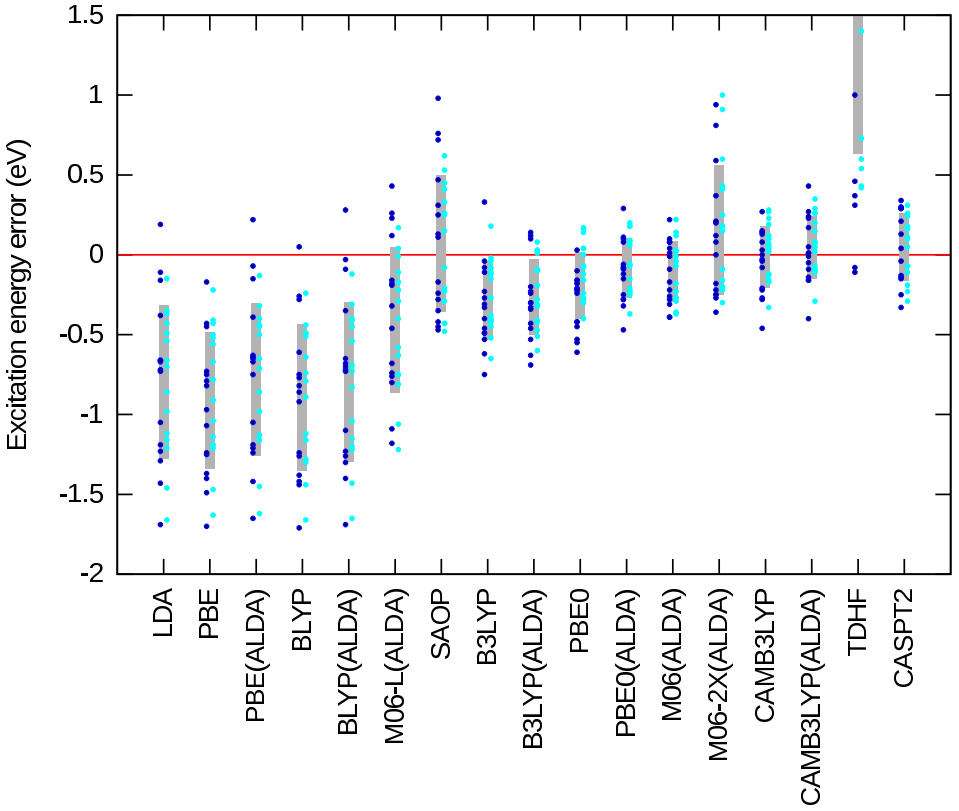


**Figure 9.1**: *Errors with respect to IHFSCC-SD for all excitations and all molecules. The gray boxes enclose a range of one sample standard deviation above and below the average error. Dots show individual errors for each excitation energy. The two highest (DFT) states for NUO+ has been left out of the analysis. (ALDA) — evaluated using the ALDA approximation.*

#### 9.5.2.1 General Trends

Employing the statistical measures, trends can be identified. To demonstrate this, we first discuss the MUE for which LDA and the investigated GGA functionals show essentially similar results for all molecules, i.e., large underestimations for GGAs with no clear improvement over LDA. The meta-GGA functional M06–L on the other hand does improve considerably over both LDA and GGAs, almost halving the error. For the (meta)hybrids the errors further decrease about four times than those obtained for GGAs or LDA. We thereby note that, while for NUN and $UO_2^{2+}$ the excitation energies are generally underestimated, slight overestimations are obtained for $NUO^+$ by some functionals.

The B3LYP functional shows larger MUEs than PBE0 or M06(XALDA), while

the latter two yield nearly identical results which is not surprising as M06 bears a number of similarities to PBE0 (about the same amount of Hartree–Fock exchange, as well as exchange and correlation functionals based on those of PBE). It is nevertheless unfortunate that the higher flexibility in the functional form available for M06 does not translate into better accuracy than observed for PBE0. However, this may be due to the ALDA approximation employed in the current ADF implementation of this functional.

For the M06-2X(XALDA) functional, in spite of having the same functional form as M06 (except for the amount of Hartree–Fock exchange), a worse performance is observed than for B3LYP, again indicating the important role played by the exchange energy. The model potential (SAOP) performs comparably to M06-2X(XALDA), while the range-separated CAM-B3LYP functional tends to improve upon PBE0 or M06. Furthermore, CAM-B3LYP generally matches the performance of CASPT2, even slightly outperforming it for NUN and $UO_2^{2+}$.

Nearly the same ranking of functional performance is seen for the largest absolute errors (Max), which are generally two to three times larger than the corresponding MUEs. The superior performance of (meta)hybrids and CAM-B3LYP compared to LDA or GGAs is evident for all three molecules. Interestingly, while the (meta)hybrid functionals yield a sightly better agreement with IHFSCC-SD for NUN and $UO_2^{2+}$ in comparison to $NUO^+$, for (meta)GGAs the opposite is true.

We believe that, as stated above for the ionization potentials, the large errors observed for LDA and GGAs have to do with a poor description of exchange energies, that are quite different for the ground and excited-states. The exchange–correlation kernel plays a significant role in determining the accuracy, in particular, the amount of HF exchange incorporated in the exchange–correlation kernel is important as the differences between M06(XALDA) and M06-2X(XALDA), and the similarities between PBE0(XALDA) and M06(XALDA) indicate. However, it remains to be seen whether or not the same will hold for other actinide compounds, especially in connection to typical charge-transfer or Rydberg-type excitations (and where one would expect CAM-B3LYP to clearly outperform the other hybrids).

Providing an understanding of the differences in standard deviation between the different groups of functionals, on the other hand, represents a much more difficult task. At this time, it can only be speculated that, at least to some extent, N-SIE effects, which affect the various exited-states differently, will be important. Hence, calculations with functionals that show large N-SIE, as it is the case with GGAs [233, 241, 242], can be expected to exhibit larger standard deviations. In this respect, the SAOP potential is perhaps an interesting example. We have already discussed that SAOP reduces the SIE by correcting the long-range part

of the potential. However, since SAOP was conceptualized to be used with the ALDA approximation, the errors inherent to the LDA functional find themselves back into the response calculation (as indicated by the large standard deviations for the excitation energies). These errors are incidentally of about the same order of any other calculations with (meta)GGAs and, more generally, of calculations with the ALDA kernel.

It is also worth noting that, in spite of its better performance on the mean error compared to the investigated (local) GGA functionals, M06–L(ALDA) ultimately remains more in line with (local) GGAs than with the (meta)hybrids. At this point it cannot be excluded that improvements could be seen if one departed from the ALDA kernel given which, as discussed below, can have significant effects on individual excitations.

#### 9.5.2.2 ALDA or Exact Derivatives in the Kernel?

In order to judge whether the ALDA approximation significantly changes the electronic spectrum of the investigated molecules, we performed calculations with the PBE, PBE0, BLYP, B3LYP and CAM-B3LYP exchange–correlation functionals incorporating and excluding ALDA. The observed effects of the ALDA approximation is depicted in Figure (9.2) for the lowest two excitations for each of the molecules considered. Figure (9.2) and the values in Tables (9.1) through (9.2) suggest that the effect of ALDA is small for the singlet states, while a surprisingly large discrepancy occurs for the triplet states, especially in the lowest electronic transitions where differences up to 0.4 eV are observed. For the higher transitions, the effect is smaller for all investigated molecules and functionals reducing to a difference up to 0.04. In particular, PBE0 and B3LYP suffer to a smaller extent from the ALDA approximation for the triplet energies than PBE and BLYP, due to the fractional Hartree–Fock exchange still present in the kernel. We may thus expect that the ALDA approximation severely effects the triplet energies for the M06-L functional (for which an implementation of the full kernel is not yet available) but less so for M06 and especially M06-2X which contain a large portion of Hartree–Fock exchange. Finally, we should note that it is difficult to remove the ALDA ansatz for SAOP due to its construction as a model potential, and that the large errors (see Fig. (9.1)) in the triplet energies cannot be easily remedied.

#### 9.5.2.3 Comparison to Previous Calculations and Benchmarks

The results discussed above are in line with those from recent benchmark calculations on different molecular databases that do not include molecules containing heavy centers [81, 244, 244–248]. In particular, the recent comparison of the M06

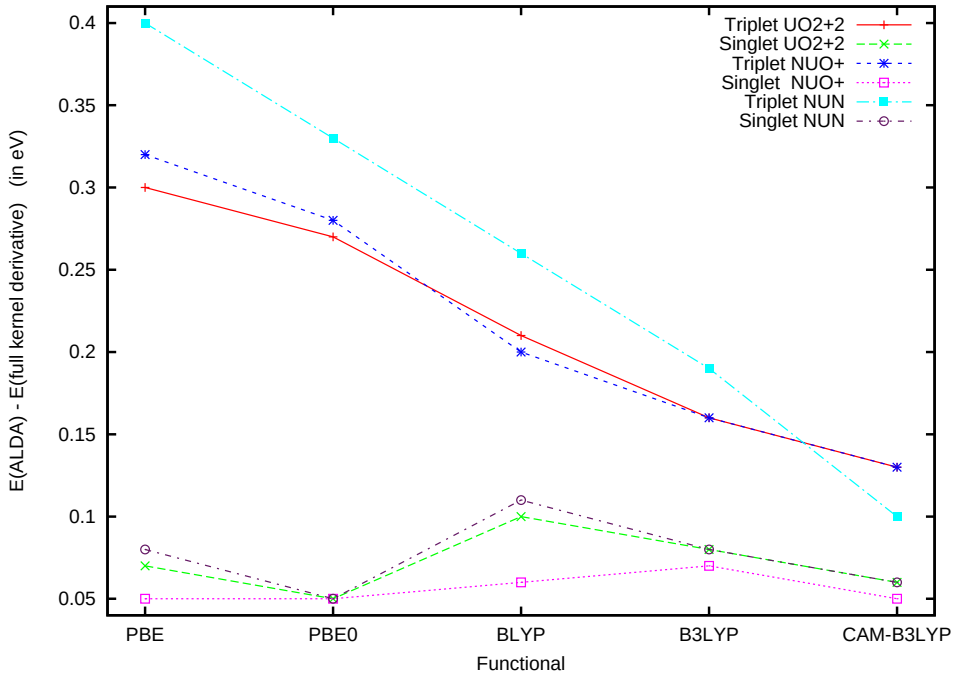


**Figure 9.2**: *Errors for the first singlet and triplet $\Phi$ states of the $UO_2^{2+}$, NUN and $NUO^+$ molecules due to the ALDA approximation for the PBE, PBE0, BLYP, B3LYP and CAM-B3LYP functionals.*

family to other functionals by Jacquemin and coworkers [81] points to the same general trends observed here: M06 does show the best overall performance and is close to PBE0, while M06-2X performance slightly worse. Furthermore, M06-L outperforms different GGAs, but still cannot match the accuracy of conventional hybrid functionals such as B3LYP.

It is difficult to directly compare our MUE values to those of Jacquemin and coworkers [81], or those of Silva–Junior and coworkers [247, 248], due to the different methodologies used to obtain the reference values (and the extent to which basis set effects can influence the WFT [248] or TD-DFT [249] results). We can nevertheless observe a rather good agreement between our MUE and those of the literature for hybrid functionals such as M06 or B3LYP (and similarly for the unsigned errors shown in Fig. (9.1)). For GGAs, on the other hand, the values in the literature seem to be much smaller than ours. At this point, it remains difficult to estimate whether this is definitely a degradation of performance for the GGAs for actinides or whether this is an artifact due to the limited size of our benchmark set.

Considering now calculations on molecules with heavy elements, we can confirm the observations of Bast *et al.* for the uranyl spectrum [197] who included spin–orbit coupling and compared the performance of functionals relative to the LR-CCSD results of Réal and coworkers [200]. While the latter have not considered the M06 family of functionals, they also reported a lowest MUE for CAM-B3LYP with LDA and GGAs severely underestimating the excitation energies.

Comparing our results to the benchmark calculations of Zhao and Truhlar (Table 17 in Ref. [87]), where a broad range of excitation energies calculated with different functionals are compared to reference values, we do not see the same drastic improvement going from hybrid functionals (B3LYP, PBE0) to meta-hybrids (M06, M06-2X). In our application, M06-2X brings the excitation energies too close to the Hartree–Fock values and introduces significant errors. Most likely this discrepancy between our particular molecules and excitations and the data presented by Zhao and Truhlar is due to the fact that we do not include Rydberg or extreme charge-transfer states in our benchmark. In these cases it is crucial to use functionals with a correct treatment of the nonlocality of the change in the electron density. Based on our results, we cannot recommend M06-2X for the systems and excitations studied in this work, despite its good performance in other benchmarks.

## 9.6 Conclusions

We investigated the performance of different classes of approximate exchange–correlation functionals in describing ten low-lying valence excitations for the uranyl ion $UO_2^{2+}$ and two isoelectronic analogs, $NUO^+$ and NUN, by comparing them to wave function calculations (CASPT2 and Fock-space coupled cluster). A marked characteristic of such systems, all of which are closed-shell species in the ground-state, is that the low-lying excited-states under consideration correspond to excitation from the $\sigma, \pi$ bonding orbitals to unoccupied orbitals which are essentially uranium $f$-orbitals.

We can identify the following trends regarding the functional's performance: i) LDA and (meta)GGAs show somewhat larger mean errors than (meta)hybrids or model potentials such as SAOP; however, the standard deviation for those is significantly larger than for the (meta)hybrid functionals. ii) one hardly observes an improvement for metaGGAs or meta hybrids in comparison to GGAs or hybrids, excepting the improvement of the mean error for M06-L over the GGAs; and iii) The performance of M06, PBE0 and CAM-B3LYP approaches that of CASPT2, both in terms of relatively small MAEs and standard deviations for

the excitations. Of course, with only three molecules studied, one cannot rule out that the present agreement is fortuitous, but based on this benchmark M06, PBE0 and especially CAM-B3LYP appear appropriate for quantitative studies of actinide spectroscopy. Other hybrid functionals such as M06-2X and B3LYP are suited for (semi)quantitative or qualitative work, but we would strongly argue against employing non-hybrid (meta)GGAs even for qualitative investigations of excited-states of actinyls.

In view of those trends, we believe that, while the correlation functional does play an important role in the accuracy of results, as seen in the differences between different functionals of the same kind (GGAs, hybrids etc), what appears to be a critical factor governing the accuracy of the functionals tested is the degree of non-locality introduced through inclusion of HF exchange in hybrids or meta-hybrids. We could thereby rationalize why: i) hybrids outperform their pure GGA counterparts; ii) M06-L(ALDA) shows stronger improvement over the GGAs regarding the mean error but not in the standard deviation; iii) the SAOP model yields excellent ionization potentials and mean errors for the excitation energies but has standard deviations similar to GGAs.

It is also clear that one must go beyond the ALDA approximation, given the rather large differences observed between the low-lying triplet states. Equally (or perhaps more) important, however, is that non-local effects should also be incorporated to the exchange–correlation kernel, as done for all (meta)hybrids and CAM-B3LYP, if one wishes to approach the accuracy of methods such as CASPT2.

Finally, it is noteworthy that for excitation energies the choice of the relativistic (spin–free) Hamiltonian is almost irrelevant, so one can safely investigate the spectra of actinide-containing molecules with the more approximate two-component methods (such as ZORA), instead of using four-component approaches.

# 10

# How Reliable Are Electronic Spectra from Relativistic Time-Dependent Density Functional Theory?

> Scientific views end in awe and mystery, lost at the edge in uncertainty, but they appear to be so deep and so impressive that the theory that it is all arranged as a stage for God to watch man's struggle for good and evil seems inadequate.
>
> Richard Feynman

Adopted from:
Tecmer, P., Bast, R., Ruud, K., Visscher, L., *J. Phys. Chem. A*, **116** (2012), 7397–7404.

## 10.1 Abstract

Four-component relativistic time-dependent density functional theory is used to study charge-transfer excitation energies of the uranyl molecule as well as the uranyl tetrachloride complex. Adiabatic excitation energies and vibrational frequencies of the excited-states are calculated for the lower-energy range of the spectrum. The results for TD-DFT with the CAM-B3LYP exchange–correlation functional for the $[UO_2Cl_4]^{2-}$ system are in good agreement with the experimentally observed spectrum as well as with other theoretical data. Use of the global hybrid B3LYP gives qualitatively correct results, while the BLYP functional yields results

that are qualitatively wrong due to the too low CT states calculated with this functional. The applicability of the overlap diagnostic of Peach *et al.* [J. Chem. Phys. 128, 044118 (2008)] to identify such CT excitations is investigated for a wide range of vertical transitions employing three different approximate exchange–correlation functionals, BLYP, B3LYP and CAM-B3LYP.

## 10.2 Introduction

Experimental and theoretical chemists show a continued interest in uranium chemistry, which is not only due to its importance in nuclear energy production and nuclear waste separation [18, 19, 184, 250], but also because of the potential use of uranium in catalysis [20, 251]. The most studied uranium compound is the uranyl cation $[UO_2]^{2+}$ that is found as a stable unit in many crystal environments and in solution [4]. Since the bare cation is difficult to assess by experimental techniques, much attention has been devoted to calculations in order to determine its properties. Nowadays, high-level theoretical predictions for bond lengths and electronic spectra are available [35, 126]. Similarly, in order to provide further insights and to connect to experimental work, accurate theoretical investigations of ligated complexes are desirable. This represents a more difficult task since ligation increases the size of the system to be studied and involves electron donation into the unoccupied f-orbitals that are strongly split by SOC. Nevertheless, the chemical properties of uranyl are covered in a number of papers addressing its electronic structure, ionization potentials, bonding to various ligands and electronic spectra [23, 25, 35, 36, 96, 97, 126, 197, 203, 252–255].

The uranyl molecule is found as a small building block in larger uranium–containing complexes [5], in which the uranium metal center is coordinated by ligands in the equatorial plane resulting in a square, pentagonal or hexagonal bipyramidal structure [256]. In this process, the valence orbitals of the uranyl compound change their energetic ordering and mix with the ligand orbitals to a varying extent. While some of this reordering can be explained by simple ligand-field arguments, it is of interest to apply higher-level methods that include the ligands explicitly. One possible application is to use rational design of complexing ligands to tune the properties of uranium-containing complexes employed in catalysis [20, 251, 257], or to improve the process of nuclear waste separation and immobilization [250, 258]. Most important in this respect is the interaction of the uranyl molecule with its nearest ligands in the equatorial plane, perpendicular to the axial $UO_2$–unit [4, 5, 198, 256, 259]. Typically, these equatorial ligands are bonded to the uranium atom in a much weaker fashion than the axial oxygen atoms

and their influence on the uranyl unit can be considered as a perturbation that affects the uranium-oxo bonds, but does not fundamentally change the intrinsic properties of bonding [5, 32, 35, 36, 260]. An indirect measure for the effects of the ligands on the two internal uranyl bonds is established by studying the changes in the U–O stretching vibrations [186, 204, 261]. More direct is the study of the effect of ligation on the electronic spectrum, considering the lowest excitations that comprise transitions internal to the uranyl unit, in particular, excitations from the lowest bonding orbitals ($\sigma_g, \pi_g, \pi_u, \sigma_u$) to the non-bonding $\delta_u$ and $\phi_u$ orbitals [5].

Theoretical modelling of ligation requires quantum-chemical methods that provide the necessary accuracy (better than about 2 000 $cm^{-1}$ or 0.25 eV) at an acceptable computational cost. Very accurate results can be obtained with highly correlated wave function methods (*e.g.* coupled cluster [101, 102, 262] or complete active space second order perturbation theory [103, 104]) but, due to a steep computational scaling with the size of the active space, application of these methods is often limited to model complexes [96, 126, 252, 263, 264]. Larger complexes with organic ligands are typically treated by DFT [48, 49] that has a much lower computational cost [188]. In the DFT approach, the electronic spectrum is usually obtained via its time-dependent generalization, TD-DFT [54, 55, 58]. While being a standard method for organic molecules, TD-DFT is not yet much tested for actinide complexes for which the correct ordering of energetically close-lying excitations to the different metal $f$-type orbitals is crucial. Due to the presence of ligand-to-metal charge-transfer states, the well-known problem of TD-DFT in describing CT and Rydberg type electronic transitions [64, 265] should be considered. Since this problem arises due to the near-sightedness of the local or generalized gradient exchange–correlation kernel, significant improvements can be achieved by including a fraction of exact exchange in the kernel. The family of range-separated hybrid exchange–correlation functionals, of which the CAM-B3LYP [90] is one of the most widely-used examples, looks particularly promising in this respect [233, 266]. As discussed in the preceding chapter (see also Ref. 96), accurate results were obtained when excitation energies obtained with this functional were benchmarked against coupled-cluster data. For a more detailed discussion of the performance of different exchange–correlation functionals on small uranium species and the quality of calculated electronic transitions, we refer the reader to Ref. 96.

In this chapter, we will analyze in more detail why long-range separated hybrid exchange–correlation functionals perform so well for actinyl molecules. It is known that they dramatically improve upon the description of Rydberg and charge-transfer transitions [116, 244, 267–269] but it remains surprising that they are also able to give an improvement for excitations in small triatomic actinide

cations. The benefit of including exact exchange for charge-transfer excitations is well-understood: Dreuw *et al.* [265] pointed out that conventional generalized-gradient approximation functionals produce large errors when the occupied and virtual orbitals involved in the electronic transition are spatially well separated since the excitation energies then reduce to just the orbital energy differences, whereas they should yield a difference between an ionization potential (for the region from which the electron leaves) and an electron affinity (for the region it is transferred to). Gritsenko and Baerends [270] analyzed this problem further and proposed to interpolate between the correct asymptotic expressions for localized and CT excitations applying the distance between the occupied and virtual charge densities involved in the transition as a criterium. In later work, Neugebauer and coworkers [271] implemented this correction in a computationally simple protocol and studied the performance of the resulting functional in a number of model systems. A different approach was undertaken by Peach *et al.* [272]: rather than defining a corrected functional, they employed the distance between occupied and virtual orbital densities to quantitatively correlate the character of the electronic excitation with the expected error in a GGA calculation. This yields a simple diagnostic test in which the spatial overlap in a given electronic excitation is measured by the $\Lambda$ value, which reads

$$\Lambda = \frac{\sum_{i,a} \kappa_{ia}^2 O_{ia}}{\sum_{i,a} \kappa_{ia}^2}, \tag{10.1}$$

where $O_{ia}$ are moduli of the two orbitals (occupied and virtual), $O_{ia} = \langle |\Psi_a||\Psi_i| \rangle$, and $\kappa_{ia} = X_{ia} + Y_{ia}$ are elements of the solution vectors of the TD-DFT generalized eigenvalue problem (see Section (5.3) for more details) [55]. Based on the $\Lambda$ value, three different categories of electronic excitations were defined: Rydberg (roughly $0.08 \leq \Lambda \leq 0.27$), charge-transfer ($0.06 \leq \Lambda \leq 0.72$) and local ($0.45 \leq \Lambda \leq 0.89$) excitations [272]. The relatively wide range of $\Lambda$ for CT excitations is associated with the fact that these type of transitions can possess both short- and long-range character with the short-range excitations sometimes being difficult to distinguish from local excitations [65, 273]. In this chapter, we will study the applicability of the $\Lambda$ diagnostic tool to identify possible problems in the TD-DFT description of actinide complexes.

As model compound, we chose the uranyl tetrachloride ion $[UO_2Cl_4]^{2-}$, which is convenient for the following reasons: (i) it exhibits a well-defined closed-shell ground state, (ii) its $D_{4h}$ point group symmetry simplifies the study of the equatorial ligand effects, (iii) an experimental electronic spectrum of the $Cs_2UO_2Cl_4$ crystal is available as a reference, and (iv) it is large enough to enable charge-

transfer excitations yet small enough to allow for a detailed analysis.

We will first briefly revisit the uranyl molecule before presenting our theoretical investigations of the electronic spectrum of the uranyl tetrachloride molecule. Due to the importance of SOC, we apply a relativistic SOC TD-DFT approach. Our aims are to assign the character of each transition with respect to its origin *i.e.,* local, charge-transfer or Rydberg types, compare it to the calculated value of the $\Lambda$ parameter, and study the excitation energy employing exchange–correlation functionals that are based on the same exchange–correlation functional (BLYP) but differ in the inclusion of exact exchange (BLYP [74, 75]: none, B3LYP [83, 84]: global hybrid with 20 % exact exchange, CAM-B3LYP [90]: local hybrid with 19% of exact exchange at short-range and 65% at long-range).

## 10.3 Computational Details

### 10.3.1 Geometry and Basis Sets

The structure of uranyl tetrachloride as it is found in the cesium chloride host [274] shows a distortion from $D_{4h}$ symmetry. For our purposes, it is more suitable to consider an idealized structure since firstly the differences to the true structure are not significant [35, 36] and secondly the use of a higher symmetry allows both for a drastic reduction of computational expenses and simplification of analysis. Assignments are therefore given according to the full $D_{\infty h}$ symmetry of uranyl and for the idealized $D_{4h}$ structure of uranyl tetrachloride, respectively. All calculations were performed in the $D_{2h}$ point group symmetry, which is the highest possible symmetry for TD-DFT calculations in the DIRAC10 program [275].

The ground-state energy minimum was obtained from a calculation employing the CAM-B3LYP exchange–correlation functional and the triple–$\zeta$ basis set of Dyall [215] for the uranium atom and the aug-cc-pVTZ basis sets of Dunning [216] for the oxygen and chlorine atoms. At this structure, ($R_e$ (U–O) = 1.764 Å and $R_e$ (U–Cl) = 2.712 Å), vertical excitation energies were calculated. Geometries of the excited-states were obtained by varying the U–O bond lengths simultaneously (symmetric stretch) in steps of 0.01 Å in a range from 1.70 to 1.90 Å, while the U–Cl bond lengths were kept frozen at the ground-state equilibrium distance of 2.712 Å[29, 274]. The points on the resulting potential energy curve were subsequently fitted to a second order polynomial to obtain minima and adiabatic excitation energies. Five points closest to the minima were used to numerically evaluate vibrational frequencies employing the five-point stencil formula.

### 10.3.2 Relativity

The all–electron TD-DFT calculations were performed with a development version of the DIRAC10 program [275]. The four-component Dirac–Coulomb Hamiltonian was used, i.e., relativistic corrections from the two–electron Darwin as well as the Breit terms were neglected. Moreover, the $(SS|SS)$ integrals that originate from the small component of the four-component Dirac spinor were replaced by a simple point-charge model [219]. We should note that non-relativistic exchange–correlation approximations have been applied since it has been shown that such an approximation works well in combination with four-component relativistic densities [197].

### 10.3.3 TD-DFT

Excitation energies were obtained with a non-collinear approach of TD-DFT, as implemented in the DIRAC10 program [197]. The adiabatic approximation with a full derivative of the functional was used in the exchange–correlation kernel. Tight convergence criteria of $10^{-8}$ a.u. were used for the TD-DFT solver to obtain converged excitation energies. For every irreducible representation in the $D_{2h}$ point group, the 15 lowest roots were taken into account in the TD-DFT solver. The overlap diagnostic method of Peach *et al.* [272] was implemented into a development version of the DIRAC10 code and used in TD-DFT calculations with three different approximate exchange–correlation functionals: BLYP [74, 75], B3LYP [83, 84] and CAM-B3LYP [90].

Since the detailed discussion by Denning in his review paper of 1992 [276], in which he concluded that all observed lower-energy states (below 29 000 $cm^{-1}$) are of *gerade* symmetry, most studies have been limited to *gerade* states. This is also sufficient for our purposes. However, we should note that a number of low-energy *ungerade* states emerges in this part of the spectrum when the BLYP functional is used. We have not analyzed these low-lying states in detail since they represent an artifact of the BLYP functional.

## 10.4 Results and Discussion

### 10.4.1 Vertical Excitation Energies

For a comprehensive analysis of the spectrum of uranyl and uranyl tetrachloride, we refer to the review papers by Denning [5, 30, 276]. At low energy, the spectrum is characterized by transitions from the $\sigma_u$ HOMO to the $\phi_u$ and $\delta_u$ uranium orbitals. These transitions are split by the crystal field and by spin–orbit interactions and

could be considered to have some CT character due to the fact that the HOMO is a bonding combination of uranium $5f$- and $6p$- and oxygen $2p$-orbitals, while the $\phi_u$ and $\delta_u$ orbitals are non-bonding uranium $5f$-orbitals. In the CASSCF calculations performed by Pierloot and van Besien [35], this orbital contains only 30 to 40% oxygen character, including transition of considerable local character with respect to the uranium atom. A Mulliken population analysis of this orbital for different LYP-based functionals points to even stronger localization with the oxygen character amounting to only 26%, while the contribution from the chloride ions remains negligible in the uranyl chloride calculation. It is therefore convenient to first discuss the transitions in the bare uranyl species before turning to the calculations considering the full-fledged ligands. From Table (10.1), the qualitative differences between the three functionals employed are evident. As expected, the B3LYP functional yields too low excitation energies when compared to CAM-B3LYP and underestimates transition energies by up to 2 000 $\mathrm{cm}^{-1}$. Even larger deviations up to 5 000 $\mathrm{cm}^{-1}$ from the reference CAM-B3LYP excitation energies are observed for the BLYP exchange–correlation functional.

The errors can be correlated with the overlap diagnostic values that are also given in Table (10.1): for transitions to the $\phi_{\frac{5}{2}u}$ orbital, error values of 5 000 and 2 000 $\mathrm{cm}^{-1}$ are obtained with diagnostic parameters $\Lambda$=0.5 and $\Lambda$=0.49 for BLYP and B3LYP, respectively. The errors in the transitions to the other spin–orbit component, the $\phi_{\frac{7}{2}u}$ orbital, are approximately 4 000 and 1 500 $\mathrm{cm}^{-1}$ for BLYP and B3LYP, respectively, for a similar diagnostic value of $\Lambda$=0.5. Smaller errors of about 3 000 $\mathrm{cm}^{-1}$ are found in the excitation energies that correspond to the transitions from the $\sigma_u$ to the $\delta_u$ orbitals: $^1\Sigma_g^+ \rightarrow {}^3\Delta_g$ and $^1\Sigma_g^+ \rightarrow {}^1\Delta_g$ and again correlate reasonably well with the $\Lambda$ values. An exception is the fourth $E_g$ state in Table (10.1) which exhibits a difference of about 4 500 $\mathrm{cm}^{-1}$.

For all transitions, the $\Lambda$ diagnostic values are above 0.45 which was defined as the lower threshold for local excitations by Peach *et al.* [272]. However, the rather large error values, which are partly corrected by the global hybrid functional and, even to a larger extent, by the long-range separated hybrid, are probably best interpreted to arise from the very different nature of the exchange interactions in the partly bonding $\sigma_{\frac{1}{2}u}$ orbital and the pure $f$-orbitals to which the electron is excited. Since all these transitions can still be considered as local, and due to the high symmetry (cf. Table (10.2)), their characterization is straightforward.

However, this situation changes for the uranyl tetrachloride molecule. Matching the transitions calculated by the different exchange–correlation functionals represents a more difficult task because of the admixture of artificially low-lying states corresponding to a CT from the chloride ligands. This is also evident from the $\Lambda$

**Table 10.1**: *SOC vertical excitation energies in cm$^{-1}$; $D_{4h}$ characterization and assignment in terms of internal uranyl excitations; the $\Lambda$ parameter is given in parenthesis (all transition energies are aligned with the CAM-B3LYP values for the uranyl tetrachloride molecule).*

| Symmetry$^{\dagger}$ | Type$^{\pm}$ | $[UO_2]^{2+}$ | | | $[UO_2Cl_4]^{2-}$ | | |
|---|---|---|---|---|---|---|---|
| $D_{4h}$( internal $[UO_2^]2+$) | | BLYP | B3LYP | CAM-B3LYP | BLYP | B3LYP | CAM-B3LYP |
| $E_g$, $\sigma_{\frac{1}{2}u} \rightarrow \delta_{\frac{3}{2}u}$ | L | 12 955(0.62) | 14 423(0.61) | 15 709(0.61) | 17 236(0.50) | 18 010(0.47) | 19 235(0.44) |
| $B_{1g}$, $\sigma_{\frac{1}{2}u} \rightarrow \phi_{\frac{5}{2}u}$ | L | 7 492(0.50) | 10 699(0.49) | 12 502(0.49) | 16 026(0.50) | 18 179(0.44) | 19 473(0.44) |
| $B_{2g}$, $\sigma_{\frac{1}{2}u} \rightarrow \phi_{\frac{5}{2}u}$ | L | 7 492(0.50) | 10 699(0.49) | 12 502(0.49) | 16 471(0.50) | 18 721(0.44) | 20 037(0.44) |
| $E_g$, $\sigma_{\frac{1}{2}u} \rightarrow \phi_{\frac{5}{2}u}$ | L | 8 990(0.50) | 12 132(0.49) | 13 913(0.49) | 16 053(0.50) | 19 672(0.44) | 21 093(0.48) |
| $B_{2g}$, $\sigma_{\frac{1}{2}u} \rightarrow \delta_{\frac{3}{2}u}$ | L | 14 711(0.61) | 16 341(0.61) | 17 673(0.60) | 17 911(0.51) | 20 397(0.45) | 21 800(0.46) |
| $B_{1g}$, $\sigma_{\frac{1}{2}u} \rightarrow \delta_{\frac{3}{2}u}$ | L | 14 711(0.61) | 16 341(0.61) | 17 673(0.60) | 17 936(0.51) | 20 440(0.45) | 21 897(0.47) |
| $E_g$, $\sigma_{\frac{1}{2}u} \rightarrow \phi_{\frac{7}{2}u}$ | L | 17 053(0.50) | 19 555(0.56) | 21 044(0.56) | 22 056(0.49) | 24 325(0.38) | 25 700(0.47) |
| $A_{2g}$, $\sigma_{\frac{1}{2}u} \rightarrow \phi_{\frac{7}{2}u}$ | L | 14 867(0.49) | 17 774(0.49) | 19 587(0.48) | 23 161(0.44) | 25 701(0.35) | 27 223(0.43) |
| $A_{1g}$, $\sigma_{\frac{1}{2}u} \rightarrow \phi_{\frac{7}{2}u}$ | L | 14 867(0.49) | 17 774(0.49) | 19 587(0.48) | 23 187(0.45) | 25 758(0.35) | 27 271(0.43) |
| $E_g$, $\sigma_{\frac{1}{2}u} \rightarrow \delta_{\frac{5}{2}u}$ | L | 18 413(0.50) | 21 149(0.52) | 22 912(0.56) | 24 413(0.44) | 27 754(0.35) | 29 778(0.42) |
| $B_{2g}$, $\sigma_{\frac{1}{2}u} \rightarrow \delta_{\frac{5}{2}u}$ | L | 23 068(0.52) | 24 805(0.49) | 26 803(0.55) | 23 964(0.50) | 28 247(0.39) | 30 588(0.46) |
| $E_g$, $\pi(Cl)_{\frac{3}{2}u} \rightarrow \phi_{\frac{5}{2}u}$ | CT | | | | 21 121(0.44) | 29 101(0.37) | 30 803(0.42) |
| $B_{1g}$, $\sigma_{\frac{1}{2}u} \rightarrow \delta_{\frac{5}{2}u}$ | L | 23 068(0.52) | 24 805(0.49) | 26 803(0.55) | 24 271(0.45) | 28 680(0.39) | 30 956(0.42) |
| $B_{2g}$, $\pi(Cl)_{\frac{3}{2}u} \rightarrow \phi_{\frac{5}{2}u}$ | CT | | | | 22 336(0.41) | 28 992(0.38) | 31 144(0.40) |
| $B_{1g}$, $\pi(Cl)_{\frac{3}{2}u} \rightarrow \phi_{\frac{5}{2}u}$ | CT | | | | 22 311(0.43) | 27 792(0.33) | 32 628(0.33) |

$^{\dagger}$ Symmetry correspondences are given in Table (10.2).
$^{\pm}$ L and CT denote local and charge-transfer excitation energies, respectively.

**Table 10.2**: *Subduction of the relevant irreducible representations of $D_{\infty h}$ point group towards those of the $D_{4h}$ subgroup [277].*

| $D_{\infty h}$ | $D_{4h}$ |
|---|---|
| $\sigma_g^+$ | $a_{1g}$ |
| $\sigma_u^+$ | $a_{1u}$ |
| $\pi_g$ | $e_g$ |
| $\pi_u$ | $e_u$ |
| $\delta_g$ | $b_{1g} \oplus b_{2g}$ |
| $\delta_u$ | $b_{1u} \oplus b_{2u}$ |
| $\phi_g$ | $e_g$ |
| $\phi_u$ | $e_u$ |
| $\gamma_g$ | $a_{1g} \oplus a_{2g}$ |
| $\gamma_u$ | $a_{1u} \oplus a_{2u}$ |

values that drop to 0.33–0.51 and scatter upon changing the density functional. In order to rationalize these differences, we will also compare our results to theoretical studies presented in the literature. In Table (10.3), the SOC vertical excitation energies obtained with the CAM-B3LYP exchange–correlation functional are compared to those of a semiempirical crystal field model (CFT) [278], to TD–DFT results obtained by Pierloot *et al.* [36], to the SAOP [92, 93] model potential, and to two sets of CASPT2 data [35, 260] with SOC included *a posteriori*. All of these methods deal with the $[UO_2Cl_4]^{2-}$ model system, that is include only the first shell of anions. Due to the different choices of the active space, the two SOC-CASPT2 studies yield different spectra. While Pierloot and van Besien chose a similar active space for the uranyl tetrachloride molecule as is optimal for the bare uranyl molecule, Ruipérez and Wahlgren [260] decreased the number of non-bonding orbitals in the $[UO_2]^{2+}$ unit and included an additional $3p$-orbital from each of the chlorides to the active orbital space to allow for charge-transfer transitions from the ligands to the uranyl. In their studies, the first CT excitation from the chloride ligand to the uranium metal center was indeed calculated at 33 226 $cm^{-1}$, followed by a manifold of other CT transitions at higher energy.

When comparing our CAM–B3LYP results to the SOC-CASPT2 [35, 260] values, all low-energy CAM-B3LYP excitations turn out to be about 2 000–3 000 $cm^{-1}$ lower in energy than those obtained by SOC-CASPT2 [35]. For the higher-energy excitations, the agreement with the results of Ruipérez and Wahlgren [260] is quite good. In comparison to the SAOP TD-DFT data of Pierloot *et al.* [36], we see absolute differences in excitation energies of around 1 000 $cm^{-1}$ for most

excitation energies except the a $B_{1g}$, c $B_{2g}$ and d $E_g$ states, where the difference increases up to 2 000 $cm^{-1}$ and c $B_{1g}$ where difference increased up to 3 000 $cm^{-1}$. With CAM–B3LYP, the first true CT state appears well above 30 000 $cm^{-1}$, in agreement with the calculation of Ruipérez and Wahlgren[260].

**Table 10.3**: *SOC vertical excitation energies in $cm^{-1}$ for the $UO_2Cl_4^{2-}$ molecule: comparison of different methods with experiment.*†

| Symmetry | CF | TD-DFT | | CASPT2 | |
|---|---|---|---|---|---|
| $D_{4h}$ | Model[a] | SAOP[b] | CAM-B3LYP | Ruipérez[c] | Pierloot[d] |
| a $E_g$ | 20 126 | 20 954 | 19 235 | 22 870 | 21 024 |
| a $B_{2g}$ | 20 643 | 20 884 | 20 037 | 23 090 | 21 273 |
| a $B_{1g}$ | 21 045 | 21 335 | 19 473 | 23 745 | 22 125 |
| b $E_g$ | 22 603 | 22 108 | 21 093 | 24 450 | 22 859 |
| b $B_{1g}$ | 22 022 | 22 420 | 21 897 | 24 636 | 24 056 |
| b $B_{2g}$ | 21 997 | 22 570 | 21 800 | 25 222 | 24 339 |
| c $E_g$ | 26 146 | 26 882 | 25 700 | 26 143 | 27 494 |
| a $A_{2g}$ | 27 809 | 27 678 | 27 223 | 28 580 | 29 842 |
| a $A_{1g}$ | 27 813 | 27 682 | 27 271 | 28 746 | 29 849 |
| c $B_{1g}$ | 27 412 | 27 666 | 30 956 | 30 158 | 31 991 |
| d $E_g$ | 29 417 | 28 364 | 29 778 | 30 326 | 31 961 |
| c $B_{2g}$ | 27 785 | 28 561 | 30 588 | 31 052 | 32 523 |

† All electronic transitions are local (L) to the $[UO_2]^{2+}$ ion.
a) Ref. 278; b) Ref. 36; c) Ref. 260; d) Ref. 35;

If we now return to Table (10.1), we note that the pure GGA functional BLYP puts the chloride-to-uranyl CT states in between two groups of local excitations in the region from 21 000 to 22 000 $cm^{-1}$. The $\sigma_{\frac{1}{2}u} \rightarrow \phi_{\frac{5}{2}u}$ transitions remain relatively pure and are significantly shifted up by the Pauli repulsion from the equatorial chloride ligands. This repulsion is smaller for the $\delta_u$ orbitals which makes the lowest excitation a $\sigma_{\frac{1}{2}u} \rightarrow \delta_{\frac{3}{2}u}$ transition. For these transitions, a stronger mixing with CT states can be observed, which for some of them leads to large shifts relative to the CAM-B3LYP and other reference values. Notably, the third $B_{2g}$ transition at 23 964 $cm^{-1}$ contains significant mixing with a CT state at 22 336 $cm^{-1}$ while still resulting in a large $\Lambda$ value of 0.50. For the remaining states in this group, the $\Lambda$ value is lower than in the uranyl molecule, correctly indicating the increased admixture of CT character.

Adding exact exchange via the global hybrid functional B3LYP shifts the CT states up to the region of the $\phi_{7/2u}$ excitations and leads to an increased mixing between L and CT states. This is evident from the $\Lambda$ value which drops below 0.4

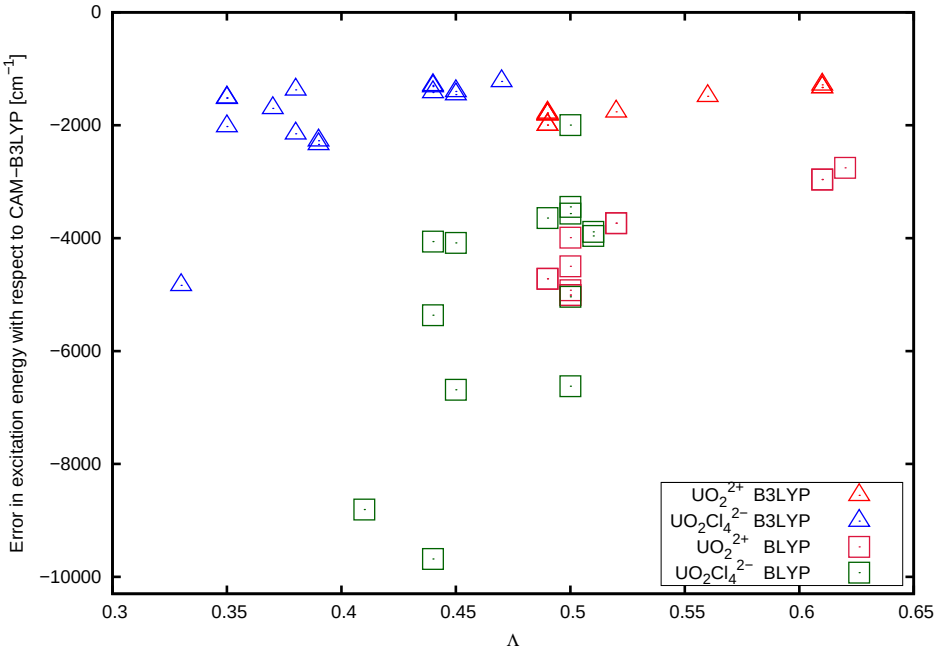


**Figure 10.1**: *Error in the excitation energies made by the BLYP and B3LYP exchange–correlation functionals in comparison with reference data (CAM-B3LYP).*

for a whole range of states. These values are the lowest ones observed in this study, although the differences with respect to reference values are not significantly larger than in uranyl. For the B3LYP functional the Λ-diagnostic therefore indicates a larger error than can be actually found. Turning to CAM-B3LYP, the higher amount of exact exchange in the limit pushes the CT states beyond this region and restores an unambiguous identification in terms of L and CT states. Furthermore, all 12 (including the 4 two-fold degenerate $E_g$) states that may be formed out of the uranyl $\sigma_u$ to $\phi_u$ and $\delta_u$ transitions remain comparatively pure. We should note that this observation could only be made by analyzing the excitations in detail (employing an decomposition of the orbitals and the coefficients obtained in the TD-DFT calculations) and studying the trend when changing the exchange–correlation functional. The Λ-diagnostic is useful, but condenses information into a single number that may be difficult to interpret when severe mixing between states occurs, as in the case of the B3LYP calculation.

The general performance of the overlap diagnostic test is further illustrated in Figure (10.1), where the differences in excitation energies between CAM-B3LYP and BLYP as well as CAM-B3LYP and B3LYP as a function of the BLYP and B3LYP Λ values are plotted. Indeed, the better performance of B3LYP over

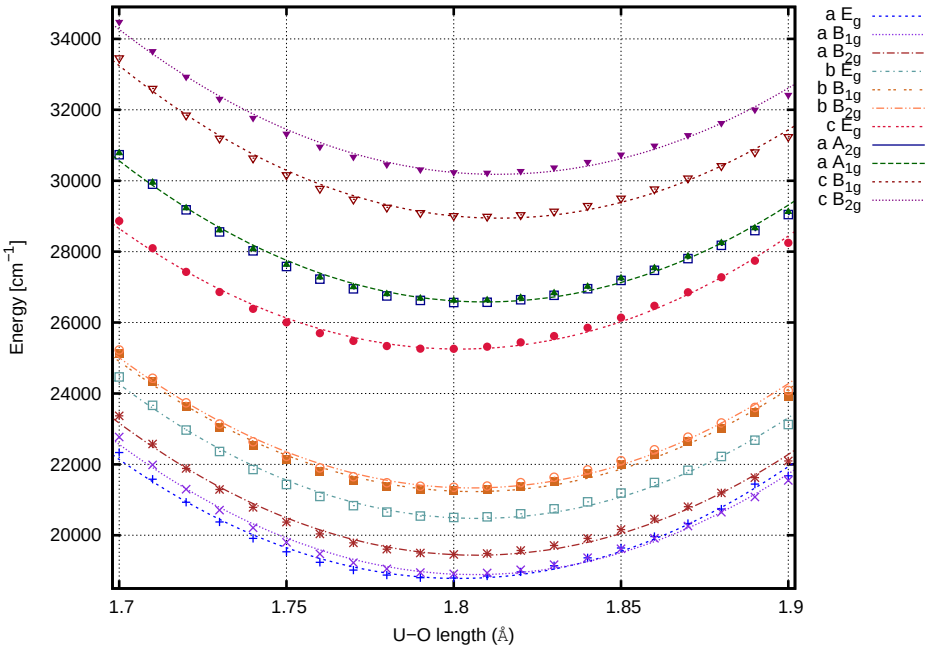


**Figure 10.2**: *Excited-state curves of* $[UO_2Cl_4]^{2-}$ *along the symmetric U-O stretching mode.*

BLYP is visible, while for BLYP a clear trend can be observed for the uranyl ion where smaller Λ-values correspond to large discrepancies between BLYP and CAM-B3LYP. For the uranyl tetrachloride molecule, correlation is evident but outliers are also present, as aforementioned.

### 10.4.2 Adiabatic Excitation Energies

The vertical excitation energies are sufficient for a qualitative comparison to experimental values. However, a more precise analysis is also possible since the high resolution of the experimental spectrum allows to identify band origins and to determine adiabatic excitation energies. In so doing, we calculated the adiabatic excitation spectrum of uranyl tetrachloride with the CAM-B3LYP functional. The results are summarized in Table (10.4) and compared to experimental data, as well as to SOC-CASPT2 and SOC configuration interaction (SOC-CI) [279] values. We should note that our CAM-B3LYP and the reference SOC-CASPT2 [35] calculations correspond to the idealized $D_{4h}$ structure, while the SOC-CI [254] calculations allowed for a small distortion consistent with the X-ray structure of $UO_2Cl_4Cs_2$ [274].

The CAM-B3LYP excited-state curves are plotted in Figure (10.2) which

**Table 10.4**: *SOC adiabatic excitation energies and vibrational frequencies: comparison of different methods with experiment. In references, where the distortion from the ideal $D_{4h}$ point group symmetry was taken into account, we have averaged excitation energies in the $E_g$ symmetry.*†

| Sym. | CASPT2[a] | | | SOC-CI[b] | | | CAM-B3LYP | | | Experiment[c] | |
|---|---|---|---|---|---|---|---|---|---|---|---|
| $D_{4h}$ | $R_e$ (U–O) [Å] | $T_e$ [cm$^{-1}$] | $\omega_e$ [cm$^{-1}$] | $R_e$ (U–O) [Å] | $T_e$ [cm$^{-1}$] | $\omega_e$ [cm$^{-1}$] | $R_e$ (U–O) [Å] | $T_e$ [cm$^{-1}$] | $\omega_e$ [cm$^{-1}$] | $\omega_e$ [cm$^{-1}$] | $T_e$ [cm$^{-1}$] |
| x $A_{1g}$ | 1.783 | - | 819 | 1.728 | - | 968 | 1.764 | - | 819 | - | 832 |
| a $E_g$ | 1.836 | 20 028 | 712 | 1.790 | 20 363 | 885 | 1.802 | 18 792 | 728 | 20 096 | 715 |
| a $B_{2g}$ | 1.844 | 20 330 | 703 | 1.792 | 21 013 | 879 | 1.807 | 19 451 | 733 | 20 406 | 710 |
| a $B_{1g}$ | 1.826 | 21 139 | 698 | 1.790 | 21 838 | 878 | 1.806 | 18 890 | 736 | 21 316 | 696 |
| b $E_g$ | 1.846 | 21 809 | 711 | 1.794 | 22 819 | 874 | 1.808 | 20 480 | 738 | 22 051 | 711 |
| b $B_{1g}$ | 1.846 | 22 984 | 721 | 1.806 | 24 618 | 902 | 1.806 | 21 231 | 736 | 22 406 | 717 |
| b $B_{2g}$ | 1.847 | 23 228 | 714 | 1.806 | 24 780 | 900 | 1.806 | 21 333 | 739 | 22 750 | 711 |
| c $E_g$ | 1.842 | 26 534 | 722 | 1.805 | 26 763 | 904 | 1.802 | 25 234 | 738 | 26 222 | 725 |
| a $A_{2g}$ | 1.854 | 28 527 | 703 | 1.808 | 29 169 | 896 | 1.810 | 26 533 | 741 | 27 720 | 705 |
| a $A_{1g}$ | 1.854 | 28 530 | 703 | 1.807 | 29 145 | 890 | 1.809 | 26 585 | 742 | 27 757 | 705 |
| c $B_{1g}$ | - | - | - | 1.816 | 33 510 | - | 1.814 | 28 952 | 724 | 29 277 | 680 |
| c $B_{2g}$ | - | - | - | 1.817 | 34 159 | - | 1.813 | 30 192 | 709 | 29 546 | 734 |

† All of the electronic transitions have local (L) $[UO_2]^{2+}$ character.
a) Ref. 35; b) Ref. 254; c) Ref. 29, 276

clearly illustrates the different nature of the states. The six lowest-lying excitations up to b $B_{2g}$ that arise from the uranyl $^3\Phi$ and $^1\Phi$ states remain close in energy, indicating only a modest perturbation by the chloride ions. The calculated bond lengths are 0.04 Å shorter than the SOC-CASPT2 values, but agree well with the SOC-CI values of Matisika and Pitzer [254]. The first excited-state curve (a $E_g$) crosses the second excited curve (a $B_{1g}$) at *approximately* 1.84 Å. This crossing was also observed in a SOC-CASPT2 study (Fig. 2 in Ref. 35) at about 0.02 Å to the right of the minimum with the only difference being that a second excited state of $B_{2g}$ character was obtained. The CAM-B3LYP incorrectly predicts the first $B_{1g}$ excited state below the first $B_{2g}$ state with respect to SOC-CASPT2, SOC-CI and experimental data.

All the bands in this region of the spectrum represent pure internal uranyl transitions and are characteristic for uranyl compounds (excitations from the lowest occupied $\sigma$ orbitals to the non-bonding $f_\phi$ and $f_\delta$ orbitals of the uranium VI ion) [5, 35, 36, 96, 97, 126].

The second part of the spectrum is separated from the first one by *approximately* 4 000 $cm^{-1}$, which agrees very well with experimental data [29]. Apart from the c $E_g$ state, these $\Delta$ states have a slightly longer U–O bond length of up to 1.814 Å (c $B_{1g}$). Similar observation can be made in the SOC-CASPT2 and SOC-CI studies (see Table (10.4)), although the former predicts somewhat longer bond lengths, while for the latter shorter bond distances are observed in general.

The overall agreement between CAM-B3LYP and SOC-CI is very good in terms of U–O bond distances. Nevertheless, the obtained bond lengths are 0.03–0.04 Å lower than those of SOC-CASPT2, which should account for a more complete description of dynamical correlation. Both correlated methods yield local excitation energies that are about 1 500 $cm^{-1}$ higher than the CAM-B3LYP values and represent an excellent match to experiment. This indicates that CAM-B3LYP systematically underestimates the local transitions, but is capable of predicting the correct ordering of the high-lying states.

The good quality of the CAM-B3LYP functional is also confirmed by the vibrational frequencies listed in Table (10.4). The calculated numerical vibrational frequencies agree well with the SOC-CASPT2 results and significantly outperform those of SOC-CI. The CAM-B3LYP vibrational spectra differs from the experimental one by only 20 $cm^{-1}$ in the lower spectral region, while for the higher-lying states the discrepancy increases up to 40 $cm^{-1}$.

## 10.5 Conclusions

We have investigated the local and charge-transfer states of the uranyl tetrachloride complex with three different exchange–correlation functionals (BLYP, B3LYP and CAM-B3LYP). In order to characterize the states, we have implemented and applied the overlap diagnostic test of Peach *et al.* [272] in a four-component relativistic framework to verify whether this tool can provide an adequate identification of the character of the states.

Our studies indicate that the GGA BLYP is not able to reproduce the electronic spectra of this complex. Already for excitations local to uranyl, qualitative differences to reference data can be observed, while the errors amount to more than 10 000 $cm^{-1}$ when considering CT excitations from the ligands. These errors are alleviated by the use of the global hybrid B3LYP, but at the same time, leaving the ligand to metal CT states quantitatively incorrect. Furthermore, B3LYP can be used for a qualitative estimate of the lower electronic transitions, while the more refined CAM-B3LYP functional is certainly preferable for a quantitative investigation of the electronic spectrum. The accuracy of four-component TD-DFT using the CAM-B3LYP functional approaches that of SOC-CASPT2 and SOC-CI. In our current implementation of the four-component TD-DFT method we can treat rather large systems (up to about 40 atoms or 300 electrons) and still larger systems are easily accessible by applying a two-component approach to treat relativity. More importantly, the TD-DFT method employing CAM-B3LYP also provides access to a spectral region that is dominated by CT states, which are difficult to treat within active space methods since the required size of the active space would become prohibitively large.

We conclude that the overlap diagnostic method represents an useful tool in identifying CT states. However, more experience with its applications to actinide-containing complexes is necessary since the presence of electronically different internal states, i.e., inside the actinyl ion, restricts the range of diagnostic values to lower values that are common for lighter elements. The error for these kinds of transitions can be partly traced back to rather different orbitals which are chemically active in the actinide atoms, leading to large differences in exchange interactions already for atomic transitions.

# 11

# The Electronic Spectrum of $CUONg_4$ (Ng = Ne, Ar, Kr, Xe): New Insights in the Interaction of the CUO Molecule with Noble Gas Matrices

> The most beautiful thing we can experience is the mysterious. It is the source of all true art and science.
>
> Albert Einstein

Adopted from:
Tecmer, P., van Lingen, H. J., Gomes, A. S. P., Visscher, L., accepted for publication in *J. Chem. Phys.*.

## 11.1 Abstract

The electronic spectrum of the CUO molecule was investigated with the IHFSCC-SD (intermediate Hamiltonian Fock-space coupled cluster with singles and doubles) method and with TD-DFT (time-dependent density functional theory) employing the PBE and PBE0 exchange–correlation functionals. The importance of both spin–orbit coupling and correlation effects on the low-lying excited-states of this molecule are analyzed and discussed.

Noble gas matrix effects on the energy ordering and vibrational frequencies of the lowest electronic states of the CUO molecule were investigated with density functional theory (DFT) and TD-DFT in a supermolecular as well as a frozen density embedding (FDE) subsystem approach. This data is used to test the suitability of the FDE approach to model the influence of different matrices on

the vertical electronic transitions of this molecule. The most suitable potential was chosen to perform relativistic WFT-in-DFT (wave function theory in density functional theory) calculations to study the vertical electronic spectra of the CUO and $CUONg_4$ with IHFSCC-SD method.

## 11.2 Introduction

The chemistry of uranium remains fascinating and challenging, with implications that go beyond the use of fissionable $^{235}U$ in nuclear energy, with *e.g.* a growing interest in possible applications in catalysis [20, 251]. This is due to uraniums wide range of oxidation states (+6, +5, +4 and +3) and coordination geometries [5, 15, 198, 256]. These features arise from the availability of the spatially rather different $5f$-, $6d$-, $7s$- and $7p$-orbitals that are energetically close and do participate in the chemical bonding.

Many uranium complexes contain the uranyl ($UO_2^{2+}$) species, perhaps the best studied of its molecular oxides due to its predominance in the aqueous chemistry of uranium. For this ion (but also for non-oxide isoelectronic species such as NUN) the uranium metal center forms strong triple bonds with the axial ligands [5, 23, 25, 27, 203, 205, 254, 280]. The high stability and linear structure of these U(VI) species is well explained by the "pushing from below" model proposed by Tatsumi and Hoffmann [229]. In the linear structure the strong interaction between the semicore uranium $6p$-orbitals and the oxygen $2p$-orbitals brings the energy of the $\sigma_u$ HOMO (highest occupied molecular orbital) close to that of the $5f$-orbitals of the uranium leading to a significant $5f$ participation in this orbital [281]. The accompanying lowering of the energy leaves a large HOMO-LUMO gap for the cation, making uranyl an archetypical closed-shell species. For other isoelectronic species such as $NUO^+$ or CUO the picture is slightly different since the bonds are not equal, even though both can still be regarded as triple bonds. To the diminishing electronegativity of N and C with respect to O there corresponds a decreasing HOMO-LUMO gap, as seen in various theoretical studies [28, 280] as a marked decrease of ionization potentials and the lowest electronic excitation energies on going from $UO_2^{2+}$ to NUN, $NUO^+$ and up to CUO [96].

For CUO in particular, the HOMO has a predominantly U–C bonding character with the UO bond lying at significantly lower energy [28]. Moreover, a point is reached where low-lying triplet excited states are so close to the ground state that some theoretical approaches predict them to be the electronic ground state [27, 28]. This suggests that even weakly bound equatorial ligands can play an important role in establishing the precise ordering of states in the lower part of the spectrum.

This agrees with the findings in the extensive experimental studies of CUO trapped in noble gas matrices that spurred the interest of theoreticians in this molecule. Tague *et al.* [282] excited uranium atoms in excess of CO by laser ablation and found that uranium can insert in the triple CO bond and form the CUO molecule. The experimentally measured U–C and U–O stretching vibrations are 853 $cm^{-1}$ and 804 $cm^{-1}$ in an argon matrix, but when the same experiment was carried out by Zhou *et al.* [31] in a solid neon matrix, they found the U–C and U–O frequencies at 1047 $cm^{-1}$ and 872 $cm^{-1}$. Later on, a similar experiment was carried out for krypton and xenon matrices as well. Again, a large red shift ($\approx$70 and $\approx$200 $cm^{-1}$ for the U–O and U–C stretching modes, respectively) was observed, relative to the data obtained in the neon matrix [26, 283, 284]. This large red shift in the vibrational spectra suggest that the ground state of CUO depends on the noble gas environment, with the weakly interacting neon atoms the system favors a singlet ground state while the stronger interaction in the heavier noble gas matrices, *i.e.*, argon, krypton or xenon [9, 284, 285], produces a triplet ground state in which also a nonbonding uranium $5f_\phi$ or $5f_\delta$ is occupied (or a mixture thereof if spin–orbit coupling is accounted for [28]). Direct validation for this hypothesis could come from electronic spectroscopy on CUO in these matrices. Such data is available for other uranium compounds [286, 287] in noble gas matrices, but to the best of our knowledge CUO has not yet been studied in this manner. One thus has to rely on theoretical predictions for the electronic spectra. In the theoretical treatment one needs to accurately describe not only electron correlation but also, because of the heavy atoms involved (U, Xe), both scalar and spin–orbit relativistic effects.

These requirements pose significant challenges [170] to calculations, especially because the electronic states may have a marked multi-reference character. Suitable methodologies are, for instance, the relativistic formulations [136, 138, 139] of the Fock-space coupled cluster singles and doubles (FSCC-SD [101, 121, 141]) method, or the spin–orbit complete active space second-order perturbation theory (SO-CASPT2 [103, 104]). The recent work of Infante *et al.* [288], who employed the spin–orbit coupling restricted active space second order perturbation (SOC-RASPT2 [289]) method to investigate the $UO_2Ar_4$ species, can be considered to be at the limit of what is currently feasible employing wave function based approaches. Since the CUO species has less symmetry, an all-atom treatment is still out of reach. The Fock-space based approaches are less affected by active space limitations, but are computationally more expensive than the PT2 ones and at present are also not able to tackle a full seven atom model (both experimental and theoretical studies suggest coordination of four noble gas atoms in the equatorial plane perpendicular to the CUO unit [9, 284, 285]).

This leaves as alternative the use of so-called embedding approaches in which interactions from the environment are modeled in a simplified manner [122]. Since both the molecule of interest and the environment consist of neutral molecules, and because the dipole moments of the two states of interest of CUO do not differ much (3.5 Debye in the singlet state and 2.4 Debye in the excited triplet state[26]), the most important factor is probably a combination of Pauli repulsion and weak coordination from the equatorial ligands. Most embedding methods are not able to capture such subtle effects as they are usually designed to describe primarily electrostatic interactions. A method that should in principle be able to capture both Pauli repulsion and (to lesser extent) weak coordination bonds is the so-called WFT-in-DFT embedding, first proposed by Carter and coworkers [158–160], for studying the electronic spectra of impurities on solids and surfaces [290, 291]. In this method, one divides the system of interest in an active part (for which the spectra are to be calculated with a given wave function method) and an environment that is described by DFT. This type of approach has been applied successfully in describing the effect of chloride-actinyl interactions on the $f$-$f$ spectra of the $NpO_2^{2+}$ cation [161]. The WFT-in-DFT FDE scheme is theoretically well-defined and suitable for extension to coupled subsystems [292] and can provide an enormous reduction of both computational cost and the complexity of the data that is to be analyzed. We therefore think it is of interest to use the CUO noble gas interaction as another test case for the feasibility of the approach in describing uranium coordination chemistry. As we will use the method in its uncoupled formulation, we need to ascertain that there is no coupling between the electronic excitations on CUO with those of the environment [149], something that can be explored at DFT level. In addition, we will use a monomer expansion of the wave function which will also limit the possibilities to describe donation from the noble gas orbitals into the CUO orbitals. This system therefore constitutes a stringent test for the applicability of this simplest form of WFT-in-DFT embedding, but one in which there is a fair chance of success given the fact that DFT-in-DFT typically works well for such weak interactions [155, 293–297].

In this work our initial goal was to investigate the use of WFT-in-DFT embedding for determining the electronic structure of the model $CUONg_4$ (Ng=Ne, Ar, Kr and Xe) systems, with particular emphasis on the still debated issue of whether or not there is a change in the nature of the ground state (between singlet and triplet) for the different noble gas ligands. While carrying out the TD-DFT calculations that were used to validate the embedding procedure, we obtained new insights in the effect of including exact exchange in the TD-DFT description of this molecule that are worthwhile to report as well. These will be discussed in

section (11.4.1).

## 11.3 Computational Details

Our investigations required three types of calculations: geometry optimization and calculation of vibrational frequencies for the two possible ground-states of the CUO molecule, TD-DFT calculations of the isolated, embedded and supermolecular species, and IHFSCC-SD calculation of the isolated and embedded species. For the latter two we also need to discuss the generation of the embedding potential that was used. We will partition the section on computational details accordingly.

### 11.3.1 Geometry Optimization and Harmonic Frequencies

We performed spin–free DFT geometry optimization and analytical frequency calculations with the TURBOMOLE 5.10 package [298–300] employing the PBE0 exchange–correlation functional [85, 86] in conjunction with the def-TZVP (triple-$\zeta$ valence polarization) basis sets [301]. For the heavy elements (uranium and xenon) small-core effective potentials were utilized [302, 303].

Geometries and structures were obtained for the $^1\Sigma^+$,$^3\Phi$ states of CUO and the $^1A_1(^1\Sigma^+)$ and $^3E(^3\Phi)$ states for the $CUONg_4$ (Ng=Ne, Ar, Kr, Xe) models. All the DFT calculations were performed in $C_{2v}$ point group symmetry with the multiple grid option m5, that is, a coarser grid during SCF iterations and a more precise grid at the final SCF iteration and the gradient evaluation, as implemented in the TURBOMOLE 5.10 program package.

### 11.3.2 Time-Dependent Density Functional Theory and Time-Dependent Hartree–Fock

All–electron spin–free TD-DFT [54, 55] calculations were carried out with the ADF2010 package [208, 209, 304] in the $C_{2v}$ point group symmetry with the PBE [76] and PBE0 [85, 86] exchange–correlation functional and the TZ2P (triple–$\zeta$ double polarization) basis sets from the ADF repository [214]. Scalar relativistic effects were incorporated through the ZORA (zeroth-order regular approximation) Hamiltonian [177]. The spin–free TD-DFT vertical excitation energies were obtained at the optimized geometries within the adiabatic LDA approximation, in which the local (in time and space) functional derivative of the LDA functional is used in the TD-DFT kernel. The exact (not fitted) density was used to evaluate all exchange–correlation contributions, with the numerical integration accuracy option set to a value of 10.

For every molecule we determined the 30 lowest-lying (singlet and triplet) states, which was sufficient to characterize the 22 transitions corresponding to excitations from the $25a_1$ ($f_\sigma\{U\} + p_\sigma\{C\}$) and $12b_1/b_2(f_\pi\{U\})$ orbitals to the $26a_1(f_\sigma\{U\} + s_\sigma\{C\} + p_\sigma\{C\})$, $13b_1/b_2(f_\phi\{U\})$, $27a_1/5a_2(f_\delta\{U\})$ and $28a_1/6a_2(f_\delta\{U\})$ orbitals of the CUO molecule and the same kind of orbitals for the $CUONg_4$ compounds.

In addition we carried out TD-HF calculations with the same basis set and setup as for the TD-DFT runs.

### 11.3.3 Frozen Density Embedding

DFT-in-DFT [146–148, 305, 306] calculations were performed with the ADF2010 [208, 209, 304] package, using a development version of the PYADF [307] scripting framework. The same settings as specified above for the supermolecular Kohn–Sham (KS) runs were employed for the DFT part.

In the FDE setup the total electronic density of the CUO complexes ($CUONg_4$, Ng=Ne, Ar, Kr, Xe) was partitioned into the density of CUO and a $Ng_4$ environment and subsequently updated in 9 freeze-and-thaw cycles [148] to allow for polarization of both the environment and the active system. We utilized the monomolecular basis set expansion, in which only basis functions belonging to the currently active system are used. This expansion introduces an additional approximation with respect to the supermolecular calculations which is typically small for the cases with limited overlap between the embedded subsystem and the environment [154]. Since the PBE0 exchange–correlation functional is orbital-dependent it can not be used to provide an exchange–correlation contribution to the embedding potential. We chose to use the PBE [76] exchange–correlation for this contribution, following earlier work on orbital–dependent functionals [156, 161, 308, 309]. For the kinetic energy component of the embedding potential we tested out a number of different functionals: the Thomas–Fermi (TF) [50, 150, 310] functional, the NDSD functional of Wesołowski and coworkers [311] (which contains a TF component but was developed especially for FDE), the PW91K [153] functional, and PW91K with the long-distance correction proposed by Jacob and Visscher [308] (PW91K-CJCORR). This procedure yielded converged embedding potentials that were subsequently used in WFT-in-DFT calculations as well as DFT-in-DFT calculations to allow for comparison with supermolecular results.

These FDE TD-DFT calculations were carried out in the uncoupled approach [312] in which the response of the environment to the electronic excitation is neglected and in which charge-transfer excitations are not taken into account. The validity of the first approximation was investigated by performing exploratory cal-

culations with the coupled excitation framework of Neugebauer [157] from which we found that these couplings are indeed negligibly small.

### 11.3.4 Wave Function Theory

The WFT-in-DFT calculations were done using the FDE–implementation [161] in the DIRAC10 [275] relativistic quantum chemical package.

The IHFSCC-SD (intermediate Hamiltonian Fock-space coupled cluster with singles and doubles [136, 138, 139]) method with a Dirac–Coulomb (DC) Hamiltonian, where $(SS|SS)$ integrals have been approximated by a point charge model [219], was used. The valence double–$\zeta$ basis set of Dyall [215] (dyall.v2z) for the uranium atom and the augmented correlation consistent polarized valence double–$\zeta$ basis sets of Dunning [216] ( aug-cc-pVDZ) for oxygen and carbon atoms were employed.

In the Fock-space coupled cluster [130, 132] method a diagonalization of an effective Hamiltonian yields amplitudes and eigenvalues of the set of states that is related to a closed-shell reference system (sector $(0h, 0p)$) by electron annihilation $(h)$, creation $(p)$ or both [132–134, 313, 314].

For CUO, the conventional approach would be to obtain the excitation energies that we are interested in by selecting the appropriate active space for a sector $(1h, 1p)$ ("one hole, one particle") calculation of the Fock-space. This procedure does, however, lead to convergence problems while determining the "one particle" (electron affinity or sector $(0h, 1p)$ of Fock-space) amplitudes that are required as input for the sector $(1h, 1p)$ calculation. These problems could be traced back to the presence of a number of low-lying Rydberg orbitals, that appear at lower energies than the local orbitals of interest (*i.e.*, those that are involve in the lowest electronic transitions) in the CUO molecule. These problems with Rydberg orbitals were not encountered in the earlier work of Infante and Visscher [28] due to lack of very diffuse functions in their basis. Since we are now interested in the interaction with the environment, augmented basis sets are clearly preferable, so we needed to find a way around this problem. This can be done by calculating the electronic spectrum via sector $(0h, 2p)$ of Fock-space, *i.e.*, starting from the $CUO^{2+}$ as a reference system and calculating excitation energies as differences between the second electron affinities that are obtained in this sector. With this choice of reference system, the local orbitals are all below the diffuse orbitals and fully converged results can be obtained.

For the systems we investigated, all spinors with energies $\epsilon \in$ [-3.00;80.00] a.u. were correlated, which correspond to 11 occupied (22 electrons) and about 350 virtual spinors. This corresponds to slightly larger active spaces with respect to

**Table 11.1**: *Number of electrons correlated in the CUO and $CUONg_4$ complexes (CUO embedded in the $Ng_4$ potential generated with the PW91K-CJCORR kinetic energy functional) in sector $(0h, 2p)$ of the IHFSCC-SD method. All the virtual orbitals were correlated up to 0.4 au.*

| **System** | inactive occ. | active $P_m$ virt. | active $P_i$ virt. | inactive virt. |
|---|---|---|---|---|
| CUO | 22 | 16 | 100 | 238 |
| $CUONe_4$ | 22 | 18 | 98 | 238 |
| $CUOAr_4$ | 22 | 18 | 94 | 242 |
| $CUOKr_4$ | 22 | 18 | 90 | 246 |
| $CUOXe_4$ | 22 | 18 | 90 | 246 |

those employed in our earlier work on the $UO_2^{2+}$, NUN and $NUO^+$ molecules [96, 126], and significantly enlarged the valence active space in comparison with the previous work of Infante and Visscher [28]. A detailed description of the active spaces for each particular molecule is given in Table (11.1) of the supplementary material.

## 11.4 Results and Discussion

We start with a brief discussion of the electronic structure of the CUO molecule, for which we obtained TD-DFT results with functionals that were not yet applied to this molecule. In order to focus on the essential physical aspects at play, in the discussion that follows we will employ a spin–free model in which the question of ordering of the lowest electronic states reduces to the discussion of a gap between a closed-shell singlet and an open-shell triplet state. We may thereby take over some of the knowledge gained in non-relativistic calculations on light molecules to the current species.

### 11.4.1 Electronic Structure of the CUO Molecule

The relative energies of the singlet $\sigma^2$ and triplet $\sigma^1\phi^1$ states of the CUO compound have been intensively debated for a number of years as the different electronic structure methods that have been used did not give a consistent picture. While disagreeing on the precise energy difference, all methods give qualitatively the same picture with respect to the bond length and vibrational frequency difference between these two states. The $\sigma^1\phi^1$ ($^3\Phi$) state has longer U–O and in particular

U–C bond lengths than the $\sigma^2$ ($^1\Sigma^+$) state. This is easily explained by the transfer of an electron from a bonding U–C orbital to the non-bonding $5f_\phi$-orbital of the uranium atom. Inclusion of spin–orbit coupling (SOC) gives the same qualitative picture with some admixture of the $^3\Delta_2$ state into the lower $^3\Phi_2$ state that lowers this state relative to the $^1\Sigma_0^+$ state which is in first order not affected by SOC.

Roos *et. al* [27] performed CASPT2 calculations with *a posteriori* included SOC and predicted the $^3\Phi_2$ to be the ground state of CUO. Later on, Infante and Visscher [28] applied a relativistic coupled cluster with singles doubles and perturbative triples — CCSD(T) method — as well as the Fock-space coupled cluster with singles and doubles — FSCC-SD — method. They found a strong stabilization of the $^1\Sigma_0^+$ state by the dynamic correlation effects and concluded that this state should be the ground state for an isolated molecule. This supports the explanation that was put forward to explain the experimental findings. Recently Yang *et al.* [280] published SOC configuration interaction with singles and doubles (CISD [279]) calculations that are in qualitative agreement with these coupled cluster results. They determined the$^1\Sigma_0^+$ state to be the lowest state in both $^1\Sigma_0^+$ and $\Phi_2$ optimized geometries. Noticeable is the large discrepancy (amounting to about 1 eV) between the different electronic structure methods employed so far. From the results of Infante and Visscher it appears that adding dynamical correlation, by correlating more electrons or improving the basis set, favors the more compact $^1\Sigma_0^+$ state, thus yielding a larger gap. It is therefore of interest to see what a DFT treatment of electron correlation gives.

Taking the $^1\Sigma_0^+$ as the reference state we chose the DFT-optimized structure of this state, with U–O and U–C bonds of 1.779 and 1.733 Å, respectively, for spin–free vertical excitation calculations. In the following discussion we will focus on excitations from the $\sigma$ (HOMO) orbital to the virtual $\sigma$, $\delta$ and $\phi$ molecular orbitals. These transitions give rise to the $^{1,3}\Sigma$, $^{1,3}\Delta$ and $^{1,3}\Phi$ excited-states. While the $\delta$- and $\phi$-orbitals also play an important role in some molecules isoelectronic to the $UO_2^{2+}$ such as NUN and $NUO^+$, CUO is special in having also a relatively low–lying $\sigma$ virtual orbital. In most studies this orbital has been ignored, but we will see that it can play a role in some of the calculations.

In agreement with ΔSCF calculations with the same functionals that place the $^3\Phi$ below the reference $^1\Sigma^+$ state, TD-DFT calculations with the PBE [76] and PBE0 [85, 86] exchange–correlation functionals indicate a excitation energy for this triplet state. As states with negative excitation energies are not calculated by the standard TD-DFT algorithm [55], we added a very small admixture of Hartree–Fock (HF=0.1%) exchange to the PBE exchange–correlation functional to force the program to use the algorithm for hybrid functionals. As shown in

**Table 11.2**: *Spin–free vertical excited-states of the CUO molecule with respect to the* $^1\Sigma^+$ *ground state (in eV): a comparison of different methods.*

| Symm. | TD-DFT(PBE) | | | TD-HF | CASPT2[a] | CCSD[b] | CCSD(T) | | IHFSCC |
|---|---|---|---|---|---|---|---|---|---|
| | HF=0% | HF=0.1% | HF=25% | | | | Ref. b | Ref. c | |
| $^3\Sigma^+$ | 0.80 | 0.80 | 1.03 | 1.68 | - | - | - | - | 0.88 |
| $^3\Phi$ | - | -0.13 | -0.20 | -0.55 | 0.09 | 0.77 | 0.83 | 0.68 | 1.34 |
| $^3\Delta$ | 0.41 | 0.41 | 0.46 | 2.35 | 0.54 | - | - | - | 1.36 |
| $^1\Sigma^+$ | 1.47 | 1.48 | 1.77 | 2.85 | - | - | - | - | 1.50 |
| $^1\Delta$ | 0.71 | 0.71 | 0.98 | 2.83 | 0.72 | - | - | - | 1.53 |
| $^1\Phi$ | 0.10 | 0.10 | 0.50 | 1.41 | 0.59 | - | - | - | 1.67 |

*a*) Ref. 27; *b*) Ref. 28; *c*) Ref. 316

Table (11.2) this admixture does not affect the energies of remaining states, but indicates a negative singlet-triplet gap of -0.13 eV. As found elsewhere (see *e.g.*, [315] for a recent discussion), such artificially low triplet states are more likely to occur when the fraction of exact exchange is larger. With 25% of exact exchange (the PBE0 exchange–correlation functional) the $^3\Phi$ state lies 0.20 eV below the $^1\Sigma^+$ state and the separation increases to 0.55 eV for the 100% of exact exchange in the TD-HF method. At the same time the exchange splitting between the $^3\Phi$ and $^1\Phi$ increases dramatically from 0.23 eV (PBE) to 1.96 eV (TD-HF). Concerning the trend noted previously in the WFT calculations, in which an improvement of the description of dynamical correlation lowered the $^1\Sigma$ relative to the $^3\Phi$ state, we find qualitative agreement by defining TD-HF as the most uncorrelated method and TD-DFT with PBE as the most correlated method.

For the WFT-based methods we note that the spin–free CASPT2 calculations of Roos *et. al* [27] predict the $^3\Phi$ state slightly above the singlet state by 0.09 eV, but this is not enough for this state to remain the lowest when SOC is accounted for. Since dynamical correlation is only included up to the second-order in perturbation theory, one can again fit these results in a trend leading from HF (predicting the $^3\Phi$ state to be the ground state by 0.5 eV) to the coupled cluster methods that predict a $^1\Sigma_0^+$ ground-state. This trend is even stronger when including our new IHFSCC-SD [136, 138, 139] data that were obtained using a larger basis set and active space than was feasible earlier [28]. From these calculations we obtain the $^3\Phi$ state at even more than 1.3 eV above the closed-shell $^1\Sigma^+$ state, with an open-shell $^3\Sigma^+$ state being the first excited state at 0.88 eV.

We believe that the new DFT and CC results are interesting because they clearly illustrate the difficulties in finding a proper description of the balance between exchange and correlation (in a DFT picture) and static and dynamic correlation (in a WFT picture) for actinides. The model exchange–correlation hole

**Table 11.3**: *Spin–orbit vertical excited-states of the CUO molecule with respect to the* $^1\Sigma_0^+$ *ground state (in eV): a comparison of different methods.*

| State† | IHFSCC-SD(*22e*) | CCSD(T)(*34e*)[a] | CASPT2(*12e*)[b] | SO-CISD(*24e*)[c] |
|---|---|---|---|---|
| $^3\Sigma_1^+$ | 0.81 | - | - | - |
| $^3\Phi_2$ | 0.94 | 0.60 | -0.36 | 0.30 |
| $^3\Phi_3$ | 1.01 | - | -0.15 | 0.57 |
| $^3\Delta_1$ | 1.22 | - | 0.19 | 0.58 |
| $^3\Delta_2$ | 1.28 | - | 0.31 | - |

† - subscripts denote Ω-values and upperscripts spin multiplicity;

a) Ref. 28; b) Ref. 27; c) Ref. 280

used in the DFT approach will have to provide an equally good description of the strong angular correlation found in the radially localized $\phi$-orbitals as well as for the qualitatively different correlation in the $\sigma$ bonding orbital. This is difficult to achieve on basis of information from only the electron density and its gradient, while adding exchange in a hybrid approach has a limited value as this brings along the large error in the HF description. For the WFT methods the challenge is equally large as an electron in the $\phi$-orbital will have a stronger interaction with the semicore electrons than an electron in a more extended $\sigma$-orbital, requiring a well-balanced basis set and a substantial number of electrons to be correlated. We plan to study these aspects in more detail in another publication.

Coming back to the main topic of this paper, we also analyzed the influence of the spin–orbit coupling on the transitions. The results are listed in Table (11.3) in which we kept the major LS-designation but added the Ω values, which is the only proper quantum number after inclusion of SOC. Besides the relativistic splitting of all the triplet states, there is no qualitative difference with the spin–free transition energies.

### 11.4.2 The CUONg$_4$ Models.

In this section we investigate how the interaction with the environment affects the lowest electronic states. We focus on the $^1\Sigma^+$ and $^3\Phi$ states, but also consider the fate of the $^3\Sigma^+$ state when the system is confined in a matrix.

#### 11.4.2.1 Geometries and Vibrational Frequencies

Table (11.4) lists all the geometries and vibrational frequencies obtained in this work. We observe a slight increase of the U–C and U–O bond distances due to the environment that becomes stronger when we attach heavier, more polarizable, noble gas (Ng) atoms. The four attached noble gas atoms move slightly out of the equatorial plane with a C–U–Ng angle slightly larger than 90° in the singlet states and slightly smaller than 90° in the triplet states of the $CUOXe_4$ complex.

The weakening of the U–C and (to less extent) U–O bond in the triplet state is most clearly visible in the U–C and U–O stretch vibrations. For the bare molecule the U–C stretch is lower by 227 $cm^{-1}$ in the triplet state than in the singlet state. Compared to this difference the matrix effects are much weaker with a shift of 31 (48) $cm^{-1}$ of the U–C stretch for the singlet (triplet) state in the model for the xenon matrix. The experimentally observed shift of 238 $cm^{-1}$ of the U–C stretch upon going from neon to argon does therefore best match with the 195 $cm^{-1}$ difference between the vibration of the singlet state in the neon model and the triplet state in the argon model. This is already discussed in detail by Andrews and coworkers [284] who obtained slightly different values but a qualitatively similar trend with the PW91 functional. The new data with hybrid functionals provides further support for their interpretation. Note that only trends can be reliably compared, for a more complete comparison with the experimental values it might be necessary to include more than just four noble gases around the CUO to model the matrix. Moreover, it might be necessary to consider also anharmonic effects [318].

#### 11.4.2.2 Ground-State DFT Study.

To simplify the comparison between the CUO and $CUONg_4$ complexes, we will use (idealized) $C_{4v}$ point group symbols, with in parenthesis the $C_{\infty v}$ designations to indicate the parentage of the states or orbitals. We define the zero of our energy scale as the $^1A_1(^1\Sigma^+)$ state of CUO with a cage of four Ng atoms at infinite distance and plot in Figure (11.1) the variation of the binding energy of the $^1A_1(^1\Sigma^+)$ and the $^3E(^3\Phi)$ states as a function of Ng type. This interaction with the cage is indeed slightly more pronounced in the triplet state with the largest difference occurring when moving from neon to argon, but the difference is only 0.04 eV. This can only change the order of two states if they are already very nearly degenerate. As discussed already in the section of TD-DFT, the PBE0 functional places the triplet slightly below the singlet already for the bare CUO

**Table 11.4**: *Optimized structures and vibrational spectra calculated using DFT with PBE0 exchange–correlation functional in the $C_{2v}$ point group symmetry. Bond distances are given in Å, angles in degrees and frequencies in $cm^{-1}$. Reference theoretical studies are presented in round brackets and experimental data in square brackets.*

| System | d(U–C) | d(U–O) | d(U–Ng) | CUNg | $\nu_{UC}$ | $\nu_{UO}$ |
|---|---|---|---|---|---|---|
| $CUO(^1\Sigma^+)$ | 1.733(1.714[a],1.770[b],1.757[d],1.738[f]) | 1.779(1.759[a], 1.795[b],1.798[d],1.785[f]) | | | 1175(1269[a],1089[d],1183[e],1182[f]) | 927(960[a],870[d],917[e],922[f]) |
| $CUONe_4(^1\Sigma^+)$ | 1.734(1.769[d]) | 1.782(1.805[d]) | 3.315 | 99.7 | 1170(983[d])[1047[d]] | 923(847[d])[872[d]] |
| $CUOAr_4(^1\Sigma^+)$ | 1.738(1.774[d]) | 1.788(1.811[d]) | 3.416 | 95.8 | 1156(963[d]) | 913(840[d]) |
| $CUOKr_4(^1\Sigma^+)$ | 1.741(1.775[d]) | 1.790(1.812[d]) | 3.455 | 94.5 | 1145(947[d]) | 908(839[d]) |
| $CUOXe_4(^1\Sigma^+)$ | 1.747(1.782[d]) | 1.793(1.813[d]) | 3.554 | 92.4 | 1127(942[d]) | 901(839[d]) |
| $CUO(^3\Phi)$ | 1.836(1.814[a], 1.871[b],1.857[d]) | 1.808(1.789[a], 1.818[b],1.825[d]) | | | 948(893[d]) | 879(828[d]) |
| $CUONe_4(^3\Phi)$ | 1.840(1.862[d]) | 1.811(1.828[d]) | 3.147 | 91.7 | 942(884[d]) | 872(819[d]) |
| $CUOAr_4(^3\Phi)$ | 1.845(1.868[c],1.871[d]) | 1.815(1.843[c],1.833[d]) | 3.309 | 90.4 | 932(881[c],869[d])[835[c],853[d]] | 868(824[c],814[d])[793[c],804[d]] |
| $CUOKr_4(^3\Phi)$ | 1.848(1.873[c],1.874[d]) | 1.817(1.839[c],1.835[d]) | 3.374 | 89.9 | 926(876[c],864[d])[832[c],842[d]] | 864(822[c],810[d])[790[c],797[d]] |
| $CUOXe_4(^3\Phi)$ | 1.853(1.875[c],1.879[d]) | 1.818(1.833[c],1.836[d]) | 3.514 | 88.6 | 917(870[c],860[d])[830[c]] | 860(819[c],808[d])[789[c]] |

a) MRSOCISD Ref. 280; b) SO-CASPT2 Ref. 27; c) DFT/PW91 Ref. 284; d) DFT/PW91 Ref. 9;
e) DFT/PBE0 Ref. 317; f) DFT/PBE0 Ref. 318; g) Ref. 26

molecule and considering optimized structures for the triplet state reinforces that conclusion.

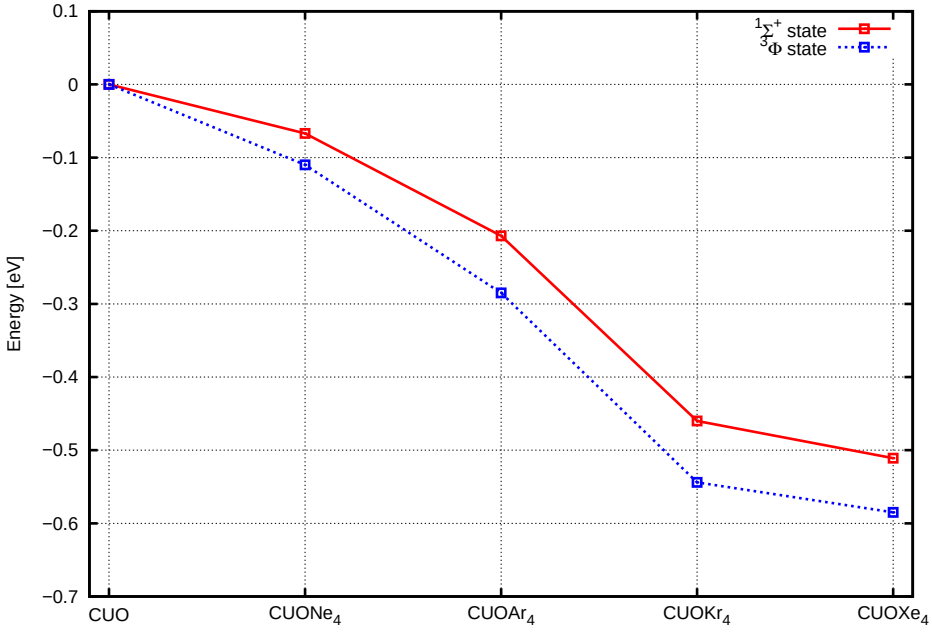


**Figure 11.1**: *Total bonding energies of the $CUONg_4$ complexes w.r.t. to the $^1\Sigma^+$ (solid line) and $^3\Phi$ (dashed line) states of the CUO system (DFT calculations in ADF).*

#### 11.4.2.3 Excitation Energies from TD-DFT

To understand the trends in excitation energies, it is instructive to look at the changes in the valence orbital energies of CUO induced by the attachment of the Ng atoms. We consider the closed-shell singlet calculation in which we have as HOMO a bonding U–C $\sigma$-orbital, as LUMO a nonbonding $\sigma$-orbital, and at higher energy a $\phi$- and two $\delta$-orbitals. These orbitals are depicted in Figure (11.2). When adding the Ng atoms the two $\delta$-orbitals are split by the ligand field into $27a_1$ and $5a_2$, and the $28a_1$ and $6a_2$ orbitals, respectively. In Figure (11.3)(a) we plot the energy difference of all relevant virtual orbitals relative to the HOMO to get a first indication of the effect of the environment on excitation energies. The diffuse non-bonding $\sigma$-orbital, which is the LUMO in bare CUO and $CUONe_4$, is pushed up by the repulsive interaction with the closed-shell ligands and rises in the argon system above the $\phi$-orbitals, and in krypton and xenon also above the lower $\delta$-orbital $27a_1$. This indicates that this orbital is indeed of less interest in explaining the electronic structure of the molecule in the matrix.

**Figure 11.2**: *$CUONe_4$ orbitals involved in the lowest-lying electronic transitions visualized with an isosurface value of 0.03 in the ADFGUI [319].*

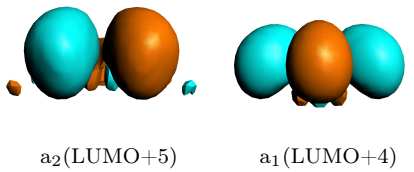

$a_2$(LUMO+5) $a_1$(LUMO+4)

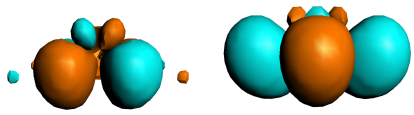

$a_2$(LUMO+3) $a_1$(LUMO+2)

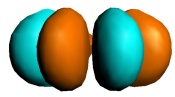

e(LUMO+1)

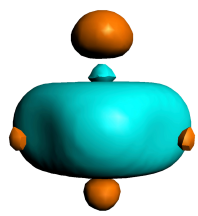

$a_1$(LUMO)

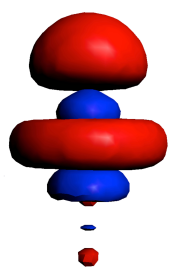

$a_1$(HOMO)

**Figure 11.3**: *Lowest-lying valence orbital energies of the CUO ($^1\Sigma^+$) and the $CUONg_4$($^1A_1$) complexes from the supermolecular and DFT-in-DFT/PBE0 calculations using different kinetic energy functionals in ADF. Orbital energies are given relative to the energy of HOMO for all the compounds.*

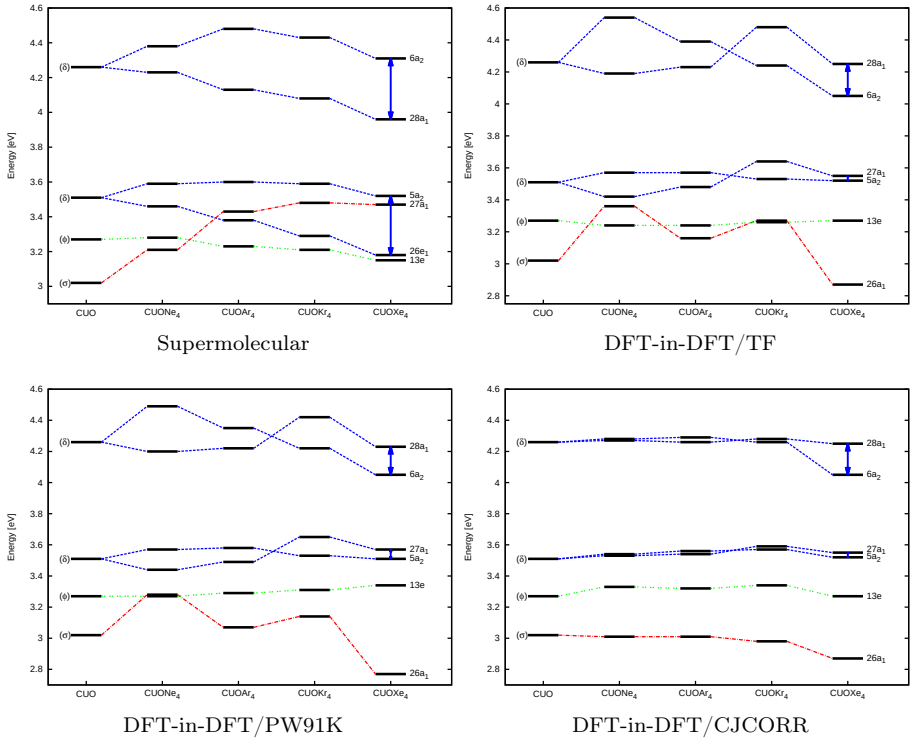


Spin–free excitation energies are listed in Table (11.5), with the negative transition energies indicating a triplet ground-state. In agreement with the ΔSCF calculations, we find small effects on the transition energies, except for the large effect on the b $^3A_1(^1\Sigma^+)$ and d $^1A_1(^3\Sigma^+)$ states that correspond to excitation to the diffuse $\sigma$-orbital. These transitions rapidly shift to higher energies when adding the noble gas cage. Other changes in the electronic spectrum introduced by the noble gas environment are relatively small for the lowest-lying excitations (difference less than 0.1 eV, see Figure (11.4)). Those results are shown in supermolecular case, where the differences in the electronic transitions between the bare CUO and the $CUONg_4$ complexes are plotted. We note a relatively large difference between the Ne and Ar cage, but as already seen in the orbital energy differences, an overall surprisingly small effect of the matrix given the experimental findings.

**Table 11.5**: *Spin-free vertical excitation energies of the CUO($^1\Sigma^+$) and CUONg$_4$($^1A_1$) from the KS/TD-DFT/PBE0 approach (in eV).*

| **Symmetry**† | CUO | $CUONe_4$ | $CUOAr_4$ | $CUOKr_4$ | $CUOXe_4$ |
|---|---|---|---|---|---|
| $a^3E$ ($^3\Phi$) | -0.204 | -0.222 | -0.233 | -0.253 | -0.231 |
| $a^3A_1$ ($^3\Delta$) | 0.464 | 0.431 | 0.384 | 0.211 | 0.368 |
| $a^3A_2$ ($^3\Delta$) | 0.464 | 0.440 | 0.399 | 0.259 | 0.385 |
| $a^1E$ ($^1\Phi$) | 0.504 | 0.472 | 0.434 | 0.333 | 0.411 |
| $a^1A_1$ ($^1\Delta$) | 0.983 | 0.951 | 0.915 | 0.839 | 0.891 |
| $a^1A_2$ ($^1\Delta$) | 0.983 | 0.978 | 0.960 | 0.892 | 0.949 |
| $b^3A_1$ ($^3\Sigma^+$) | 1.029 | 1.245 | 1.598 | 1.930 | 1.826 |
| $c^3A_1$ ($^3\Gamma$) | 1.317 | 1.289 | 1.274 | 1.234 | 1.281 |
| $b^3A_2$ ($^3\Gamma$) | 1.317 | 1.289 | 1.275 | 1.236 | 1.284 |
| $d^3A_1$ ($^3\Delta$) | 1.324 | 1.296 | 1.281 | 1.245 | 1.289 |
| $c^3A_2$ ($^3\Delta$) | 1.324 | 1.296 | 1.281 | 1.243 | 1.289 |
| $b^1A_1$ ($^1\Gamma$) | 1.484 | 1.455 | 1.438 | 1.405 | 1.441 |
| $b^1A_2$ ($^1\Gamma$) | 1.484 | 1.455 | 1.438 | 1.404 | 1.440 |
| $c^1A_1$ ($^1\Delta$) | 1.726 | 1.693 | 1.666 | 1.653 | 1.620 |
| $c^1A_2$ ($^1\Delta$) | 1.726 | 1.710 | 1.698 | 1.671 | 1.692 |
| $b^3E$ ($^3\Phi$) | 1.773 | 1.748 | 1.736 | 1.698 | 1.745 |
| $c^3E$ ($^3\Phi$) | 1.775 | 1.765 | 1.761 | 1.737 | 1.773 |
| $d^1A_1$ ($^1\Sigma^+$) | 1.771 | 1.938 | 2.156 | 2.323 | 2.248 |

† We use the $C_{4v}$ point group symmetry annotation with $C_{\infty v}$ irreps indicated in parenthesis.

### 11.4.3 DFT-in-DFT Electronic Structure of the CUONg$_4$ Compounds.

#### 11.4.3.1 The Quality of Embedding Potential

We now investigate whether to represent the subtle effect on the environment can be represented by an FDE embedding potential. Two criteria may be used to quantify the quality of the FDE-approach: 1) the reproduction of the ground-state density of the complex and 2) the error in the calculated transition energies. These errors can be evaluated exactly in DFT and are supposed to carry over to the WFT description.

To assess the first error we compare the electron density calculated within the DFT-in-DFT framework to the supermolecular density. This criterium tests the accuracy of the approximation used for the non-additive parts of the kinetic energy and exchange–correlation functionals. For the latter we restrict ourselves to the PBE functional to remain as close as possible to the PBE0 hybrid functional used in the supermolecular calculation. For the repulsive kinetic energy contribution

**Figure 11.4**: *Influence of noble gas environment on the electronic transitions of the* $CUONg_4(^1A_1)$ *compounds from the KS/DFT/PBE0 calculations in ADF.*

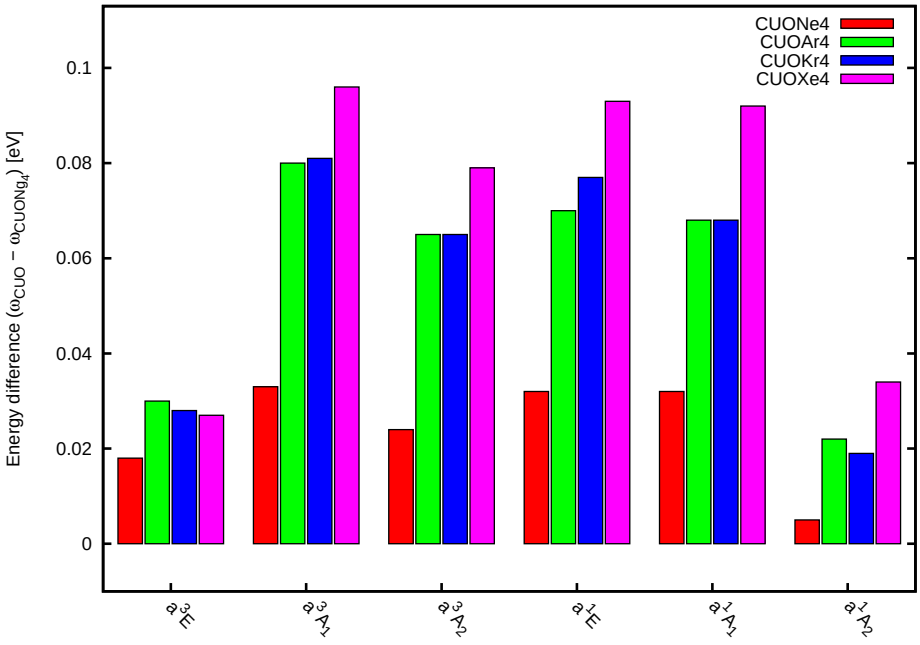


to the embedding potential that models the Pauli repulsion of the Ng cage, we used the simplest local TF [50, 150, 310] and the often more robust [154] gradient-corrected functional PW91K [153]. Since underestimation of the Pauli repulsion may give rise to unphysical transfer of electron density from the active center to the environment subsystem — the so-called "electron leak" problem [295, 308, 320], we also considered the NDSD [311] functional and the zero-overlap correction of Jacob and Visscher [308] that eliminate such problems. We used the error measures defined by Bernard *et al.* [321]: integrated absolute errors in the electron density, the integrated root mean square errors in the electron density and the magnitude of the errors in the dipole moment. While the former two strictly depend on the absolute size of the error in the electron density, the latter also provides information on its spatial redistribution. The size of the errors is taken relative to the sum-of-fragment density obtained by simply superimposing the density of the cage and the density of the bare CUO molecule.

The simple TF potential provides a reasonable description and has even the smallest errors measures for the complex with xenon (see Table (11.6)). For the neon cage PW91K provides the best description, while for the other two cases, argon and krypton, no unambiguously best functional can be selected. In correct-

**Table 11.6**: *Integrated errors in the electron density: $\Delta^{abs}$ (absolute) and $\Delta^{rms}$(root mean square), magnitude of the error in the dipole moment $|\Delta_\mu|$ for the sum of fragments and the DFT-in-DFT/PBE0 calculations with a different approximate non-additive kinetic energy functionals. The most accurate values are marked in boldface.*

| **System** | | $\Delta^{abs} \times 10^{-3}$ | $\Delta^{rms} \times 10^{-3}$ | $\|\Delta_\mu\|$(D) |
|---|---|---|---|---|
| $^1CUONe_4$ | Sum of fragments | 1.35 | 0.99 | 0.183 |
| | FDE (TF) | 4.57 | 0.03 | 0.029 |
| | FDE (NDSD) | 4.84 | 0.03 | 0.033 |
| | FDE (PW91K) | **2.32** | **0.02** | **0.010** |
| | FDE (PW91K-CJCORR) | 6.23 | 0.04 | 0.171 |
| $^1CUOAr_4$ | Sum of fragments | 2.76 | 1.39 | 0.354 |
| | FDE (TF) | 1.42 | 1.39 | 0.146 |
| | FDE (NDSD) | 1.40 | **0.06** | **0.139** |
| | FDE (PW91K) | **1.39** | 0.07 | 0.261 |
| | FDE (PW91K-CJCORR) | 1.66 | 0.09 | 0.370 |
| $^1CUOKr_4$ | Sum of fragments | 2.71 | 1.23 | 0.225 |
| | FDE (TF) | 1.08 | **0.06** | **0.089** |
| | FDE (NDSD) | 1.10 | 0.06 | 0.115 |
| | FDE (PW91K) | **1.03** | 0.06 | 0.188 |
| | FDE (PW91K-CJCORR) | 1.33 | 0.85 | 0.348 |
| $^1CUOXe_4$ | Sum of fragments | 2.27 | 0.11 | 0.205 |
| | FDE (TF) | **1.36** | **0.07** | **0.178** |
| | FDE (NDSD) | 1.41 | 0.07 | 0.222 |
| | FDE (PW91K) | 1.40 | 0.08 | 0.302 |
| | FDE (PW91K-CJCORR) | 1.40 | 0.08 | 0.307 |

ing for charge-leak artifacts, the Jacob and Visscher [308] correction reduces the embedding potential too much, underestimating the interaction between CUO and the cage. This can have an adverse effect on the dipole moment, when compared to its parent functional, PW91K. For the NDSD [311] kinetic energy functional that is based on the TF functional we see an improvement relative to TF for the Ar and Kr complexes but a slightly worse performance for the Ne and Xe complexes.

The best overall performance for the two cases that are of most interest, neon and argon, is therefore obtained with the PW91K kinetic energy functional. More interesting than these errors in the density is, however, the effect on the valence orbital energies of the DFT-in-DFT $CUONg_4$ complexes. These results are indicative of the errors that can be expected in the supermolecular spectra. This data are given in Figures (11.3)(b)–(11.3)(d) . From the figures we observe that the effect of the cage is generally underestimated by the FDE approach: while in

KS/DFT the $26a_1$ orbital is the LUMO only for the CUO and $CUONe_4$ molecules, with FDE it is *e.g.*, always found as LUMO for $CUOXe_4$. Even more troublesome is the fact that the order of the $26a_1$ and $13b_1/b_2$ orbitals is reversed (crossing of the blue dashed lines between Ar and Kr) for the heavier noble gas cages. To check whether these artifacts are due to the freeze-and-thaw procedure we also did some test calculations in which the density of unperturbed Ng atoms was used to represent the density of the cage, but this gave the same picture.

More insight can be obtained by analyzing the three separate components of the potential: the electrostatic (Coulomb and nuclear), and the non-additive exchange–correlation and kinetic energy components. In Figures (11.5)–(11.6) these are plotted along the Ne–U–Ne and Ar–U–Ar lines in an idealized geometry

**Figure 11.5**: *Contributions to the total embedding potential from the electrostatic, non-additive exchange–correlation and non-additive kinetic energy — TF to the left and NDSD to the right — components along the Ng–U–Ng axis in the* $CUONg_4(^1A_1)$ *complexes (in hartree).*

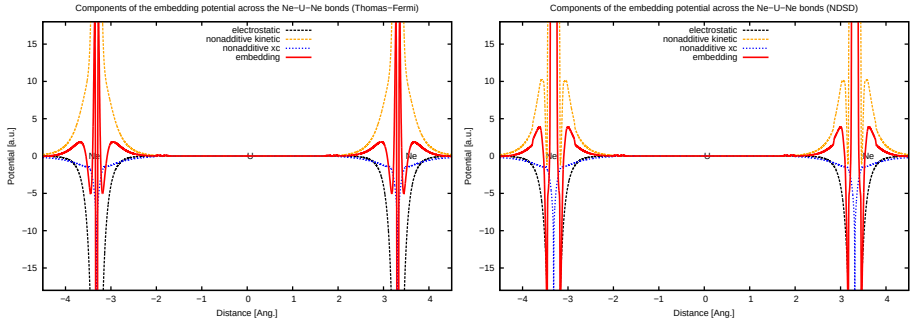


$CUONe_4$ molecule, TF $CUONe_4$ molecule, NDSD

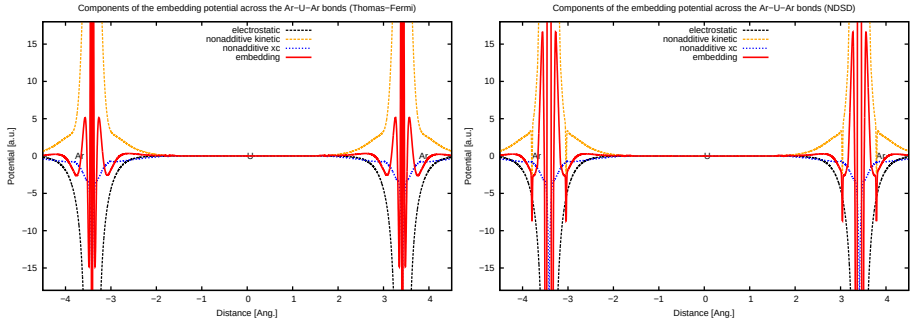


$CUOAr_4$ molecule, TF $CUOAr_4$ molecule, NDSD

(with the Ng all exactly in the equatorial plane). In all pictures we see that it is the balance between the large attractive electrostatic and the repulsive kinetic energy

**Figure 11.6**: *Contributions to the total embedding potential from the electrostatic, non-additive exchange–correlation and non-additive kinetic energy — PW91K to the left and PW91K-CJCORR to the right — components along the Ng–U–Ng axis in the $CUONg_4(^1A_1)$ complexes (in hartree).*

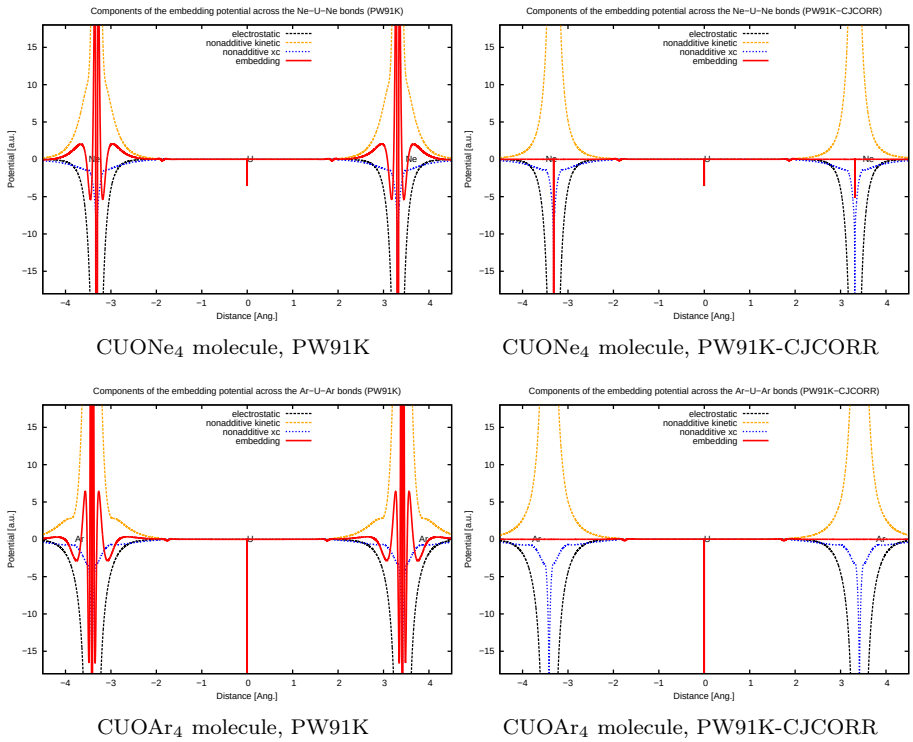


$CUONe_4$ molecule, PW91K

$CUONe_4$ molecule, PW91K-CJCORR

$CUOAr_4$ molecule, PW91K

$CUOAr_4$ molecule, PW91K-CJCORR

components that determines the potential. This balance is more difficult to obtain when the electrostatic terms become larger, as is the case for the heavier Ng atoms. The exact potential should furthermore reflect the shell structure of the atoms that also becomes more pronounced for the heavier atoms. For the uncorrected TF and PW91K potentials the shell structure mainly arises from the compensation of the monotonously negative Coulomb potential by the monotonously positive kinetic energy component, while for the NDSD approach the switching function that is used to interpolate between two functional forms also introduces oscillations in the kinetic energy component for the heavier Ng atoms. The Jacob and Visscher correction [308] operates on the full potential and reduces this in the vicinity of the nuclei to obey an exact limit for non-overlapping systems. For the current system this leads to an almost complete reduction of the potential which explains the too small orbital energy shifts for this approach.

#### 11.4.3.2 Excitation Energies from Embedded TD-DFT

As the goal of the embedding approach is to reproduce the supermolecular approach, that is the data in Table (11.5), we directly compare the DFT-in-DFT to the reference supermolecular excitation energies in Figure (11.7). As was expected

**Figure 11.7**: *Accuracy of different approximate non-additive kinetic energy functionals on the spin–free vertical electronic spectra of the $CUONg_4$ ($^1A_1$) complexes with respect to the supermolecular (KS/TD-DFT/PBE0) reference data (in eV). Red bars correspond to $CUONe_4$, green to $CUOAr_4$, blue to $CUOKr_4$ and violet to $CUOXe_4$ complexes.*

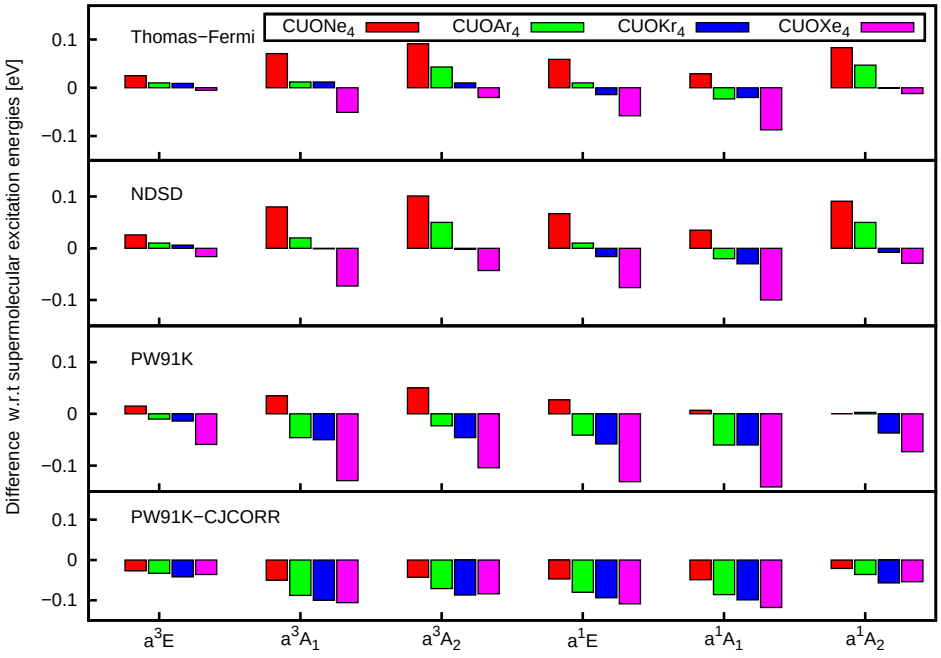


from the errors seen in the orbital energies, none of the kinetic energy approximations is able to reproduce the KS/TD-DFT/PBE0 results for the heavier Ng matrices. Errors are largest in absolute magnitude for the $^{1,2}A$ and $^{1,3}A_2$ excited-states in heavier noble gases. All embedding potentials do shift the $^3E$ state above the $^1A_1$ ground-state. For all excitations the effect of the environment is small and the PW91K functional provides the relatively best performance, in agreement with the density error analysis discussed above.

**Table 11.7**: *SOC vertical excitation energies of the CUO and CUO$Ng_4$ complexes from the WFT-in-DFT: IHFSCC-SD via sector $(0h, 2p)$ for the bare CUO subsystem and embedded in the $Ng_4$ DFT-in-DFT/PBE0/PW91K potential.*

| State† | CUO | CUO$Ne_4$ | CUO$Ar_4$ | CUO$Kr_4$ | CUO$Xe_4$ |
|---|---|---|---|---|---|
| $^3\Sigma_0^+$ | $0.81^{\pm}$ | 1.02 | 0.85 | 0.76 | 0.65 |
| $^3\Sigma_1^+$ | 0.81 | 1.02 | 0.85 | 0.76 | 0.65 |
| $^3\Phi_2$ | 0.94 | 0.84 | 0.89 | 0.93 | 0.97 |
| $^3\Phi_3$ | 1.01 | 0.94 | 0.98 | 1.02 | 1.06 |
| $^3\Delta_1$ | 1.23 | 1.07 | 1.27 | 1.30 | 1.33 |
| $^3\Delta_2$ | 1.28 | 1.17 | 1.31 | 1.34 | 1.37 |
| $^1\Sigma_0$ | 1.37 | 1.51 | 1.36 | 1.31 | 1.21 |
| $^3\Phi_4$ | 1.60 | 1.53 | 1.57 | 1.61 | 1.64 |
| $^3\Delta_3$ | 1.69 | 1.58 | 1.58 | 1.67 | 1.64 |
| $^1\Delta_2$ | 1.72 | 1.68 | 1.75 | 1.78 | 1.76 |
| $^1\Phi_3$ | 1.79 | 1.73 | 1.76 | 1.79 | 1.80 |

† - subscripts denote Ω-values and upperscripts spin multiplicity;
± - the differences between $^3\Sigma_0^+$ and $^3\Sigma_1^+$ states are less than 0.01 eV;

### 11.4.4 WFT-in-DFT Electronic Structure of the CUO$Ng_4$ Compounds.

Considering all the information discussed above we find that the PW91K kinetic energy functional can give a qualitative description of the neon and to a less extent argon environments, although quantitative agreement correct trends are not reached not reached. We therefore decided to select this embedding potential to perform WFT-in-DFT calculations and check whether the same environment effects are found.

The SOC WFT-in-DFT excitation energies are listed in Table (11.7). The effect of noble gas environment on the transitions is clearly much too small to cause a ground state change in the WFT calculations, but just sufficient, in the case of neon, to place the $\Phi_2$ excited state below the two $^3\Sigma^+$ states. For argon this trend is reversed, in contrast to the supermolecular DFT calculations, which is due to the larger error in the embedding potential for this system. This error is larger still when utilizing an embedding with heavier Ng atoms, and leads to meaningless results as expected on basis of the DFT-in-DFT results.

## 11.5 Conclusions and Outlook

We have optimized geometries and calculated vibrational frequencies of the CUO and $CUONg_4$ complexes in the $^1\Sigma^+$ and $^3\Phi$ states using the PBE0 hybrid exchange–correlation functional. The significant difference in characteristic U–O and U–C vibrational frequencies that was observed in experiments, is in agreement with previous work, explained by a difference of electronic ground state ( $^1\Sigma^+$ to $^3\Phi$) in the neon and argon matrix, respectively. The direct effect of environment is smaller than 50 $cm^{-1}$ for the U–O and U–C stretching frequencies.

Since analysis of the vibrational spectra provides only an indirect measure for the energetic ordering of the electronic states, we also investigated this ordering directly for CUO and the $CUONg_4$ model compounds. The spin–free and spin–orbit IHFSCC-SD excitation energies of the CUO molecule, indicate that this molecule has a singlet ground-state, which is in line with earlier Fock-space coupled cluster studies by one of us [28] and the CISD calculations of Yang *et al.* [280]. These coupled cluster energies were used to assess to accuracy of hybrid TD-DFT/PBE0 excitation energies. It turns out that both components of PBE0 exchange–correlation functional — DFT and HF part — are insufficiently accurate. This issue can be related to the well–known "triplet instability" problem [315, 322, 323], caused by the large exchange splitting in the $5f$-shell, that is strongly overestimated in Hartree–Fock theory.

Compared to the large energy splittings predicted by the WFT approaches, the low-lying excited-states show only minor perturbations due to the noble gas environment. An exception are the $^{3,1}\Sigma$ excited-states that originate from electron transfer to the diffuse virtual $f_\sigma$-orbital. This diffuse orbital, and the corresponding transitions, are shifted to a much higher energy by the equatorial ligands.

Since the perturbations are small, we expected that these could be captured by the FDE approach, but it turns out that none of the currently available kinetic energy functionals is able to yield results with the desired chemical accuracy of less than 0.25 eV. For the $CUONe_4$ model the PW91K kinetic energy functional provides a reasonable agreement with a supermolecular approach, but for the complexes with heavier noble gases all kinetic energy functional produce too small ligand field splittings and a qualitatively incorrect result. WFT-in-DFT calculations on the $CUONg_4$ systems should, however, be feasible as soon as embedding potentials improve because the analysis of the densities shows that a density partitioning into a CUO and an environment density is indeed well possible.

As a side result of our work we note the importance of further development of exchange–correlation functionals that can provide qualitatively correct xc splittings for actinides. While for the $UO_2^{2+}$, NUN and $NUO^+$ molecules good agree-

ment between the TD-DFT and IHFSCC-SD electronic excitations can be reached, this is currently not the case for the CUO molecule.

# 12

# Reliable Modeling of the Electronic Spectra of Realistic Uranium Complexes

The most exciting phrase to hear in science, the one that heralds the most discoveries, is not "Eureka!" (I found it!) but "That's funny..."

Isaac Asimov

Adopted from:
Tecmer, P., Govind, N., Kowalski, K., De Jong, W. A., Visscher, L., submitted to *J. Chem. Phys.*, (2012).

## 12.1 Abstract

We present a EOMCCSD (equation of motion coupled cluster with singles and doubles) study of excited states of the small $[UO_2]^{2+}$ and $[UO_2]^{+}$ model systems as well as the larger $U^{VI}O_2$(saldien) complex. In addition, the triples contribution within the EOMCCSDT and CR-EOMCCSD(T) (completely renormalized EOMCCSD with the non-iterative triples) approaches for the $[UO_2]^{2+}$ and $[UO_2]^{+}$ systems as well as the active-space variant of the CR-EOMCCSD(T) method — CR-EOMCCSd(t) — for the $U^{VI}O_2$(saldien) molecule are investigated. These electronic excitation energies serve as a reference for time-dependent density functional (TD-DFT) calculations, in which the fraction of exact exchange at long inter-electronic distances in the CAM-B3LYP exchange–correlation functional is assessed.

The coupled cluster data was employed as benchmark to chose the "best" appropriate exchange–correlation functional for subsequent TD-DFT studies on the

transition energies as well as on the corresponding oscillator dipole strengths of the open-shell $[U^{V}O_2(\text{saldien})]^-$ molecule in a DMSO environment. Furthermore, the influence of the saldien ligands on the electronic structure and excitation energies of the $[UO_2]^+$ molecule is analyzed. The electronic spectrum obtained from our TD-DFT calculations using the CAM-B3LYP exchange–correlation functional for the $[U^{V}O_2(\text{saldien})]^-$ in DMSO is in good agreement with the experimental data of Takao *et al.* [Inorg. Chem. 49, 2349–2359, (2010)].

## 12.2 Introduction

Over the past decade, studies on early actinides, *e.g.*, Np, U, Pu, and Am with the oxidation states +5 and +6, became a very active area of research for chemists due to their unique coordination properties [4–6, 15, 324, 325]. These actinides exhibit dissimilar solubility and mobility in polar solvents, meaning that a large number of highly coordinated actinide-containing complexes with different stabilities can be created [1]. Understanding the complex process of ligation present in these actinides is a crucial feature for assessing the feasibility of storing and disposing nuclear waste [18, 19, 258] as well as for designing possible catalysts [20, 251].

Penta- and hexavalent actinides are unstable in aqueous solution and hydrolyze instantly to create strongly bonded linear molecules [5] of the form: $[AcO_2]^{1+/2+}$. Interestingly, in aqueous environment these actinyl ions can coexist in both oxidation states, showing dissimilar chemical properties [258]. In addition, the identification of some of the penta- and hexavalent dioxoactinides is limited by the fact that they can create aggregates as a result of the so-called cation-cation interactions (CCI) [326]. Besides that, all these systems can change their oxidation state relatively easily, which makes the identification and separation of the individual cations even more complicated. The V- and VI-valued dioxoactinides can be further coordinated in the equatorial plane by three to six ligands and can hence form square, pentagonal or hexagonal bipyramidal geometrical structures, respectively. Since the valence orbital energy levels in the early actinides are very close to each other, changes in the coordination sphere might indirectly modify the electronic structure of the actinide center and as a consequence affect the stability of the V- and VI-valued actinyl compounds [5, 257, 327].

This rather complex valence electronic structure of actinide-containing molecules [5, 24, 29, 325] makes an analysis of the equatorial ligand field and its influence on the bare dioxocations difficult. For a better understanding of the role of the chemical environment and the nature of its binding to the bare dioxoactinides, it is instructive to first investigate the lowest-lying transition energies from

the valence occupied molecular orbitals to the lowest-lying virtual $f_\sigma$-, $f_\pi$-, $f_\delta$- and $f_\phi$-orbitals of the actinide atom center of this triatomic species. Changes in the excitation energies of the actinyl complexes with respect to the $[AcO_2]^{1+/2+}$ moiety carry unique information about the oxidation state and the surrounding environment [328]. This knowledge can be further used to obtain desired properties of the actinide model complexes in solution, *cf.* complexation, solubility, redox, oxidation state and sorption [2, 258]. Moreover, in comparison with, for instance, vibrational spectroscopy, the electronic spectra provide direct insights into the chemical bonding and rearrangement of the low-lying excited states from which the former can be derived.

The predominant actinide dioxocation is the uranyl cation $[UO_2]^{2+}$ that can be found as a small building block of larger uranium-containing complexes [4, 5, 29, 198, 256, 276, 329]. The linearity of the $[UO_2]^{1+/2+}$ units is almost always preserved upon coordination, with only small deviations of up to 5 degrees being observed so far [4, 17, 256, 330]. While the VI-valued uranyl is known from its high stability, the opposite is true for the V-valued uranyl — $[UO_2]^+$. The latter is very unstable and immediately disproportionates [331] in acidic solution into the tetravalent and hexavalent uranium species,

$$2[UO_2]^+ + 4H^+ \rightleftharpoons [UO_2]^{2+} + U^{4+} + 2H_2O. \tag{12.1}$$

Despite this reaction, there are a few stable $[UO_2]^+$ complexes, which can be obtained by (i) reduction of $H^+$ cations in solution or (ii) obstruction of the CCI [326, 332–334] between the $[UO_2]^+$ units. The former condition is satisfied when the $[CO_3]^{2-}$ ligands in alkaline solution are provided and leads to the stable $[U^VO_2(CO_3)_3]^{5-}$ molecular complex [335]. The latter is fulfilled by the presence of multidentate ligands, like for instance N,N'-di-salicylidene-o-phenylenediaminate (saloph), dibenzoylmethanate (dbm) or N,N'-di-salicylidenediethylenetriaminate ($saldien^{2-}$) in dimethyl sulfoxide (DMSO), which due to steric interactions can effectively prohibit the CCI. At the moment, only three such complexes are known: $[U^VO_2(saloph)_2DMSO]^-$, $[U^VO_2(dmb)_2DMSO]^-$ and $[U^VO_2(saldien)DMSO]^-$ [32, 34, 336–338].

It is important to stress here that the small number of existing pentavalent actinide-containing complexes and the difficulties encountered with their isolation, limit the chemical knowledge about them [17]. Therefore it is desirable to close this gap by means of quantum chemical calculations. In particular, the role of the multidentate ligands upon complexation and its influence on the $[UO_2]^+$ unit requires explanation. Very helpful in this respect would be a reliable theoretical study devoted to the electronic structure and electronic spectra of V-valued uranyl

species. The latter can be further directly compared to available experimental spectra.

The electronic spectra of the pentavalent uranyl complexes were studied in the visible and near-infrared regions by photochemical and electrochemical reduction of the hexavalent uranium compounds [3, 328, 337, 339], showing a common nature of all the recorded transition energies in the range of 4 000 – 30 000 $cm^{-1}$, *i.e.*, 0.5 – 3.7 eV. Since the five-valued dioxouranyl possesses empty $f$-orbitals, the detected absorption bands were assigned either to "pure" $f$–$f$ transitions between the $5f^1_\phi$ and $5f^1_\delta$ configurations or to charge-transfer excitations from the axial oxygen and other equatorial ligands to the uranium atomic $f$-orbitals, commonly know as the LMCT. A detailed analysis of the latter transitions is usually impossible in experimental studies, and theoretical calculations that include the LMCT transition are therefore of great importance.

While small model systems like $U^{5+}$ and $[UO_2]^+$ have received significant attention from both experimentalists [286] and theoreticians [125, 201], theoretical studies of the larger V-valued uranium-containing complexes are rather rare [201, 330]. Quantum chemical calculations of the excited states of realistic complexes as the $U^{VI}O_2$(saldien)DMSO and $[U^{V}O_2$(saldien)DMSO$]^-$ on a sound theoretical basis have not been performed yet. The size of these systems poses quite a challenge for more reliable wave function calculations and the quality of DFT/TD-DFT, which is capable of treating larger systems, remains uncertain, as the existing exchange–correlation functionals have not been well tested for actinides.

The recent success of the time-dependent density functional theory (TD-DFT) [54, 55] with long-range separated (attenuated) hybrid exchange–correlation functionals, in describing both charge-transfer and Rydberg excitations has resulted in a number of publications in this field [249, 265, 266, 268, 340]. Inclusion of varying fractions of Hartree–Fock exchange in the exchange–correlation functional, which relies on the short and long inter-electronic distances, gives satisfactory agreement with reference wave function methods and experimental data [116, 267–269, 272, 341, 342]. It has been shown that a good balance between the amount of short-range (local) and long-range exact-exchange is crucial to reproduce the reference excitation energies of organic and transition metal compounds [116, 268, 342].

The performance of the TD-DFT for excited states of open-shell molecules is less explored. In addition to the difficulties with respect to a proper description and ordering of the energetically closely-lying virtual orbitals in the closed-shell calculations, the determination of the open-shell ground state becomes cumbersome. The quality of the ground state spin-density [71] strongly depends on the applied exchange–correlation functional and the fraction of exact-exchange [343]

which has a significant impact on the excitation energies.

In general, the TD-DFT approach in conjunction with the range-separated hybrid exchange–correlation functionals has been employed only for a few model actinide-containing compounds. The previous chapters on the vertical excitation energies of the small closed-shell triatomic actinide molecules [96] indicated that the accuracy of the complete active space second order perturbation theory (CASPT2) [103, 104] and the intermediate Hamiltonian Fock-space coupled cluster with singles and doubles (IHFSCC-SD) methods [136, 138, 139] can be approached with TD-DFT when the long-range separated CAM-B3LYP [90] exchange–correlation functional is employed. Moreover, another study [344] showed that the four-component TD-DFT formulation with the above-mentioned exchange–correlation functional can produce a reliable electronic spectrum of the medium-sized, closed-shell $[UO_2Cl_4]^{2-}$ molecule. Besides employing the CAM-B3LYP exchange–correlation functional, it is easy to access the higher-lying excitation energies of the $[UO_2Cl_4]^{2-}$ system, which are dominated by a number of dense charge-transfer transitions. Therefore, it seems to be appropriate to employ the CAM-B3LYP exchange–correlation functionals for the electronic spectra of larger actinide-containing molecules that include LMCT transitions. The LMCT excitations often appear in the region of the spectrum that is difficult to access by wave function methods and for which most of the conventional exchange–correlation functionals (local and global hybrids) usually fail [36, 200].

We would like to note here that an accurate description of the excited states of the above mentioned uranyl-saldien complexes employing desirable and highly correlated wave function methods like, for instance, multi-reference coupled cluster [101, 102, 121, 262] or genuine CASPT2 [103, 104], is not feasible for such realistic systems containing full-fledged ligands due to the steep scaling with respect to the size of the active space. However, correlated, large scale wave function calculations of excited states are still feasible with an efficient implementation of the equation of motion coupled cluster with singles and doubles approach. Recent extensions of this method to the non-iterative triples within a given orbital space, called the active space variant of completely renormalized equation of motion coupled cluster with singles doubles and non-iterative triples [345] method, could serve as a reference for the DFT/TD-DFT benchmark since its recent performance is very encouraging [116].

The CR-EOMCCSD(T) method was successfully applied to excited state studies in a number of chemically important compounds [342, 345, 346], and very recently even to small actinide-based complexes [347, 348]. Therefore, it is of interest to extend its application to large actinide compounds, where scalar rela-

tivistic effects are incorporated via the effective core potential [6, 302].

Our goal here is to find a proper theoretical model for the experimentally observed electronic transitions together with the corresponding intensities for the $[U^{V}O_2(saldien)]^-$ open-shell species in DMSO [34, 337, 338] and assign the character of the above mentioned LMCT transitions.

In order to assess the accuracy of TD-DFT, we first investigate the theoretically simpler, closed-shell molecules $[UO_2]^{2+}$, $[UO_2]^{+}$ and $U^{VI}O_2(saldien)$. Second, we adjust the amount of the long-range exact exchange by comparing TD-DFT excitation energies to the CR-EOMCCSd(t) data. Finally, we compare the electronic spectra of the $[U^{V}O_2(saldien)]^-$ molecule in DMSO obtained within the TD-DFT framework employing an adjusted CAM-B3LYP exchange–correlation functional to the experimental data.

## 12.3 Computational Details

### 12.3.1 Structure Optimization

We optimized the structures of the $U^{VI}O_2(saldien)$, $U^{VI}O_2(saldien)DMSO$ and the $[U^{V}O_2(saldien)]^-$ complexes within the DFT framework with a development version of the NWChem 6.1 quantum chemical package [349–351]. We have utilized the B3LYP [83, 84] exchange–correlation functional on a fine integration grid (accuracy of $10^{-7}$) in conjunction with the DZP (double-$\zeta$ polarization) basis set of Dunning [352]. Scalar relativistic effects were incorporated by the effective core potential in the uranium atom (78 electrons in the core if not stated otherwise) [353]. The geometry convergence criteria were set up to $10^{-6}$, $10^{-5}$ and $0.5 \times 10^{-4}$ for the energy, density and gradient, respectively.

We performed these structure optimization to check whether such a single molecule possesses a different geometry from the crystal structure. Since the structure of the VI-valued complexes ($U^{VI}O_2(saldien)$ and $U^{VI}O_2(saldien)$*DMSO) remained unchanged and resembled the structures recorded in the X-ray experiment [34], and since it was not possible to obtain convergence for the $[U^{V}O_2(saldien)]^-$*DMSO, we have used the crystallographic structures for all systems in this chapter.

### 12.3.2 Time-Dependent Density Functional Theory

The spin-free TD-DFT vertical excitation energies were obtained with the adiabatic approximation to the exchange–correlation kernel [55] in a conjunction

with the CAM-B3LYP [90] exchange–correlation functional as implemented in the NWChem 6.1 quantum chemical package [349–351].

The main goal of this work is to compare the theoretical transition energies with experiment. We restrict ourself to the spin–free singlet-singlet excitation energies, but note that the influence of SOC may distribute the intensities somewhat. We assume that this does not lead to large differences in the interpretation.

In order to explore the quality of the obtained electronic transitions, we have used two versions of the CAM-B3LYP [90] exchange–correlation functional which differ in the amount of exact-exchange at the long-range inter-electronic distances. The first variant of the CAM-B3LYP exchange–correlation functional used in this work, CAM-B3LYP-A, comprises 19% of exact-exchange at short ($\alpha = 0.19$) and 46% of the exact-exchange at long inter-electronic distances ($\beta = 0.46$), *cf.* Eq. 5.77. The second one, CAM-B3LYP-B, corresponds to $\alpha = 0.19$ and $\beta = 0.81$, respectively. We have employed the standard attenuation factor [90] of $\mu = 0.33$ for both CAM-B3LYP variants. We refer the reader to the following articles [90, 267, 341] for a detailed discussion on this and related topics.

Due to the small energy gap between the HOMO and LUMO in the $[U^{V}O_2(\text{saldien})]^{-}$ complex, we have employed the Tamm–Dancoff approximation (TDA [354]) to the full TD-DFT framework for this molecule. It has already been shown that this algorithmically simpler alternative to TD-DFT can be almost as accurate as the full TD-DFT approach when singlet-singlet type of excitations are considered [354]. In order to check if this is also the case in our system, we calculated the excitation energies in the $U^{VI}O_2$(saldien) molecule with and without the TDA approximation.

In addition, we also analyzed the effect of the DMSO on the vertical excitation energies within the TD-DFT framework in a conjunction with the conductor-like screening model (COSMO) [142] (with a dielectric constant of 47.13 [355]).

### 12.3.3 Equation of Motion Coupled Cluster

The coupled cluster calculations were carried out with the tensor contraction engine (TCE) [356–359] implementation of the EOMCCSD, CR-EOMCCSD(T), CR-EOMCCSd(t) and EOMCCSDT methods in the NWChem 6.1 quantum chemical package [349–351].

For the CR-EOMCCSd(t) method, we tested three different variants of the virtual active spaces for the first excited state in the $U^{VI}O_2$(saldien) molecule, *i.e.*, we correlated orbitals in energy ranges: $\epsilon \in [-1.0; 1.5]$, $\epsilon \in [-1.0; 2.0]$ and $\epsilon \in [-1.0; 2.5]$ *a.u.*, which gave the $\delta_K^{\text{CR-EOMCCSd(t)}}$ corrections (Eq. 6.31) of +0.13, +0.11 and +0.12 eV, respectively. This shows that the size of the tested virtual

active spaces does not significantly affect the triples correction and is far below the desired chemical accuracy, which is found to be less than 0.25 eV [96, 344]. Therefore, we have employed the smallest active space ($\epsilon \in [-1.0; 1.5]$) for the remaining higher-lying excited states within the CR-EOMCCSd(t) formalism to minimize the computational expenses.

## 12.4 Results and Discussion

First, we focus on the assessment of the CAM-B3LYP-A and CAM-B3LYP-B exchange–correlation functionals to the EOMCCSD, CR-EOMCCSD(T) and EOMCCSDT methods for the excited-state calculations.

### 12.4.1 Assessment of the TD-DFT Results

We start our discussion with the small model systems: $[UO_2]^{2+}$ and $[UO_2]^{+}$ which serve as a starting point for the analysis of the complete $U^{VI}O_2$(saldien) complex.

#### 12.4.1.1 $[\mathbf{UO_2}]^{2+}$

The ground-state electronic structure of the $[UO_2]^{2+}$ molecule is well-known and it has been investigated many times by different quantum chemical approaches which led to a consistent picture [5, 23, 25, 360]. It has been agreed that the valence electronic structure of this VI-valued dioxocation is a closed-shell moiety and comprises the $\pi_g$, $\sigma_g$, $\pi_u$ and $\sigma_u$ MOs as the highest occupied and $\phi_u$ and $\delta_u$ MOs as the lowest unoccupied orbital, with $\sigma_u$ and $\phi_u$ being the HOMO and LUMO, respectively. The occupied MOs are combination of the U($5f$), U($6d$) and O($2p$) atomic orbitals and possess a bonding character, while the non-bonding $\phi_u$ and $\delta_u$ MOs have a rather pure U($5f$) character.

Table (12.1) lists the lowest-lying excitation energies of the $[UO_2]^{2+}$ molecule. The left-hand side of Table (12.1) comprises the excited-state calculations in all electron basis sets (aug-cc-pVTZ for O and dyall.v3z for U atoms, respectively) and the right-hand side contains the ECP on the uranium atom (Stuttgart ECP) and all electron DZP basis set on the oxygen atoms. For a straightforward comparison of the excited states, new calculations were performed at the same geometry as in Ref. 96, *i.e.*, with a linear structure of uranyl and a U–O distance equal 1.708 Å.

The differences in the excited states found for the two different sets of the CAM-B3LYP-A calculations could be attributed either to the size of the basis sets or to the ECP. In order to eliminate the former, we carried out additional calculations with an aug-cc-pVTZ basis set for O and an ECP for U to check the

**Table 12.1**: *Singlet-singlet spin–free vertical excitation energies of the $[UO_2]^{2+}$ molecule ($r_{UO}$=1.708 Å): comparison of different methods (in eV).*

| Excitation[a] | | All electron | | | ECP | | | | |
|---|---|---|---|---|---|---|---|---|---|
| Sym. | Character | CAM-B3LYP-A | CASPT2 | IHFSCC-SD | CAM-B3LYP-A | CAM-B3LYP-B(TDA) | EOMCCSD | CR-EOMCCSD(T) | EOMCCSDT |
| $^1\Phi_g$ | $\sigma_u \rightarrow \phi_u$ | 3.07 | 3.24 | 3.40 | 2.94 | 3.33 | 4.25(3.88) | 4.35(3.90) | 4.28 |
| $^1\Delta_g$ | $\sigma_u \rightarrow \delta_u$ | 3.69 | 3.57 | 3.88 | 3.37 | 3.73 | 4.48(4.27) | 4.63(4.30) | 4.49 |
| $^1\Gamma_g$ | $\pi_u \rightarrow \phi_u$ | 4.65 | 4.78 | 4.83 | 4.32 | 4.82 | 5.51(5.35) | 5.91(5.53) | 5.68 |
| $^1\Phi_u$ | $\sigma_g \rightarrow \phi_u$ | 4.81 | 4.74 | 4.85 | 4.52 | 5.00 | 5.63(5.64) | 6.31(5.97) | 5.80 |
| $^1\Delta_u$ | $\sigma_g \rightarrow \delta_u$ | 4.99 | 4.71 | 4.64 | 4.53 | 4.88 | 5.16(5.38) | 5.84(5.70) | 4.88 |

*values in parenthesis correspond to the small ECP (60 electrons in the core)
a) Ref. 96

completeness of the basis set. The excitation energies obtained with the larger basis set differ by less than 0.05 eV (results not shown), therefore we can assume that the smaller DZP basis set, which has to be employed in the full-fledged complex, is qualitatively accurate and the difference between the two sets of CAM-B3LYP-A data most probably originates from the ECP. The overall agreement between the all-electron and ECP calculations employing the CAM-B3LYP-A exchange–correlation functional is good, only in the two highest excited states, *i.e.*, $^1\Phi_u$ and $^1\Delta_u$, the difference is somehow larger and increases up to 0.29 and 0.46 eV, respectively. Comparing the CAM-B3LYP-A results obtained with the ECP to the reference CASPT2 and IHFSCC-SD methods, a qualitative agreement can be observed.

Let us now turn to the excitation energies obtained for the CAM-B3LYP-B exchange–correlation functional. As a consequence of the larger amount of exact-exchange in this functional, all the excited states are shifted up in energy by about 0.3 eV compared to CAM-B3LYP-A, which brings them very close to the CASPT2 and IHFSCC-SD electronic transitions. The average difference between the latter two is less than 0.2 eV. Therefore the CAM-B3LYP-B exchange–correlation functional outperforms CAM-B3LYP-A with respect to the excited states of the $[UO_2]^{2+}$ molecule.

Surprisingly, the excitation energies obtained from the EOMCCSD method overshoot the IHFSCC-SD results by more than 1 eV. The addition of triples from the CR-EOMCCSD(T) results in excited states which are even further apart from the reference. An inclusion of the full triples within the EOMCCSDT method does not change this picture significantly. In order to check whether this might be an effect of slower convergence with the basis set of the CC approach compared to DFT, we performed additional calculations with the aug-cc-pVTZ basis set for the oxygen atoms. It turns out that the excited states are barely effected when the basis set is increased, a difference less than 0.03 eV (results not shown) eliminates a basis set issue as a cause of the discrepancy.

Since the correlation of electrons in pseudo orbitals might introduce errors, we carried out an additional EOMCCSD and CR-EOMCCSD(T) calculations with a small ECP (60 electrons in the core) [361]. It turns out that for this particular molecule the small core ECP works better than the large core ECP and brings all of the excited states close to the all-electron reference data, as shown by the numbers in parenthesis in Table (12.1). The small core ECP represents the nodal structure of the uranium atom in the VI-valued uranyl more accurately and hence results in smaller artifacts due to the ECP approximation.

#### 12.4.1.2 $[UO_2]^+$

The electronic structure of the $[UO_2]^+$ molecule differs from that of $[UO_2]^{2+}$ by one additional electron placed on the non-bonding $\phi_u$ or $\delta_u$ MOs. The relative energies of the $\sigma_u^2\phi_u^1$ and $\sigma_u^2\delta_u^1$ configurations of the V-valued uranyl are very close to each other and therefore difficult to distinguish even by accurate quantum chemical methods [201]. One additional electron on the non-bonding $5f$-orbital weakens the U–O bond and as a consequence the stability of the $[UO_2]^+$ system compared to $[UO_2]^{2+}$. The lowest part of the electronic spectrum of this molecule comprises transitions from the $\delta$ MO to the $\phi_u$ and $\delta_u$ MOs which are listed in Table (12.2), where the TD-DFT results are compared to the CASPT2 data of Ruiperez *et al.* [201] and the CC results obtained from the EOMCCSD, EOMCCSD(T) methods at a U–O distance of 1.742 Å and IHFSCC-SD for a U–O bond length of 1.708 Å.

The TD-DFT/CAM-B3LYP-A approach predicts the same ground state $\sigma_u^2\phi_u^1$ configuration as CASPT2. However, the excitation energies deviate from both CASPT2 and CC results. The higher-lying excited states suffer from spin contamination and therefore are not presented in the table. The CAM-B3LYP-B exchange–correlation functional on the other hand predicts the $\sigma_u^2\delta_u^1$ configuration to be the ground state which is in line with the EOMCCSD and CR-EOMCCSD(T) data. TD-DFT excitation energies obtained for the CAM-B3LYP-B exchange-correlation functional overshoot significantly wave function reference data.

The overall agreement between the excited states obtained from the CASPT2 and EOMCCSD methods is very good, the differences are less than 0.25 eV. Both methods predict, however, different ground-state configurations: CASPT2 and IHFSCC-SD favor the $\sigma_u^2\phi_u^1$ configuration, while for EOMCCSD and CR-EOMCCSD(T) the $\sigma_u^2\delta_u^1$ configuration is preferred. Inclusion of the non-iterative triples in the EOMCCSD method predicts even a stronger preference of the $\sigma_u^2\delta_u^1$ configuration (0.25 eV) with respect to EOMCCSD (0.08 eV). The CR-EOMCCSD(T) approach raises the energy of the first excited state ($^2\Phi_u$) and lowers the rest of the excited states compared to the CASPT2 and EOMCCSD methods. The largest effect of the triples — up to 0.5 eV — is found for the $^2\Sigma_g$ and $^2\Delta_g$ excited states.

Because of one additional electron in the $[UO_2]^+$ system the valence electronic structure is different from the that of $[UO_2]^{2+}$ and as a result the low-lying transitions in the V-valued uranyl involve mainly the HOMO and the HOMO–1 and are not affected by the size of the ECP core as it was the case for the VI-valued uranyl. A even better situation will be encountered in the $U^{VI}O_2$(saldien) molecule, where the saldien$^{2-}$ ligand will donate two additional electrons to the $[UO_2]^{2+}$ unit. Hence, the small ECP with 78 electrons in the core should be quite reliable.

**Table 12.2**: *Singlet-singlet spin–free vertical excitation energies of the $[UO_2]^+$ molecule ($r_{UO}$=1.742 Å): comparison of different methods (in eV).*

| Excitation | | TD-DFT | | WFT | | | |
|---|---|---|---|---|---|---|---|
| Sym. | Configuration | CAM-B3LYP-A | CAM-B3LYP-B(TDA) | CASPT2[a] | EOMCCSD | CR-EOMCCSD(T) | IHFSCC-SD[b] |
| $^2\Phi_u$ | $\sigma_u^2\phi_u^1$ | 0.00 | 0.71 | 0.00 | 0.08 | 0.25 | 0.00 |
| $^2\Delta_u$ | $\sigma_u^2\delta_u^1$ | 0.56 | 0.00 | 0.11 | 0.00 | 0.00 | 0.05 |
| $^2\Pi_u$ | $\sigma_u^2\pi_u^1$ | 1.06 | 3.06 | 2.22 | 2.36 | 2.13 | 2.67 |
| $^2\Sigma_g$ | $\sigma_u^2\sigma_g^1$ | - | 4.21 | 2.29 | 2.22 | 1.63 | 1.91 |
| $^2\Delta_g$ | $\sigma_u^2\delta_g^1$ | - | 4.95 | 2.31 | 2.53 | 2.03 | 1.93 |

a) Ref. 201 b) this data was taken from the calculations performed in Ref. 96

**Figure 12.1**: *Structure of the uranyl-saldien complex drawn with ADFGUI [319].*

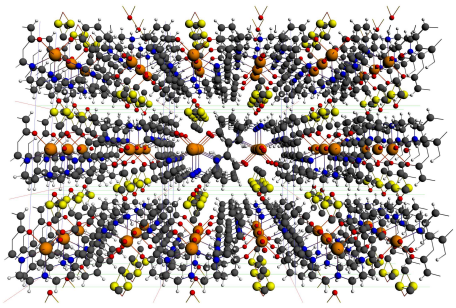

(a) The crystal structure

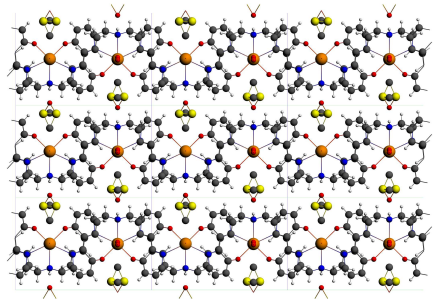

(b) One layer of molecular saldiens from the crystal structure

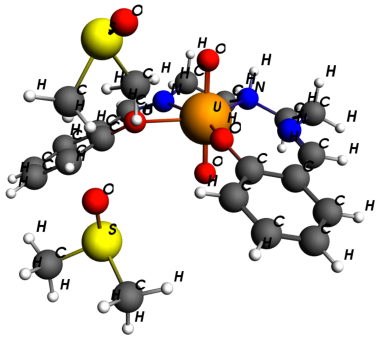

(c) Model system with 2 DMSOs

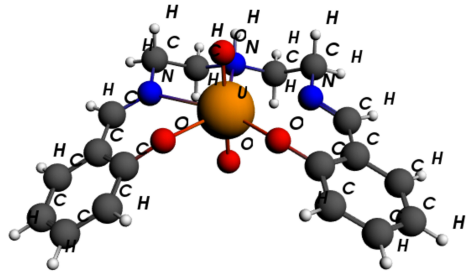

(d) Model system without DMSO

#### 12.4.1.3 $U^{VI}O_2$(saldien)

The molecular geometry of $U^{VI}O_2$(saldien) was taken from the X-ray crystal structure [34] which is presented in Figure (12.1)(a). The plain view across this structure in Figure (12.1)(b) shows that the $U^{VI}O_2$(saldien) compound does not directly interact with the DMSO molecule and therefore can be easily separated from the whole crystal structure (see Figure (12.1)(a)). The smallest model $U^{VI}O_2$(saldien) system has a structure as illustrated in Figure (12.1)(d).

In the closed-shell $U^{VI}O_2$(saldien) complex the $[UO_2]^{2+}$ unit is no longer linear, the O–U–O angle reduces slightly to 176° upon coordination by the pentavalent

**Table 12.3**: *Lowest singlet-singlet vertical excitation energies for the $U^{VI}O_2$saldien molecule (in eV). Comparison of the TD-DFT and CR-EOMCCSD(t) methods.*

| TD-DFT | | | | | | | | WFT | | | |
|---|---|---|---|---|---|---|---|---|---|---|---|
| CAM-B3LYP-A | | CAM-B3LYP-B | | CAM-B3LYP-B(TDA) | | CAM-B3LYP-B* | | EOMCCSD | | CR-EOMCCSD(t) | |
| character | energy | character | energy | character | energy | character | energy | character | energy | character | energy |
| $\sigma \rightarrow \delta$ | 2.94 | $\sigma \rightarrow \delta$ | 3.39 | $\sigma \rightarrow \delta$ | 3.46 | $\sigma \rightarrow \delta$ | 3.49 | $\sigma \rightarrow \delta$ | 3.43 | $\sigma \rightarrow \delta$ | 3.57 |
| $\sigma \rightarrow \delta$ | 2.96 | $\sigma \rightarrow \delta$ | 3.42 | $\sigma \rightarrow \delta$ | 3.49 | $\sigma \rightarrow \delta$ | 3.51 | $\sigma \rightarrow \delta$ | 3.55 | $\sigma \rightarrow \delta$ | 3.73 |
| $\sigma \rightarrow \phi$ | 3.19 | $\sigma \rightarrow \phi$ | 3.56 | $\sigma \rightarrow \phi$ | 3.57 | $\sigma \rightarrow \phi$ | 3.70 | $\sigma \rightarrow \phi$ | 3.82 | $\sigma \rightarrow \phi$ | 3.74 |
| $\pi \rightarrow \delta$ | 3.25 | $\pi \rightarrow \delta$ | 3.78 | $\pi \rightarrow \delta$ | 3.84 | $\pi \rightarrow \delta$ | 3.92 | - | - | - | - |
| $\pi \rightarrow \delta$ | 3.32 | $\sigma \rightarrow \phi$ | 3.87 | $\pi \rightarrow \delta$ | 3.90 | $\pi \rightarrow \delta$ | 3.98 | - | - | - | - |
| $\sigma \rightarrow \phi$ | 3.42 | $\pi \rightarrow \delta$ | 3.95 | $\pi \rightarrow \delta$ | 4.01 | $\pi \rightarrow \delta$ | 4.04 | - | - | - | - |
| $\pi \rightarrow \phi$ | 3.72 | $\pi \rightarrow \delta$ | 4.13 | $\pi \rightarrow \delta$ | 4.22 | $\sigma \rightarrow \phi$ | 4.30 | - | - | - | - |
| $\pi \rightarrow \phi$ | 3.75 | $\pi \rightarrow \delta$ | 4.36 | $\sigma \rightarrow \phi$ | 4.39 | $\pi \rightarrow \delta$ | 4.43 | - | - | - | - |
| $\pi \rightarrow \phi$ | 3.93 | $\pi \rightarrow \phi$ | 4.39 | $\pi \rightarrow \delta$ | 4.48 | $\pi \rightarrow \delta$ | 4.52 | - | - | - | - |
| $\sigma \rightarrow \delta$ | 3.95 | $\pi \rightarrow \phi$ | 4.53 | $\pi \rightarrow \phi$ | 4.57 | $\pi \rightarrow \phi$ | 4.57 | - | - | - | - |

*TD-DFT calculations embedded in COSMO

**Figure 12.2**: *Evaluation of the lowest-lying valence orbitals of uranyl upon saldien ligation. These DFT/CAM-B3LYP-B orbital energies were adjusted to the energy of the HOMO.*

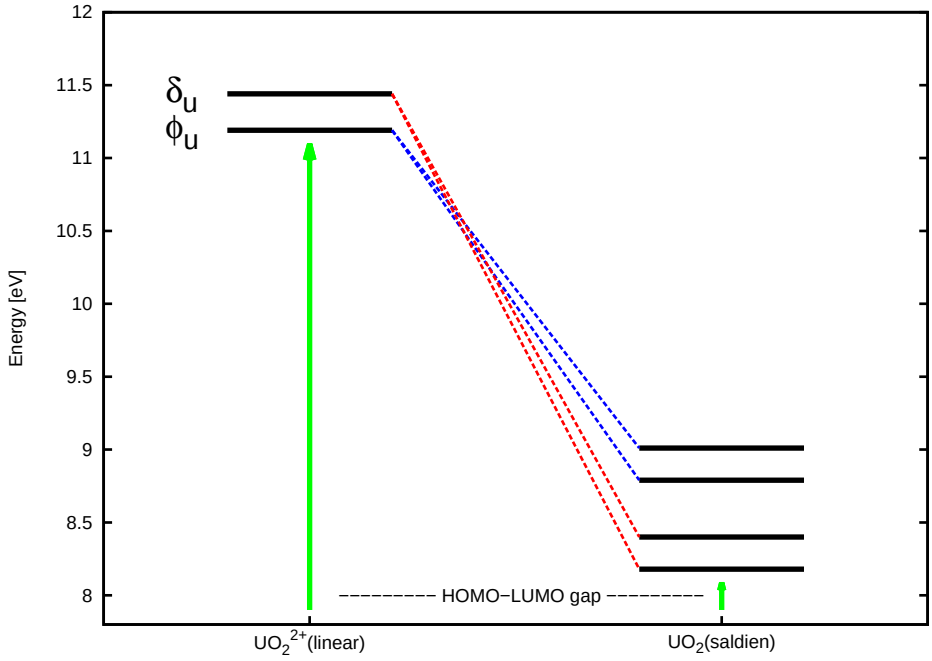


saldien. However, the main differences in the electronic structure and as a result in the excitation energies between these two systems are caused by the ligand field and not by the bend geometry of the uranyl itself. The presence of saldien in the equatorial plane of the VI-valued uranium system reduces the HOMO–LUMO gap from 11.19 eV in the bare cation to 8.18 eV in the coordinated molecule. It is important to note that the $\delta$-orbital now becomes the LUMO. Moreover, as a consequence of the ligand field both the $\phi_u$ and $\delta_u$ virtual MOs are split by about 0.25 eV as illustrated in Figure (12.2).

Table (12.3) list all the transition energies obtained for the $U^{VI}O_2$(saldien) system. Because of the low $C_s$ point group symmetry, the main character of excitations are given instead of the symmetry of the electronic transitions. The lowest-lying transitions are the internal uranyl excitations and the higher-lying are dominated by the LMCT transitions. The latter comprises the electron transfer from $\pi$ to either $\phi$ or $\delta$ orbitals.

The first three excited states determined by the TD-DFT/CAM-B3LYP-A approach that appear at 2.94, 2.96 and 3.19 eV, respectively, correspond to the excitations from $\sigma$-orbital to the two $\delta$- and one $\phi$-orbitals. Electron transfer to

the second component of the $\phi$-orbital appears at slightly higher energy, *i.e.*, 3.42 eV, and is separated from the lowest internal uranyl transitions by the two LMCT transitions ($\pi \rightarrow \delta$). These dominate also in the highest part of the electronic spectrum.

Employing the CAM-B3LYP-B exchange–correlation functional, the whole spectrum of the $U^{VI}O_2$(saldien) molecule is shifted up in energy by 0.35–0.50 eV as a result of an increased amount of exact exchange. As a consequence the LMCT transitions appear at higher energies compared to the CAM-B3LYP-A results. This observation is in line with our previous findings in the $[UO_2Cl_4]^{2-}$ molecule where the larger amount of exact exchange moved the charge-transfer states closer to the experimental values [344]. Now, between the two low-lying $\sigma \rightarrow \phi$ excitation energies there is only one LMCT transition (see Table (12.3)). Besides that, the qualitative agreement between these two versions of the CAM-B3LYP exchange–correlation functionals is rather good. It is interesting to note that the large HOMO–LUMO separation in both $[UO_2]^{2+}$ and $U^{VI}O_2$(saldien) compounds as illustrated in Figure (12.2) does not correspond to the high excitation energy between these two orbitals, *i.e.*, the $\sigma_u$- and $\phi_g$-orbitals. As can be seen in Table 12.3, the larger orbital energy difference between these two in the bare uranyl (11.19 eV) leads to a smaller excitation energy than in the complete system for the CAM-B3LYP-B exchange–correlation functional, 3.33 *vs.* 3.39 eV, respectively. This signifies the importance of the exchange–correlation kernel in the determination of the excited states of this kind of uranium complexes.

In addition to the regular TD-DFT approach we also tested the accuracy of the Tamm–Dancoff approximation for the CAM-B3LYP-B exchange–correlation functional. It turns out that this simpler approach can be successfully used to model the singlet-singlet electronic spectra of the $U^{VI}O_2$(saldien) compound as there is almost no difference (less than 0.1 eV) with respect to the full TD-DFT approach.

Yet, an additional calculations have been carried out to check the influence of the DMSO on the excitation energies of the $U^{VI}O_2$(saldien) system as DMSOs are present in the X-ray structure (see Figure (12.1)). The presence of DMSO was modeled within the COSMO approach. Our results shown in Table (12.3) do not show any significant deviation from the calculations without COSMO, and therefore confirms our previous assumption that the $U^{VI}O_2$(saldien) system does represent an adequate model.

On the right hand side of Table 12.3, excitation energies obtained from the EOMCCSD and CR-EOMCCSd(t) methods are listed. The CR-EOMCCSd(t) approach rises the energy of the first two excited states and lowers the third elec-

**Table 12.4**: *Lowest singlet-singlet vertical excitation energies for the $[U^{VI}O_2(saldien)]^-$ molecule (in eV). Comparison of the TDA/CAM-B3LYP-B and experimental results.*

| $[U^{V}O_2(saldien)]^-$ | | | $[U^{V}O_2(saldien)]^-$*2DMSO | | | Experiment[a] | |
|---|---|---|---|---|---|---|---|
| character | int. $\times 10^{-5}$ | energy | character | int. $\times 10^{-5}$ | energy | int.* | energy |
| $\delta \rightarrow \sigma$ | 3.0 | 0.63 | $\delta \rightarrow \sigma$ | 2.0 | 0.72 | 155 | 0.65 |
| $\delta \rightarrow \sigma$ | 0.0 | 1.00 | $\delta \rightarrow \sigma$ | 1.0 | 1.06 | 140 | 0.90 |
| $\delta \rightarrow \phi$ | 1.0 | 1.35 | $\delta \rightarrow \sigma$ | 2.0 | 1.44 | 300 | 1.49 |
| $\delta \rightarrow \pi$ | 2.0 | 2.37 | $\delta \rightarrow \sigma$ | 40.0 | 2.55 | 380 | 1.77 |
| $\delta \rightarrow \pi$ | 1.0 | 2.46 | $\delta \rightarrow \pi$ | 0.0 | 2.60 | 310 | 1.97 |
| $\sigma \rightarrow \sigma$ | 0.0 | 2.84 | $\sigma \rightarrow \sigma$ | 4.0 | 2.69 | - | - |
| $\sigma \rightarrow \sigma$ | 0.0 | 2.87 | $\delta \rightarrow \sigma$ | 3.0 | 2.70 | - | - |
| $\sigma \rightarrow \sigma$ | 5.0 | 3.46 | $\delta \rightarrow \sigma$ | 467.0 | 3.18 | - | - |
| $\pi \rightarrow \sigma$ | 2.0 | 3.52 | $\delta \rightarrow \sigma$ | 486.0 | 3.26 | - | - |
| $\pi \rightarrow \sigma$ | 3.0 | 3.59 | $\delta \rightarrow \sigma$ | 570.0 | 3.28 | 12500 | 3.33 |

* Experimental intensities are given by the molar absorption in $M^{-1}cm^{-1}$
*a*) Ref. 337

tronic transition compared to EOMCCSD. Examining the TD-DFT results one can clearly see that the closest excitation energies to the CC data are those obtained from the CAM-B3LYP-B exchange–correlation functional. The agreement between the CR-EOMCCSd(t) and CAM-B3LYP-B is very good, with differences of at most 0.22 eV. This finding agrees well with the previous theoretical studies of excited states in large molecules that consist of light elements [267, 269, 342].

### 12.4.2 Electronic Spectra of $[U^{V}O_2(saldien)]^-$ in DMSO

Based on the experience gained in the previous section, we can expect that TD-DFT is capable of predicting reliable excited states in the large actinide molecules which contain the $[UO_2]^{2+}$-unit. As the final test for the CAM-B3LYP-B exchange–correlation functional we compare the excitation energies obtained from it to the experimental data. We have used the same geometry as of the $U^{VI}O_2$(saldien).

The negative charge around the uranyl-saldien complex might lead to a stronger interaction with the DMSO environment than in the neutral $U^{VI}O_2$(saldien) system. In order to check this, we employed also excited-state calculations with two DMSO molecules which are explicitly included, as shown in Figure (12.1)(c).

All low-lying excited states and their intensities are tabulated in Table

(12.4), in which we investigated the two model systems: $[U^{V}O_2(saldien)]^-$ and $[U^{V}O_2(saldien)]^-$*2DMSO. The excitation energies obtained for both systems are almost identical in the lower part of the spectrum, but differ in the higher regions of the spectra, where other than internal uranyl transitions are present. The electronic transitions calculated for the smaller model compound are higher in energy and possess much lower intensities than those in the model with two explicit DMSO units. The electronic spectrum of the $[U^{V}O_2(saldien)]^-$*2DMSO molecule fits better the experimental data both in terms of energies and their intensities. For the first three excited states, deviations from experimental results are less than 0.2 eV and all these states are assigned to $\delta \rightarrow \sigma$ internal uranyl electronic transitions.

A much larger deviation is found for the two higher lying excited states observed in the experiment, *i.e.*, with energy of 1.77 and 1.97 eV. We assign them to different $\delta \rightarrow \sigma$ theoretically determined transitions at 2.55 and 2.69/2.70 eV based on their intensities. We assume that these excited states deviate from experiment because of the incompleteness of our theoretical model molecule — $[U^{V}O_2(saldien)]^-$*2DMSO. These particular transitions involve some charge transfer from the axial oxygen atoms of the uranyl unit, which also might be affected by another $[U^{V}O_2(saldien)]^-$ molecule on the top or on the bottom in the crystal structure, *cf.* Figure (12.1)(a).

The highest excited state recorded in experiment corresponds to 3.33 eV and exhibits a very high and broad intensity. We found a number of states with high intensities in this range of energy, *i.e.* 3.18, 3.26 and 3.28 eV, respectively. Since the last one (3.28 eV) with the main character of $\delta \rightarrow \sigma$ has the highest intensity, we thus assign this transition to the experimental value of 3.33 eV. Most probably the other theoretically determined states at 3.18 and 3.26 also contribute to the experimental spectrum, but they are difficult to detect due to a broad band with a molar absorption of 12500 $M^{-1}cm^{-1}$ at 3.33 eV. Such an intense molar absorption is attributed to the spin and Laporte allowed transitions.

## 12.5 Conclusions and Outlook

We calculated the spin–free vertical excitation energies of the $[UO_2]^+$, $[UO_2]^{2+}$, $U^{VI}O_2(saldien)$ molecules employing the TD-DFT/CAM-B3LYP-A, TD-DFT/CAM-B3LYP-B, EOMCCSD, CR-EOMCCSd(t)/EOMCCSD(T) approaches. A qualitative agreement between the TD-DFT and CC excited states has been observed. Among the two CAM-B3LYP variants, the CAM-B3LYP-B performs best in terms of absolute transition energies compared to CASPT2 and

CC data.

The small ECP with 78 electrons in the core gives incorrect results for the $[UO_2]^{2+}$ system as a results of transition energies which origin from the deeper part of the valence region in the system. This ECP is, however, sufficient for the $[UO_2]^{+}$ and $U^{VI}O_2$(saldien) molecules, which do not involve the transitions from the deeper occupied orbitals for which the ECP approximation is more sensitive.

For the electronic spectrum based on the $[U^{V}O_2(\text{saldien})]^{-}$*2DMSO model system, TD-DFT/CAM-B3LYP-B correctly model the experimentally recorded spectrum of the $[U^{V}O_2(\text{saldien})]^{-}$ in DMSO in terms of excitation energies and their intensities. The overall agreement is very good, only two of the transitions are overestimated by 0.6–0.7 eV in calculations. We think that this discrepancy is caused by the incompleteness of the $[U^{V}O_2(\text{saldien})]^{-}$*2DMSO system due to the possible interaction of the axial oxygen between two such units in the crystal structure. This hypothesis is currently investigated in our laboratory employing the FDE approach.

# Summary

Theoretical prediction of electronic spectra of uranium-containing complexes remains quite a challenge for quantum chemistry since it requires an accurate treatment of both correlation and relativistic effects at the same time. While reliable electronic excitation energies can be obtained from correlated wave function approaches that take relativistic effects into account, they are, however, limited to small system sizes. This includes small model complexes but prevents the treatment of full-fledged ligands. Large complexes that are of interest in nuclear waste reprocessing or in catalysis can only be investigated within a DFT framework based on the Kohn–Sham formalism. Since in Kohn–Sham DFT the exact exchange–correlation functional remains unknown, the accuracy of DFT calculations strongly depends on the applied approximations thereof and on which class of molecules or properties the density functional has been designed for. However, currently available approximate exchange–correlation functionals do not contain heavy elements like actinides in their parametrization sets, which may result in severe drawbacks when actinide-containing compounds are described by means of DFT. Hence, a thorough knowledge about the performance of DFT in studying such complexes is desirable, in particular, since actinides posses active and chemically different $f$-orbitals compared to lighter elements for which common density functionals are optimized. Although DFT or its time-dependent extension TD-DFT represent the methods of choice when large molecules and their properties are to be investigated, a systematic study of the excited-states of uranium compounds with different approximate exchange–correlation functionals has not yet been performed. This raises the question about the reliability and accuracy of the excitation energies obtained by TD-DFT. In order to gain first insights into the performance

of TD-DFT in a systematic way, we gradually defined a suitable benchmark set of small and medium-sized model complexes which represent essential building blocks in uranium-containing complexes and possess interesting electronic features. The excitation spectra of these benchmark molecules have been tested against highly accurate *ab initio* data obtained by CASPT2, CR-EOMCCSD(T) or IHFSCC-SD.

In a preliminary study (chapter 9), we chose three small-sized and isoelectronic uranium containing model complexes as the starting benchmark set: $UO_2^{2+}$, $NUO^+$ and NUN. This choice was deliberately made, since all complexes represent the building blocks found in larger uranium-containing complexes which are, *e.g.*, important in the processing of nuclear waste. The accuracy of different classes of exchange–correlation energy functionals, *i.e.*, local (LDA), GGA (PBE and BLYP), meta-GGA (M06-L), hybrid (B3LYP and PBE0), meta-hybrid (M06 and M06-2X), range-separated hybrid (CAM-B3LYP) and model SAOP potential, has been assessed by comparing spin–free vertical excitation energies determined by TD-DFT to reference data obtained by the CASPT2 and IHFSCC-SD approaches. It turns out that only the PBE0, M06 and CAM-B3LYP exchange–correlation energy functionals can qualitatively reproduce the reference data, while the other investigated exchange–correlation functionals yield transition energies with errors up to 1.5 eV. In particular, the CAM-B3LYP exchange–correlation functional performed best in reproducing the excitation energies of our small benchmark set, even outperforming CASPT2. Besides, we found that the relativistic ZORA Hamiltonian correctly reproduces the spin–free excitation energies of the DC Hamiltonian.

In a subsequent study (chapter 10), we extended the test set with the $[UO_2Cl_4]^{2-}$ complex which well-represents the $Cs_2UO_2Cl_4$ unit of the whole crystal structure that has been investigated experimentally by means of electronic spectroscopy. Due to its superiority demonstrated for the isoelectronic test set, the CAM-B3LYP exchange–correlation functional is applied to investigate the electronic spectrum of $[UO_2Cl_4]^{2-}$ under the effects of spin–orbit coupling. The electronic spectrum calculated by the long-range separated exchange–correlation functional CAM-B3LYP agrees well with the experimentally recorded adiabatic electronic spectrum. In addition, the larger amount of exact exchange at long interelectronic distances favors to recover higher-lying charge-transfer excited-states in the electronic spectrum. It is worth to mention that such transition energies are difficult to obtain with standard wave function methods.

In chapter 11, the benchmark set was further enlarged by the CUO molecule that is also isoelectronic to $UO_2^{2+}$, $NUO^+$ and NUN. The special feature of CUO is its greater sensitivity to a ground-state change compared to the other three-atomic test molecules. In experiments, a large red shift of the U–O and U–C stretching

vibrations is observed when the noble gas matrix is changed from neon, over argon and krypton to xenon. This characteristic red shift was assigned to a ground-state change of the CUO molecule resulting from interactions of the complex core with the noble gas matrix. In order to verify this hypothesis, we analyzed the electronic structure and the low-lying excited-states of the bare CUO molecule as well as the CUO moiety embedded in different noble gas cages.

For the bare CUO complex, comparison to FSCC-SD reference data indicates large errors in the vertical spin–free excitation energies obtained in TD-DFT calculations employing the PBE0 exchange–correlation functional. A detailed analysis of the failure of TD-DFT denotes a significant triplet instability error for CUO which is associated with the amount of exact exchange present in the exchange–correlation functional. In particular, a larger fraction of exact exchange corresponds to more pronounced triplet instabilities.

As model cages of the CUO molecule surrounded by the noble gas matrix, the $CUONg_4$ systems have been constructed, where Ng is one of the noble gases Ne, Ar, Kr or Xe, respectively. In order to simulate the noble gas environment, the total system has been partitioned in a FDE approach where the active system contains the bare CUO molecule, while the four noble gas atoms constitute the environment. Furthermore, the performance of different kinetic energy functionals has been investigated, *i.e.*, Thomas–Fermi, NDSD, PW91K and PW91K-CJCORR. Analyzing the integrated errors in the densities as well as the valence molecular orbitals demonstrates that none of the currently available kinetic energy functionals yields qualitatively accurate embedding potentials for all model systems studied, except for the PW91K kinetic energy functional which results in acceptable embedding potentials for the $CUONe_4$ and $CUOAr_4$ nobel gas cages. The embedding potential obtained with the PW91K kinetic energy functional is then utilized in WFT-in-DFT calculations employing the IHFSCC-SD method for the CUO core embedded in the $Ng_4$ potential obtained from DFT calculations. In opposite to what was suggested in experiments, our WFT-in-DFT studies do not predict a ground-state change when the noble gas cage is changed from neon to argon cages.

The results and insights gained in the above mentioned benchmark studies for small and medium-seized complexes could then be applied to study the excitation spectra of two larger uranium-containing compounds most efficiently, the $UO_2$(saldien) and $[UO_2(\text{saldien})]^-$ complexes (chapter 12). For the closed-shell $UO_2$(saldien) system, the CR-EOM-CCSD(T) approach was applied as reference calculation to assess the accuracy of the vertical spin–free excitation energies obtained from TD-DFT calculations employing the CAM-B3LYP exchange–

correlation functional which turned out to be superior for the small benchmark molecules. In particular, the amount of exact exchange in CAM-B3LYP has been adjusted at the long-range distance so that DFT and coupled cluster results do match. This optimized exchange–correlation functional designed to fit the reference excitation energies, is further employed to investigate the electronic spectrum of the open-shell $[UO_2(\text{saldien})]^-$ complex for which also experimental data is available. Our modified TD-DFT calculations qualitatively reproduces the experimental transition energies including their intensities.

Based on the benchmark studies as well as on the analysis of excitation spectra for full-fledged uranium complexes, general conclusions can be drawn. Notably, it is possible to obtain qualitatively correct electronic spectra of uranium-containing complexes within the TD-DFT framework employing the CAM-B3LYP exchange–correlation functional as long as the $UO_2^{2+}$ moiety is the structurally characteristic unit of the investigated compound. Furthermore, CAM-B3LYP allows to access higher-lying charge-transfer excited-states which are otherwise difficult to obtain in wave function based approaches. We have also demonstrated that the choice of the Hamiltonian is not of prior importance since the low-lying transition energies of uranium-containing complexes can be well-represented by approximate Hamiltonians, *e.g.*, the ZORA Hamiltonian. However, we also illustrated that new exchange–correlation functional need to be constructed which could describe different kinds of uranium-containing molecules at the same account, simultaneously yielding reliable excitation energies. Our studies provide deeper insights and instrumental information for a further development of such functionals.

# Samenvatting

**Naar betrouwbaar modelleren van aangeslagen toestanden van uraniumverbindingen**

De theoretische voorspelling van elektronische spektra van uraniumhoudende complexen blijft een behoorlijke uitdaging voor de kwantumchemie omdat het tegelijkertijd een nauwkeurige behandeling vereist van zowel correlatie als relativistische effecten. Alhoewel betrouwbare elektronische excitatieenergieën verkregen kunnen worden met gecorreleerde golffunctiemethodes die rekening houden met relativistische effecten, blijven de toepassingen ervan beperkt tot kleine systeemgrootten die kleine modelcomplexen omvatten waarbij de volledige liganden worden genegeerd. Omvangrijke complexen die interessant zijn voor de verwerking van nucleair afval of in katalyse kunnen alleen worden onderzocht met dichtheidsfuntionaaltheorie (DFT) waarvan het Kohn-Sham formalisme de meest gangbare uitwerking is. Omdat in Kohn-Sham DFT de exacte uitwissel-correlatie functionaal onbekend blijft, hangt de nauwkeurigheid van een DFT berekening sterk af van de gekozen benaderingen ervan en voor welke klasse van moleculen of eigenschappen de dichtheidsfunctionaal is ontworpen. Echter, de huidige beschikbare benaderde uitwissel-correlatie functionalen bevatten geen zware elementen zoals actiniden in hun parametrisatiesets, waardoor de beschrijving van actinidehoudende verbindingen met DFT tot ernstige tekortkomingen zou kunnen leiden. Daarom zou een grondige kennis over de werking van DFT voor zulke complexen wenselijk zijn, met name omdat actiniden actieve *f*-orbitalen hebben met een geheel eigen

chemisch karakter, die geen rol spelen in lichtere elementen waarvoor de normale dichtheidsfunctionalen geoptimaliseerd zijn. Alhoewel DFT al dan niet met tijdsafhankelijke extensie (TD-DFT) de voorkeursaanpak is wanneer grote moleculen en hun eigenschappen onderzocht moeten worden, heeft een systematische studie van de aangeslagen toestanden van uraniumverbindingen met verscheidene benaderde uitwissel-correlatie functionalen nog niet plaatsgevonden. Dit roept de vraag op over de betrouwbaarheid en nauwkeurigheid van de excitatie-energieën verkregen met TD-DFT. Om op een systematische manier tot een eerste inzicht te komen in de werking van TD-DFT hebben we geleidelijk een geschikte referentieset van kleine tot middelgrote modelcomplexen gedefinieerd die essentiële bouwstenen van uraniumhoudende complexen representeren en interessante elektronische kenmerken hebben. We hebben de excitatiespectra van deze referentiemoleculen langs de meetlat gelegd van uiterst nauwkeurige *ab initio* gegevens, verkregen met CASPT2, CR-EOMCCSD(T) of IHFSCC-SD.

Als een voorbereidende studie (hoofdstuk 9) kozen we drie kleine, isoelectronische uraniumhoudende modelcomplexen als uitgangsreferentieset: $UO_2^{2+}$, $NUO^+$ en NUN. Deze keuze was doelbewust omdat al deze complexen bouwstenen representeren die men aantreft in grotere uraniumhoudende complexen die bijvoorbeeld van belang zijn voor het verweken van nucleair afval. De nauwkeurigheid van verscheidene klassen van uitwissel-correlatie energiefunctionalen, namelijk van de klasse lokaal (LDA), gradiënt gecorrigeerd (PBE en BLYP), meta-GGA (M06-L), hybride (B3LYP en PBE0), meta-hybride (M06 en M06-2X), bereik-gescheiden hybride (CAM-B3LYP) en modelpotentiaal (SAOP), is onderzocht door spinvrije verticale excitatie-energieën verkregen met tijdsafhankelijke DFT te vergelijken met referentiegegevens verkregen met de CASPT2 en IHFSCC-SD methodes. Het blijkt dat alleen de BPE0, M06 en CAM-B3LYP functionalen kwalitatief de referentiedata kunnen reproduceren, terwijl de overige onderzochte functionalen fouten tot op 1.5 eV maken voor de overgangsenergieën. Met name slaagt CAM-B3LYP er het beste in om de excitatie-energieën te reproduceren van onze kleine referentieset, en verslaat in dit geval zelfs CASPT2. Tevens hebben we kunnen vaststellen dat de ZORA Hamiltoniaan correct de spinvrije excitatie-energieën reproduceert van de DC Hamiltoniaan.

In een vervolgstudie (hoofdstuk 10) hebben we de testset uitgebreid met het $[UO_2Cl_4]^{2-}$ complex dat een goede representant is van de $Cs_2UO_2Cl_4$ basiseenheid van de gehele kristalstructuur die experimenteel is onderzocht met elektronspectroscopie. Vanwege de gedemonstreerde superioriteit voor de isoelektronische testset, pasten wij de CAM-B3LYP functionaal toe om het elektronische spectrum van $[UO_2Cl_4]^{2-}$ te onderzoeken onder invloed van spin-baan-koppeling. Het met de

lange-dracht gescheiden uitwissel-correlatie functionaal CAM-B3LYP berekende spectrum vertoont een goede overeenkomst met het experimenteel waargenomen adiabatische elektronische spectrum. Met name CAM-B3LYPSs grotere hoeveelheid van exacte uitwisselinteractie op grote interelektronische afstanden bevordert het correct vinden van hoger gelegen met ladingsoverdracht gepaard gaande aangeslagen toestanden in het elektronische spectrum. Het is vermeldenswaardig dat zulke overgansenergieën moeilijk te verkrijgen zijn met standaard golffunctiemethodes.

In hoofdstuk 11 breidden we de referentieset verder uit met het CUO molekuul dat eveneens isoelektronisch is met $UO_2^{2+}$, $NUO^+$ en NUN. Het bijzondere aan CUO is de grotere gevoeligheid voor een verandering in de grondtoestand in vergelijking tot de andere drieatomige moleculen. Experimenteel wordt een grote roodverschuiving waargenomen in de U–O en U–C strekvibraties wanneer de edelgasmatrix wordt veranderd van neon naar argon, krypton of xenon. Deze karakteristieke roodverschuiving werd toegeschreven aan een verandering in de grondtoestand van het CUO molecuul veroorzaakt door de interactie ervan met de matrix van edelgas. Om deze hypothese te verifiëren hebben we de elektronische structuur en de laag liggende aangeslagen toestanden geanalyseerd van zowel het kale CUO molekuul als het CUO als onderdeel van de verschillend edelgasomgevingen.

Voor het vrije CUO molecuul laat een vergelijking met IHFSCC-SD referentiedata grote fouten zien in de verticale spinvrije excitaties die verkregen zijn met TD-DFT berekeningen met de PBE0 uitwissel-correlatie functionaal. Een gedetailleerde analyse van de fout toont aan dat er een significante triplet-instabiliteitfout is, die gerelateerd is aan de gebruikte hoeveelheid exacte uitwisselenergie in de uitwissel-correlatie functionaal. Een grotere fractie van de exacte uitwisselenergieterm correspondeert met meer uitgesproken tripletinstabiliteiten.

Als kooimodellen voor het CUO molecuul omringd door een edelgasmatrix hebben we $CUONg_4$ systemen beschouwd, met Ng één van de edelgassen Ne, Ar, Kr of Xe. Om de edelgasomgeving te modelleren hebben we het totale systeem verdeeld in een bevroren-dichtheid-inkapseling-benadering waar CUO het actieve systeem is en de dichtheid van de vier edelgasatomen bevroren blijft. We hebben ook de werking van verschillende kinetische dichtheidsfunctionalen onderzocht, om precies te zijn deze: Thomas-Fermi, NDSD, PW91K en tot slot PW91K-CJCORR. Een analyse van de geïntegreerde fouten in de dichtheden en de valentie moleculaire orbitalen toont aan dat geen van de huidige beschikbare kinetische energiefunctionalen nauwkeurige inkapselpotentialen levert voor de onderzochte systemen, met uitzondering van de PW91K functionaal, die resulteert in acceptabele inkapselpotentialen

voor de $CUONe_4$ en $CUOAr_4$ edelgaskooien. De inkapselpotentiaal verkregen met de PW91K kinetische energiefunctionaal hebben we ingezet in golffunctietheorie-in-DFT berekeningen gebruik makende van de IHFSCC-SD methode voor de CUO kern, ingekapseld in de $Ng_4$ potentiaal van de DFT berekeningen. In tegenstelling tot wat door het experiment werd gesuggereerd, laten onze berekeningen geen grondtoestandverandering zien wanneer de kooi van edelgas veranderd wordt van neon naar argon.

De resultaten en inzichten verkregen met de bovengenoemde referentiestudie voor kleine en middelgrote complexen konden vervolgens worden aangewend om zeer efficiënt de excitatiespectra van twee grote uranium bevattende verbindingen te bestuderen, namelijk de $UO_2$(saldien) en $[UO_2(\text{saldien})]^-$ complexen (hoofdstuk 12). Voor het gesloten-schil $UO_2$(saldien) systeem pasten wij de CR-EOMCCSD(T) methode toe als referentieberekening om de nauwkeurigheid te schatten van verticale spinvrije excitatie-energieën die verkregen zijn met TD-DFT berekeningen gebruik makende van de CAM-B3LYP functionaal die de beste bleek voor de kleine moleculen in de referentieset. Met name werd de hoeveelheid exacte uitwisselenergie in CAM-B3LYP aangepast voor de lange afstand om de DFT en gekoppelde cluster resultaten te laten overeenkomen. Deze geoptimaliseerde uitwissel-correlatie functionaal, gemaakt om de referentie excitatie-energieën te fitten, zetten we vervolgens in om het elektronische spectrum van het open-schil $[UO_2(\text{saldien})]^-$ complex te bestuderen waarvoor ook experimentele gegevens beschikbaar zijn. Onze aangepaste TD-DFT berekeningen reproduceren kwalitatief de experimentele overgangsenergieën, inclusief hun intensiteiten.

Gebaseerd op zowel de referentiestudies als de analyse van de excitatiespectra voor realistische uraniumcomplexen kunnen algemene conclusies worden getrokken. In het bijzonder is het mogelijk om kwalitatief correcte elektronische spectra te verkrijgen voor uraniumhoudende complexen binnen het TD-DFT kader met gebruikmaking van de CAM-B3LYP functionaal onder de voorwaarde dat het $UO_2^{2+}$ deel ervan de structureel karakteristieke eenheid is van de onderzochte stof. Bovendien geeft de CAM-B3LYP functionaal ons toegang tot hoger liggende aangeslagen toestanden met een ladingsoverdracht karakter, die anders maar moeilijk te verkrijgen zijn met een op golffuncties gebaseerde aanpak. We hebben ook aangetoond dat het beschouwen van viercomponentige Hamiltonianen niet van groot belang is, omdat de laag liggende overgangsenergieën van uraniumhoudende complexen al goed door tweecomponentige Hamiltonianen gerepresenteerd worden, zoals bijvoorbeeld de ZORA Hamiltoniaan. Echter hebben we ook aangetoond dat nieuwe uitwissel-correlatie functionalen ontworpen moeten worden om verschillende soorten uranium bevattende moleculen te beschrijven, en tegelijkertijd betrouwbare

excitatie-energieën te leveren. Onze studies verschaffen dieper inzicht en belangrijke informatie voor de verdere ontwikkeling van zulke functionalen.

# List of acronyms

| | |
|---|---|
| **1-SIE** | one-electron self-interaction error |
| **ADF** | Amsterdam density functional theory program package |
| **au** | atomic units |
| **ALDA** | adiabatic local density approximation |
| **au** | atomic (unit) |
| **aug-cc-pVDZ** | augmented correlation consistent polarization valence double-zeta (basis set) |
| **aug-cc-pVTZ** | augmented correlation consistent polarization valence triple-zeta (basis set) |
| **B86** | Becke 1986 (xc functional) |
| **B88** | Becke 1988 (xc functional) |
| **B3LYP** | Becke three parameter Lee–Yang–Parr (xc functional) |
| **BLYP** | Becke–Lee–Yang–Parr (xc functional) |
| **CAM-B3LYP** | Coulomb attenuation method Becke three parameter Lee–Yang–Parr (xc functional) |
| **CAM-B3LYP-A** | Coulomb attenuation method Becke three parameter Lee–Yang–Parr with $\beta$=0.46 (xc functional) |
| **CAM-B3LYP-B** | Coulomb attenuation method Becke three parameter Lee–Yang–Parr with $\beta$=0.81 (xc functional) |

| | |
|---|---|
| **CASPT2** | complete active space second order perturbation theory (method) |
| **CASSCF** | complete active space self-consistent field theory (method) |
| **CC** | coupled cluster (method) |
| **CCSD** | coupled cluster with singles and doubles (method) |
| **CCSDT** | coupled cluster with singles, doubles and triples (method) |
| **CCSD(T)** | coupled cluster with singles, doubles and perturbative triples (method) |
| **CFM** | crystal field model |
| **CI** | configuration interaction (method) |
| **CIS** | configuration interaction with singles (method) |
| **CISD** | configuration interaction with singles and doubles (method) |
| **CISDT** | configuration interaction with singles, doubles and triples (method) |
| **CR-EOMCCSD(T)** | completely renormalized equation of motion coupled cluster with singles, doubles and non-iterative triples (method) |
| **CR-EOMCCSd(t)** | active space variant of completely renormalized equation of motion coupled cluster with singles, doubles and non-iterative triples (method) |
| **CSF** | configuration state function |
| **COSMO** | conductor-like screening model |
| **CT** | charge-transfer (excitation) |
| **DC** | Dirac–Coulomb (Hamiltonian) |
| **def-TZVP** | default triple zeta valence polarization (basis set) |
| **DFT** | density functional theory |
| **DFT-in-DFT** | density functional theory in density functional theory |
| **DIRAC** | Dirac program package |
| **DKH2** | second order Douglas–Kroll–Hess (Hamiltonian) |
| **DMSO** | dimethyl sulfoxide |
| **DZP** | double-zeta polarization (basis set) |
| **EA** | electron affinity |

| | |
|---|---|
| **EFP** | effective fragment potential (method) |
| **EOMCC** | equation of motion coupled cluster (method) |
| **EOMCCSD** | equation of motion coupled cluster with singles and doubles (method) |
| **EOMCCSDT** | equation of motion coupled cluster with singles, doubles and triples (method) |
| **ECP** | effective core potential (method) |
| **eV** | electronvolt (unit) |
| **FCI** | full configuration interaction (method) |
| **FDE** | frozen density embedding |
| **FS** | Fock-space |
| **FSCC** | Fock-space coupled cluster (method) |
| **FSCC-SD** | Fock-space coupled cluster with singles and doubles (method) |
| **GEA** | gradient expansion approximation |
| **GGA** | general gradient approximation |
| **HF** | Hartree–Fock (method) |
| **HS** | Hilbert-space |
| **HOMO** | highest occupied molecular orbital |
| **IHFSCC** | intermediate Hamiltonian Fock-space coupled cluster (method) |
| **IHFSCC-SD** | intermediate Hamiltonian Fock-space coupled cluster with singles and doubles (method) |
| **IP** | ionization potential |
| **KS** | Kohn–Sham |
| **LDA** | local density approximation |
| **L** | local (excitation) |
| **LMCT** | ligand-to-metal charge-transfer (excitation) |
| **LR-CCSD** | linear response coupled cluster with singles and doubles |
| **LSDA** | local spin-density approximation |
| **LUMO** | lowest unoccupied molecular orbital |

| | |
|---|---|
| **LYP** | Lee–Yang–Parr (xc functional) |
| **M06** | global hybrid Minnesota 2006 (xc functional) |
| **M06-L** | meta-GGA Minnesota 2006 (xc functional) |
| **M06–2X** | Minnesota 2006 (M06) with double amount (54%) of exact exchange (xc functional) |
| **MLCT** | metal-to-ligand charge-transfer (excitation) |
| **NDSD** | non-decomposable (kinetic energy functional) |
| **MO** | molecular orbital |
| **MR** | multi-reference |
| **MOLCAS** | Molcas program package |
| **MS-CASPT2** | multi-state complete active space second order perturbation theory (method) |
| **MUE** | mean unsigned error |
| **N-SIE** | N-electron self-interaction error |
| **NWChem** | North-Western Chemistry program package |
| **PBE** | Perdew–Becke–Ernzerhof (xc functional) |
| **PBE0** | Perdew–Becke–Ernzerhof with 25% of exact exchange (xc functional) |
| **PT2** | second order perturbation theory (method) |
| **PW91K** | Perdrew–Wang (kinetic energy functional) |
| **CJCORR** | Jacob correction to Perdrew–Wang (kinetic energy functional) |
| **PYADF** | python scripting framework to ADF program (program) |
| **QM/MM** | mixed molecular mechanic/quantum mechanics (method) |
| **R** | Rydberg (excitation) |
| **SAOP** | statistical average of orbital potential (model potential) |
| **SCF** | self-consistent field (theory) |
| **SIE** | self-interaction error |
| **SOC** | spin–orbit coupling |
| **S-T** | singlet-triplet splitting |

| | |
|---|---|
| **TCE** | tensor contraction engine |
| **TD-DFT** | time-dependent density functional theory |
| **TF** | Thomas–Fermi (kinetic energy functional) |
| **TD-HF** | time-dependent Hartree–Fock (method) |
| **TD-KS** | time-dependent Kohn–Sham (equation) |
| **TURBOMOLE** | Turbomole program package |
| **TZ2P** | triple-zeta double polarization (basis set) |
| **UEG** | uniform electron gas |
| **VWN** | Vosko–Wilk–Nusair (xc functional) |
| **WFT** | wave function theory |
| **WFT-in-DFT** | wave function theory in density functional theory |
| **XALDA** | adiabatic local density approximation with inclusion of exact exchange in the kernel |
| **xc** | exchange–correlation |
| **ZORA** | zeroth order regular approach (Hamiltonian) |

# Bibliography


[1] Cotton, S. *Lanthanide and actinde chemistry*. Wiley, 2005.

[2] Morss, L. R., Edelstein, N. M., Fuger, J. *The Chemistry of the Actinide and Transactinide Elements*. Springer, 2010.

[3] Binnemans, K., Lanthanides and actinides in ionic liquids, *Chem. Rev.*, **107** (2007) 2592.

[4] Fortier, S., Hayton, T. W., Oxo ligand functionalization in the uranyl ion ($UO_2^{2+}$), *Coord. Chem. Rev.*, **254** (2010) 197.

[5] Denning, R. G., Electronic structure and bonding in actinyl ions and their analogs, *J. Phys. Chem. A*, **111** (2007) 4125.

[6] Dolg, M., Cao, X., Relativistic pseudopotentials: Their development and scope of applications, *Chem. Rev.*, **112** (2012) 403.

[7] Reiher, M., Wolf, A. *Relativistic Quantum Chemistry. The Fundamental Theory of Molecular Science*. Wiley, 2009.

[8] Saue, T., Relativistic hamiltonians for chemistry: A primer, *Chem. Phys. Chem*, **3** (2012) 3077.

[9] Liang, B., Andrews, L., Li, J., Bursten, B. E., On the noble-gas-induced intersystem crossing for the CUO molecule: Experimental and theoretical investigations of $CUO(Ng)_n$ (Ng = Ar, Kr, Xe; n = 1, 2, 3, 4) complexes in solid neon, *Inorg. Chem.*, **43** (2004) 882.

[10] Arnold, P. L., Patel, D., Wilson, C., Love, J. B., Reduction and selective oxo group silylation of the uranyl dication., *Nature*, **451** (2008) 7176.

[11] Arnold, P. L., Pecharman, A.-F., Hollis, E., Yahia, A., Maron, L., Parsons, S., Love, J. B., Uranyl oxo activation and functionalization by metal cation coordination., *Nature Chemistry*, **2** (2010) 1056.

[12] Pan, Q.-J., Shamov, G. A., Schreckenbach, G., Binuclear uranium(VI) complexes with a "Pacman" expanded porphyrin: Computational evidence for highly unusual bis-actinyl structures, *Chem. Eur. J.*, **16** (2010) 2282.

[13] Pogány, P., Kovács, A., Varga, Z., Bickelhaupt, F. M., Rudy, J., Theoretical study of the structure and bonding in $ThC_2$ and $UC_2$., *J. Phys. Chem. A*, **116** (2012) 747.

[14] Arnold, P. L., Jones, G. M., Odoh, S. O., Schreckenbach, G., Magnani, N., Love, J. B., Strongly coupled binuclear uranium-oxo complexes from uranyl oxo rearrangement and reductive silylation., *Nature Chemistry*, **4** (2012) 221.

[15] Pepper, M., Bursten, B. E., The electronic structure of actinide-containing molecules: a challenge to applied quantum chemistry, *Chem. Rev.*, **91**(5) (1991) 719.

[16] Allen, F. H., The Cambridge Structural Database: a quarter of a million crystal structures and rising. , *Acta Cryst.*, **B58** (2002) 380.

[17] Arnold, P. L., Love, J. B., Patel, D., Pentavalent uranyl complexes., *Coord. Chem. Rev.*, **253** (2009) 1973.

[18] Nash, K., A review of the basic chemistry and recent developments in trivalent f-elements separations, *Solvent Extr. Ion Exch.*, **11**(729) (1993) 11729.

[19] Nash, K. L., Barrans, R. E., Chiarizia, R., Dietz, M. L., Jensen, M., Rickert, P., Moyer, B. A., Bonnesen, P. V., Bryan, J. C., Sachleben, R. A., Fundamental investigations of separations science for radioactive materials, *Solvent Extr. Ion Exch.*, **18**(729) (2000) 605.

[20] Hutchings, G. J., Heneghan, C. S., Hudson, I. D., Taylor, S. H., Uranium-oxide-based catalysts for the destruction of volatile chloro-organic compounds, *Nature*, **384** (1996) 341.

[21] Ephritikhine, M., The vitality of uranium molecular chemistry at the dawn of the XXIst century., *Dalton Trans.*, **21** (2006) 2501.

[22] Hunt, R. D., T.Yustein, J., Andrews, L., Matrix infrared-spectra of NUN formed by the insertion of uranium atoms into molecular nitrogen, *J. Chem. Phys.*, **98** (1993) 6070.

[23] Pyykkö, P., Li, J., Runeberg, N., Quasirelativistic pseudopotential study of species isoelectronic to uranyl and the equatorial coordination of uranyl, *J. Phys. Chem.*, **98** (1994) 4809.

[24] Brown, D. R., Denning, R. G., Stable analogs of the uranyl ion containing the –NUN– group, *Inorg. Chem.*, **35** (1996) 6158.

[25] Kaltsoyannis, N., Computational study of analogues of the uranyl ion containing the -NUN- unit: Density functional theory calculations on $UO_2^{2+}$, $UON^+$, $UN_2$, $UO(NPH_3)^{3+}$, $U(NPH_3)_2^{4+}$, $[UCl_4NPR_3]$ (R = H, Me), and $[UOCl_4NP(C_6H_5)_3]$, *Inorg. Chem.*, **39** (2000) 6009.

[26] Li, J., Bursten, B. E., Liang, B., Andrews, L., Noble gas-actinide compounds: Complexation of the CUO molecule by Ar, Kr, and Xe atoms in noble gas matrices, *Science*, **295** (2002) 2242.

[27] Roos, B. O., P.-O.Widmark„ Gagliardi, L., The ground state and electronic spectrum of CUO: a mystery, *Faraday Discuss.*, **124** (2003) 57.

[28] Infante, I., Visscher, L., The importance of spin-orbit coupling and electron correlation in the rationalization of the ground state of the CUO molecule, *J. Chem. Phys.*, **121**(12) (2004) 5783.

[29] Barker, T. J., Denning, R. G., Thorne, J. R. G., Applications of two-photon spectroscopy to inorganic compounds. 1. Spectrum and electronic structure of dicesium tetrachlorodioxouranate, *Inorg. Chem.*, **26**(1) (1987) 1721.

[30] Denning, R. G., Morrison, I. D., The electronic structure of actinyl ions: the excited-state absorption spectrum of $Cs_2UO_2Cl_4$, *Chem. Phys. Lett.*, **180** (1991) 101.

[31] Zhou, M., Andrews, L., Li, J., Bursten, B. E., Reaction of laser-ablated uranium atoms with CO: Infrared spectra of the CUO, CUO-, OUCCO, ($\eta$(2)C-2)$UO_2$, and $U(CO)_x$ (x=1-6) molecules in solid neon, *J. Am. Chem. Soc.*, **121** (1999) 9712.

[32] Mizuoka, K., Kim, S.-Y., Hasegawa, M., Hoshi, T., Uchiyama, G., Ikeda, Y., Electrochemical and spectroelectrochemical studies on $UO_2$(saloph)L (saloph = N,NâĂŸ-disalicylidene-o-phenylenediaminate, L = dimethyl sulfoxide or N,N-dimethylformamide), *Inorg. Chem.*, **42** (2003) 1031.

[33] Lue, C. J., Jin, J., Ortiz, M. J., Rienstra-Kiracofe, J. C., Heaven, M. C., Electronic spectroscopy of $UO_2$ isolated in a solid Ar matrix, *J. Am. Chem. Soc.*, **126** (2004) 1812.

[34] Takao, K., Tsushima, S., Takao, S., Scheinost, A. C., Bernhard, G., Ikeda, Y., Hennig, C., X-ray absorption fine structures of uranyl(V) complexes in a nonaqueous solution, *Inorg. Chem.*, **48** (2009) 9602.

[35] Pierloot, K., van Besien, E., Electronic structure and spectrum of $UO_2^{2+}$ and $UO_2Cl_4^{2-}$, *J. Chem. Phys.*, **123** (2005) 204309.

[36] Pierloot, K., van Besien, E., van Lenthe, E., Baerends, E. J., Electronic spectrum of $UO_2^{2+}$ and $[UO_2Cl_4]^{2-}$ calculated with time-dependent density functional theory, *J. Chem. Phys.*, **126** (2007) 194311.

[37] Planck, M., Distribution of energy in the normal spectrum, *Verhand. Deutsche Physikal. Gesell.*, **2** (1900) 237.

[38] Einstein, A., Generation and conversion of light with regard to a heuristic point of vieiw, *Ann. der Physik*, **17** (1905) 132.

[39] Kołos, W. *Chemia kwantowa*. PWN, 1978.

[40] Gumiński, K., Petelenz, P. *Elementy chemii teoretycznej*. PWN, 1989.

[41] Piela, L. *The ideas of qunatum chemistry*. Elsevier, 2007.

[42] Harris, D. C., Bertolucci, M. D. *Symmetry and spectroscopy. An introduction to vibrational and electronic spectroscopy*. Dover, 1989.

[43] Atkins, P. W. *Podstawy chemii fizycznej*. PWN, 2002.

[44] Atkins, P. W. *Chemia fizyczna*. PWN, 2003.

[45] Born, M., Oppenheimer, J. R., Zur quantentheorie der molekeln, *Ann. Physic*, **84** (1927) 457.

[46] Schrödinger, E., An undulatory theory of the mechanics of atoms and molecules, *Phys. Rev.*, **28** (1926) 1049.

[47] Koch, W., Holthausen, M. C. *A Chemis's Guide to Density Functional Theory*. Wiley, 2001.

[48] Hohenberg, P., Kohn, W., Inhomogeneous electron gas, *Phys. Rev.*, **136** (1964) 864.

[49] Kohn, W., Sham, L. J., Self-consistent equations including exchange and correlation effects, *Phys. Rev.*, **140** (1965) 1133.

[50] Thomas, L. H., The calculation of atomic fields, *Math. Proc. Camb. Phil. Soc*, **23** (1927) 542.

[51] Dirac, P. A. M., Note on exchange phenomena in the Thomas atom, *Proc. Camb. Phil. Soc*, **26**(376) (1930.

[52] Cremer, D., Density functional theory: coverage of dynamic and non-dynamic electron correlation effects, *Mol. Phys.*, **99** (2001) 1899.

[53] Cohen, A. J., Mori-Sánchez, P., Yang, W., Challenges for Density Functional Theory, *Chem. Rev.*, **112** (2012) 289.

[54] Runge, E., Gross, E. K. U., Density-functional theory for time-dependent systems, *Phys. Rev. Lett.*, **52** (1984) 997.

[55] Casida, M. E. *Recent Advances in Density Functional Methods, Part I*. Word Scientific, 1995.

[56] Mahan, G. D., Subbaswamy, K. R. *Local Density Theory of Polarizability*. Plenum, 1990.

[57] van Leeuwen, R., Causality and symmetry in time-dependent density-functional theory, *Phys. Rev. Lett.*, **80** (1998) 1280.

[58] Marques, M. A. L., Ullrich, C. A., Rubio, A., Burke, K., Gross, E. K. U. Time-Dependent Density Functional Theory. In *Lecture notes in physics*. Springer, 2006.

[59] Petersilka, M., Gross, E. K. U., Burke, K., Excitation energies from time-dependent density-functional theory using exact and approximate potentials, *Int. J. Quantum Chem.*, **80** (2000) 534.

[60] Görling, A., Time-dependent Kohn–Sham formalism, *Phys. Rev. A*, **55** (1997) 2630.

[61] van Leeuwen, R., Key concepts in time-dependent density-functional theory, *Int. J. Mod. Phys. B*, **50** (2001) 1969.

[62] Marques, M. A. L., Gross, E. K. U., Time-dependent density functional theory, *Annu. Rev. Phys. Chem.*, **44** (2004) 110.

[63] Burke, K., Werschnik, J., Gross, E. K. U., Time-dependent density functional theory: Past, present, and future, *J. Chem. Phys.*, **123** (2005) 062206.

[64] Dreuw, M., Weisman, J. L., Head-Gordon, M., Long-range charge-transfer excited states in time-dependent density functional theory require non-local exchange, *J. Chem. Phys.*, **119** (2003) 2943.

[65] Tozer, D. J., Relationship between long-range charge-transfer excitation energy error and integer disontinuity in Kohn–Sham theory, *J. Chem. Phys.*, **119** (2003) 12697.

[66] Mundt, M., Kümmel, S., Derivative discontinuities in time-dependent density-functional theory, *Phys. Rev. Lett.*, **95** (2005) 203004.

[67] Vieira, D., Capelle, K., Ullrich, C. A., Physical signatures of discontinuities of the time-dependent exchange–correlation potential, *Phys. Chem. Chem. Phys.*, **11** (2009) 4647.

[68] Bauernschmitt, R., Ahlrichs, R., Treatment of electronic excitations within the adiabatic approximation of time-dependent density-functional theory, *Chem. Phys. Lett.*, **250** (1996) 454.

[69] Ceperlay, D. M., Alder, B. J., Ground state of the electron gas by a stochastic method, *Phys. Rev. Lett.*, **45** (1980) 566.

[70] Vosko, S. H., Wilk, L., Nusair, M., Accurate spin-dependent electron liquid correlation energies for local spin-density calculations - A critical analysis, *Can. J. Phys.*, **58** (1980) 1200.

[71] Gunnarsson, O., Lundqvist, B. I., Exchange and correlation in atoms, molecules, and solids by the spin-density-functional formalism, *Phys. Rev. B*, **13** (1976) 4274.

[72] Tozer, D. J. Density functional theory. In *European Summerschool in Quantum Chemistry*. Per-Olof Widmark, 2009.

[73] Parr, R. G., Yang, W. *Density Functional Theory of atoms and molecules*. Oxford, 1989.

[74] Becke, A., Density-functional exchange-energy approximation with correct asymphotic-behavior, *Phys. Rev. A*, **38** (1988) 3098.

[75] Lee, C., Yang, W., Parr, R. G., Development of the Colle-Salvetti correlation-energy formula into a functional of the electron-density, *Phys. Rev. B*, **37** (1988) 785.

[76] Perdew, J. P., Burke, K., Ernzerhof, M., Generalized gradient approximation made simple, *Phys. Rev. Lett.*, **77** (1996) 3865.

[77] Zhao, Y., Truhlar, D. G., A new local density functional for main-group thermochemistry, transition metal bonding, thermochemical kinetics, and noncovalent interactions, *J. Chem. Phys.*, **125** (2006) 13126.

[78] Voorhis, T. V., Scuseria., G. E., A novel form for the exchange–correlation energy functional, *J. Phys. Chem.*, **109** (1998) 400.

[79] Zhao, Y., Schultz, N. E., Truhlar, D. G., exchange–correlation functional with broad accuracy for metallic and nonmetallic compounds, kinetics, and noncovalent interactions, *J. Chem. Phys.*, **123** (2005) 161103.

[80] Zhao, Y., Truhlar, D. G., Density functionals with broad applicability in chemistry, *Acc. Chem. Res.*, **41** (2008) 157.

[81] Jacquemin, D., Perpéte, E. A., Ciofini, I., Adamo, C., Valero, R., Zhao, Y., Truhlar, D. G., On the performances of the M06 family of density functionals for electronic excitation energies, *J. Chem. Theory Comput.*, **6** (2010) 2071.

[82] Nalewajski, R. F. *Podstawy i metody chemii kwantowej*. PWN, 2001.

[83] Becke, A. D., Density-functional thermochemistry. III. The role of exact exchange, *J. Chem. Phys.*, **98** (1993) 5648.

[84] Stephens, P. J., Devlin, F. J., Chabalowski, C. F., Frisch, M. J., Ab initio calculation of vibrational absorption and circular dichroism spectra using density functional force fields, *J. Phys. Chem.*, **98** (1994) 11623.

[85] Ernzerhof, M., Scuseria, G., Assessment of the Perdew-Burke-Ernzerhof exchange–correlation functional, *J. Chem. Phys.*, **110** (1999) 5029.

[86] Grimme, S., Accurate description of van der Waals complexes by density functional theory including empirical corrections, *J. Comput. Chem.*, **25** (2004) 1463.

[87] Zhao, Y., Truhlar, D. G., The M06 suite of density functionals for main group thermochemistry, thermochemical kinetics, noncovalent interactions, excited states, and transition elements: two new functionals and systematic testing of four M06-class functionals and 12 other functionals, *Theor. Chem. Acc.*, **120** (2008) 215.

[88] Tawada, Y., Tsuneda, T., Yanagisawa, S., A long-range-corrected time-dependent density functional theory, *J. Chem. Phys.*, **120** (2004) 8425.

[89] Iikura, H., Tsuneda, T., Yanai, T., K.Hirao,, A long-range correction scheme for generalized-gradient-approximation exchange functionals, *J. Chem. Phys.*, **112** (2001) 3540.

[90] Yanai, T., Tew, D. P., Handy, N. C., A new hybrid exchange–correlation functional using the Coulomb-attenuating method (CAM-B3LYP), *Chem. Phys. Lett.*, **393** (2004) 51.

[91] van Leeuwen, R., Baerends, E. J., exchange–correlation potential with correct asymptotic-behavior, *Phys. Rev. A*, **49** (1994) 2421.

[92] Gritsenko, O., Schipper, P., Baerends, E., Approximation of the exchange–correlation Kohn–Sham potential with a statistical average of different orbital model potentials, *Chem. Phys. Lett.*, **302** (1999) 199.

[93] Schipper, P. R. T., Gritsenko, O. V., van Gisbergen, S. J. A., Baerends, E. J., Molecular calculations of excitation energies and (hyper)polarizabilities with a statistical average of orbital model exchange–correlation potentials, *J. Chem. Phys.*, **112** (2000) 1344.

[94] Gritsenko, O. V., van Leeuwen, R., van Lenthe, E., Baerends, A. J., Molecular Kohn–Sham exchange–correlation potential from the correlated ab-initio electron-density, *Phys. Rev. A*, **51** (1995) 1944.

[95] Gritsenko, O. V., van Leeuwen, R., Baerends, A. J., Direct approximation of the long- and short-range components of the exchange–correlation Kohn–Sham potential, *Int. J. Quantum Chem.*, **61** (1997) 231.

[96] Tecmer, P., Gomes, A. S. P., Ekström, U., Visscher, L., Electronic spectroscopy of $UO_2^{2+}$, $NUO^+$ and NUN: an evaluation of time-dependent density functional theory for actinides, *Phys. Chem. Chem. Phys.*, **13** (2011) 6249.

[97] Wei, F., Wu, G., Schwarz, W. H. E., Li, J., Geometries, electronic structures, and excited states of $UN_2$, $NUO^+$, and $UO_2^{2+}$ : a combined CCSD(T), RAS/CASPT2 and TDDFT study, *Theor. Chem. Acc.*, **129** (2011) 467.

[98] Szabo, A., Ostlund, N. S. *Modern Quantum Chemistry: Introduction to Advanced Electronic Structure Theory.* McGraw-Hill, 1989.

[99] Helgaker, T., Jørgensen, P., Olsen, J. *Molecular Electronic-Structure Theory.* Wiley, 2000.

[100] Roos, B. Multiconfigurational quantum chemistry for ground and excited-states. In *Radiation Induced Molecular Phenomena in Nucleic Acids*, p. 125. Springer, 2008.

[101] Bartlett, R. J., Musiał, M., Coupled-cluster theory in quantum chemistry, *Rev. Mod. Phys.*, **79** (2007) 291.

[102] Lyakh, D. I., Musiał, M., Lotrich, V. F., Bartlett, . J., Multireference nature of chemistry: The coupled-cluster view, *Chem. Rev.*, **112** (2012) 182.

[103] Andersson, K., Malmqvist, P.-A., Roos, B. O., Sadlej, A. J., Woliński, K., Second-order perturbation theory with a CASSCF reference function, *J. Phys. Chem.*, **94** (1990) 5483.

[104] Andersson, K., Malmqvist, P.-A., Roos, B. O., Second-order perturbation theory with a complete active space self-consistent field reference function, *J. Chem. Phys.*, **96** (1992) 1218.

[105] Pulay, P., A perspective on the CASPT2 method., *Int. J. Quantum Chem.*, **111** (2011) 3273.

[106] Ghigo, G., Roos, B. O., Malmqvist, P.-A., A modified definition of the zeroth order Hamiltonian in multii-configurational perturbation theory (CASPT2), *Chem. Phys. Lett.*, **396** (2004) 142.

[107] Coester, F., Kümmel, H., Short-range correlations in nuclear wave functions, *Nucl. Phys.*, **17** (1960) 477.

[108] Cižek, J., On correlation problem in atomic and molecular systems. Calculation of wavefunction components in ursell-type expansion using quantum-field theoretical methods, *J. Chem. Phys.*, **17** (1960) 4256.

[109] Crawford, C. D., III, H. F. S. An introduction to coupled cluster theory for computational chemists. In *Reviews in Computational Chemistry*, Volume 14, p. 33. Wiley, 2008.

[110] Rowe, D. J., Equations-of-motion method and extended shell model, *Rev. Mod. Phys.*, **40** (1968) 153.

[111] Sekino, H., Bartlett, R. J., A linear response, coupled cluster theory for excitation energy*, *Int. J. Quantum Chem.*, **18** (1984) 255.

[112] Geersten, J., Rittby, M., Bartlett, R. J., The equation-of-motion coupled cluster method: Excitation energies of Be and CO, *Chem. Phys. Lett.*, **164** (1989) 57.

[113] Kowalski, K., Piecuch, P., New coupled-cluster methods with singles, doubles, and noniterative triples for high accuracy calculations of excited electronic states, *J. Chem. Phys.*, **120**(4) (2004) 1715.

[114] Kowalski, K., Olson, R. M., Krishnamoorthy, S., Tipparaju, V., Apra, E., Role of many-body effects in describing low-lying excited states of pi-conjugated chromophores: High-level equation-of-motion coupled-cluster studies of fused porphyrin systems, *J. Chem. Theory Comput.*, **7** (2011) 2200.

[115] Piecuch, P., Kowalski, K., Pimienta, I. S. O., Method of moments of coupled cluster equations: externally correlated approaches employing configuration interaction wave function, *Int. J. Mol. Sci.*, **3** (2002) 475.

[116] Kowalski, K., Krishnamoorthy, S., Villa, O., Hammond, J. R., Govind, N., Active-space completely-renormalized equation-of-motion coupled-cluster formalism: Excited-state studies of green fluorescent protein, free-base porphyrin, and oligoporphyrin dimer, *J. Chem. Phys.*, **132** (2010) 154103.

[117] Lindgren, I., A Coupled-Cluster approach to the Many-Body Perturbation Theory for open-shell systems, *Int. J. Quantum Chem.*, **12** (1978) 13.

[118] Kowalski, K., Piecuch, P., Complete set of solutions of the generalized Bloch equation, *Int. J. Quantum Chem.*, **80** (2000) 757.

[119] Jeziorski, B., Monkhorst, H. J., Coupled-cluster method for multideterminantal reference states, *Phys. Rev. A*, **24** (1981) 1668.

[120] Lindgren, I., Mukherjee, D., On the connectivity criteria in the open-shell coupled-cluster theory for general model spaces, *Phys. Rep.*, **151** (1987) 93.

[121] Ivanov, V. V., Lyakh, D. I., Adamowicz, L., Multireference state-specific coupled-cluster methods. State-of-the-art and perspectives, *Phys. Chem. Chem. Phys.*, **11** (2009) 2355.

[122] Gomes, A. S. P., Jacob, C. R., Quantum-chemical embedding methods for treating local electronic excitations in complex chemical systems, *Annu. Rep. Prog. Chem., Sect. C*, **108** (2012) 222.

[123] Schwerdtfeger, P. *Relativistic electronic structure theory.Part II. Applications.* Elsevier, 2002.

[124] Haque, M. A., Mukherjee, D., Application of cluster expansion techniques to open-shells: Calculation of difference energies, *J. Chem. Phys.*, **23** (1985) 651.

[125] Infante, I., Vilkas, M., Ishikawa, I., U.Kaldor,, Visscher, L., A Fock space coupled cluster study on the electronic structure of the $UO_2$, $UO_2^+$, $U^{4+}$, and $U^{5+}$ species, *J. Chem. Phys.*, **127** (2007) 124308.

[126] Réal, F., Gomes, A. S. P., Visscher, L., Vallet, V., Eliav, E., Benchmarking electronic structure calculations on the bare $UO_2^{2+}$ ion: How different are single and multireference electron correlation methods?, *J. Phys. Chem. A*, **113**(45) (2009) 12504.

[127] Hughes, S. R., Kaldor, U., Fock-space coupled-cluster method: The (1,2) sector, *Phys. Rev. A*, **47** (1993) 4705.

[128] Malrieu, J.-P., Durand, P., Daudey, J.-P., Intermediate Hamiltonians as a new class of effective Hamiltonians, *J. Phys. A*, **18** (1985) 809.

[129] Mukherjee, D., Aspects of linked cluster expansion in general model space many-body perturbation and coupled-cluster theory, *Int. J. Quantum Chem.*, **30** (1986) 409.

[130] Koch, S., Derivation and pilot application of a scheme for intermediate Hamiltonians in Fock-space, *Theor. Chem. Acc.*, **81** (1991) 169.

[131] Meissner, L., On multiple solutions of the Fock-space coupled-cluster method, *Chem. Phys. Lett.*, **255** (1996) 254.

[132] Meissner, L., Fock-space coupled-cluster method in the intermediate Hamiltonian formulation: Model with singles and doubles, *J. Chem. Phys.*, **108** (1998) 9227.

[133] Meissner, L., Malinowski, P., Intermediate Hamiltonian formulation of the valence-universal coupled-cluster method for atoms, *Phys. Rev. A*, **61** (2000) 062510.

[134] Meissner, L., Malinowski, P., Nowaczyk, A., Application of the intermediate Hamiltonian valence-universal coupled-cluster method to atomic systems with one valence electron, *J. Chem. Phys.*, **116** (2002) 7362.

[135] Landau, A., Eliav, E., Kaldor, U., Intermediate Hamiltonian Fock-space coupled-cluster method, *Chem. Phys. Lett.*, **313** (1999) 399.

[136] Landau, A., Eliav, E., Ishikawa, Y., Kaldor, U., Intermediate Hamiltonian Fock-space coupled-cluster method: Excitation energies of barium and radium, *J. Chem. Phys.*, **113** (2000) 9905.

[137] Landau, A., Eliav, E., Intermediate Hamiltonian Fock-space coupled-cluster method in the one-hole one-particle sector: Excitation energies of xenon and radon, *J. Chem. Phys.*, **115** (2000) 6862.

[138] Landau, A., Eliav, E., Ishikawa, Y., Kaldor, U., Intermediate Hamiltonian Fock-space coupled cluster method in the one-hole one-particle sector: Excitation energies of xenon and radon, *J. Chem. Phys.*, **115** (2001) 6862.

[139] Visscher, L., Eliav, E., Kaldor, U., Formulation and implementation of the relativistic Fock-space coupled cluster method for molecules, *J. Chem. Phys.*, **115**(21) (2001) 9720.

[140] Infante, I., Gomes, A. S. P., Visscher, L., On the performance of the intermediate Hamiltonian Fock-space coupled-cluster method on linear triatomic molecules: The electronic spectra of $NpO^{2+}$, $NpO_2^{2+}$, and $PuO_2^{2+}$ , *J. Chem. Phys.*, **125** (2006) 074301.

[141] Meissner, L., Musiał, M. Intermediate Hamiltonian formulations of the Fock-space coupled-cluster method: details, comparisons, examples. In *Recent Progress in Coupled Cluster Methods*, p. 395. Springer, 2010.

[142] Klamt, A., Schuurmann, G., COSMO - a new approach to dielectric screening in solvents with explicit expressions for the screening energy and its gradient, *J. Chem. Soc. Perkin Trans.*, **2** (1993) 799.

[143] Tomasi, J., Mennucci, B., Cammi, R., Quantum mechanical continuum solvation models, *Chem. Phys.*, **105** (2005) 2999.

[144] Warshel, A., Levitt, M., Theoretical studies of enzymic reactions: Dielectric, electrostatic and steric stabilization of the carbonium ion in the reaction of lysozyme, *J. Mol. Biol.*, **103** (1976) 227.

[145] Gordon, M. S., Freitag, M. A., Bandyopadhyay, P., Jensen, J. H., Kairys, V., Stevens, W. J., The effective fragment potential method: A QM-based MM approach to modeling environmental effects in chemistry, *J. Phys. Chem. A*, **105** (2001) 293.

[146] Senatore, G., Subbaswamy, K. R., Density dependence of the dielectric constant of rare-gas crystals, *Phys. Rev. B*, **34** (1986) 5754.

[147] Wesolowski, T. A., Warshel, A., Frozen density functional approach for ab initio calculations of solvated molecules, *J. Phys. Chem.*, **97** (1993) 8050.

[148] Wesolowski, T. A., Weber, J., Kohn–Sham equations with constrained electron density: An iterative evaluation of the ground-state electron density of interacting molecules, *Chem. Phys. Lett.*, **248** (1996) 71.

[149] Neugebauer, J., Subsystem-based theoretical spectroscopy of biomolecules and biomolecular assemblies, *ChemPhysChem*, **10** (2009) 3148.

[150] Lieb, E. H., Thomas–Fermi and related theories of atoms and molecules, *Rev. Mod. Phys.*, **53** (1981) 603.

[151] Yang, W., Gradient correction in Thomas-Fermi theory, *Phys. Rev. A*, **34**(6) (1986) 4576.

[152] Wang, L., Teter, M. P., Kinetic-energy functional of the electron density, *Phys. Rev.*, **45**(23) (1992) 13196.

[153] Lembarki, A., Chermette, H., Obtaining a gradient-corrected kinetic-energy functional from the perdew-wang exchange functional, *Phys. Rev. A*, **50** (1994) 5328.

[154] Götz, A. W., Beyhan, S. M., Visscher, L., Performance of kinetic energy functionals for interaction energies in a subsystem formulation of density functional theory, *J. Chem. Theory Comput.*, **5** (2009) 3161.

[155] Jacob, C. R., Wesolowski, T. A., Visscher, L., Orbital-free embedding applied to the calculation of induced dipole moments in $CO_2$–X (X=He, Ne, Ar, Kr, Xe, Hg) van der Waals complexes, *J. Chem. Phys.*, **123** (2005) 174104.

[156] Laricchia, S., Fabiano, E., Sala, F. D., Frozen density embedding with hybrids, *J. Chem. Phys.*, **133** (2010) 164111.

[157] Neugebauer, J., Photophysical properties of natural light-harvesting complexes studied by subsystem density functional theory, *J. Phys. Chem. B*, **112** (2008) 2207.

[158] Govind, N., Wang, Y. A., da Silva, A. J. R., Carter, E., Accurate ab initio energetics of extended systems via explicit correlation embedded in a density functional environment, *Chem. Phys. Lett.*, **295** (1998) 129.

[159] Govind, N., Wang, Y. A., Carter, E. A., Electronic-structure calculations by first-principles density-based embedding of explicitly correlated systems, *J. Chem. Phys.*, **110** (1999) 7677.

[160] Huang, P., Carter, E. A., Self-consistent embedding theory for locally correlated configuration interaction wave functions in condensed matter, *J. Chem. Phys.*, **125** (2006) 084102.

[161] Gomes, A. S. P., Jacob, C. R., Visscher, L., Calculation of local excitations in large systems by embedding wave-function theory in density-functional theory, *Phys. Chem. Chem. Phys.*, **10** (2008) 5353.

[162] Pyykko, P., Relativistic effects in structural chemistry, *Chem. Rev.*, **88** (1988) 563.

[163] Dirac, P. A. M., On the theory of quantum mechanics, *Proc. Roy. Soc. London Ser. A*, **112** (1926) 661.

[164] Davydov, A. S. *Qunatum mechanics.* Pergamon, 1965.

[165] Visscher, L. An introduction to relativistic quantum chemistry. In *European Summerschool in Quantum Chemistry.* Per-Olof Widmark, 2009.

[166] Dyall, K. G., K. Fægri, J. *Introduction to Relativistic Quantum Chemistry.* Oxford, 2007.

[167] Breit, G., The effect of retardation on the interaction of two electrons, *Phys. Rev.*, **34** (1929) 553.

[168] Gaunt, J. A., Triplets of helium, *Proc. R. Soc. Lon.*, **A122** (1929) 513.

[169] Brown, G. E., Ravenhall, D. G., On the interaction of 2 electrons, *Proc. R. Soc. London*, **208** (1951) 552.

[170] Fleig, T., Relativistic wave-function based electron correlation methods, *Chem. Phys.*, **395** (2011) 2.

[171] Barysz, M. Two-component methods. From Douglas–Kroll to exact infinite–order method. In *Theoretical chemistry and physics of heavy and superheavy elements*. Springer, 2003.

[172] Foldy, L. L., Wouthuysen, S. A., On the Dirac theory of spin 1/2 particles and its non-relativistic limit, *Phys. Rev.*, **78** (1950) 29.

[173] Sikkema, J., Visscher, L., Saue, T., Ilias, M., The molecular mean-field approach for correlated relativistic calculations., *J. Chem. Phys.*, **131**(12) (2009) 124116.

[174] Liu, W., Ideas of relativistic quantum chemistry, *Mol. Phys.*, **108** (2010) 1679.

[175] Autschbach, J., Relativistic effects, *J. Chem. Phys.*, **136** (2012) 150902.

[176] Chang, C., Pelissier, M., Durand, P., Regular two-component Pauli-like effective Hamiltonians in Dirac theory, *Phys. Scr*, **34** (1986) 394.

[177] van Lenthe, E., Baerends, E. J., Snijders, J. G., Relativistic regular two–component Hamiltonians, *J. Chem. Phys.*, **99** (1993) 4597.

[178] van Lenthe, E., Baerends, E. J., Snijders, J. G., Relativistic total energy using regular approximations, *J. Chem. Phys.*, **101** (1994) 9783.

[179] Douglas, M., Kroll, N., Quantum electrodynamical corrections to the fine structure of helium, *Ann. Phys.*, **82** (1974) 89.

[180] Hess, B. A., Relativistic electronic-structure calculations employing a two-component no-pair formalism with external-field projection operators, *Phys. Rev. A*, **32** (1986) 3742.

[181] Nakajima, T., Hirao, K., The higher-order Douglas–Kroll transformation, *J. Chem. Phys.*, **113** (2000) 7786.

[182] Wolf, A., Reiher, M., Hess, B. A., The generalized Douglas–Kroll transformation, *J. Chem. Phys.*, **117** (2002) 9215.

[183] van Wüllen, C., Relation between different variants of the generalized Douglas–Kroll transformation through sixth order, *J. Chem. Phys.*, **120** (2004) 7307.

[184] Horwitz, E. P., Kalina, D. G., Diamond, H., Vandegrift, G. F., Schulz, W. W., The TRUEX process - a process for the extraction of the transuranic elements from nitric-acid wastes utilizing modified PUREX solvent, *Solvent Extr. Ion Exch.*, **3** (1985) 75.

[185] Ismail, N., Heully, J.-L., Saue, T., Daudey, J.-P., Marsden, C. J., Theoretical studies of the actinides: method calibration for the $UO_2^{2+}$ and $PuO_2^{2+}$ ions, *Chem. Phys. Lett.*, **300** (1999) 296.

[186] Groenewold, G. S., Gianotto, A. K., McIlwain, M. E., van Stipdonk, M. J., Kullman, M., Moore, D. T., Polfer, N., Oomens, J., Infante, I., Visscher, L., Siboulet, B., de Jong, W. A., Infrared spectroscopy of discrete uranyl anion complexes, *J. Phys. Chem. A*, **112** (2008) 508.

[187] Privalov, T., Macak, P., Schimmelpfennig, B., Fromager, E., Grenthe, I., Wahlgren, U., Electron transfer in uranyl(VI)–uranyl(V) complexes in solution, *J. Am. Chem. Soc.*, **126** (2004) 9801.

[188] Schreckenbach, G., Shamov, G. A., Theoretical actinide molecular science, *Acc. Chem. Res.*, **43**(1) (2010) 19.

[189] Michelini, M. C., Marçalo, J., Russo, N., Gibson, J. H., Gas-phase reactions of uranate ions $UO_2^-$, $UO_3^-$, $UO_4^-$, and $UO_4H^-$, with methanol: a convergence of experiment and theory, *Inorg. Chem.*, **49**(8) (2010) 3836.

[190] Iché-Tarrat, N., Marsden, C. J., Examining the performance of DFT methods in uranium chemistry: Does core size matter for a pseudopotential?, *J. Phys. Chem. A*, **112** (2008) 7632.

[191] Shamov, G. A., Schreckenbach, G., Vo, T. N., A comparative relativistic DFT and ab initio study on the structure and thermodynamics of the oxofluorides of uranium(IV), (V) and (VI), *Chem. Eur. J.*, **13** (2007) 4932.

[192] Schreckenbach, G., Shamov, G. A., Theoretical actinide molecular science, *Acc. Chem. Res.*, **43** (2010) 19.

[193] Rosa, A., Baerends, E. J., van Gisbergen, S. J. A., van Lenthe, E., Groeneveld, J. A., Snijders, J. G. S., Electronic spectra of $M(CO)_6$ (M = Cr, Mo, W) revisited by a relativistic TDDFT approach, *J. Am. Chem. Soc.*, **121**(44) (1999) 10356.

[194] van Gisbergen, S. J. A., Groeneveld, J. A., Rosa, A., Snijders, J. G., Baerends, E. J., Excitation energies for transition metal compounds from time-dependent density functional theory. Applications to $MnO_4^-$, $Ni(CO)_4$, and $Mn_2(CO)_{10}$, *J. Phys. Chem. A*, **103** (1999) 6835.

[195] van Gisbergen, S. J. A., Rosa, A., Ricciardi, G., Baerends, E. J., Time-dependent density functional calculations on the electronic absorption spectrum of free base porphin, *J. Chem. Phys.*, **111** (1999) 2499.

[196] Notter, F.-P., Dubillard, S., Bolvin, H., A theoretical study of the excited states of $AmO_2^{n+}$, n=1,2,3, *J. Chem. Phys.*, **128** (2008) 164315.

[197] Bast, R., Jensen, H. J. A., Saue, T., Relativistic adiabatic time-dependent density functional theory using hybrid functionals and noncollinear spin magnetization, *Int. J. Quantum Chem.*, **109** (2009) 2091.

[198] Fortier, S., Wu, G., Hayton, T. W., Synthesis of a nitrido-substituted analogue of the uranyl ion, $[N{=}U{=}O]^+$, *J. Am. Chem. Soc.*, **132** (2010) 6888.

[199] Spencer, L. P., Yang, P., Scott, B. L., Batista, E. R., Boncella, J. M., Uranium(VI) bis(imido) chalcogenate complexes: Synthesis and density functional theory analysis, *Inorg. Chem.*, **48** (2009) 2693.

[200] Réal, F., Vallet, V., Marian, C., Wahlgren, U., Theoretical investigation of the energies and geometries of photoexcited uranyl(VI) ion: A comparison between wave-function theory and density functional theory, *J. Chem. Phys.*, **127** (2007) 214302.

[201] Ruipérez, F., Danilo, C., Réal, F., Flament, J.-P., Vallet, V., Wahlgren, U., An ab initio theoretical study of the electronic structure of $UO_2^+$ and $[UO_2(CO_3)_3]^{5-}$, *J. Phys. Chem. A*, **113**(45) (2009) 1420.

[202] Bast, R. *Quantum chemistry beyond the charge density.* PhD thesis, I'Université Luis Pasteur, Strasburg, 2007.

[203] Matsika, S., Zhang, Z., Brozell, S. R., Blaudeau, J.-P., Wang, Q., Pitzer, R. M., Electronic structure and spectra of actinyl ions, *J. Phys. Chem. A*, **105** (2001) 3825.

[204] Zhou, M., Ismail, N., Marsden, C., Andrews, L., Infrared spectra of $UO_2$, $UO_2^+$, and $UO_2^-$ in solid neon, *J. Phys. Chem. A*, **104** (2000) 5495.

[205] Gagliardi, L., Roos, B. O., Multiconfigurational quantum chemical methods for molecular systems containing actinides, *Chem. Soc. Rev.*, **36**(6) (2007) 893.

[206] Macchia, G. L., Infante, I., Raab, J., Gibson, J. K., Gagliardi, L., A theoretical study of the ground state and lowest excited states of $PuO^{0/+/+2}$ and $PuO_2^{0/+/+2}$, *Phys. Chem. Chem. Phys.*, **48** (2008) 7278.

[207] Gomes, A. S. P., Visscher, L., Bolvin, H., Saue, T., Knecht, S., Fleig, T., Eliav, E., The electronic structure of the triiodide ion from relativistic correlated calculations: A comparison of different methodologies, *J. Chem. Phys.*, **133** (2010) 064305.

[208] te Velde, G., Bickelhaupt, F. M., van Gisbergen, S. J. A., Guerra, C. F., Baerends, E. J., Snijders, J. G., Ziegler, T., Chemistry with ADF, *J. Comput. Chem.*, **22** (2001) 931–967.

[209] Guerra, C. F., Snijders, J. G., te Velde, G., Baerends, E. J., Towards an order-N DFT method, *Theor. Chem. Acc.*, **99** (1998) 391.

[210] ADF2009.01, SCM, Theoretical Chemistry, Vrije Universiteit, Amsterdam, The Netherlands, `http://www.scm.com`.

[211] DIRAC, a relativistic ab initio electronic structure program, Release DIRAC08 (2008), written by L. Visscher, H. J. Aa. Jensen, and T. Saue, with new contributions from R. Bast, S. Dubillard, K. G. Dyall, U. Ekström, E. Eliav, T. Fleig, A. S. P. Gomes, T. U. Helgaker, J. Henriksson,

M. Iliaš, Ch. R. Jacob, S. Knecht, P. Norman, J. Olsen, M. Pernpointner, K. Ruud, P. Sałek, and J. Sikkema (see http://dirac.chem.sdu.dk).

[212] Ekström, U., Visscher, L., Bast, R., Thorvaldsen, A. J., Ruud, K., Arbitrary-order density functional response theory from automatic differentiation, *J. Chem. Theory Comput.*, **6**(7) (2010) 1971.

[213] Johnson, B. G., Gill, P. M. W., Pople, J. A., The performance of a family of density functional methods, *J. Chem. Phys.*, **98** (1993) 5612.

[214] van Lenthe, E., Baerends, E. J., Optimized Slater-type basis sets for the elements 1-118, *J. Comput. Chem.*, **24** (2003) 1142.

[215] Dyall, K. G., Relativistic double-zeta, triple-zeta, and quadruple-zeta basis sets for the actinides Ac-Lr, *Theor. Chem. Acc.*, **491** (2007) 483.

[216] Dunning, T. H., Gaussian basis sets for use in correlated molecular calculations. I. The atoms boron through neon and hydrogen, *J. Chem. Phys.*, **90** (1989) 1007.

[217] Kendall, R. A., Dunning, T. H., Harrison, R. J., Electron-affinities of the 1st-row atoms revisited - systematic basis-sets and wave-functions, *J. Chem. Phys.*, **96** (1989) 6796.

[218] Visscher, L., Saue, T., Approximate relativistic electronic structure methods based on the quaternion modified Dirac equation, *J. Chem. Phys.*, **113** (2000) 3996.

[219] Visscher, L., Approximate molecular relativistic Dirac-Coulomb calculations using a simple Coulombic correction, *Theor. Chem. Acc.*, **98** (1997) 68.

[220] Karlström, G., Lindh, R., Malmqvist, P.-A., Roos, B. O., Ryde, U., Veryazov, V., Widmark, P.-O., Cossi, M., Schimmelpfennig, B., Neogrady, P., Seijo, L., MOLCAS: a program package for computational chemistry, *Comput. Mat. Sci.*, **28** (2003) 222.

[221] Finley, J., Malmqvist, P.-A., Roos, B. O., , Serrano-Andrés, L., The multi-state CASPT2 method, *Chem. Phys. Lett.*, **288** (1998) 299.

[222] Douglas, N., Kroll, N. M., Quantum electrodynamical corrections to fine-structure of helium, *Ann. Phys.*, **82** (1974) 89.

[223] Hess, B. A., Relativistic electronic-structure calculations employing a 2-component no-pair formalism with external-fields projection operators, *Phys. Rev. A*, **33** (1986) 3742.

[224] Widmark, P.-O., Malmqvist, P.-A., Roos, B. O., Density-matrix averaged atomic natural orbital (ANO) basis-sets for correlated molecular wave-functions. 1-st row atoms, *Theor. Chem. Acc.*, **77** (1990) 291.

[225] Forsberg, N., Malmqvist, P.-A., Multiconfiguration perturbation theory with imaginary level shift, *Chem. Phys. Lett.*, **274** (1997) 196.

[226] Landau, A., Eliav, E., Ishikawa, Y., Kaldor, U., Mixed-sector intermediate Hamiltonian Fock-space coupled cluster approach, *J. Chem. Phys.*, **121** (2004) 6634.

[227] Lee, T. J., Taylor, P. R., A diagnostic for determining the quality of single-reference electron correlation methods, *Int. J. Quantum Chem.*, **23** (1989) 199.

[228] Fromager, E., Real, F., Wahlin, P., Wahlgren, U., Jensen, H. J. A., On the universality of the long-/short-range separation in multiconfigurational density-functional theory. II. Investigating f(0) actinide species, *J. Chem. Phys.*, **131** (2009) 054107.

[229] Tatsumi, K., Hoffmann, R., Bent cis d0 $MoO_2^{2+}$ vs. linear trans $d^0f^0$ $UO_2^{2+}$: a significant role for nonvalence 6p orbitals in uranyl, *Inorg. Chem.*, **19** (1980) 2656.

[230] Janak, J. F., Proof that $\frac{\partial E}{\partial n_i} = \epsilon$ in density-functional theory, *Phys. Rev. B*, **18**(12) (1978) 7165.

[231] Chong, D. P., Gritsenko, O. V., Baerends, E. J., Interpretation of the Kohn–Sham orbital energies as approximate vertical ionization potentials, *J. Chem. Phys.*, **117** (2002) 1760.

[232] Ruzsinszky, A., Perdew, J. P., Csonka, G. I., Vydrov, O. A., Scuseria, G. E., Spurious fractional charge on dissociated atoms: Pervasive and resilient self-interaction error of common density functionals, *J. Chem. Phys.*, **125** (2006) 194112.

[233] Mori-Sánchez, P., Cohen, A. J., Yang, W. T., Many-electron self-interaction error in approximate density functionals, *J. Chem. Phys.*, **125** (2006) 201102.

[234] Kümmel, S., Kronin, L., Orbital-dependent density functionals: Theory and applications, *Rev. Mod. Phys.*, **80** (2008) 3.

[235] Körzdorfer, T., Kümmel, S., Mundt, M., Self-interaction correction and the optimized effective potential, *J. Chem. Phys.*, **129** (2008) 014110.

[236] Tozer, D. J., Handy, N. C., On the determination of excitation energies using density functional theory, *Phys. Chem. Chem. Phys.*, **2** (2000) 2117.

[237] Krieger, J. B., Li, Y., Iafrate, J., Construction and application of an accurate local spin-polarized Kohn–Sham potential with integer discontinuity - exchange-only theory, *Phys. Rev. A*, **45** (1992) 101.

[238] Teale, A. M., Proft, F. D., Tozer, D. J., Orbital energies and negative electron affinities from density functional theory: Insight from the integer discontinuity, *J. Chem. Phys.*, **129** (2008) 044110.

[239] Cohen, A. J., Mori-Sanchez, P., Yang, W., Development of exchange–correlation functionals with minimal many-electron self-interaction error, *J. Chem. Phys.*, **126** (2007) 191109.

[240] Janesko, B. G., Henderson, T. M., Scuseria, G. E., Screened hybrid density functionals for solid-state chemistry and physics, *Phys. Chem. Chem. Phys.*, **11** (2009) 443.

[241] Henderson, T. M., Izmaylov, A. F., Scalmani, G., Scuseria, G. E., Can short-range hybrids describe long-range-dependent properties?, *J. Chem. Phys.*, **131** (2009) 044108.

[242] Song, J.-W., Watson, M. A., Nakata, A., Hirao, K., Core-excitation energy calculations with a long-range corrected hybrid exchange–correlation functional including a short-range gaussian attenuation (LCgau-BOP), *J. Chem. Phys.*, **129** (2008) 184113.

[243] Capelle, K., A bird's-eye view of density-functional theory, *J. Braz. Phys. Soc.*, **36** (2006) 1318.

[244] Jacquemin, D., Perpéte, E. A., Ciofini, I., Adamo, C., On the performances of the M06 family of density functionals for electronic excitation energies, *J. Chem. Theory Comput.*, **6** (2010) 1532.

[245] Preat, J., Jacquemin, D., V. Wathelet, J.-M. A., Perpéte, E. A., TD-DFT investigation of the UV spectra of pyranone derivatives, *J. Phys. Chem. A*, **110**(26) (2006) 8144.

[246] Rohrdanz, M. A., Martins, K. M., Herbert, J. M., A long-range-corrected density functional that performs well for both ground-state properties and time-dependent density functional theory excitation energies, including charge-transfer excited states, *J. Chem. Phys.*, **130** (2009) 054112.

[247] Silva-Junior, M. R., Schreiber, M., Sauer, S. P. A., Thiel, W., Benchmarks for electronically excited states: Time-dependent density functional theory and density functional theory based multireference configuration interaction, *J. Phys. Chem.*, **129** (2008) 104103.

[248] Silva-Junior, M. R., Schreiber, M., Sauer, S. P. A., Thiel, W., Benchmarks of electronically excited states: Basis set effects on CASPT2 results, *J. Phys. Chem.*, **133** (2010) 174318.

[249] Ciofini, I., Adamo, C., Accurate evaluation of valence and low-lying Rydberg states with standard time-dependent density functional theory, *J. Phys. Chem. A*, **111**(25) (2007) 5549.

[250] Sood, D. D., Patil, S., Chemistry of nuclear fuel reprocessing: Current status, *J. Radioanyl. Nuc. Chem.*, **203**(2) (1995) 547.

[251] Zhang, Z. T., Konduru, M., Dai, S., Overbury, S. H., Uniform formation of uranium oxide nanocrystals inside ordered mesoporous hosts and their potential applications as oxidative catalysts, *Chem. Commun.*, **20** (2002) 2406.

[252] de Jong, W. A., Visscher, L., Nieuwpoort, W. C., On the bonding and the electric field gradient of the uranyl ion, *J. Mol. Struct. THEOCHEM*, **458** (1999) 41.

[253] Zhang, Z., Pitzer, R. M., Application of relativistic quantum chemistry to the electronic energy levels of the uranyl ion, *J. Phys. Chem. A*, **103** (1999) 6880.

[254] Matsika, M., Pitzer, M., Actinyl ions in $Cs_2UO_2Cl_4$, *J. Phys. Chem. A*, **105** (2001) 637.

[255] Infante, I., Kovacs, A., Macchia, G. L., Shahi, A. R. M., Gibson, J. K., Gagliardi, L., Ionization energies for the actinide mono- and dioxides series, from Th to Cm: theory versus experiment., *J. Phys. Chem. A*, **114** (2010) 6007.

[256] Burns, P. C., Ikeda, Y., Czerwinski, K., Advances in actinide solid-state and coordination chemistry, *MRS Bulletin*, **35** (2010) 868.

[257] Nocton, G., Horeglad, P., Vetere, V., Pécaut, J., Dubois, L., Maldivi, P., Edelstein, N. M., Mazzanti, M., Synthesis, structure, and bonding of stable complexes of pentavalent uranyl, *J. Am. Chem. Soc.*, **132** (2009) 495.

[258] Choppin, G. R., Actinide speciation in the environment, *J. Radioanyl. Nuc. Chem.*, **273** (2007) 695.

[259] Liu, G., Jensen, M., Theoretical analysis of optical spectra of uranyl in complexes, *Chem. Phys. Lett.*, **499** (2010) 178.

[260] Ruipréz, F., Wahlgren, U., Charge-transfer in uranyl(VI) halides $[UO_2X_4]^2$ (X = F, Cl, Br, and I). A quantum chemical study of the absorption spectra, *J. Phys. Chem. A*, **114** (2010) 3615.

[261] Wang, X., Andrews, L., Li, J., Burst-n, B. E., Significant interactions between uranium and noble-gas atoms: Coordination of the $UO_2^+$ cation by Ne, Ar, Kr, and Xe atoms, *Angew. Chem. Int. Ed.*, **43** (2004) 2554.

[262] Jeziorski, B., Multireference coupled-cluster Ansatz, *Mol. Phys.*, **108** (2010) 3043.

[263] Gagliardi, L., Grenthe, I., Roos, B. O., A theoretical study of the structure of tricarbonatodioxouranate, *Inorg. Chem.*, **40** (2001) 2976.

[264] van Besien, E., Pierloot, K., Görller-Walrand, C., Electronic spectra of uranyl chloride complexes in acetone: a CASSCF/CASPT2 investigation, *Phys. Chem. Chem. Phys.*, **8** (2006) 4311.

[265] Dreuw, M., Head-Gordon, M., Failure of time-dependent density functional theory for long-range charge-transfer excited states: The zincbacteriochlorin-bacterlochlorin and bacteriochlorophyll-spheroidene complexes, *J. Am. Chem. Soc.*, **126**(12) (2004) 4007.

[266] Tokura, S., Tsuneda, T., Hirao, K., Long-range-corrected time-dependent density functional study on electronic spectra of five-membered ring compounds and free-base porphyrin, *J. Theor. Comput. Chem.*, **5**(4) (2006) 925.

[267] Govind, N., Valiev, M., Jensen, L., Kowalski, K., Excitation energies of zinc porphyrin in aqueous solution using long-range corrected time-dependent density functional theory, *J. Phys. Chem. A*, **113** (2009) 6041.

[268] Jensen, L., Govind, N., Excited states of DNA base pairs using long-range corrected time-dependent density functional theory, *J. Phys. Chem. A*, **113** (2009) 9761.

[269] Glaesemann, K. R., Govind, N., Krishnamoorthy, S., Kowalski, K., EOMCC, MRPT, and TDDFT studies of charge-transfer processes in mixed-valence compounds: Application to the spiro molecule, *J. Phys. Chem. A*, **114** (2010) 8764.

[270] O.Gritsenko,, Baerends, E. J., Asymptotic correction of the exchange–correlation kernel of time-dependent density functional theory for long-range charge-transfer excitations, *J. Chem. Phys.*, **119** (2004) 655.

[271] Neugebauer, J., Gritsenko, O. V., Baerends, E. J., Assessment of a simple correction for the long-range charge-transfer problem in time-dependent density functional theory, *J. Chem. Phys.*, **124** (2006) 214102.

[272] Peach, M. J. G., Benfield, P., Helgaker, T., Tozer, D. J., Excitation energies in density functional theory: An evaluation and a diagnostic test, *J. Chem. Phys.*, **128** (2008) 044118.

[273] Peach, M. J. G., Le Sueur, C. R., Ruud, K., Guillaume, M., Tozer, D. J., TDDFT diagnostic testing and functional assessment for triazene chromophores, *Phys. Chem. Chem. Phys.*, **11** (2009) 4465.

[274] Watkin, D. J., Denning, R. G., Prout, K., Structure of dicesium tetrachlorodioxouranium(VI), *Acta Crystallogr.*, **C47** (1991) 2517.

[275] DIRAC, a relativistic ab initio electronic structure program, Release DIRAC10 (2010), written by T. Saue, L. Visscher and H. J. Aa. Jensen, with contributions from R. Bast, K. G. Dyall, U. Ekström, E. Eliav, T. Enevoldsen, T. Fleig, A. S. P. Gomes, J. Henriksson, M. Iliaš, Ch. R. Jacob, S. Knecht, H. S. Nataraj, P. Norman, J. Olsen, M. Pernpointner, K. Ruud, B. Schimmelpfennig, J. Sikkema, A. Thorvaldsen, J. Thyssen, S. Villaume, and S. Yamamoto (see `http://dirac.chem.vu.nl`).

[276] Denning, R. G., Electronic structure and bonding in actinyl ions, *Struct. Bonding*, **79**(1) (1992) 215.

[277] Altmann, S. L., Herzig, P. *Point-group theory tables.* Oxford, 1994.

[278] Liu, G. K., Analysis of electronic states and energy level structure of uranyl in compounds, *J. Phys. Chem. A*, **115** (2011) 12419.

[279] Yabushita, S., Zhang, Z., Pitzer, R. M., Spin-orbit configuration interaction using the graphical unitary group approach and relativistic core potential and spin-orbit operators, *J. Phys. Chem. A*, **103** (1999) 5791.

[280] Yang, T., Tyagi, R., Zhang, Z., Pitzer, R. M., Configuration interaction studies on the electronic states of the CUO molecule, *Mol. Phys.*, **107** (2009) 1193.

[281] Dyall, K., Bonding and bending in the actinyls., *Mol. Phys.*, **96** (1999) 511.

[282] Tague, T. J., Andrews, L., Hunt, R. D., Matrix infrared spectra of the products of uranium-atom reactions with carbon monoxide and carbon dioxide, *J. Phys. Chem.*, **97** (1993) 10920.

[283] Liang, B., Andrews, L., Li, J., Bursten, B. E., Noble gas-actinide compounds: Evidence for the formation of distinct $CUO(Ar)_{4-n}(Xe)_n$ and $CUO(Ar)_{4-n}(Kr)_n$ (n = 1, 2, 3, 4) complexes, *J. Am. Chem. Soc.*, **124** (2002) 9016.

[284] Andrews, L., Liang, B., Li, J., Bursten, B. E., Noble gas-actinide complexes of the CUO molecule with multiple Ar, Kr, and Xe atoms in noble-gas matrices, *J. Am. Chem. Soc.*, **125** (2003) 3126.

[285] Liang, B., Andrews, L., Li, J., Bursten, B. E., Bonding of multiple noble-gas atoms to cuo in solid neon: CUO(Ng)(n) (Ng = Ar, Kr, Xe; n=1, 2, 3, 4) complexes and the singlet-triplet crossover point, *Chem. Eur. J.*, **9** (2003) 4781.

[286] Goncharov, V., Kaledin, L. A., Heaven, M. C., Probing the electronic structure of $UO^+$ with high-resolution photoelectron spectroscopy, *J. Phys. Chem.*, **125** (2006) 133202.

[287] Jin, J., Gondalia, R., Heaven, M. C., Electronic spectroscopy of $UO_2Cl_2$ in isolated solid Ar, *J. Phys. Chem. A*, **113** (2009) 12724.

[288] Infante, I., Andrews, L., Wang, X., Gagliardi, L., Noble gas matrices may change the electronic structure of trapped molecules: The UO(2)(Ng)(4) [Ng = Ne, Ar] case, *Chem. Eur. J.*, **16** (2010) 12804.

[289] Malmqvist, P.-A., Pierloot, K., Shahi, A. R. M., Cramer, C. J., L.Gagliardi,, The restricted active space followed by second-order perturbation theory method: Theory and application to the study of $CuO_2$ and $Cu_2O_2$ systems, *J. Chem. Phys.*, **128** (2008) 204109.

[290] Klüner, T., Wang, Y. A., Govind, N., Carter, E. A., Prediction of electronic excited states of adsorbates on metal surfaces from first principles, *Phys. Rev. Lett.*, **86** (2001) 5954.

[291] Klüner, T., Govind, N., Wang, Y. A., Carter, E. A., Periodic density functional embedding theory for complete active space self-consistent field and configuration interaction calculations: Ground and excited states, *J. Chem. Phys.*, **116** (2002) 42.

[292] Höfener, S., Gomes, A. S. P., Visscher, L., Molecular properties via a subsystem density functional theory formulation: A common framework for electronic embedding, *J. Chem. Phys.*, **136** (2012) 044104.

[293] Wesołowski, T. A., Application of the DFT-based embedding scheme using an explicit functional of the kinetic energy to determine the spin density of $Mg^+$ embedded in Ne and Ar matrices., *Chem. Phys. Lett.*, **311** (1999) 87.

[294] Wesołowski, T. A., Tran, F., Gradient-free and gradient-dependent approximations in the total energy bifunctional for weakly overlapping electron densities, *J. Chem. Phys.*, **118** (2003) 2072.

[295] Fux, S., Kiewisch, K., Jacob, C. R., Neugebauer, J., Reiher, M., Analysis of electron density distributions from subsystem density functional theory applied to coordination bonds, *Chem. Phys. Lett.*, **461** (2008) 353.

[296] Kiewisch, K., Eickerling, G., Reiher, M., Neugebauer, J., Topological analysis of electron densities from Kohn–Sham and subsystem density functional theory, *J. Chem. Phys.*, **128** (2008) 044114.

[297] Beyhan, S. M., Götz, A. W., Jacob, C. R., Visscher, L., The weak covalent bond in NgAuF (Ng=Ar, Kr, Xe): A challenge for subsystem density functional theory, *J. Chem. Phys.*, **132** (2010) 044114.

[298] TURBOMOLE V5.10 2008, a development of University of Karlsruhe and Forschungszentrum Karlsruhe GmbH, 1989-2007, TURBOMOLE GmbH, since 2007; available from `http://www.turbomole.com`.

[299] Treutler, O., Ahlrichs, R., Efficient molecular numerical integration schemes, *J. Chem. Phys.*, **102** (1995) 346.

[300] von Arnim, M., Ahlrichs, R., Performance of parallel TURBOMOLE for density functional calculations, *J. Comput. Chem.*, **19** (1998) 1746.

[301] Eichkorn, K., Weigend, F., Treutler, O., Ahlrichs, R., Auxiliary basis sets for main row atoms and transition metals and their use to approximate Coulomb potentials, *Theor. Chem. Acc.*, **97** (1997) 119.

[302] Cao, X., Dolg, M., Segmented contraction scheme for small-core actinide pseudopotential basis sets, *J. Mol. Struct. THEOCHEM*, **673** (2004) 203.

[303] Nicklass, A., Dolg, M., Stoll, H., Preuss, H., An-initio energy-adjusted pseudopotentials for the noble-gases ne through Xe - calculation of atomic dipole and quadrupole polarizabilities, *J. Chem. Phys.*, **102** (1995) 8942.

[304] ADF2010.01, SCM, Theoretical Chemistry, Vrije Universiteit, Amsterdam, The Netherlands, `http://www.scm.com`.

[305] Cortona, P., Self-consistently determined properties of solids without band-structure calculations, *Phys. Rev. B*, **44**(16) (1991) 8454.

[306] Cortona, P., Direct determination of self-consistent total energies and charge densities of solids: A study of the cohesive properties of the alkali halides, *Phys. Rev. B*, **46**(4) (1992) 2008.

[307] Jacob, C. R., Beyhan, S. M., Bulo, R. E., Gomes, A. S. P., Götz, A. W., Kiewisch, K., Sikkema, J., Visscher, L., Software news and updates PyADF—a scripting framework for multiscale quantum chemistry, *J. Comput. Chem.*, **32**(10) (2011) 2328.

[308] Jacob, C. R., Beyhan, S. M., Visscher, L., Exact functional derivative of the nonadditive kinetic-energy bifunctional in the long-distance limit, *J. Chem. Phys.*, **126** (2007) 234116.

[309] Pavanello, M., Neugebauer, J., Linking the historical and chemical definitions of diabatic states for charge and excitation energy transfer reactions in condensed phase, *J. Chem. Phys.*, **135** (2011) 134113.

[310] von Fermi, I., Eine statistische Methode zur Bestimmung einiger Eigenschaften des Atomsund ihre Anwendung auf die Theorie des periodischen Systems der Elemente., *Z. Phys.*, **36** (1928) 73.

[311] Lastra, J. M. G., Kamiński, J. W., Wesolowski, T. A., Orbital-free effective embedding potential at nuclear cusps, *J. Chem. Phys.*, **129** (2008) 074107.

[312] Casida, M. E., Wesolowski, T. A., Generalization of the Kohn–Sham equations with constrained electron density formalism and its time-dependent response theory formulation, *Int. J. Quantum Chem.*, **96** (2004) 577.

[313] Meissner, L., A Fock-space coupled-cluster method fully utilizing valence universal strategy, *J. Chem. Phys.*, **103** (1995) 8014.

[314] Jankowski, K., Meissner, L., Rubiniec, K., Model study of the impact of orbital choice on the accuracy of coupled-cluster energies. III. state-universal coupled-cluster method, *Int. J. Quantum Chem.*, **67** (1998) 239.

[315] Peach, M. J. G., Williamson, M. J., Tozer, D. J., Influence of triplet instabilities in TDDFT, *J. Chem. Theory Comput.*, **7** (2011) 3578.

[316] Bursten, B. E., Drummond, M. L., Li, J., The quantum chemistry of d- and f-elements complexes: from an approximate existence to functional hapiness, *Faraday Discuss.*, **124** (2003) 1.

[317] Odoh, S. O., Schreckenbach, G., Theoretical study of the structural properties of plutonium IV and VI complexes, *J. Phys. Chem. A*, **114** (2010) 1957.

[318] Clavaguéra-Sarrio, C., Ismail, N., Marsden, C. J., Bégue, D., Pouchan, C., Calculation of harmonic and anharmonic vibrational wavenumbers for triatomic uranium compounds XUY, *Chem. Phys.*, **302** (2004) 1.

[319] ADFGUI 2011, SCM, Amsterdam, The Netherlands, `http://www.scm.com`.

[320] Dułak, M., Wesołowski, T. A., On the electron leak problem in orbital-free embedding calculations, *J. Chem. Phys.*, **124** (2006) 164101.

[321] Bernard, Y. A., Dułak, M., Kamiński, J. W., Wesołowski, T. A., The energy-differences based exact criterion for testing approximations to the functional for the kinetic energy of non-interacting electrons, *J. Phys A-Mat. Theor.*, **41** (2008) 055302.

[322] Čižek, J., Paldus, J., Stability conditions for the solutions of the Hartree–Fock equations for atomic and molecular systems. Application to the Pi electron model of cyclic polyenes, *J. Chem. Phys.*, **47** (1967) 3976.

[323] Lutnæs, O. B., Helgaker, T., Jaszuński, M., Spin–spin coupling constants and triplet instabilities in Kohn–Sham theory, *Mol. Phys.*, **108** (2010) 2579.

[324] Kovacs, A., Konings, R. J. M., Computed vibrational frequencies of actinide oxides $AnO^{0/+/2+}$ and $AnO_2^{0/+/2+}$ (An = Th, Pa, U, Np, Pu, Am, Cm), *J. Phys. Chem. A*, **115** (2012) 6646.

[325] Wang, D., van Gunsteren, W. F., Chai, Z., Recent advances in computational actinoid chemistry., *Chem. Soc. Rev.*, 2012.

[326] Steele, H., Taylor, R. J., A theoretical studies of the inner-sphere disproportionation reaction mechanism of the pentavalent actinyl ions, *Inorg. Chem.*, **46** (2007) 6311.

[327] Infante, I., Andrews, L., Wang, X., Gagliardi, L., Noble gas matrices may change the electronic structure of trapped molecules: The UO(2)(Ng)(4) [Ng = Ne, Ar] case, *Chem. Eur. J.*, **43** (2010) 12804.

[328] Mizuoka, K., Tsushima, S., Hasegawa, M., Hoshi, T., Ikeda, Y., Electronic spectra of pure uranyl(V) complexes: charcteristic absorption bands duo to a $U^VO_2$ core in visable and near-infrared regions, *Inorg. Chem.*, **44** (2005) 6211.

[329] Minasian, S. G., Keith, J. M., Batista, E. R., Boland, K. S., Clark, D. L., Conradson, S. D., Kozimor, S., Martin, R. L., Schwarz, D. E., Shuh, D. K., Wagner, G. L., Wilkerson, M. P., Wolfsberg, L. E., Yang, P., Determining relative f and d orbital contributions to M-Cl covalency in MCl(6)(2-) (M = Ti, Zr, Hf, U) and UOCl(5)(-) using Cl K-Edge X-ray absorption spectroscopy and Time-Dependent Density Functional Theory., *J. Am. Chem. Soc.*, **134** (2012) 5586.

[330] Spezia, R., Siboulet, B., Abadie, S., Vuilleumier, R., Vitorge, P., Stability and instability of the isoelectronic $UO_2^{2+}$ and $PaO_2^+$ actinyl oxo-cations in aqueous solution from Density Functional Theory based molecular dynamics, *J. Phys. Chem. B*, **115** (2011) 3560.

[331] Ekstrom, A., Kinetics and mechanism of the disproportionation of uranium(V), *Inorg. Chem.*, **13** (1974) 2237.

[332] Madic, C., B, G., Morriseau, J. C., Moulin, J. P., Cation-cation complexes of pentavalent actinides-I: Spectrophotometric study of complexes between neptunium (V) and $UO_2^{2+}$ and $NpO_2^{2+}$ ions in aqueous perchloric and nitric solutions, *J. Inorg. Nucl. Chem.*, **41**(1027) (1979.

[333] Burdet, F., Pecaut, J., Mazzanti, M., Isolation of a tetrameric cation-cation complex of pentavalent uranyl, *J. Am. Chem. Soc.*, **128** (2006) 16512.

[334] Mougel, V., Pécaut, J., Mazzanti, M., New polynuclear U(IV)-U(V) complexes from U(IV) mediated uranyl(V) disproportionation., *Chem. Commun.*, **48** (2012) 868.

[335] Cohen, D., The preparation and spectrum of uranium(V) ions in aqueous solutions, *J. Inorg. Nucl. Chem.*, **32** (1970) 3525.

[336] Mizuoka, K., Ikeda, Y., Structural changes of uranyl moiety with reduction from U(VI) to U(V), *Radiochim. Acta.*, **92** (2004) 631.

[337] Takao, K., Kato, M., Takao, S., Nagasawa, A., Bernhard, G., Hennig, C., Ikeda, Y., Molecular structure and electrochemical behavior of uranyl(VI) complex with pentadentate Schiff base ligand: Prevention of uranyl(V) cation-cation interaction by fully chelating equatorial coordination sites, *Inorg. Chem.*, **49** (2010) 2349.

[338] Takao, K., Kato, M., Takao, S., Nagasawa, A., Scheinost, A. C., Bernhard, G., Hennig, C., Ikeda, Y., Structural and electrochemical studies on uranyl(VI) complex with pentadentate Schiff base ligand: A guide to stable uranyl(V), *IOP Conf. Series Materials Science and Engineering*, **9** (2010) 012030.

[339] Gritzner, G., Selbin, J., Studies of dioxouranium(V) dimethylsulphoxide in dimethylsulphoxide, *J. Inorg. Nucl. Chem.*, **30** (1968) 1799.

[340] Plötner, J., Tozer, D. J., Dreuw, A., Dependence of excited state potential energy surfaces on the spatial overlap of the Kohn–Sham orbitals and the amount of nonlocal Hartree–Fock exchange in time-dependent density functional theory, *J. Chem. Theory Comput.*, **6**(8) (2010) 2315.

[341] Andzelm, J., Rinderspacher, C., Rawlett, A. M., Dougherty, J., Baer, R., Govind, N., Performance of DFT methods in the calculation of optical spectra of TCF-chromophores, *J. Chem. Theory Comput.*, **5** (2009) 2835.

[342] Lopata, K., Reslan, R., Kowaska, M., Neuhauser, D., Govind, N., Kowalski, K., Excited-state studies of polyacenes: A comparative picture using EOMCCSD, CR-EOMCCSD(T), range-separated (LR/RT)-TDDFT, TD-PM3, and TD-ZINDO, *J. Chem. Theory Comput.*, **7** (2011) 3686.

[343] Ipatov, A., Cordova, F., Doriol, L. J., Casida, M. E., Excited-state spin-contamination in time-dependent density-functional theory for molecules with open-shell ground states, *J. Mol. Struct. THEOCHEM*, **914** (2009) 60.

[344] Tecmer, P., Bast, R., Ruud, K., Visscher, L., Charge-transfer excitations in uranyl tetrachloride ($[UO_2Cl_4]^2$): How reliable are electronic spectra from relativistic time-dependent density functional theory?, *J. Phys. Chem. A*, **116** (2012) 7397.

[345] Kowalski, K., Piecuch, P., New coupled-cluster methods with singles, doubles, and noniterative triples for high accuracy calculations of excited electronic states, *J. Chem. Phys.*, **120** (2004) 1715.

[346] Wloch, M., Gour, J. R., Kowalski, K., Piecuch, P., Extension of renormalized coupled-cluster methods including triple excitations to excited electronic states of open-shell molecules, *J. Chem. Phys.*, **122** (2005) 214107.

[347] Dau, P. D., Su, J., Liu, H.-T., Huang, D.-L., Li, J., Wang, L.-S., Photoelectron spectroscopy and the electronic structure of the uranyl tetrachloride dianion: $UO_2Cl_4^2$, *J. Phys. Chem.*, **137**(6) (2012) 064315.

[348] Dau, P. D., Su, J., Liu, H.-T., Liu, J.-B., Huang, D.-L., Li, J., Wang, L.-S., Observation and investigation of the uranyl tetrafluoride dianion ($UO_2F_4^{2-}$) and its solvation complexes with water and acetonitrile, *Chem. Sci.*, **3**(4) (2012) 1137.

[349] Valiev, M., Bylaska, E., Govind, N., Kowalski, K., Straatsma, T., van Dam, H., Wang, D., Nieplocha, J., Apra, E., Windus, T., de Jong, W., NWChem: A comprehensive and scalable open-source solution for large scale molecular simulations, *Comput. Phys. Commun.*, **181** (2010) 1477.

[350] van Dam, H., de Jong, W. A., Bylaska, E., Govind, N., Kowalski, K., Straatsma, T., Valiev, M., NWChem: scalable parallel computational chemistry, *Rev. Comput. Mol. Sci.*, **1** (2011) 888.

[351] NWChem 6.1, `http://www.nwchem-sw.org`.

[352] Dunning, T. H., Gaussian basis functions for use in molecular calculations. I. contraction of (9s5p) atomic basis sets for the first-row atoms, *J. Chem. Phys.*, **53** (1970) 2823.

[353] Küchle, W., Dolg, M., Stoll, H., Preuss, H., Ab initio pseudopotentials for Hg through Rn, *Mol. Phys.*, **74** (1991) 1245.

[354] Hirata, S., Head-Gordon, M., Time-dependent density functional theory within the Tamm-Dancoff approximation, *Chem. Phys. Lett.*, **314** (1999) 291.

[355] Sanjay, M. P., Kumbharkhane, A. C., Mehrotra, S. C., Dielectric study of dimethyl sulfoxide-water mixtures using the time-domain technique, *J. Chem. Soc., Faraday Trans.*, **88** (1992) 433.

[356] Hirata, S., Tensor contraction engine: Abstraction and automated parallel implementation of configuration-interaction, coupled-cluster, and many-body perturbation theories, *J. Phys. Chem. A*, **107** (2003) 9887.

[357] Hirata, S., Higher-order equation-of-motion coupled-cluster methods, *J. Chem. Phys.*, **121** (2004) 51.

[358] Hirata, S., Fan, P.-D., Auer, A. A., Nooijen, M., Piecuch, P., Combined coupled-cluster and many-body perturbation theories, *J. Chem. Phys.*, **121** (2004) 12197.

[359] Kowalski, K.and Krishnamoorthy, S., Olson, R., Tipparaju, V., Apra, E. Scalable implementations of accurate excited-state coupled cluster theories: Application of high-level methods to porphyrin-based systems. In *International Conference for High Performance Computing, Networking, Storage and Analysis*, 2011.

[360] de Kock, R. I., Baerends, E. J., Boerrighter, P. M., Snijders, J. G., On the nature of the first excited-state of uranyl ion, *Chem. Phys. Lett.*, **105** (1984) 308.

[361] Dyall, K. D., Formal analysis of effective core potential methods, *J. Chem. Inf. Comput. Sci.*, **41** (2001) 30.

# List of publications

1. Paweł Tecmer, André Severo Pereira Gomes, Ulf Ekström and Lucas Visscher
"Electronic spectroscopy of $UO_2^{2+}$, $NUO^+$ and NUN: An Evaluation of Time-Dependent Density Functional Theory for actinides"
*Phys. Chem. Chem. Phys.*, **2011**, 13, 6249–6259.

2. Paweł Tecmer, Radovan Bast, Kenneth Ruud and Lucas Visscher
"Charge-transfer excitations in uranyl tetrachloride ($[UO_2Cl_4]^{2-}$): how reliable are electronic spectra from relativistic time-dependent density functional theory?"
*J. Phys. Chem. A*, **2012**, 116, 7397–7404.

3. Paweł Tecmer, Henk van Lingen, André Severo Pereira Gomes and Lucas Visscher
"The Electronic Spectrum of $CUONg_4$ (Ng = Ne, Ar, Kr, Xe): New Insights in the Interaction of the CUO Molecule with Noble Gas Matrices" accepted for publication in *J. Chem. Phys.*

4. Paweł Tecmer, Niranjan Govind, Karol Kowalski, Wibe A. de Jong and Lucas Visscher
"Realiable theoretical modeling of the electronic spectra of $U^{VI}O_2$(saldien) and $[U^{V}O_2(\text{saldien})]^-$ complexes."

submitted to *J.* Chem. Phys.

5. Paweł Tecmer, André Severo Pereira Gomes, Stefan Knecht and Lucas Visscher
   "Importance of spin–orbit and Gaunt interactions in the electronic spectra of small uranium compounds: $UO_2^{2+}$, $NUO^+$ and NUN. The relativistic time-dependent density functional theory and intermediate Hamiltonian Fock-space coupled cluster study."
   in preparation

6. Paweł Tecmer, Niranjan Govind, Wibe A. de Jong and Lucas Visscher
   "Implementation of static frozen density embedding scheme in NWChem quantum chemical package. Application to $U^{VI}O_2$(saldien) and $[U^{V}O_2(\text{saldien})]^-$ complexes."
   in preparation

# List of Figures

# List of Tables

# Acknowledgments

In this place, I would like to give many thanks to a number of people, who contributed directly and indirectly in the development of this thesis.

First and foremost, I would like to thank my supervisor Lucas Visscher. I am very grateful that I had a chance to be a member of your group. I am really impressed by your knowledge and passion to relativistic quantum chemistry as well as chemistry of heavy elements, in particular to actinides. You have shown me how to tackle and solve scientifically challenging problems, I have learned a lot from you. I am also very grateful that I could join so many interesting schools and conferences.

Second, I would like to thank André Severo Pereira Gomes, who introduced me into electronic spectroscopy of actinides and assisted with the technically complicated IHFSCC calculations in the Dirac program.

Many other people have contributed through scientific discussions, and I shall like to mention here Katharina Boguslawski, Radovan Bast, Stefan Knecht, Ulf Ekström, Sebastian Höefener, Trond Saue, Hans Jørgen Aagaard Jensen, Łukasz Mentel, Andranik Kazaryan, Gopakumar Gopinadhanpillai, Kenneth Ruud, Markus Reiher, Samuel Fux, Jetze Sikkema, Christoph Jacob, Florent Réal, Fernando Ruipérez, Ivan Infante, Evert Jan Baerends, Oleg Gritsenko, Vladimir Pelmenschikov, Andreas Götz, Mojgan Heshmat, Karin Kiewisch, Klaas Giesbertz and Dariusz Kędziera.

Thanks to all the people at the PNNL, in particular Niranjan Govind, Karol Kowalski, Eric Bylaska and Bert de Jong.

Many thanks to the SCM team, in particular I shall like to mention here Erik

van Lenthe, Pier Philipsen [1] , Olivier Visser, Stan van Gisbergen, Alexei Yakovlev, Stefano Borini and Mirco Franchini.

In the same way I would like to thank Dirac community people.

I would like to thank all the people at the Theoretical Chemistry group at the VU University Amsterdam, in particular Sharmila Jaddoe, Rosa Bulo, Matt Kundrat and Frieda Vansina for making very nice and friendly atmosphere.

I also would like to thank all the people at the Theoretical Chemistry group at ETH Zürich.

Many thanks to my master students: Anna Hehn and Henk van Lingen, I really enjoyed working with you.

Finally, a cordial thanks to my polish friends in Amsterdam Ela Krępska and Olek Banaś as well as the beach volleyball team at the VU.

Składam serdeczne podziekowania dla mojej rodziny, w szczególności chciałbym wymienić tutaj mamę, tatę, Dawida, tesćiów, Łukasza, bacię Jadzię, Agnieszkę i Paulinę za wsparcie podczas studiow doktorskich.

Kasiu, dziękuje Ci za ogrom pracy, który włożyłaś podczas pisania mojej pracy doktorskiej i Twoje liczne komentarze. Nasze naukowe dyskusje znacznie wpłynęły na kształt i rozwój tej pracy oraz zaowocowały wieloma nowymi pomysłami. Oby było tak dalej, ♡.

[1] An additional thank for the translation of the summary of this thesis in Dutch.